Fakultät für Mathematik und Naturwissenschaften | RWTH AACHEN UNIVERSITY

Structural and Electronic Characterization of MBE-grown Topological Insulator Thin Films

Von der Fakultät für Mathematik und Naturwissenschaften der RWTH Aachen University zur Erlangung des akademischen Grades einer Doktorin der Naturwissenschaften genehmigte Dissertation

vorgelegt von

Xiao Hou, M.Sc.

aus

China

Berichter*:* Priv. Doz. Dr. Lukasz Plucinski

Prof. Dr. rer. nat. Joachim Mayer

Tag der mündlichen Prüfung: 04.11.2025

Diese Dissertation ist auf den Internetseiten der Universitätsbibliothek verfügbar.

Eidesstattliche Erklärung

Declaration of Authorship

I, Xiao Hou

declare that this thesis and the work presented in it are my own and has been generated by me as the result of my own original research.

Hiermit erkläre ich an Eides statt / I do solemnely swear that:

1. This work was done wholly or mainly while in candidature for the doctoral degree at this faculty and university;

2. Where any part of this thesis has previously been submitted for a degree or any other qualification at this university or any other institution, this has been clearly stated;

3. Where I have consulted the published work of others or myself, this is always clearly attributed;

4. Where I have quoted from the work of others or myself, the source is always given. This thesis is entirely my own work, with the exception of such quotations;

5. I have acknowledged all major sources of assistance;

6. Where the thesis is based on work done by myself jointly with others, I have made clear exactly what was done by others and what I have contributed myself;

7. Parts of this work have been published before as:

Jalil, Abdur Rehman, Xiao Hou et al. "Phase-Selective Epitaxy of Trigonal and Orthorhombic Bismuth Thin Films on Si (111)." Nanomaterials 13.14 (2023): 2143.

Munich, 24.11.2025

Abstract

As a new class of quantum matter, topological insulators (TIs) have attracted significant attention in the field of condensed matter physics due to their exotic intrinsic physical properties. TIs, which exhibits either two-dimensional (2D) or three-dimensional (3D) topology, are materials that are insulating in the bulk and conducting at the edge or surface. This behavior arises from the presence of the gapless edge or surface states at the boundary, which are protected by time-reversal symmetry and exhibit spin momentum locking. Such unique properties provide an excellent platform for developing novel electronic and spintronic devices, as well as potential applications including topological quantum computing.

This work focuses on the systematic study of epitaxial growth of 2D and 3D TIs via molecular beam epitaxy (MBE) and atomic-scale structural characterization via scanning transmission electron microscope (STEM). In addition, the surface electronic structures of TI thin films and bulk crystals are investigated using angle-resolved photoemission spectroscopy (ARPES).

Bi is classified as a higher-order topological insulator (HOTI); however, Bi in thin-film form is proposed to exhibit 2D topology. This study is extended in-depth to achieve controlled growth of various Bi phases, including the trigonal phase (demonstrated as HOTI) and the orthorhombic phase (theoretically predicted to be a 2D TI). It has also been observed that the thickness plays a significant role in controlling the lattice strain of the orthorhombic phase, which directly influences its topology. Later, Sb is incorporated into the Bi thin film to form the BiSb alloy, which can also serve as a promising platform for realizing a 2D TI.

Apart from 2D TIs, 3D TIs, especially $Bi_xSb_yTe_z$, suffer from the high density of point defects, resulting in the formation of electronic puddles. However, by replacing Sb with Sn, which is also a p-type dopant, the $Sn_xBi_yTe_z$ alloy presents a new material platform, which has been adopted in this study. Various stoichiometries such as $SnBi_4Te_7$, $SnBi_2Te_4$ and $Sn_2Bi_2Te_5$ are grown and structurally characterized, providing another opportunity to engineer the topological band structure.

Finally, the focus is shifted to $Mn_xBi_yTe_z$, a magnetic topological insulator (MTI), where the Mn acts as magnetic dopant incorporated into Bi_2Te_3. Particularly, $MnBi_6Te_{10}$ has been intensively investigated by circular dichroism ARPES, revealing the orbital angular momentum features of the electronic band structure of one of the two Bi_2Te_3 terraces on the cleaved crystal. The results are further supported by theoretical calculations.

In short, this study not only provides an alternative platform to yield 2D topology, but also offers a promising approach to tune the Fermi level of 3D TIs through topological band engineering via Sn doping. This work can be further extended to fabricate novel and

sophisticated quantum device architectures on a scalable platform.

Contents

1 Introduction **1**

2 Theoretical Background **4**
2.1 Quantum Hall Effect and Quantum Spin Hall Effect 4
2.2 Band Inversion and Origin of the Topological State 6
2.2.1 Spin Orbit Coupling 6
2.3 Two-dimensional Topological Insulator (2D TI) 9
2.4 Three-dimensional Topological Insulator (3D TI) 10
2.4.1 Strong Topological Insulator 11
2.5 High-order Topological Insulator (HOTI) 12
2.6 Magnetic Topological Insulator (MTI) 13
2.7 Topological Phase Transition 14

3 Experimental Setup **16**
3.1 Molecular Beam Epitaxy (MBE) 16
3.1.1 Van der Waals Epitaxy 19
3.1.2 Substrate Preparation 20
3.2 Surface Characterization 21
3.2.1 Scanning Electron Microscopy (SEM) 21
3.2.2 Atomic Force Microscopy (AFM) 23
3.3 Structural Characterization 24
3.3.1 X-Ray Diffraction (XRD) 24
3.3.2 Transmission Electron Microscopy (TEM) 27
3.4 Angle-resolved Photoemission Spectroscopy (ARPES) 35
3.4.1 Sample Preparation 35
3.4.2 ARPES machine at PGI-6 37
3.4.3 NanoESCA Beamline at Elettra 40

4 Current Challenges in the field of Topological Insulator **42**
4.1 Material Challenges 43
4.1.1 2D Topological Insulator 43
4.1.2 3D Topological Insulator 43
4.2 Growth Challenges 47
4.2.1 Substrate Influenced Challenge 47
4.2.2 General Defects 49

5 Phase-Selective Epitaxy of Trigional and Orthorhombic Bismuth Thin Films **57**
5.1 Growth of Bi/BiSb Thin Films on Si (111) Substrate 60
5.1.1 Growth Optimization of Bi_{TRIG} Phase 60
5.1.2 Thickness-dependent Growth of Bi_{TRIG} thin film 63
5.1.3 Growth Realization of BiSb Thin Films 64
5.2 Growth Transformation towards Bi_{ORTH} Phase 65
5.2.1 Growth Optimization of Bi_{ORTH} Phase 65
5.2.2 Thickness-dependent Growth of Bi_{ORTH} thin film 67
5.2.3 Lattice Evaluation of Bi_{ORTH} 70
5.2.4 Buckling and Topology of Bi_{ORTH} 72
5.3 Domain Alignment of Bi Nanofilm Allotropes 73
5.4 Atomic-scale Structural Characterization via STEM 76
5.5 Summary 81

6 Stoichiometry Growth of SnBiTe Family and Structural Characterization **83**
6.1 Introduction 84
6.1.1 $(SnTe)_m(Bi_2Te_3)_n$ nomenclature and layer architecture 84
6.1.2 Epitaxy and structural characterization 84
6.2 Epitaxial growth of SnBT series 87
6.2.1 Growth parameter exploration of SnBT series 88
6.2.2 Structural characterization of the SnBT-124 thin film 88
6.2.3 Structural characterization of the SnBT-147 thin film 91
6.2.4 Structural characterization of the SnBT-225 thin film 92
6.3 STEM investigation of the SnBT thin films 94
6.3.1 Crystal Structure Analysis 94
6.3.2 Bond length Analysis 96
6.4 Transport Measurement 98
6.4.1 Hall Effect 98
6.5 Summary 102

7 ARPES investigation of Topological Insulator **104**
7.1 Circular Dichroism ARPES measurement of $MnBi_6Te_{10}$ 105
7.1.1 Material Characterization of $MnBi_6Te_{10}$ 105
7.1.2 ARPES Measurements at PGI-6 108
7.1.3 μ-ARPES Measurements at NanoESCA Beamline 114
7.2 ARPES Measurements of (V-alloyed) BST Thin Film 116
7.2.1 Vacuum Transfer of BST Thin Film 116
7.2.2 Cleaving of Te-passivated V-alloyed BST thin films using post . . 117
7.3 Summary 118

8 Conclusion and Outlook **120**

Appendix **122**

Acknowledgement **129**

List of Tables **131**

List of Figures **132**

Bibliography **150**

Curriculum Vitae **166**

Publications **167**

1 Introduction

Commentary: *In this chapter, the background and summary of this thesis are compiled, and presented by the author.*

In recent years, a new state of quantum matter, characterized by bulk insulating state with the conducting surface or edge states, has been discovered, which has attracted significant attention in the field of condensed matter physics. This new state of matter, which exhibits exotic features of the topologically protected, gapless edge or surface states that connect valence and conduction bands through a metallic linear dispersion, is known as "topological insulators (TIs)" [1–5]. Unlike the gap in conventional insulator, the bulk band gap in TI is partially inverted, due to the presence of the strong spin orbit coupling (SOC) in the material.

With the discovery of the quantum spin Hall effect, two-dimensional topological insulators (2D TI) are theoretical predicted and experimentally realized [6–8]. It features one-dimensional helical edge states with the counter propagating spin polarized edge channels, which can be potentially applied in the field of spintronics as well as the low-dissipation electronics [9–11]. Three-dimensional topological insulators (3D TI) have two-dimensional surface states on each surface, where the spin and momentum are locked perpendicular to each other. This unique property is predicted to host Majorana fermions when coupled with superconductors, which is critical to enable the topological quantum computing [12–14]. Since decades, researches have been exploring and growing 2D [15–17] and 3D TIs [18–21], while developing fabrication technologies for the realization of future devices based on TIs.

However, for 2D TIs, the choice of materials is limited, and achieving stable materials remains a challenge. In case of 3D TIs, identifying the appropriate material system to manipulate the Dirac point and the Fermi level is of crucial importance. Additionally, the incorporation of the 3D TI into quantum devices requires high crystal quality, precise topological band engineering as well as ultra-smooth and defect-free surfaces of the thin film. It has been observed that, various types of defects appearing during the growth process of TI thin films are induced by the substrate or the improper growth conditions [22–24].

This PhD thesis focuses on achieving high-quality topological thin films (in 2D and 3D regime) grown via molecular beam epitaxy (MBE) on the Si(111) substrate. The growth parameters (element source temperature and substrate temperature) of the Van-der Waals (VdW) based layered material are systematically investigated. The obtained high-quality thin film properties are characterized using various techniques, i.e. surface morphology: scanning electron microscopy (SEM) and atomic force microscopy (AFM); crystal quality: x-ray diffraction (XRD) and scanning transmission electron microscope (STEM).

Moreover, to determine the Dirac point and the Fermi level, bulk crystal and thin film TIs are measured and analyzed with angle resolved photoemission spectroscopy (ARPES).

The first stage summarizes the exploration of the bismuth in various phases, particularly Bi trigonal and orthorhombic phase, The individual phase-pure thickness-dependent growth of these phases extends the the thickness limit necessary to realize a 2D TI. In addition, the chemical variation in Sn-based Bi_2Te_3 alloy series allows the topological engineering of band structure, paving the way to achieve potential 3D TIs. This material series offers promising platform to couple with superconductors, compared with the $(Bi_xSb_{1-x})_2Te_3$ alloy. Finally, two methods are introduced and successfully employed for TI thin films to obtain clean surface of the sample to conduct ARPES measurement. Furthermore, by combining the circular dichroism measurement with ARPES, the orbital angular momentum (OAM) is revealed from the Bi_2Te_3 terrace of $MnBi_6Te_{10}$ crystal.

This thesis is organized as follows:

- **Chapter 2** provides a detailed introduction to the theoretical background of topological insulators. It includes the development of topological band theory and different types of topological insulators.
- **Chapter 3** presents the experimental techniques employed in this study.
- **Chapter 4** discusses the current challenges in the field of topological insulator from the material and growth perspective. It presents the specific dilemma associated with 2D and 3D TIs. In addition, various types of defects are encountered during the growth process are introduced and analyzed, supported by the atomic-resolution imaging obtained via STEM.
- **Chapter 5** depicts the systematic growth investigation of different Bi allotropes, i.e. the trigonal phase and orthorhombic phase, achieving the high-quality and phase-pure single crystal growth of Bi epilayers on Bi-terminated Si (111) 1×1 surfaces using MBE. The thickness-dependent growth of Bi trigonal phase has been successfully achieved. By doping 4-7% Sb into the trigonal film, $Bi_{1-x}Sb_x$ thin films with the thickness less than 4 nm can be obtained, facilitating the realization of the one-dimensional edge states. Furthermore, Bi orthorhombic phase with a thickness below 9 nm is predicted to the in the topological regime. The thickness-dependent growth of Bi orthorhombic phase is also presented in this chapter, which paves the way for the novel topological and neuromorphic applications.
- **Chapter 6** focuses on the systematic growth exploration of the three stoichiometries in the Sn-based Bi_2Te_3 series i.e. $SnBi_4Te_7$, $SnBi_2Te_4$, $Sn_2Bi_2Te_5$ on the Si (111) substrate with MBE. High-quality thin films of each stoichiometry have been successfully achieved. The transport measurement of the $SnBi_4Te_7$ thin film with different thicknesses are also discussed.
- **Chapter 7** explores different terraces of $MnBi_6Te_{10}$ through the work function mapping and the X-ray photoelectron spectroscopy (XPS). In addition, the results of the circular dichroic-angle resolved photoemission spectroscopy (CD-ARPES),

performed on one of the Bi_2Te_3 terraces in $MnBi_6Te_{10}$ crystal, is discussed in this chapter. Furthermore, two methods, i.e. *vacuum transfer* and the *post cleavage*, are employed to ensure the surface cleanliness for the ARPES measurement on TI thin films without and with capping, respectively.

- **Chapter 8** summarizes the results obtained so far and provides the outlook for this work.

2 Theoretical Background

Commentary: *This chapter presents the theoretical background on topological insulators (TIs). It has been prepared based on existing literature in the respective field. Most of the images included have been reproduced or adapted by the author from relevant papers or books, with proper citations provided in the respective captions.*

Topology is a mathematical concept that captures the invariant properties of geometric objects under continuous transformations. Objects within the same topological class can be continuously deformed into one another [25, 26].

Nowadays, the concept of topology was extended to the momentum space in solid state physics, which is related to the exotic features of electronic band structure. Therefore, a new class of materials in condensed matter physics, known as "topological insulator (TI)", is introduced. This type of materials is characterized by distinct electronic properties in the bulk and at the boundary compared to topologically trivial materials. Distinguished from trivial insulators, topological insulators are insulating in the bulk but possess conducting states on their edges (2-dimensional systems) or surfaces (3-dimensional systems), protected by the time-reversal symmetry. The emergence of the topological features can be attributed to the strong spin orbit coupling in certain materials, which leads to an inverted band gap at certain points in the Brillouin zone [1, 4, 27].

In this chapter, I will introduce the basic theoretical foundation of topological insulators and explore various sub-classes of TIs that exhibit novel topological phases.

2.1 Quantum Hall Effect and Quantum Spin Hall Effect

To describe properties of topological insulators, classical band theory is extended including the concept of topological order similar to the topology in mathematics. A topological invariant $n \in Z$ allows to distinguish the topological classes: trivial insulators with n = 0 and non-trivial insulators with $n \neq 0$.

A classical band insulator, as depicted in Fig. 2.1(a), is a material with an energy gap separating filled and empty energy bands that belongs to topologically trivial insulators (n=0). The first example of a topological state was found by von Klitzing in 1980, in form of (integer) Quantum-Hall effect (QHE) as shown in Fig. 2.1(b). In this effect, a 2D electron gas subjected to a strong magnetic field exhibits quantized conductance, characterized by topologically protected edge states ($n \neq 0$). However, the time-reversal symmetry is broken by the external magnetic field. As proposed by Haldane [29], the non-zero quantization of the Hall conductance σ_{xy} in the QHE system is expressed with:

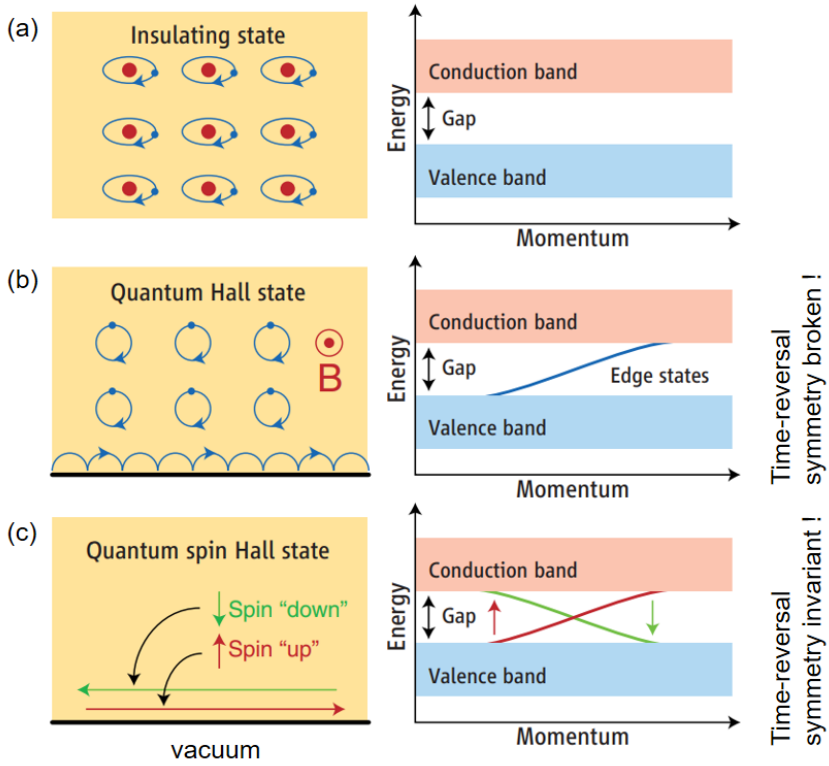

Figure 2.1: Insulating phases in two dimensions. (a) The topologically trivial insulator with electrons bound in localized orbitals (left), where its occupied valence band is separated from the empty conduction band by an energy gap (right). (b) The topological non-trivial quantum Hall state where the external strong magnetic field leads to the closed circular orbits of the electrons, allowing the charge to flow in one-dimensional edge states ("chiral" edge states). (c) The topological non-trivial quantum spin Hall state without external magnetic field, where the SOC leads to "helical" spin-polarized conducting states at the boundary. Image taken from [28].

$$\sigma_{xy} = \frac{ve^2}{h} \tag{2.1}$$

In this formula, e is the electron charge, h is the Planck's constant, and v is integer number (1,2,3...).

Inside the 2D system (the "bulk"), electrons are confined to circular cyclotron orbits due to the perpendicular magnetic field. These orbits are localized and do not contribute to net current, making the "bulk" effectively insulating. When an electron on a cyclotron orbit approaches the boundary, the electron "bounces off" and is forced back on the orbit by the magnetic field [30]. This results in an effective drift motion along the boundary, leading to a unidirectional current, as displayed in Fig. 2.1(b). The quantized Hall conductance arises from edge channels at the boundary. Charge transport in these edge channels is non-dissipative, and its direction (clockwise or anticlockwise) is determined by the sign of the charge (electron or hole) and by the direction of an applied magnetic field (up or

down) [31]. These edge channels, which are spin-degenerate and move in one direction, are referred to as chiral edge channels.

In 2005, as a spin-extended version of QHE, Kane and Mele predicted the existence of the quantum spin Hall effect (QSHE) first for the model system of graphene, where they propose that a material with SOC could host helical edge states (electrons with opposite spins move in opposite directions along the edges, without dissipation) [6, 32]. In terms of band structure there also have to exist two spin-polarized states connecting the valence band with the conduction band as shown in Fig. 2.1(c). The time reversal symmetry is preserved due to the SOC acting as the driving force instead of the additional magnetic field [7]. Besides, the spin-up and spin-down edge states exhibit reversed currents due to time reversal symmetry. As a result, there is no net charge flow, leading to the overall Hall conductance of zero. This differentiates the QSHE from QHE, but remains insufficient to distinguish the QSH insulator from a trivial band insulator. Additional invariant is needed to separate it from the normal insulator, which will be introduced in detailed in section 2.3.

In 2007, Laurens Molenkamp's group experimentally confirmed the presence of QSHE in HgTe/CdTe quantum well structures, which was the first experimental realization of a 2D topological insulator [8]. Therefore, the QSH insulator is also known as 2D topological insulator.

2.2 Band Inversion and Origin of the Topological State

As discussed in the last section, topologically non-trivial insulators in the QSHE state exhibit a band gap and can be distinguished by a topological invariant (discussed in section 2.3) that changes at an interface, where the band structure experiences a transition of closing and reopening of the band gap. The band structure of topologically non-trivial materials is characterized by a inverted band gap, which is not only for 2D topological insulator but also for 3D topological insulator. The reason for the band inversion at certain points in the Brillouin zone is spin-orbit coupling (SOC). In this section, the phenomenon of band inversion and the origin of the topological state will be discussed.

2.2.1 Spin Orbit Coupling

Spin orbit coupling (SOC) is a relativistic phenomenon in quantum mechanics, which describes the interaction between the spin of an electron and its orbital motion. As an electron travels along the trajectory around the atomic nucleus, it experiences an electric field gradient from the nucleus as an effective magnetic field (due to Lorentz transformation[1]). The magnetic field, created by the electron orbital motion, couples with the spin [33], thus leading to the SOC.

[1] $B = \frac{1}{c}(v \times E)$

Figure 2.2 shows a typical evolution of the electronic structure during the hypothetical process of increasing the SOC to its full strength. Without taking SOC into account, the bands remain trivial (insulator). By switching on the SOC, the band gap in the electronic structure undergoes gap closing, and reopening of the gap (band crossing and band inversion between the conduction band and valence band). How does gap reopening happens during the phase transition process? Here, Bi_2Se_3 is chosen as an example for detailed explanation.

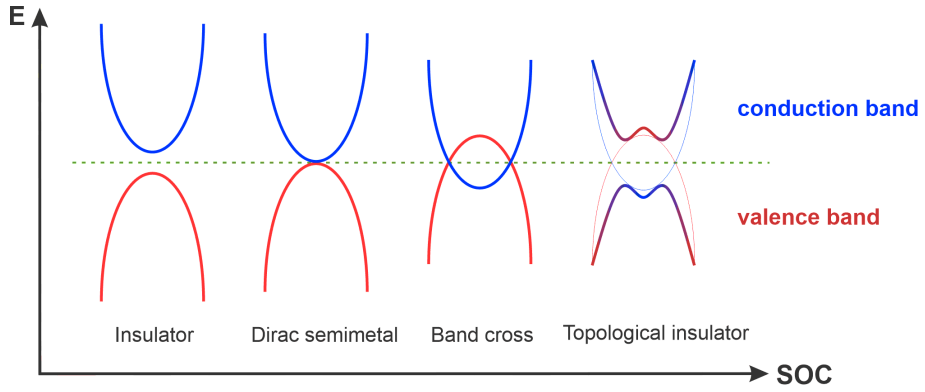

Figure 2.2: Topological phase transition from normal insulator via Dirac semimetal to the topological insulator with respect to SOC strength, adopted from [34].

The band inversion at Γ-point in Bi_2Se_3 origins in the evolution of p orbitals for Bi($6s^26p^3$) and Se($6s^24p^4$). It evolves via three stages shown in Fig. 2.3 described by Zhang *et al* in [27].

- **Chemical bonding:** In this stage, when the chemical bonding between Bi and Se atoms within a quintuple layer (QL) is considered, the p orbitals of Bi and Se are split into 5 hybridized orbitals from the pure degenerated atomic levels, thus pushing down all Se states and lifting up all Bi states. This effect brings $P1^+_{x,y,z}$ band from Bi atom and $P2^-_{x,y,z}$ band from Se atom closer. The superscripts "+/-" of the hybridized bands represent "even/odd" parity of corresponding states at Γ-point.

- **Crystal-field splitting:** The crystal-field splitting leads to further splitting of p-orbitals into p_z and $p_{x,y}$, with p_x and p_y remaining degenerate due to the xy in-plane symmetry of the crystal structure. This effect brings the Bi($P1^+_z$) band and Se($P2^-_z$) band closer to the Fermi level.

- **Spin-orbit coupling:** Taking SOC into account, the spin degeneracy is lifted up, leading to the repulsion between $P1^+_z\uparrow$ and $P1^+_{x+iy}\downarrow$ as well as similar combinations (energy levels with opposite spin orientation). Therefore, the $P1^+_z\uparrow(\downarrow)$ are pushed down while $P2^-_z\uparrow(\downarrow)$ are pushed up due to SOC. When the SOC strength is sufficiently large, the position of $P1^+_z\uparrow(\downarrow)$ and $P2^-_z\uparrow(\downarrow)$ is thus reversed, resulting in the phenomenon of band inversion in Bi_2Se_3. It is important to highlight that the parity of the bands is also switched. As shown in Fig. 2.2, after the band cross, the valence band maximum (with - parity) the conduction band minimum (with +

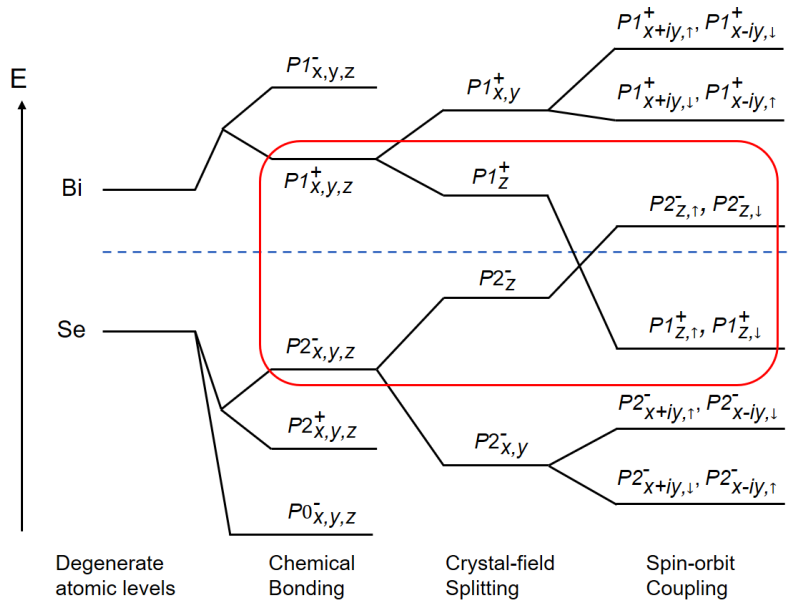

Figure 2.3: Evolution of the electronic band structure in Bi_2Se_3. Degenerated states are lifted up by chemical bonding, crystal-field splitting and SOC, band inversion happens at Γ-point in the end. Images adopted from [27].

parity) mix with each other, which enables the odd (-) parity in conduction band and the even (+) parity of the valence band.

As illustrated in Fig. 2.2 and 2.3, the strong SOC in the 3D TI (Bi_2Se_3 as the example) swaps orbitals with opposite parity across the Fermi level, giving rise to the band inversion. When a material with an inverted band structure encounters another material with non-inverted band (such as trivial insulator or vacuum), the conduction and valence bands of the TI have to switch the parity across the interface to maintain continuity. This parity alignment results in a transition region where the bands close and reopen, leading to the formation linearly dispersed metallic states, which are called topological surface states (TSS) [1, 27]. Due to the parity conservation, TSS exhibit the unique feature of spin-momentum locking [4], where the spin of every electron is 'locked' to a certain momentum. Besides, TSS are protected by the time reversal symmetry, which prevents backscattering from non-magnetic impurities. This absence of the backscattering makes the TSS robust and protected from perturbations and disorders. The exotic characteristics of the TSS facilitates potential applications in spintronics [9, 35], quantum computing [12, 36] and low-dissipation devices [37].

Generally, TIs can be classified into 2 major groups:

- 2-dimensional topological insulators: They exhibit 1D topological edge state, also known as QSH insulator (Fig. 2.1). In section 2.3, an additional topological invariant will be introduced to differentiate the QSH insulator from the trivial insulator.
- 3-dimensional topological insulators: They host 2D topological states on the surface of the material, which will be explained in section 2.4. There are also various

sub-groups with novel topological phases of 3D TI, e.g. high-order topological insulator, described in section 2.5, and magnetic topological insulator, described in section 2.6.

2.3 Two-dimensional Topological Insulator (2D TI)

As discussed in 2.1, it is not sufficient to distinguish the QSHE state from a trivial insulator based on the net charge flow in the system. Therefore, Kane and Mele [32] introduced a new invariant number v_0 (topological Z_2 invariant) to distinguish the time-reversal invariant systems with $v_0 = 1$ from the trivial insulators with $v_0 = 0$.

If the Hamiltonian $\mathbf{H}$ of the system is invariant under time-reversal operator Θ, every Bloch eigenstate $|\psi_n(\mathbf{k},\uparrow)\rangle$ and its time reversed state $\Theta|\psi_n(-\mathbf{k},\downarrow)\rangle$ with opposite wave vector and opposite spin are eigenstates of same energy (Kramers theorem) [38]. These two eigenstates are called Kramers partners, which are at least two-fold degenerate due to the two possible spin directions of a fermion (electron). Typically, as depicted in Fig. 2.2 and 2.3, the SOC lifts this degeneracy, and splits the state into spin up and spin down states in most parts of BZ. However, at certain time-reversal invariant momenta (TRIM) points in the Brillouin zone (BZ), where the momentum is invariant under time-reversal operation, the states stay degenerate. The TRIM points (Γ_{ij}) are also called Kramers points [2, 39].

Figure 2.4(a) and (b) illustrate the different TRIM points in a square 2D BZ projected on the 1D edge and the bulk 3D BZ projected on the 2D surface, respectively, while (c) and (d) are the schematic representations of the the projected band structure $E(k)$ of a crystal in 2D/3D between the two boundary TRIM points Λ_1 and Λ_2. The Kramers degenerate edge/surface states can be connected in two possible ways, which are shown by pairwise connection in (c) and a partner switching in (d). In pairwise connection, the edge/surface states will cross the Fermi level even number of times, which indicates the trivial system with non-inverted bands ($v_0 = 0$). An odd number of crossings will connect the valence band with conduction band by covering the entire band, leading to the topologically protected metallic states at the boundary ($v_0 = 1$). As demonstrated by Fu and Kane [5], the topology of the system (Z_2 invariant v_0) can be determined by the parity product of the bulk TRIM points.

For 2D TI shown in Fig. 2.4(a), there are four time-reversal invariant momenta Γ_i and a single Z_2 invariant, given by the equation 2.2.

$$(-1)^{v_0} = \prod_{i=1}^{4} \delta_i(\Gamma_i) = \prod_{i=1}^{4} * \prod_{m=1}^{N} \xi_m(\Gamma_i) \tag{2.2}$$

ξ_m is the parity eigenvalue ($\xi_m(\Gamma_i) = \pm 1 = \delta_i(\Gamma_i)$) of the occupied band m at the TRIM point Γ_i, where i is the spatial identification.

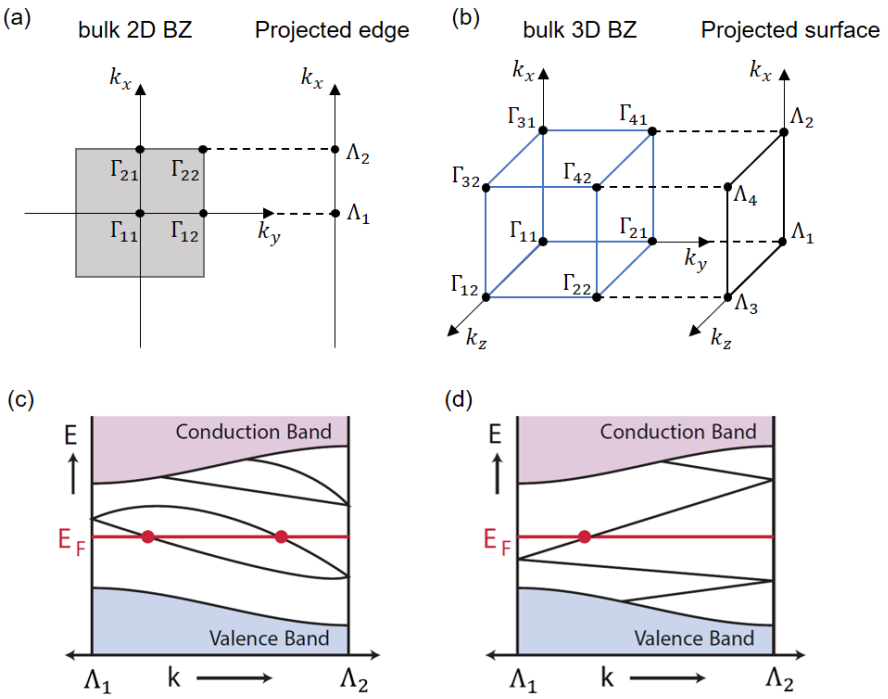

Figure 2.4: Schematic representation of the time-reversal invariant momenta (TRIM) points Γ_{ij}. (a) Projection of the 4 bulk TRIM points (black circles) in a square 2D Brillouin zone (BZ) onto the egde with 2 edge TRIM points Λ_a. (b) Projection of eight TRIM points on a cubic 3D BZ onto the surface with 4 edge TRIM points. (c)-(d) schematic illustrations of electronic dispersion between two Kramer's degenerate boundary TRIM points Λ_1 and Λ_2 for a trivial insulator $\nu_0 = 0$ in (c) and topological insulator $\nu_0 = 1$ in (d). The number of surface state crossing the Fermi level shown with red dots determine the topological properties, where the odd number of the crossing leads to the topologically protected metallic boundary states. Images adopted from [1, 5].

2.4 Three-dimensional Topological Insulator (3D TI)

After the discovery of QSH insulator state in two dimensions, its three-dimensional counterpart has been predicted theoretically and named as "3D topological insulator (3D TI)" [5, 40]. The 3D TI hosts surface states that are protected by the TRS instead of conducting edge state in 2D TI. Time-reversal invariant 3D bulk insulating state has also been characterized by Z_2 topological invariant. Different from 2D materials, the single criteria $\nu_0 = 0/1$ is not sufficient to determine whether a 3D system is topological or not. Therefore, the Z_2 invariant with a combination of variables $\nu_0;(\nu_1\nu_2\nu_3)$ is introduced to define the topological state of the 3D system. Here, ν_0 is known as strong topological index, and the other three are known as weak topological indices, where $(\nu_1\nu_2\nu_3)$ can be interpreted as Miller indices to specify the direction of vector Γ_a in the reciprocal space.

Therefore, 3D TI is classified with the Z_2 invariant into two types, strong topological insulator ($\nu_0 = 1$) and weak topological insulator ($\nu_0 = 0$ and any of the $\nu_{1,2,3} = 1$), where strong topological insulator will be introduced in following section.

2.4.1 Strong Topological Insulator

As depicted in Fig. 2.4(b), there are eight time-reversal invariant points in three dimensions. This leads to the four independent Z_2 invariants. When $v_0 = 1$ and $(v_1 v_2 v_3)$ are independent of the choice of the surface projection, similar to 2D (Eq. 2.2), the topology is determined by the parity product of the occupied bands at the eight bulk TRIMs.

$$(-1)^{v_0} = \prod_{i=1}^{8} \delta_i = \prod_{i=1}^{8} * \prod_{m=1}^{8} \xi_m(\Gamma_{ij}). \tag{2.3}$$

Considering the cubic structure in Fig. 2.4(b), the character of the projected surface TRIM Λ_a is given by the product of the two paired bulk TRIM: $\pi_a = \delta_{a1} \cdot \delta_{a2} = \pm 1$, where a represents the pair of bulk TRIMs. There will be two cases:

- If the there is no change in the surface parity invariant between two surface TRIM points ($\pi_1 \pi_2 = 1$), the states will connect pairwise and have an even number of Fermi level crossings, as shown in Fig. 2.4(c). This corresponds to a trivial insulator ($v_0 = 0$) with gapped band structure.
- If there is a change in the surface parity invariant ($\pi_1 \pi_2 = -1$), the states connect switching partner with a odd number of Fermi level cuts, resulting in the connection between valence and conduction band, as depicted in Fig. 2.4(d). This system is topological insulator ($v_0 = 1$).

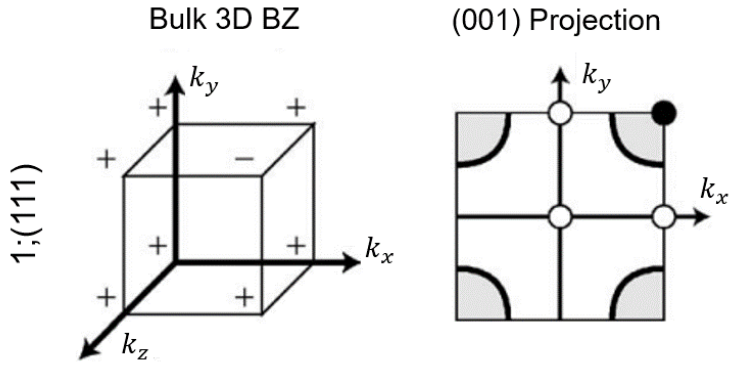

Figure 2.5: Schematic illustration of the STI with the 3D cubic BZ, which can be identified by the topological invariants $v_0;(v_1 v_2 v_3)$**.** The parity of the 8 TRIM points in 3D BZ are given in "+" for δ_i = +1 and "-" for δ_i = -1, while the 3D parity projections on the (001) surface with 4 surface TRIM points Λ_a by $\pi_a = \delta_{a1} \cdot \delta_{a2}$ are marked by white (π = +1) and black (π = -1) circles. The thick lines in the bottom panel indicate possible Fermi contours that enclose specific Λ_i. This topological class exhibits the Z_2 variant $v_0;(v_1 v_2 v_3)$ = 1;(111), with one projected surface TRIM exhibiting odd parity, so that all surfaces will have an odd number of black circles. Image adopted from [5].

.

For a strong topological insulator, as exemplified in Fig. 2.5(a), only one bulk TRIM has $\delta(\Gamma_i)$ = -1 and all other seven have $\delta(\Gamma_i)$ = +1, ensuring the surface projection TRIM points $\pi_1\pi_2\pi_3\pi_4 = -1$ in all projections direction within cubic crystal structure. The odd number of TRIM points in the projected surfaces enclosed in the Fermi contours indicates that the system has an odd number of Dirac cones on every surface.

All the conventional 3D TIs i.e. Bi_2Se_3, Bi_2Te_3 and Sb_2Te_3 exhibit $\nu_0;(\nu_1\nu_2\nu_3)$ = 1;(111) and belong to STI.

2.5 High-order Topological Insulator (HOTI)

High order topological insulator (HOTI) is a new class of topological material which hosts no 2D gapless surface states but exhibits topologically protected gapless states that propagate along one-dimensional hinges (intersection of two surface facets) or are localized at some points (corners) on the surface [41–43]. It follows a generalized bulk–boundary correspondence of higher-order: not the surfaces of the crystal, but its hinges host topologically protected conducting modes [44]. The topological character is protected by both TRS and crystal symmetries(CS) which can be classified in the following two categories [45, 46]:

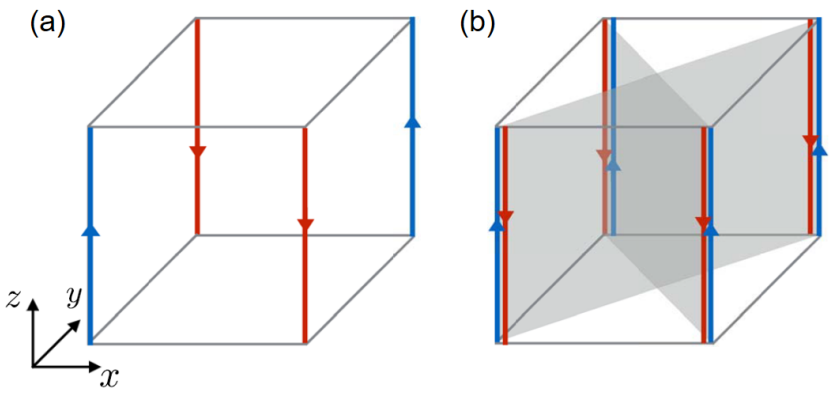

Figure 2.6: Schematic representation of two types of HOTI with topologically protected hinge excitations of second-order 3D TI. (a) Time-reversal breaking model with chiral hinge currents flowing along the corners of a cubic crystal which is protected by 4-fold rotational symmetry along along z-axis ($\hat{C}_4^z$). (b) Time-reversal invariant model with anti-propagating Kramers pairs of hinge modes. The highlighted planes in gray represent the mirror planes that protect the hinge states along the xy-plane $\hat{M}_{xy}$ and x$\bar{y}$-plane $\hat{M}_{x\bar{y}}$. Image taken from [46].

- **Chiral HOTIs**: The topology is protected by the combination of time-reversal and a 4-fold rotation symmetry. Their hinge states are chiral modes that propagate unidirectionally, similar to the edge states of a 2D quantum Hall effect, and the bulk topology is $\mathbb{Z}_2$-classified.
- **Helical HOTIs**: The topology is protected by time-reversal together with mirror symmetries. Their hinge states come in Kramers pairs of counter propagating hinge

modes, akin to the edge states of a 2D quantum spin Hall effect. The bulk topology is $\mathbb{Z}$-classified.

Bulk bismuth is the first material that has been theoretically and experimentally demonstrated to be HOTI [44]. It is one type of helical HOTIs, where their hinge modes are protected against TRS, three-fold rotational symmetry and inversion symmetry of the bismuth crystal. Later on, people also discovered the existence of edge (hinge) state in $Bi_{0.92}Sb_{0.08}$ from the family of $Bi_{1-x}Sb_x$ alloy [43]. Moreover, a quasi-1D bismuth halide, Bi_4Br_4 has the helical edge state, exhibiting the the HOTI phase belonging to $\mathbb{Z}_4$ topological classification [47].

2.6 Magnetic Topological Insulator (MTI)

In 3D TI, the massless Dirac-like dispersion of the surface state with spin–momentum locking connects the bulk valence and conduction bands as the time-reversal invariant system. Introducing a magnetic order either through doping with magnetic elements i.e. Cr, V, or Fe to 3D TIs, or by utilizing intrinsic magnetic TI, breaks the time-reversal symmetry in the system, leading to the gap opening at the surface Dirac cone [31, 48, 49]. In these magnetic topological insulators (MTIs), tuning of the Fermi level within the exchange gap results in the emergence of a quantum Hall effect in the absence of external magnetic field, known as the quantum anomalous Hall effect (QAHE) [50–52].

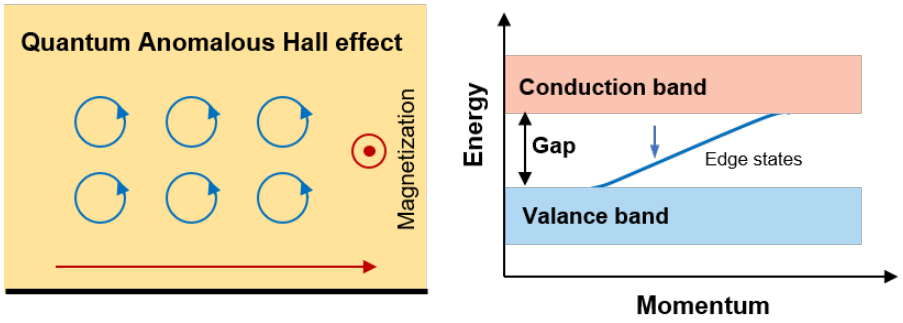

Figure 2.7: The quantum anomalous Hall edge states in magnetically doped thin films. (a) The chiral edge mode that appears in a magnetic topological insulator when the Fermi level, E_F, is located in the mass gap induced by the magnetic exchange interaction. The edge electrons conduct electricity without dissipation in one direction along the edge of the sample. (b) The gapped Dirac-like dispersion of the edge state in a MTI. Images adopted from [53].

QAHE system has dissipationless chiral edge states, where only electrons with spins opposite to the bulk magnetic moment move in a specific direction [54]. The locking mechanism between the spin and the moving direction, as well as the number of edge channels, is intrinsic to the material itself. QAHE was experimentally observed for the first time in 2013 in Cr-doped $(Bi,Sb)_2Te_3$ thin films at ultra-low temperatures up to 30 mK [55]. Later, it was also discovered in V-doped $(Bi,Sb)_2Te_3$ thin films [56] and in $MnBi_2Te_4$ flakes [57].

In the QAHE system, only one channel contributes to the conductivity, which is less susceptible to interference compared to the QSH system. This characteristic offers potential applications in low-loss electronic and spintronic devices [31, 58]. Besides, coupling MTIs with superconductors could lead to the topological superconductivity with the associated chiral Majorana edge states, which provides a promising platform to realize the fault-tolerant quantum computation [13].

2.7 Topological Phase Transition

Topological phase transition refers to the transformation of the current topological phase of a material into another topology or the switching to topologically trivial phase by engineering the band structure. This transition can be realized though physical and chemical variations in the material system. The topological phase transition can be realized in different scenarios:

- **Physical path**: The variations in the thickness of the crystal, strain in the epilayer and the applied pressure can induce topological phase transition of the system. It has been observed that 3D TIs can be transformed into 2D TIs by reducing the epilayer thickness below a critical value [59, 60]. Another example demonstrates a topological quantum phase transition between a QSH phase and a trivial insulating/metallic phase can be realized by applying strain [61].
- **Chemical path**: The topological phases of the material system can also be adjusted by varying the composition or the stoichiometry. Alloying the topological trivial material "additive" with the topological non-trivial insulator "base" enables the manipulation of the SOC strength, thus engineering the band structure. This method allows more precise control in tuning 3D topological phases [22, 62].

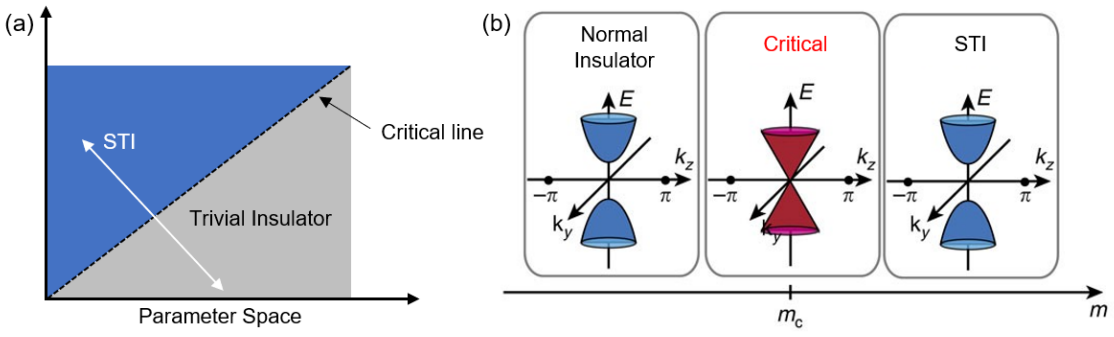

Figure 2.8: Schematic diagram representing phase transition in a STI, induced by band crossing when a single control parameter is varied in the system. The control parameter (white arrow) along the x-axis is modifying the strength of SOC and the size of inverted/non-inverted bandgap. The dotted line represents the topological-trivial transition critical value with 0 eV bandgap (phase boundary). Image adopted from [63].

Figure 2.8 demonstrates a model from Yang *et al.* [63], which indicates the phase transition between STI and the trival insulator via semimetal with chemical variation. The phase diagram of the system in Fig 2.8(a) has TRS and inversion symmetry (IS). Here, the gap-closing is tuned by a single parameter, the strength of SOC.

By incorporating the “additive” (trivial material) into “base” (non-trivial material), the strength of SOC will be reduced in the compositional alloys, resulting in the decrease of inverted band gap until the it is closed. The semimetal is, therefore, achieved at a critical value, where the bandgap reaches 0 eV. Further addition of the "additive" transforms the system into trivial phase. The corresponding evolution of the band structure with the variation of SOC is illustrated in Fig. 2.2 and Fig. 2.7(b). This phenomenon has already been observed in [60, 64]

Among conventional 3D TIs (Bi_2Te_3, Sb_2Te_3 and Bi_2Se_3), these materials exhibit STI phase and thus can be utilized as “base”. One of the “base + additive” combinations: $\mathbf{Sn_xBi_yTe_z}$ **(SnBT) = Sn +** $\mathbf{Bi_2Te_3}$, where Bi_2Te_3 serves as the "base" and Sn acts as the "additive". This combination enables the exploration of topological phase transitions within the SnBT stoichiometric series, as indicated in Fig. 2.8.

3 Experimental Setup

Commentary: *This chapter describes all experimental setups utilized in this thesis. It has been prepared based on the actual equipment configurations at the Peter Grünberg Institutes (PGI-9 and PGI-6), and the Ernst Ruska Centre (ERC) at Forschungszentrum Jülich, as well as relevant literature outlining their operating principles. Example measurements were performed by the author using the respective equipment and are presented in the corresponding sections as illustrative figures. Most of the conceptual or schematic images have been reproduced or adapted from the literature by the author, with proper citations provided within each caption.*

This chapter will introduce various experimental techniques, including epitaxial growth method for topological insulators (TIs), along with the corresponding material analysis techniques. In this study, topological thin films are prepared using molecular beam epitaxy (MBE), while scanning electron microscope (SEM) and atomic force microscope (AFM) are exploited to investigate the surface morphology of the grown thin films. X-ray diffraction (XRD) and scanning transmission electron microscope (STEM) techniques are applied to extract detailed crystallographic information. Additionally, angle-resolved photoelectron spectroscopy (ARPES) is primarily utilized to determine the electronic band structure of both thin film and bulk TIs.

3.1 Molecular Beam Epitaxy (MBE)

The concept of the MBE deposition was first proposed by Günther in 1958 [65], where materials are vaporized and deposited onto a substrate. Later, with the development of the ultrahigh vacuum (UHV) technology, Davey and Pankey implemented molecular beam epitaxy (MBE) to grow epitaxial GaAs films successfully in 1968 [66]. At the same time, Cho and Arthur developed a process that allowed the deposition of highly controlled layers of atoms on the substrate under UHV conditions, enabling the growth of high quality MBE films of of GaAs [67] and other III–V compounds [68]. This achievement leads to the rapid growth and development of the semiconductor industry [69–71]. Nowadays, MBE is one of the most advanced thin film growth techniques, where epitaxial thin films of a wide range of materials, from oxides to semiconductors and metals, can be prepared [72, 73]. In this study, MBE is employed to achieve the high quality epitaxial growth of TI thin films, which can be further embedded and fabricated into topological devices. The schematic illustration and a photograph of the MBE system used in this work are displayed in Fig. 3.1.

Figure 3.1(a) presents the schematic front view of the MBE growth chamber. This is an UHV system with the base pressure in the range of 1×10^{-10} mbar, enabling the high

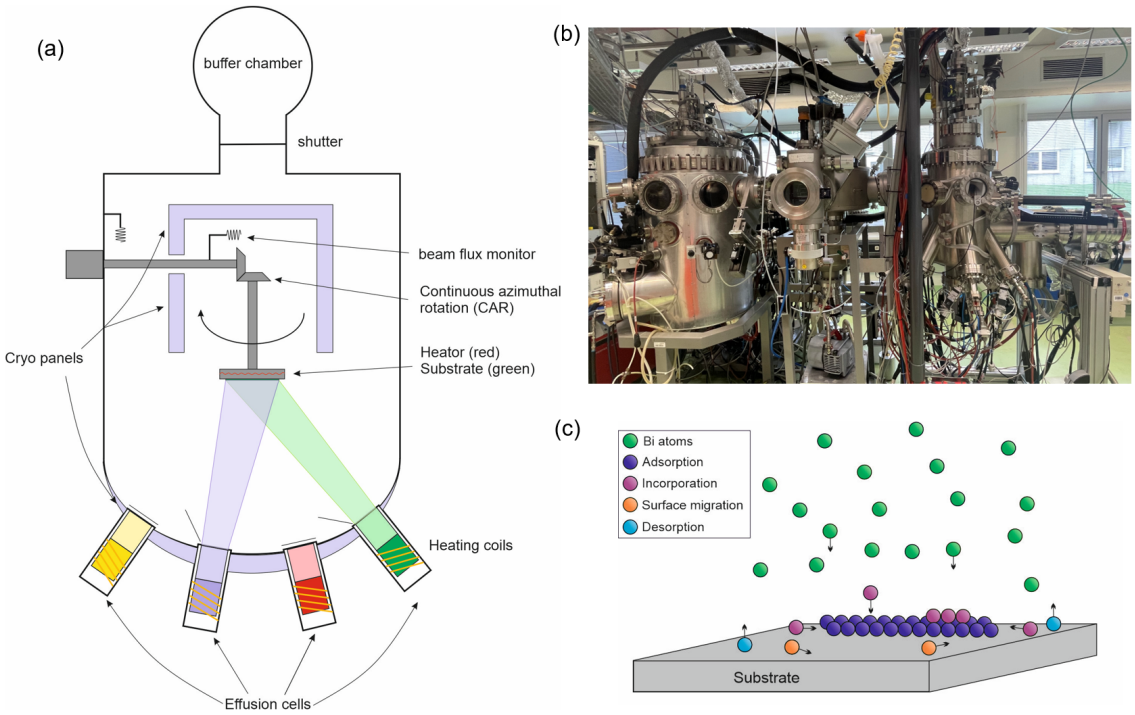

Figure 3.1: An overview of MBE machine and its working activities. (a) Schematic diagram of the MBE system showing the main components (growth chamber, buffer chamber, effusion cells, heater, cryo panels and so on). Images modified from [74]. (b) A photograph of BST-MBE chamber setup used in this study. (c) Activities happening in the growth chamber at the substrate, including adsorption, surface migration and dislocation, chemisorption and thermal desorption.

quality single crystalline growth with low impurities in large scale. The UHV environment is achieved through a combination of specialized pumps. Besides, liquid nitrogen flowing through the cryo panels (as shown in the purple color region in the Fig. 3.1(a)) contributes to the low temperature environment, which can further reduce the content of impurities in vacuum and provide better conditions for the deposition of thin films. This cooling system is usually turned on 1 hour prior to the growth to cool the growth chamber down.

To start the growth, the cleaned substrates are first placed on a 4-inch metal holder, which is then loaded into the load lock (Fig. 3.1(b)) for pumping. One typically needs to wait 5-10 minutes until the pressure in the load lock is below 1×10^{-6} mbar, then the wafer is transferred to the mid chamber (buffer chamber in Fig. 3.1(b)). The mid-chamber helps to maintain a better vacuum in the growth chamber. When the pressure drops below 1×10^{-9} mbar in the mid-chamber, the wafer is placed on the stage below the heater in the growth chamber by the transfer arm. The stage is then heated up to desired temperature by the heater (able to achieve up to 1100 °C) and is rotated by manipulating of the continuous azimuthal rotation (CAR) during the growth process.

The substrate is then heated up to remove the contamination and expose the dangling bonds on the surface. Afterwards, the effusion cells underneath the growth chamber

are prepared for the growth while cooling the substrate down to the targeted temperature. There are crucibles (typically made of PBN[1]) in the effusion cells, which contains raw materials, serving as highly controllable and efficient deposition sources for MBE. The heated coils surrounding the crucibles control the temperature, evaporating the corresponding element from the crucibles, ensuring the stability and reproducibility of the epitaxial growth. Usually, each individual crucible contains an element in solid form with a purity of at least 99.9999 % (bismuth, antimony, tellurium, etc. in this work). Bi with its relatively low melting point of 271.4 °C, first melts and then evaporates into gaseous phase after reaching their melting points. For elements like Te or Sb with higher melting temperatures, once reaching their sublimation points, the elements yield physical vapor from the cell and diffuse towards the substrate in case the shutter is opened. The relationship between vapor pressure and temperature for commonly used elements is illustrated in Fig. 3.2. For elements with extremely high melting points (over 1000 °C), such as V, Pt, Nb, W, evaporation from the effusion cell is no longer feasible due to the temperature limitation. In this case, e-beam evaporation is used, where it employs a high-energy electron beam to heat and vaporize the material directly, This technique can achieve very high temperatures (up to several thousand degrees Celsius), making it suitable for materials with high melting points. In this study, only thermal evaporation from the effusion cell is employed during the MBE growth.

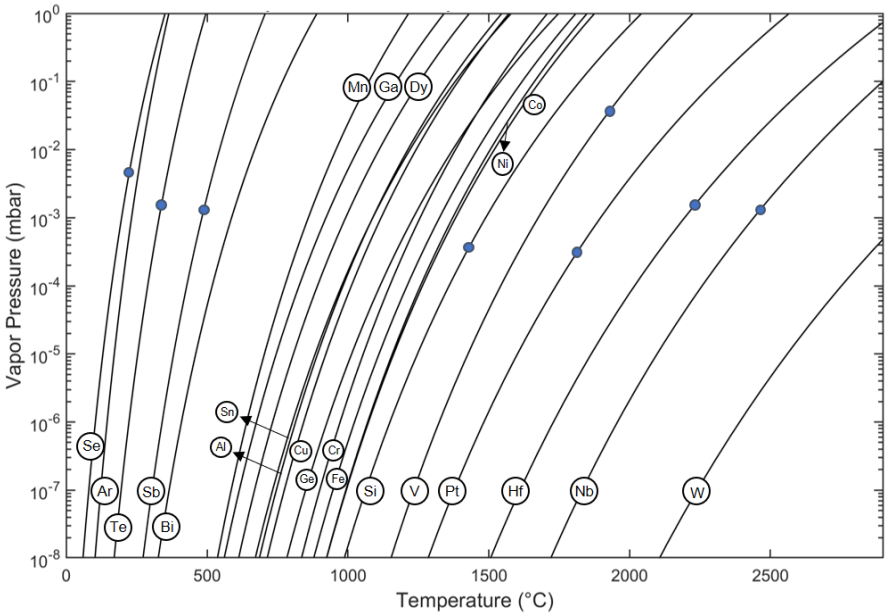

Figure 3.2: Vapor pressure of various elements as a function of temperature. The blue dots represent the melting points of corresponding elements, while their boiling points are generally too high to be included in this graphic. Data taken from the website of Dr. Eberl MBE-Komponenten GmbH [75].

When the gaseous elements reach the substrate surface, they condense and form a thin

[1]Pyrolytic Boron Nitride

film on top. Several phenomena occur during this process, (1) adsorption of the atoms imprinting on the substrate surface, (2) surface migration and dislocation of the adsorbed adatoms, (3) incorporation of the atoms into the growing crystal (chemisorption), (4) thermal desorption of the gaseous atoms. These four activities are illustrated in Fig. 3.1(c). The heating temperature of the coil to the crucibles determines the rate at which the atoms hit on the substrate surface, and the substrate temperature influences the migration and desorption rate. It is also important to note that the evaporated atoms do not interact with each other until they reach the substrate, as the reaction requires additional thermal energy provided by the heater to the substrate, and also due to the long mean free path of the atoms in the UHV environment, maintained by the cooling system of the chamber, which does not facilitate the reaction. [76–78].

Typically, reflection high-energy electron diffraction (RHEED) is integrated into the MBE to monitor the thin film growth in-situ. It is highly sensitive to surface structure and morphology, operating based on electron diffraction. RHEED enables the real-time observation of growth modes, layer-by-layer deposition, and surface reconstruction, providing immediate feedback for precise control over the deposition process [79, 80]. Since RHEED is not available in the MBE system employed in this study, the surface and structural properties of the grown thin films are characterized using a variety of techniques introduced in section 3.2 and 3.3.

3.1.1 Van der Waals Epitaxy

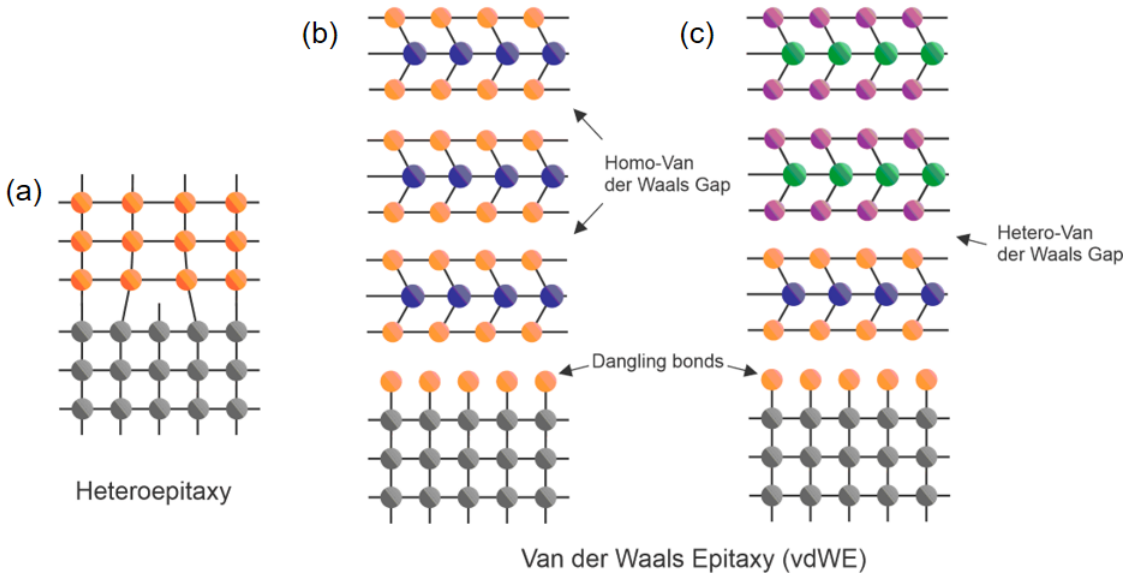

Figure 3.3: Schematic diagram of the Heteroepitaxy and Van der Waals epitaxy (vdWE). Image modified from [81].

As introduced, MBE is a technique that enables epitaxial growth of thin films. Conventional epitaxy is a film deposition process where the deposited material has the same

crystal structure as the substrate [82]. This process is driven by the strong chemical bonding, and can be classified into homoepitaxy and heteroepitaxy depending on whether the lattice constants of the grown material are the same (homoepitaxy) as or different (heteroepitaxy) from those of the substrate. However, when a significant lattice mismatch (over 10%) exists or structures differ between the substrate and the epilayer, conventional heteroepitaxy does not facilitate the high quality thin film growth. In such case, the film tends to relax itself with free dangling bonds, leading to the formation of dislocations or defects (as shown in 3.3 (a)) [83]. Hence, as an effective alternative method, van der Waals epitaxy (vdWE) can be introduced to obtain the high quality thin films on substrates that exhibit large lattice mismatches or different lattices.

Different from the heteroepitaxy, materials grown by vdWE possess robust in-plane atomic bonding, with the layers exhibiting weak van der Waals (vdW) interactions instead of the conventional covalent bond. Therefore, various 2D materials, i.e. graphene [84], $MoSe_2$ [81], or $NbSe_2$ [85], can be easily cleaved along the layers without generating dangling bonds at the cleaved surface. As illustrated in Fig. 3.3(b), the epitaxial growth of a layered material onto such surfaces occurs through vdW force, enabling heteroepitaxial growth even with a large lattice mismatch between the epilayer and the substrate [86, 87].

Besides, TIs are typical van der Waals materials with weak vdW interactions, where vdWE has also proven applicable to the 3D TIs grown on various substrates, i.e. Si [18, 88], SiO_2 [89], InP [90] and so on. In the work, Si is utilized as the substrate for the growth. Its surface can be passivated by hydrogen atoms prior to the growth. During the heating process in the MBE chamber, the hydrogen atoms are removed, and the exposed dangling bonds are subsequently saturated with Te atoms. This results in 1×1-Te surface termination, which offers a suitable platform for the vdWE. Detailed investigation is presented in Chapter 5.

3.1.2 Substrate Preparation

To achieve high-quality growth via MBE, an atomically clean, adsorbate-free substrate surface is of crucial importance. In this study, all the growth are conducted on the Si(111) substrate. Prior to loading the substrate into the MBE chamber, a series of cleaning processes are performed to remove the organic contamination of the Si substrate. A complete procedure of substrate cleaning is listed in Table 3.1, where the Si(111) wafers are used in all the growth for this work.

In the beginning, the Si wafer is coated with a resist and diced into 1×1 cm^2 that will be used as individual substrates. Acetone is first employed to remove the resist from the substrate, followed by isopropanol to remove the residual acetone. The substrate is then immersed into the deionized water (DI water) to remove the residual contamination. To eliminate the strong adhesive organic contaminants, the substrate is treated with Piranha solution (H_2SO_4 (96%):H_2O_2 (37%) = 1:1) for 15 minutes, followed by rinsing with the DI water for the same amount of time to remove the Piranha solution.

In preparation for growth, the substrate is etched with 1 % HF (Hydrofluoric Acid) to remove the native silicon oxide, saturating the dangling bonds on the Si(111) surface with

Table 3.1: An overview of the cleaning steps for Si (111) substrate [22, 88].

Step No.	Process	Chemicals	Duration
1	Resist Removal	Acetone	10 mins
2	Acetone Removal	Isopropanol	10 mins
3	Rinsing	DI Water	10 mins
4	Piranha cleaning	H_2SO_4 (96%):H_2O_2 (37%) = 1:1	15 mins
5	Rinsing	DI Water	15 mins
6	Etching	HF 1%	3 mins
7	Rinsing	DI Water	5 mins

hydrogen. The substrate is then rinsed with DI water to remove residual HF and gently dried with the nitrogon (N_2) gun. This treatment preserves the saturated bonds on the surface.

Following this sequential cleaning process, the substrate is loaded into the MBE chamber and annealed at 700 °C for 20 minutes. This treatment serves to remove the surface hydrogen atoms that terminate the dangling bonds on the Si (111). Afterwards, the substrate temperature is gradually lowered down over a period of 25 minutes to reach the desired growth temperature, typically ranging between 200-300 °C, in accordance with specific growth requirements. The dangling bonds of the Si substrate are saturated by the evaporated Te atoms (when Te based binary or ternary compounds are grown) from the effusion cells during the cooling down process, enabling the passivation of the dagnling bonds with a monolayer of Te. The 1×1-Te termination facilitates the further vdWE of the TI films as discussed in the previous section.

3.2 Surface Characterization

After obtaining the thin films from MBE, their surface features will be investigated with two main surface analytical tools, which are introduced in this section.

3.2.1 Scanning Electron Microscopy (SEM)

SEM is an electron microscopy, which is based on the interaction between electron beam and the specimen, generating different types of electrons, photons or irradiations. With emitted signal from the interaction, SEM is able to provide various qualitative information about the sample, including its topography, morphology, composition and crystallographic information [91].

During the working procedure, the SEM scans the sample surface with a focused electron beam emitted from the electron source, where they interact with each other. The signal depth ranges from less than 100 nm to approximately 5 μm into the surface, depending on the electron landing energy, the atomic number, and the density of the specimen. As illustrated in Fig. 3.4, the interaction between the primary beam and the specimen pro-

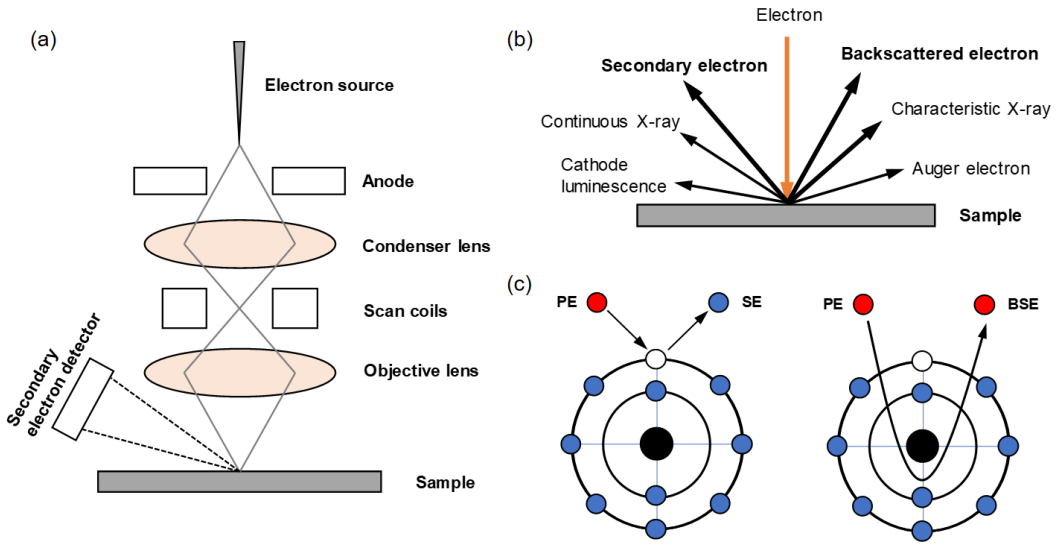

Figure 3.4: (a) Schematic illustration of a basic SEM instrument setup; (b) The interaction of electron beam with specimen and various signals emitted from the sample; (c) Mechanisms of emission of secondary electrons (SE) and backscattered electrons (BSE) from the atoms of the sample. Images modified from [92].

duces various types of signals such as secondary electrons (SE), backscattered electrons (BSE), characteristic X-rays, cathode luminescence. In the most common SEM mode, SE and BSE are two types of electrons employed for imaging.

- **SE mode:** SEs are those that escape from the specimen with kinetic energies below 50 eV, which are ejected from the orbitals by incident electron beam [93]. Due to their low energy, SEs can only escape from from the top few nanometers of the sample surface, producing images with high spatial resolutions up to 1 - 2 nm. SEs are typically detected by an Everhart-Thornley "secondary electron" detector[2] [94], as shown in Fig. 3.4(a).

- **BSE mode:** BSEs are electrons deflected from the sample by elastic scattering and primarily come from the upper layers of the specimen, typically within a maximum depth of about 20 nm. BSEs is collected by the a "doughnut" detector[3] positioned above the specimen and concentric with the electron beam. The spatial resolution in this mode is usually in the range of 5-10 nm [95].

Consequently, these two types of electrons provide different information about the sample. SE imaging yields the detailed information of the surface tomography with high resolution, whereas the BSE imaging is more sensitive to the difference in atomic number (the heavier the atoms are, the brighter they are in the image). In this work, SE mode is primarily used to observe the surface morphology of the MBE-grown thin films.

[2]This detector is composed of collector-scintillator-photomultiplier system. The dector captures SEs using a charged collector that direct them toward a scintillator, which converts the electrons into light. The generated light is travel to the photomultiplier, where it is amplified to form the corresponding image.
[3]They are either scintillator-type or semiconductor-type detectors.

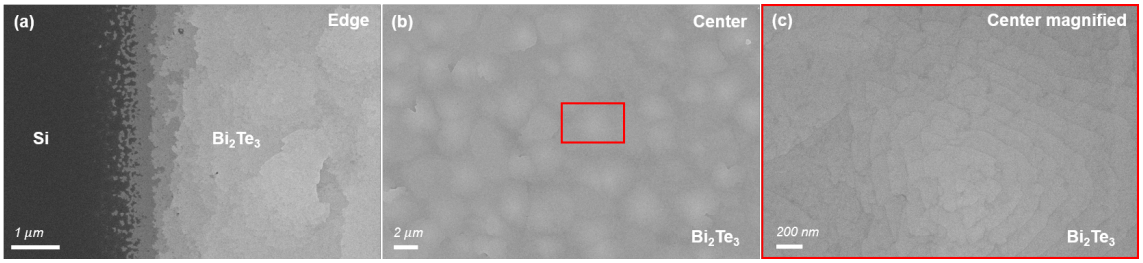

Figure 3.5: SEM SE images of Bi_2Te_3 thin film grown on 1×1 cm_2 Si(111) substrate. (a) from the edge. (b), (c) from the center of the sample, where (c) is the magnified image from the region in red box in (b).

An example is displayed in Fig. 3.5, where the SEM images provide the information of the grown thin film sample on the edge and in the center region. With the further magnification of the region inside the red box in (b), it is feasible to clearly observe how each layer in the island in the thin film is arranged, which contribute to optimizing the growth according to the surface quality. The detailed SEM investigation of the MBE-grown Bi thin films is presented in Chapter 5.

In general, SEM provides qualitative surface information over large surface areas, whereas detailed quantitative localized surface characterization can be achieved through atomic force microscopy, which will be introduced in the following section.

3.2.2 Atomic Force Microscopy (AFM)

Compared with the qualitative surface analysis via SEM, AFM is used to extract height and roughness features of the sample surface quantitatively, which offers high-resolution surface topography information down to the nanometer scale.

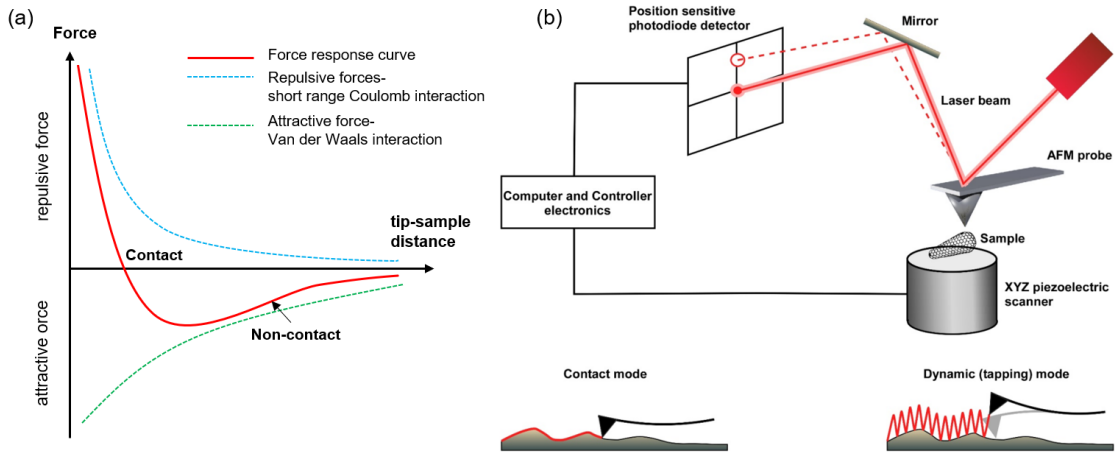

Figure 3.6: (a) Inter-atomic force vs. distance between AFM tip and sample. (b) Schematic illustration of an atomic force microscope with main components and the main modes used this this study. Image adopted from [96].

Different from the optical and electron microscopy, AFM employs the atomic force between the probe tip and the sample to image the 3D morphology of the sample, instead of lenses or beam irradiation. The tip is mounted on a cantilever and the tip size is in the range of 10-50 nanometers. As shown in the force-distance curve in Fig. 3.6(a), as the tip approaches the sample, long-range attractive forces start to increase. However, once the distance between the tip and the sample drops below a certain threshold, the repulsive force interactions emerge and increase with decreasing distance. When the tip experiences either long-range attractive forces or repulsive forces, the cantilever will bend accordingly. As illustrated in Fig. 3.6, during the measurement, the tip on the cantilever scans over the sample, the laser shines on the cantilever and gets reflected by the mirror to the position-sensitive photodiode detector (PSPD). The position of the reflected spot on the PSPD will be transferred to the computer, generating the corresponding topographic image. The controller electronics adjust the height of the cantilever under a feedback loop system.

AFM has three working modes according to the tip motion, namely contact mode, non-contact mode, and dynamic mode (intermediate mode or tapping mode). In the contact mode, the tip is always maintained in contact with the sample surface while scanning over it. In the non-contact mode, the cantilever vibrates at high frequencies and the tip is kept at a distance of 1-10 nm from the sample surface, the amplitude variation of the cantilever indicates the surface morphology of the sample. Similar to the non-contact mode, in dynamic mode the tip scans the sample surface with the oscillating cantilever. However, the tip "taps" the sample surface with a particular amplitude under this mode. The dynamic mode combines both contact mode and non-contact mode, and it has been utilized to probe the surface topography of topological thin films in this work.

3.3 Structural Characterization

In addition to the surface morphology, the crystallographic information of the thin films is critical for evaluating the film quality. Here, X-ray diffraction provides the information of the crystal quality, while the scanning transmission electron microscopy offers direct observation of the atomic arrangement with the high resolution imaging.

3.3.1 X-Ray Diffraction (XRD)

XRD is a useful analytical technique for determining the crystalline structure, and crystal stoichiometry of a thin film system. The basic principle and the working mode of XRD will be introduced in following sections.

3.3.1.1 Bragg Diffraction

Diffraction measurements in XRD work based on the Bragg's law, which describe how the incident X-rays are scattered by the atoms in a three-dimensional periodic lattice of the crystal. When the wavelength of the incident X-rays is comparable to the lattice spacing of the material, X-rays that are in phase with each other reach the crystalline material and

intersect a series of atomic planes at an angle θ to the surface [97]. The incident X-ray beam interacts with the atoms in the crystal, resulting in scattered X-rays with the same wavelength. The scattered waves can interfere with each other constructively or destructively, depending on their relative phase differences. In cases where the phase difference between the scattered waves is π (or an odd multiple of π), destructive interference occurs, leading to cancellation of the scattered X-rays. However, at certain angles, the phase difference between the scattered waves is an integer multiple of 2π, the scattered waves thus interfere constructively, producing the diffracted beam.

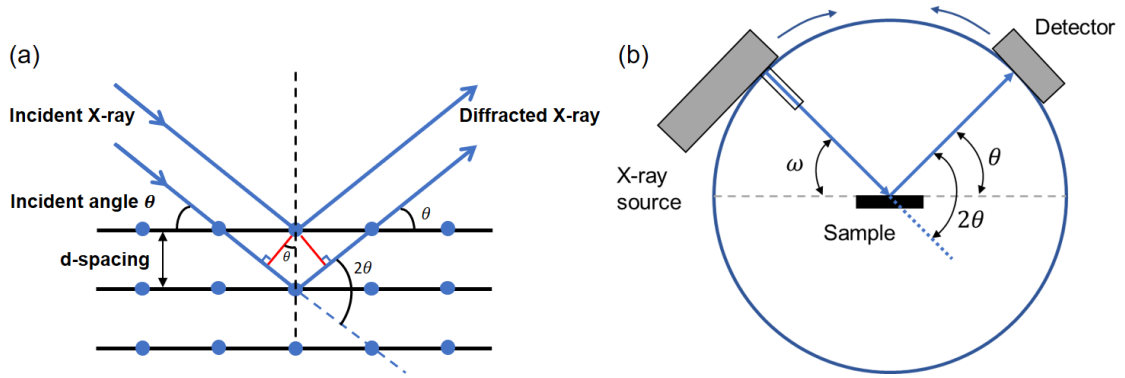

Figure 3.7: Schematic illustration of Bragg diffraction and the working principle of XRD machine. (a) Geometrical condition of the Bragg diffraction of X-rays from the lattice planes in a crystal [98]. Here, the path difference of the lower path ray and the upper ray is $2dsin\theta$, which must be an integer multiple of the wavelength to satisfy the constructive interference. (b) $\omega/2\theta$ working mode in the XRD instrument (adopted from [99]). The specimen is fixed while the X-ray source tube and the detector rotated simultaneously over certain angle ranges by the goniometer.

As depicted is in Fig. 3.7(a), Bragg diffraction occurs when the constructive interference happens at the certain angle θ based on the crystallographic planes (h,k,l) of the crystalline lattice, which can be described in the following equation:

$$n\lambda = 2d_{hkl}sin\theta, \tag{3.1}$$

n is the diffraction order (n=1,2,3...n), λ is the wavelength of the incident beam in nm, d_{hkl} is the distance between two atomic planes in nm and θ is the angle of the diffracted beam in degree.

During XRD operation, as illustrated in Fig. 3.7(b), a collimated beam of X-rays emitted from the source is scattered by the specimen over a range of angles. An X-ray detector measures the intensity of the scattered beam as a function of angle. The source tube and the detector are typically rotated in the range of 0°-120°, producing the diffraction pattern. This is the $\omega/2\theta$-scan in XRD. Besides, according to the requirement, XRD also has different measurement modes that provide a variety of information about the crystals, which will be explained in the following section.

3.3.1.2 Structural analysis via XRD

This section will introduce the structural investigation via XRD with X-ray reflectivity (XRR), X-ray diffraction (XRD), rocking curve (RC), and reciprocal space mapping (RSM). Taking Bi_2Te_3 as an example, the corresponding results are summarized in 3.8.

- **XRR:** when ω is limited at a low diffraction angle from 0° to 5°, multiple reflected waves from different surface will be collected, forming the reflectivity curve. This X-ray reflectivity (XRR) can be used to determine the density, thickness, and roughness of each layer in multilayer structures. The XRR experimental curve along with the simulation in Fig. 3.8 (a) provides the information on the thickness (17.81 ± 0.01 nm), roughness (0.46 ± 0.01 nm) and density (7.78 ± 0.01 gcm^{-3}) of Bi_2Te_3 epilayer.

- **XRD:** XRD is obtained under $\omega/2\theta$ mode. As displayed in Fig. 3.8(b), each peak in the diffraction pattern resulting from the Bragg diffraction represents a particular crystal plane of the investigated material. By matching the peaks in a diffraction pattern to a compound, it is possible to identify the elemental component of the material within in certain limit. Moreover, the intensity of the targeted peaks can also be extracted to calculate the composition of each element within the system.

- **RC:** When the 2θ angle is fixed while varying ω in a small range around the characteristic peak in XRD, the quality of the crystallinity can be addressed. This ω scan is so-called rocking curve, where the full width at half maximum (FWHM) of the peak is the key parameter to determine the growth quality. Ideally, a perfect single crystal without any defects would exhibit delta functions at specific atomic planes. In reality, however, the presence of the defects and other crystal domains will generate diffraction patterns at slightly different 2θ angles, resulting in a broadened peak. Therefore, a sharper RC indicates better crystal quality. In Fig. 3.8(c), the Gaussian fitting includes two peaks (peak 1 and peak 2). The FWHM values of peak 1 and peak 2 are 140.17 and 755.42 arcseconds, respectively. Thus, RC with the corresponding Gaussian fit provides an overall FWHM value of 195.8 arcseconds. A relatively low FWHM value reflects high crystalline quality of the thin film.

From XRD patterns, the out-of-plane lattice constant can be determined, what about the in-plane lattice? In this regard, reciprocal spacing mapping (RSM) can be used to evaluate both out-of-plane and the in-plane lattices. Depending on the geometrical diffraction process, there are two types of RSM, namely symmetric RSM and asymmetric RSM.

- **Symmetric RSM:** In this mode, the incident X-rays are reflected symmetrically from the sample, with the investigated plane parallel to the surface. It thus provides the out-of-plane lattice parameter.

- **Asymmetric RSM:** In this mode, the incident X-rays incident to a desired plane with a certain angle of sample tilt relative to the horizontal axis. The reflected signal from the incline plane to sample surface can provide information about both the in-plane and out-of-plane lattice parameters.

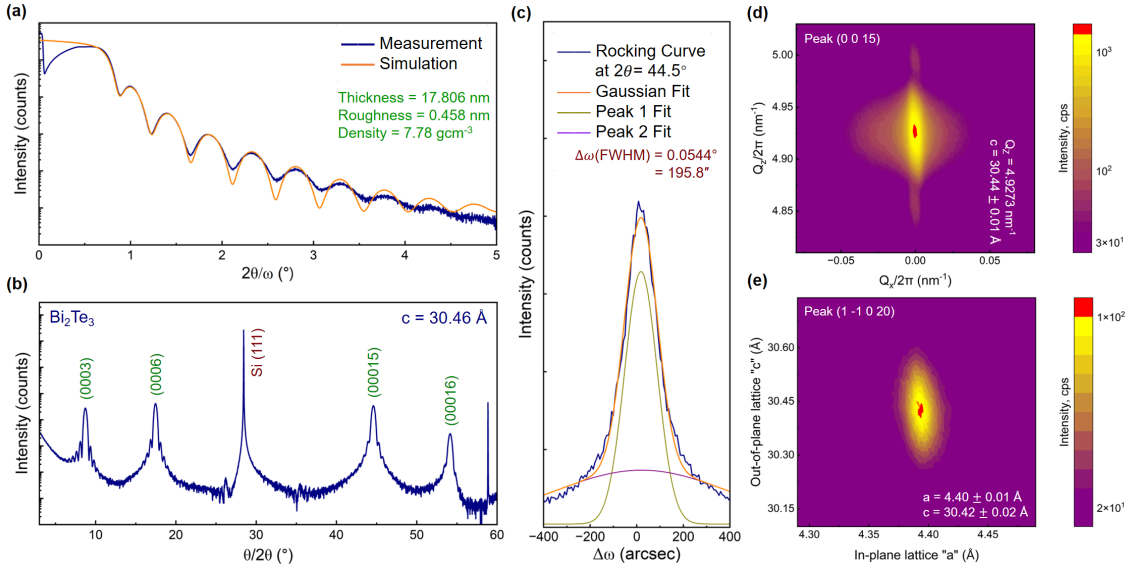

Figure 3.8: XRD characterization of Bi_2Te_3 epilayer prepared at the optimal growth parameters. (a) Measured and simulated XRR curves providing information about the thickness and roughness of the epilayer, (b) XRD $\theta/2\theta$ scan confirms the single crystallinity, (c) Rocking Curve acquired at Bi_2Te_3 (000 15) peak, (d) symmetric RSM across Bi_{TRIG} peak to evaluate the out-of-plane lattice parameter and to identify the presence of any tilted grains and (e) asymmetric RSM across Bi_2Te_3 (1 $\bar{1}$ 0 20) peak to evaluate the in-plane lattice parameters. RSM data provided by Dr. Abdur Rehman Jalil.

In-plane and out-of-plane lattice constants are calculated by equations (3.2) and (3.3) respectively.

$$a = \frac{2}{Q_{x/y}}\sqrt{\frac{h^2+k^2+hk}{3}}, \tag{3.2}$$

$$c = \frac{l}{Q_z}, \tag{3.3}$$

where $Q_{x/y}$ is the peak position alongside the in-plane direction in the reciprocal space, $Q_{x/y}$ is s the peak position alongside the out-of-plane direction in the reciprocal space. h and l are the miller indices of the peak (hkl).

3.3.2 Transmission Electron Microscopy (TEM)

In addition to XRD, TEM is another technique used for detailed structural and chemical analysis of the grown thin films. During the operation of TEM, a beam of emitted electrons passes through and interacts with an ultra-thin sample (around 20-100 nm), where the transmitted electrons are then collected by the detector underneath and form the corresponding image [100, 101]. The ultra-thin sample for TEM investigation is a lamella prepared using a specific technique, which will be introduced in section 3.3.2.2 in detail.

The first TEM was built by Max Knoll and Ernst Ruska with the resolution better than the light microscopes in 1932. Ernst Ruska received the Nobel Prize in physics in 1986 for this invention [102, 103]. Following the development of TEM, the scanning TEM (STEM) has been successfully implemented by Albert Crewe and his coworkers in 1960s, achieving a resolution of 30 Å and enabling the visualization of the single heavy atoms on thin carbon substrate [104, 105]. Over the last few decades, the implementation of the aberration corrector to TEM, particularly STEM, has significantly improved the resolution to sub-angstrom spatial resolution (0.07 nm) [106]. This improvement enables direct observation of atoms within the specimen [101, 107, 108].

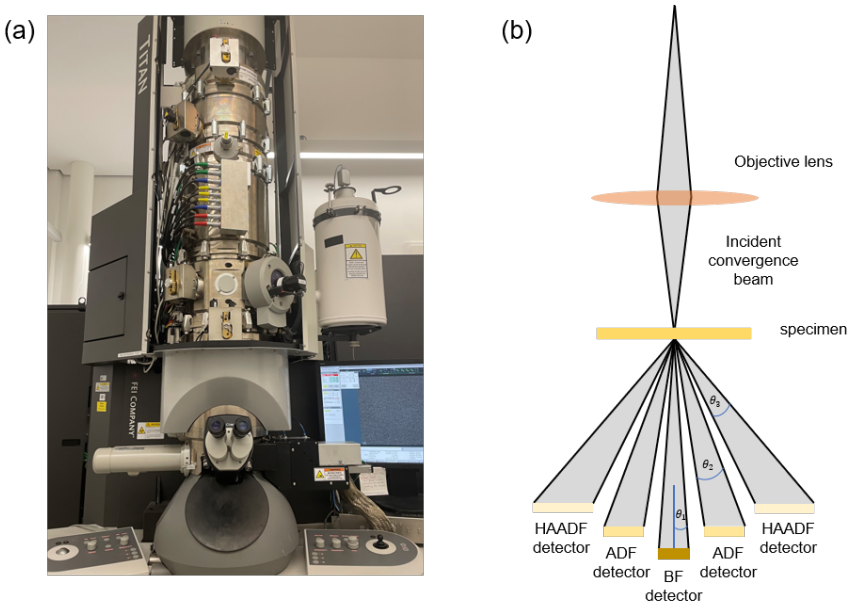

Figure 3.9: STEM system utilized in this study. (a) FEI Titan G2 80-200 ChemiSTEM, equipped with a Schottky type high-brightness electron gun (FEI X-FEG), a Cs probe corrector (CEOS DCOR), an in-column Super-X energy dispersive X-ray spectroscopy (EDX). (b) Schematic ray diagrams of convergent probe in STEM, where the HAADF, ADF and BF detectors setup is displayed with respect to the range of electron scattering angles, θ_1, θ_2 and θ_3 represent the angular ranges of the corresponding detectors relative to the vertical direction. Image modified from [100].

Nowadays, modern TEMs typically offer two operation modes, TEM mode and STEM mode.

- **TEM mode:** In this mode, a parallel electron beam illuminates the specimen and passes through the specimen, producing the TEM image of full field at once. It provides the larger field of view with shorter acquisition time compared with the following STEM mode. However, the resolution in the STEM mode is typically higher than that in TEM mode.

- **STEM mode:** In this mode, the specimen is scanned with a focused electron beam and the spot size of the focused beam is typically in the range of 0.05 to 0.2 nm [109, 110]. The incident beam scans the specimen point by point, interacting with

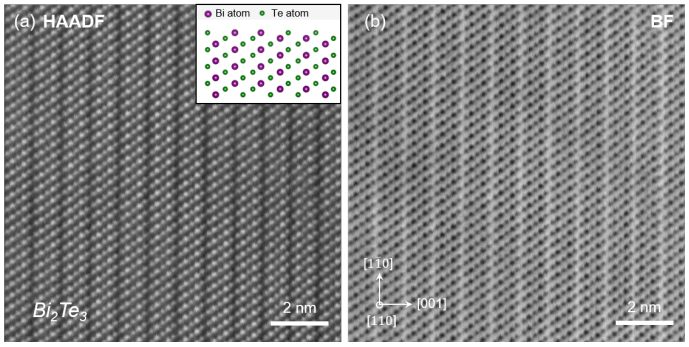

Figure 3.10: STEM images acquired along [110] projection of Bi_2Te_3. (a) HAADF image showing that brighter atoms are Bi while relative lighter ones are Te atoms. (b) BF image depicting that the heavier Bi atoms are darker than Te atoms. HAADF and BF images exhibit inverted contrast.

the atomic potential of the specimen. An annular detector positioned below the specimen collects the forward-scattered electrons and converts the received signal into current intensity, which is then visualized on the fluorescent screen and recorded digitally. Continuous scanning of a specimen area produces a scanning transmission image, where each scanned point on the specimen corresponds to an individual pixel in the STEM image. The STEM mode has been intensively employed in recent years due to its enhanced resolution, which has been utilized in this work to investigate topological insulators.

Figure 3.9(a) shows the STEM machine used in this study, while (b) illustrates different detectors positioned beneath the specimen in (a). Each detector is designed to collect certain types of information.

- **Bright-field (BF) detector:** With a collection angle $\theta_1 < 10$ mrads, this detector collects the intensities of the unscattered direct beam.
- **Annular bright-field (ABF):** This detector utilizes only the outer annulus of the bright-field disk, giving unique contrast effects. BF and ABF facilitate light element imaging, due to the small scattering angle of the electron from light element.
- **Annular dark-field (ADF) detector:** This detector captures the intensities of the scattered electrons within a collection angle of 10 mrads $< \theta_2 <$ 50 mrads.
- **High-angle annular dark-field (HAADF):** This detector collects the intensities of electrons scattered at larger angles (collection angle 50 mrads $< \theta_3 <$ 200 mrads) compared to those collected with ADF.

HAADF generates a Z-contrast image, which is beneficial to detect signals from the heavy elements. In STEM-HAADF imaging, the heavier the atom is, the brighter it will be. Meanwhile, light elements exhibit weak electron scattering at high angles, which results in lower intensities. HAADF and BF are often used together in STEM imaging due to their complementary contrasts. The relevant results are presented in Chapter 5 and 6. A representative example of Bi_2Te_3 is illustrated in Fig. 3.10.

The high-resolution STEM imaging offers the atomic-level observation of the crystal structure, enabling detailed crystal analysis of materials. Additionally, the STEM is typically equipped with chemical analytical tools, which will be introduced in the following section.

3.3.2.1 Energy Dispersive X-ray Spectroscopy (EDX)

EDX is a specialized modern technique for chemical analysis and identifying the elemental composition, attached to ChemiSTEM in Fig. 3.9(a). It is based on the energy of characteristic X-rays generated by the interaction between the electron beam in TEM and the specimen. The emitted characteristic X-ray photons have sharply defined energies that are specific to each atom [111]. The intensity of the characteristic peak in the spectrum gives the information about the relative composition in the specimen. The basic principle is illustrated in Fig. 3.11.

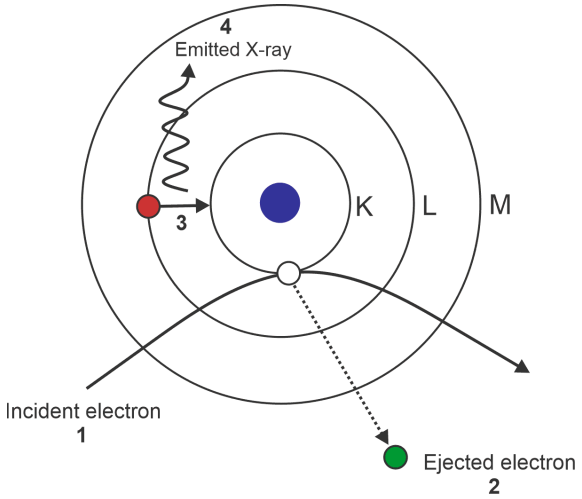

Figure 3.11: Schematic illustration of the principle of EDX. Image modified from [97].

In the initial ground state, the atom has electrons in the electron shell bound to the nucleus with critical excitation energy E_c. When an incident beam electron with an energy higher than E_c hits the atom, it can scatter an electron from the inner shell and eject it from the atom, leaving an electron hole in the inner shell (process **1** and **2** in Fig. 3.11). The energy state of the atomic vacancy is raised up from the ground state, which is energetically unstable. As a result, an electron from the outer shell (high-energy shell) undergoes a transition to the inner shell and fills the hole, thus lowering the energy state (process **3**). During the transition process, the energy difference between the outer shell and inner shell is emitted in form of X-ray photons (process **4**), which can be described in Equation (3.4) as an example of the K-L inter-shell electron transition.

$$E_{kin} = E_K - E_L \tag{3.4}$$

It should also be noted that when the energy difference of the K-L inter-shell electron transition is transferred to another L-shell electron, an "Auger electron" will be ejected instead of the characteristic X-ray emission. In general, the emission probability of characteristic X-rays increases with the atomic number, while the emission probability of Auger electrons decreases accordingly. Thus, EDX is more useful for heavy elements, especially when the element content of is low [112].

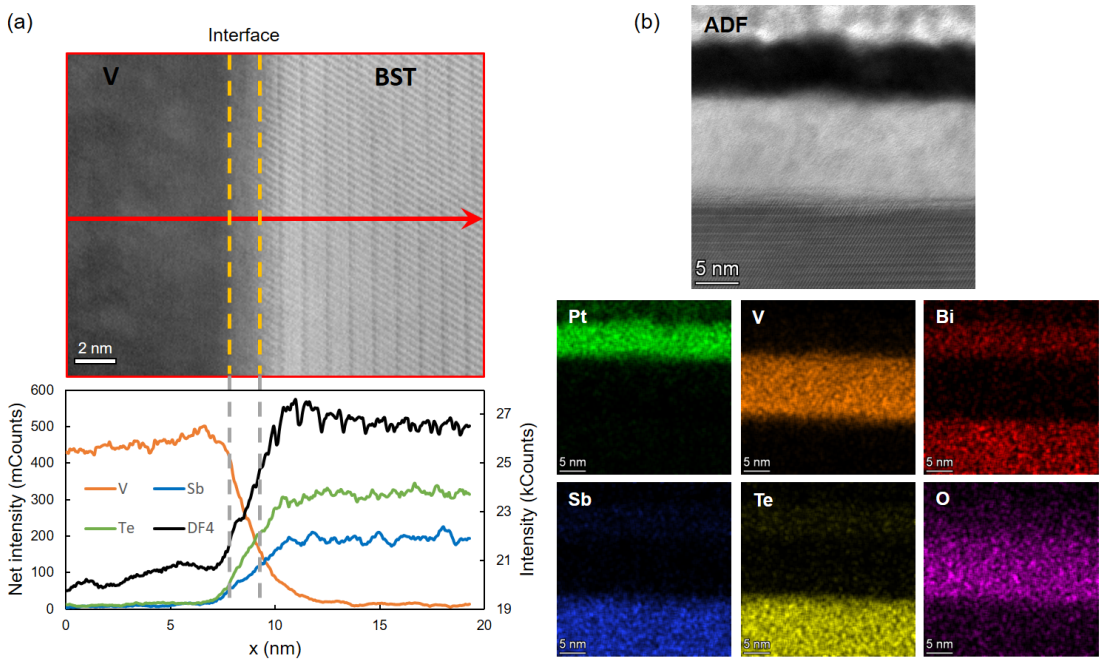

Figure 3.12: EDX investigation of a superconductor-TI system. (a) Top: ADF-STEM image of the $(Bi_xSb_{1-x})_2Te_3$-Vanadium system; Bottom: EDX area-scan spectra across the interface, showing the elemental intensity profile as a function of scanned area. (b) Top: ADF-STEM image of same material system; Bottom: elemental distribution of Pt, V, Bi, Sb, Te, O in the grown system. The sample used in this measurement was provided by Max Vaßen-Carl from PGI-9 at Forschungszentrum Jülich.

An example of STEM-EDX mapping is shown in Fig. 3.12. The interface between the V and the BST system can be mapped by the the EDX area scan across the interface region. The elemental intensity profile in the bottom of Fig. 3.12(a) is acquired along the red arrows from left to right on the top image. From the intensity profile, there is a gradual decrease in V content, whereas content of Sb and Te increase in the interface between V and BST thin film. It illustrates how the corresponding elements vary within the interface region, providing insights into the quality of the V deposition on top of BST film. In this regard, the appearance of the V within the interface and even inside BST film indicate that V diffuses into the BST thin film during the deposition process.

As shown in Fig. 3.12(b), the elemental mapping provides the information on the individual element distribution within this superconductor-TI system. It appears that Bi is also present in the Pt region according to the mapping. This observation is likely inaccurate, since some of the characteristic peaks in the Bi spectra overlap with those of Pt. Therefore, we must be careful when analysing and interpreting the XRD data.

Generally, EDX can be considered as a semi-quantitative analysing method that can provides the variation of the materials to some extend, as indicated in Fig. 3.12(a). However, the overlapping of the characteristic peaks of different elements must be considered dur-

ing the analysis to avoid invalid interpretation as displayed in (b).

3.3.2.2 Focused Ion Beam (FIB)

To conduct the TEM investigation, the specimen must be fulfill certain requirements to be compatible with the TEM machine. Therefore, the FIB is typically employed to extract and fabricate the lamella from the thin film sample.

FIB is usually combined with the SEM to form a dual beam platform, which consists of the electron source, the gallium ion (Ga^+) source, gas injection system (GIS), manipulator and detector. This system enables imaging, milling, deposition, micro machining and manipulation, which can be adopted to various applications. The FIB-SEM system used for the lamella preparation is shown in Fig. 3.13.

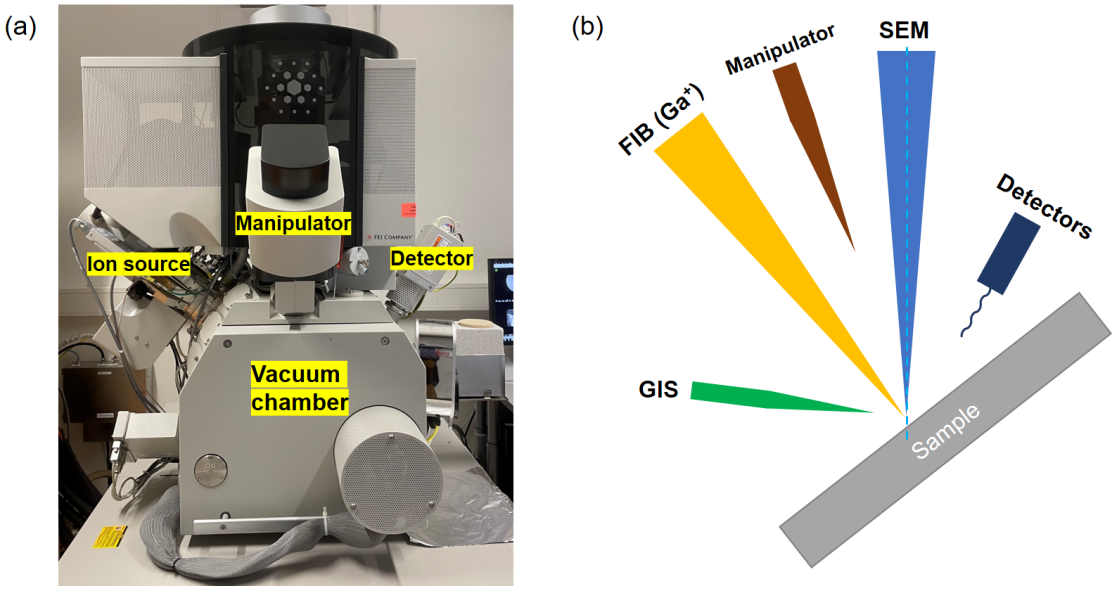

Figure 3.13: FIB-SEM system. (a) Appearance of the FEI Helios NanoLab 600i used for the lamella preparation in this work; (b) schematic illustration of the FIB-SEM system during working procedure. GIS: gas injection system.

As illustrated in the Fig. 3.13(b), the ion beam column is fixed at an angle of 52°-55°, where the electron beam is in vertical orientation. Ga^+ ion is selected as the ion source due to its low melting point (29.8°C), low volatility, low vapor pressure and because it is easily distinguishable from other elements [113, 114]. The Ga^+ ions emitted from the ion gun are accelerated at a voltage of 1-30 kV and then pass through the condenser and objective lenses. When the incident beam reaches the sample surface, it interacts with the target material, producing products that can be collected and analysed by multiple detectors. The interaction between Ga^+ ions and the target material facilitates the function of imaging, milling and deposition [115] as shown in Fig. 3.14.

- **Imaging**: The Ga^+ ion beam scanning over the sample surface triggers the emission of the secondary ions (SIs) and SEs. The emitted SIs and SEs are then collected

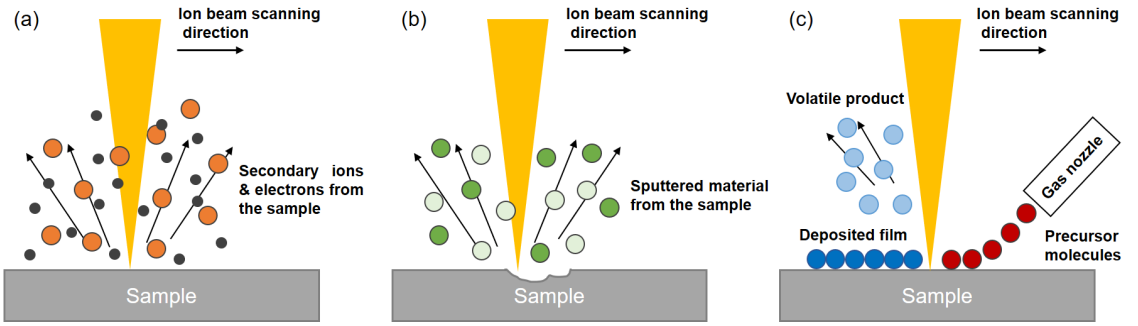

Figure 3.14: Schematic illustration of FIB operation principles: (a) imaging; (b) milling; (c) deposition. Images adopted from [116].

by detectors, generating high-resolution secondary electron images and ion images similar to the typical SEM as introduced in section 3.2.1.

- **Milling**: Material can be microscopically removed from the sample by using a high ion current beam, which is physically sputtering off the material from the sample surface. The sputtering rate depends on the acceleration voltage, the sample material, and the incidence angle [117]. The higher the beam current, the rougher the milling will be. During the normal cross-section lamella preparation, a higher beam current is usually used for rough milling in the beginning, followed by a lower current to polish the lamella in the final thinning process [115]. It is important to mention that, a high beam current can cause unexpected damage, such as material surface amorphization [118].

- **Deposition**: For deposition, a suitable gas will be injected from the GIS through a gas nozzle as precursor. These precursors are firstly sprayed onto the sample surface and then decomposed by the ion beam into volatile and non-volatile components. The volatile component desorbs from the surface while the non-volatile component remains as a deposit on the sample surface. The most commonly deposited elements are platinum (Pt) and carbon (C), typically used as the protection layers.

The dual beam FIB-SEM system is a powerful tool to fabricate the lamella specimen based on aforementioned functions. The detailed lamella preparation procedure is illustrated in Fig. 3.15.
To preserve the sample surface, a protective layer should be deposited over the region of interest prior to cutting. Due to the sensitivity of the TI materials to carbon, Pt is chosen as the protective layer to maintain the crystallinity of the thin film, even though it has curtain effect[4], which can be seen in the Appendix Fig. A1.2.

The protective layer was first deposited by electron beam, followed by ion beam, as depicted in Figure 3.15(a)-(b). This approach prevents the damage to the sample surface from the heavier Ga^+ ions during the ion beam process.

[4]Curtain effect refers to a specific type of imaging artifact with stripes of light and dark contrast (a series of parallel lines or curtains that appear in the image) [120, 121]. This effect can be induced by insufficient or improper FIB metal deposition and improper milling parameters [122].

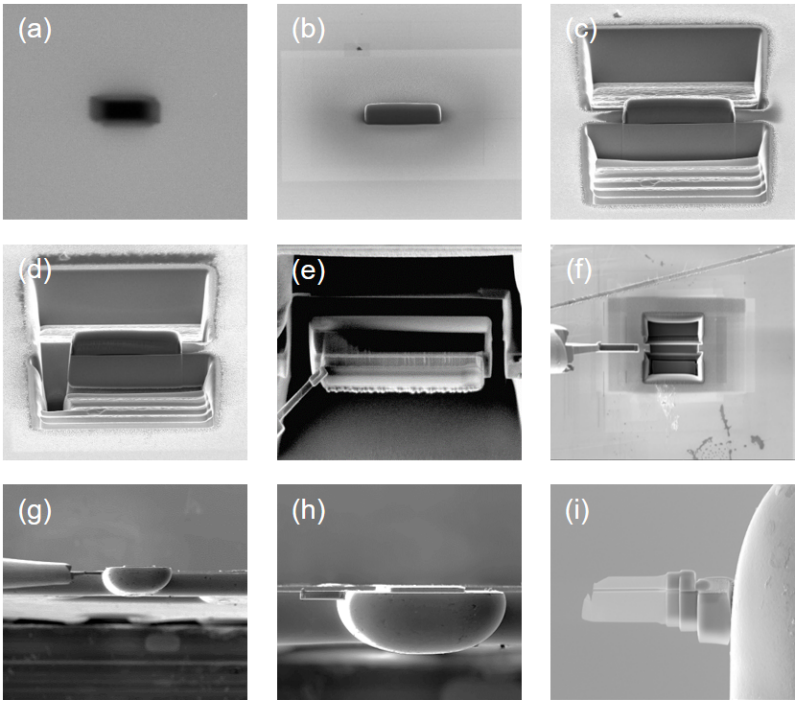

Figure 3.15: Primarily TEM lamella preparation procedure. (a) Electron beam platinum protection layer. (b) Ion beam platinum protection layer. (c) Trenches cut allowing undercut and manipulator approach. (d) Undercut and partially side cut of the lamella. (e) Connection between the needle and the lamella with cutting the side part. (f) Lift off of the lamella with the manipulator. (g) Lamella transfer to the grid. (h) Lamella attachment to the grid and cut from needle. (i) Final lamella after a series of thinning processes. Image taken from Xiao Hou's master thesis [119].

Following lamella preparation routines, trenches were cut perpendicular to the surface of the material to fabricate a free-standing lamella as shown in Fig. 3.15(c), followed with the cleaning trench procedure in same depth. The undercut in (d) was proceeded with the stage tilted at an angle of 7°. After tilting the stage back to an angle of 0°, the tip of the manipulator was then positioned at the side trench next to the lamella, which was attached to the needle tip via a small Pt deposition pad in (e). Subsequently, the lamella could be detached from the bulk material in (f).

The manipulator was then moved away from the operational range of the stage and the lamella was transfered to the grid. During this step, the lamella cast a shadow in the SEM-FIB image, which helped to determine the distance between the lamella and the grid. With the deposition of a Pt pad between lamella and gid, the lamella was able to attach to the grid in (g), enabling the removal of the needle (h) and the retraction of the manipulator.

The thinning and polishing procedures are conventionally carried out until the layer thickness below 100 nm. However, in the case of topological insulators, it is better to thin them below 50 nm within FIB, as their crystal structure tends to become amorphous or change when further thinned using the *Fischione 1040 Nanomill* machine. The final lamella is depicted in Fig. 3.15(i). It is specially modified while the milling voltage is adjusted from

30 kV, 16 kV, 8 kV, 5 kV to 1 kV with respect to the current instead of from 30 kV to 5 kV for the normal preparation procedure. This small step milling series allows a good preservation of the crystal structure of TI.

3.4 Angle-resolved Photoemission Spectroscopy (ARPES)

In addition to the surface and crystal structural analytical techniques, ARPES is used to probe the electronic band structure of topological thin films or bulk TIs. It works based on the photoelectric effect first observed by Heinrich Hertz in 1887 [123]. When a monochromatic light source with sufficient photon energy is incident upon the sample surface, electrons can be ejected from the surface. By measuring the kinetic energy and exit angle of the electrons emitted from the surface of a crystalline solid, information about momentum and energy of the electronic state of the sample is obtained, enabling ARPES to map the corresponding electronic band structure. This section will introduce the specimen preparation methods for ARPES measurements, experimental setup of the ARPES system at PGI-6 ARPES lab, and the momentum microscope at the synchrotron facility.

3.4.1 Sample Preparation

In case of the photon source energy in the ultraviolet (UV) range in ARPES, the inelastic mean free path (IMFP) is aprox. 10 Å [124]. The low IMFP prevents electrons from the deeper regions of the specimen from escaping, indicating that only the electrons from the topmost surface layers, which do not undergo inelastic scattering, contribute to the band structure. Therefore, a sample with clean surface is essential to probe the electronic band structure. However, when TIs are exposed to the air, their surfaces will be contaminated. To avoid the contamination, several methods can be employed to create a clean sample surface.

For the bulk sample, due to van-der-Waals bonding between adjacent layers, the contamination layer can be easily removed by applying mechanical forces with scotch tape in the UHV. As shown in Fig. 3.16(b) and (c), the scotch tape is connected to a grabbing wire, which will be pulled by a wobble stick under UHV condition, removing the tape from the crystal. This process, known as cleavage, can produce large area flat and clean terraces on the sample surface. The cleaved surfaces are perpendicular to the stacking direction of TI materials, which are accessible for ARPES investigation [125].

However, scotch tape cleavage method is ineffective for the thin film TIs. Until now, people have utilized two methods to maintain the surface cleanliness of the TI thin films for photoemission experiments, which will be discussed below.

- **Vacuum transfer with the vacuum suitcase:** During the entire vacuum transfer process, the sample is grown on the Si substrate, which is loaded on a specially designed metal holder (typically made of Cu), and after the growth, the holder

(with the sample on it) is picked up by the arm of the vacuum suitcase and held under vacuum. The vacuum suitcase pressure is usually in the range of 10^{-9} mbar. The suitcase is then moved to the ARPES lab, attached to the load lock chamber of the ARPES machine, and the connection is pumped for several hours. Finally, the holder is transferred onto the manipulator in the preparation chamber of the ARPES system (The system be introduced in next section 3.4.2). Throughout the entire process, the sample is kept under vacuum at all times, preventing the degradation of the sample surface. The schematic illustration of the vacuum suitcase is shown in Fig. A1.3 in the Appendix.

- **Cleavage with the post glued on the sample:** After the growth of TI thin films, an additional capping layer is usually deposited to prevent the oxidation of the thin film. However, the capping layer can not be easily removed by the scotch tape employed, as in the case of bulk samples. In recent years, people found out that if they attach a post to the sample surface using an epoxy glue such as EPO-TEK H20E (silver epoxy) or Torr Seal (as in the bottom in Fig. 3.16(a)), the sample can be in-situ cleaved by knocking off the post [126] as displayed in Fig. 3.16(e). During the cleving process, part of the thin film sample can be possibly removed along with the capping layer that attached to the glue.

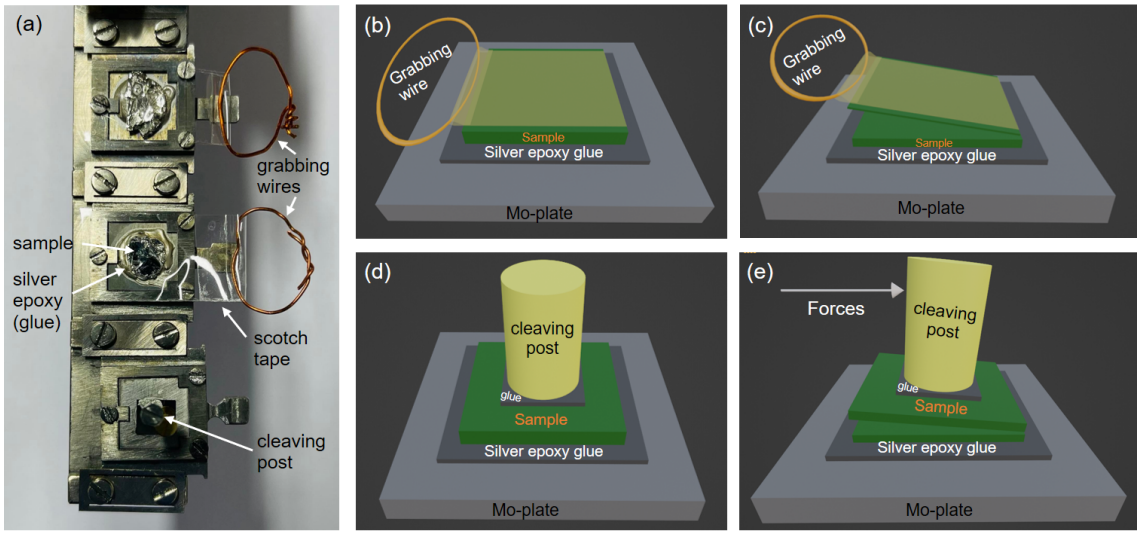

Figure 3.16: (a) Sample magazine at PGI-6 ARPES lab. Samples are glued on 10×10 mm^2 Molybdenum plates with silver epoxy. Here, the plates are mounted on the Omicron flag style holders. The samples on the top and middle are prepared for tape cleaving: the main part of the scotch tap is attached to the sample while the other side of the tape grips the wire, which is used to pull off the surface of the sample. The bottom one is prepared for post-cleaving, where two posts are attached on the sample by silver epoxy. (b) and (c) Schematic illustrations of the cleaving process using the scotch tape. (d) and (e) Schematic illustrations of the cleaving process for the TI thin films with capping using the post. The capping layer can be removed by applying forces to the post under UHV, ensuring that the surface of the TI thin film is never exposed to the atmosphere. Images were processed in collaboration with Mohammed Qahosh in PGI-6.

3.4.2 ARPES machine at PGI-6

As ARPES is a surface-sensitive technique, measurements should be conducted under UHV condition to preserve the atomically clean surface after cleavage. Besides, the UHV allows the excited electrons to travel undisturbed to the electron detector, which carry the information about the electronic structure of the sample. Therefore, the machine is a UHV system to maintain the surface cleanliness and enables the detection of unscattered electrons. The base pressure of this system is typically 5-10$\times 10^{-11}$ mbar.

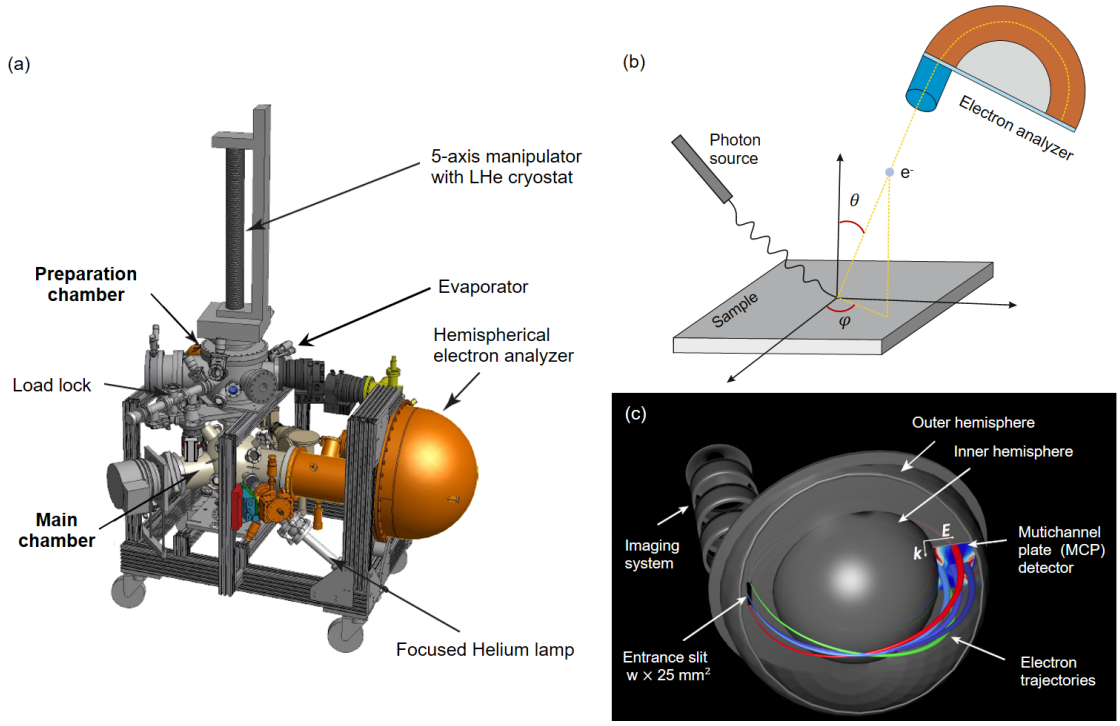

Figure 3.17: (a) Schematic view of the ARPES system at PGI-6, Forschungszentrum Jülich. The machine consists of load lock chamber, preparation chamber, main chamber, hemispherical electron analyzer, focused Helium lamp, Xe lamp and laser as photon sources, and 5-axis manipulator with a LHe cryostat. (b) Interaction of the photon with the sample. Photon source impinges on the sample surface, electrons are emitted and then pass through the hemispherical electron analyzer, having a certain kinetic energy E_{kin} and emission angle φ and θ. (c) Schematic illustration of the hemispherical electron analyzer. (a) and (c) are taken from Dr. Markus Eschbach's thesis [125].

Figure 3.17(a) presents a schematic front view of the high-resolution ARPES machine at PGI-6. The system consists of a load lock chamber, a preparation chamber, a main chamber, a hemispherical electron analyzer and different photon sources. To perform the ARPES experiment, the sample is first loaded into the load lock chamber. After 2-3 hours, when the pressure in the load lock reaches 1×10^{-8} mbar, the sample will be transferred to the sample holder on the 5-axis manipulator. The 5-axis manipulator can move in all three spatial directions (x, y, z), a full rotation around the manipulator center, and a full rotation on the sample. Besides, the manipulator is equipped with a liquid helium flow cryostat, enabling the cooling down to below 10 K at the sample position. After the sample is

cleaved in the preparation chamber (in case of layered materials), it is transferred into the main chamber to perform the photoemission experiment. Various light source are attached to the ARPES machine for measurements, where helium lamp and laser are the common sources used in this study.

3.4.2.1 Photon source

Helium lamp (He I_α 21.22 eV) and laser (6 eV) are available as the photon sources[5].

For helium lamp, the wavelength (λ_{HeI_α} = 58.43 nm) is in vacuum ultraviolet regime (VUV, λ < 200 nm), which means that the light will be absorbed by air, therefore, the lamp has to be integrated into the UHV system and the light is generated under vacuum conditions. The spot size of helium lamp is in 0.2 mm range. Besides, helium lamp can remain stable for a long time while operating, which can compensate the low flux with long measurement time.

For laser, the wavelength is $\lambda \approx 206$ nm. When the wavelength is above 200 nm, it is beyond the absorption edge of the air[6]. Hence, the laser system can be adjusted and manipulated in the ambient pressure. It also has high photon flux and small beam spot size down to 100 μm. Most importantly, it has full control of the polarization of the light, which is capable of generating both linearly polarized and circularly polarized light. The latter opens new path to the dichroism study for different materials.

3.4.2.2 Hemispherical electron analyzer

As shown in Fig. 3.17(b), after the electrons are ejected from the sample surface, they will travel through the vacuum and enter the hemispherical electron analyzer with a certain kinetic energy and angle. The schematics of the hemispherical electron analyzer is illustrated in Fig. 3.17(c). It consists of a lens system and the hemispherical capacitor analyzer. Depending on the lens settings, electrons will be projected onto the entrance slit of the hemisphere, preserving either their the spatial or angular distribution. The entrance angle, perpendicular to the slit, ranges from -15° to 15° Due to the voltage applied between the sample and the entrance slit, emitted electrons of specific initial kinetic energy will be retarded or accelerated to match the pass energy (E_{pass}). After the electrons pass through the slit, they are energy-dependently deflected by the voltage between the inner and outer hemispherical analyzer. In (c), the green, blue, and red trajectories illustrate electrons with different incoming angles, while for the beam passing the center of the lens, the different blue shadings refer to different kinetic energies. Only electrons within a kinetic energy window within the range of 8.7% - 10% of the E_{pass} will deflect through the analyzer (trajectories in (c) with different blue shading). Electrons with kinetic energy higher than 8.7% - 10% of the E_{pass} will collide with the outer hemisphere of the analyzer,

[5]There are several levels of helium lamp. He I_α:58.43 nm = 21.22 eV, He II_α:30.38 nm = 40.81 eV, and additional β lines, however, He I_α is the most intense component in the excited light. If the He I_α is set as the reference with 100% relative intensity, He II_α has an intensity of approx. 10–30% of the He I_α line, while the β lines are more than 100 times less intense and can therefore be neglected [127].

[6]The absorption edge in air generally increases sharply around 180-190 nm, due to oxygen, nitrogen and other gases [128].

while electrons with kinetic energy lower than 8.7% - 10% of the E_{pass} will collide with the inner hemisphere. Finally, a two-dimensional multichannel plate (MCP) detector system detects and multiplies the electrons, which will provide a 2D image of kinetic energy versus emission angle [125].

3.4.2.3 Interpretation of the ARPES spectra

Based on the photoelectric effect observed by Hertz [123], Einstein extended the theoretical explanation by introducing the quantum nature of light (as the discrete units of energy) [129]. According to his findings, the kinetic energy of the photoelectrons emitted from a solid is given by the following equation:

$$E_{kin} = h\nu - \Phi - E_B \tag{3.5}$$

E_{kin} is the kinetic energy of the emitted electron in vacuum, E_B is the binding energy of that electron inside the solid before it was excited, and Φ is the material-dependent work function, which is a potential barrier that the electron has to overcome to leave the solid (in most materials typically 4 - 5 eV).

$$E_B = h\nu - \Phi - E_{kin} \tag{3.6}$$

Therefore, The binding energy can be extracted based on equation 3.5, as displayed in equation 3.6. Besides, to analyse the angular image, the the emission angle is converted to $k_{\|}$ with the following equation:

$$k_{\|} = 0.512\sqrt{E_{kin}}sin\theta \tag{3.7}$$

Based on equation 3.5 and 3.7, binding energy versus $k_{\|}$ image can be plotted. Figure 3.18 presents examples of a cleaved bulk Sb_2Te_3 sample and a $(Bi_xSb_{1-x})_2Te_3$ (BST) thin film sample grown by MBE (provided by Max Vaßen-Carl from PGI-9, Forschungszentrum Jülich) measured with helium lamp and laser, respectively. The MBE grown thin films are transferred to the ARPES chamber through the vacuum suitcase.

From Fig. 3.18(a) and (b), the bulk sample provides a sharper ARPES map due to the large area flat surface after cleavage compared with thin films. Besides, (b) and (c) present ARPES maps of the vacuum-transferred thin film, which are relatively blurred due to the poor quality of the film. From the range of binding energy in the maps, laser has higher resolution than the helium lamp.

By utilizing two-dimensional detection systems and the energy dispersive plane in hemispherical analyzer, a single shot measurement yields a 2D spectrum $I(E_{kin}, k_x)$; varying the emission angle by sample rotation orthogonal to the slit introduces another angular dimension, which results in $I(E_{kin}, k_x, k_y)$; additionally, changing the photon energy enables probing the third momentum dimension, producing a four-dimensional data set

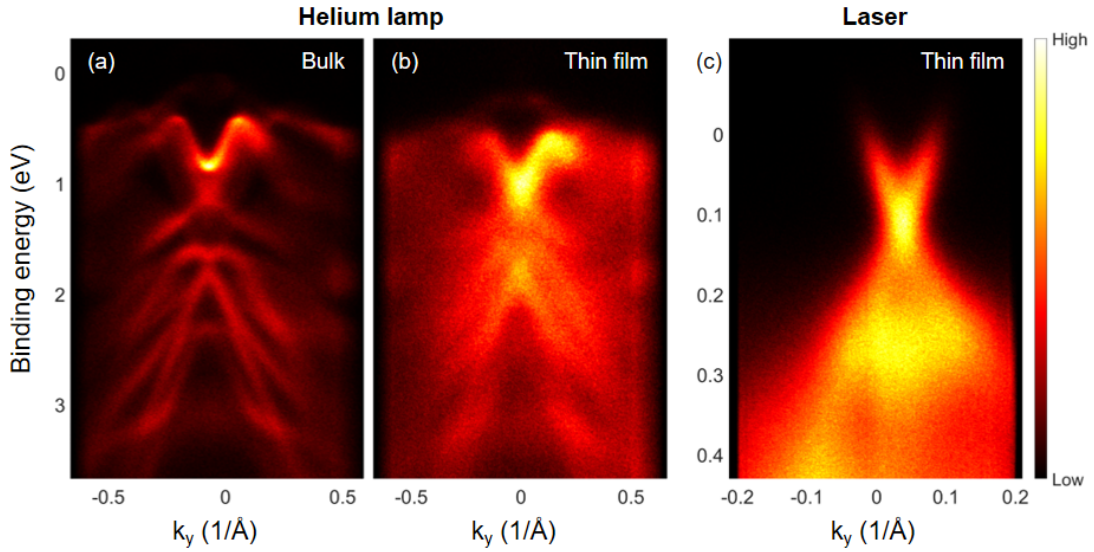

Figure 3.18: Comparison of the ARPES map of bulk and thin film sample with the helium lamp and laser: (a) ARPES $E(k_{\parallel,y})$ map of cleaved Sb_2Te_3 bulk sample measured with the helium lamp. (b) and (c) ARPES $E(k_{\parallel,y})$ maps of vacuum-transferred BST thin film measured with the helium lamp and laser, respectively. (Measurements were performed with assistance of Mohammed Qahosh.)

$I(E_{kin}, k_x, k_y, k_z)$. The momentum vectors of the electrons in vacuum are determined by measuring E_{kin} and the emission angles ϑ and φ (Fig. 3.17(b)).

$$k_x = \frac{1}{\hbar}\sqrt{2mE_{kin}}sin\theta cos\varphi \tag{3.8}$$

$$k_y = \frac{1}{\hbar}\sqrt{2mE_{kin}}sin\theta sin\varphi \tag{3.9}$$

$$k_z = \frac{1}{\hbar}\sqrt{2mE_{kin}}cos\theta \tag{3.10}$$

The components are routinely related to the sample surface $k_{\parallel} = (k_x, k_y)$ and $k_{\perp} = k_z$.

In this thesis, ARPES at PGI-6 was utilized to perform the circular dichroism angular photoemission studies with laser source on $MnBi_6Te_{10}$ bulk sample (section 7.1.2) and normal ARPES on the vacuum-transferred TI thin films with helium lamp (section 7.2).

3.4.3 NanoESCA Beamline at Elettra

In addtion to the ARPES facility at Forschungszentrum Jülich, PGI-6 also operates a beamline at the Elettra synchrotron facility in Trieste, which is equipped with a momentum microscope. The microscope can be operated in three different modes: photoemission electron microscope (PEEM) mode, energy-filtered PEEM mode, channeltron.

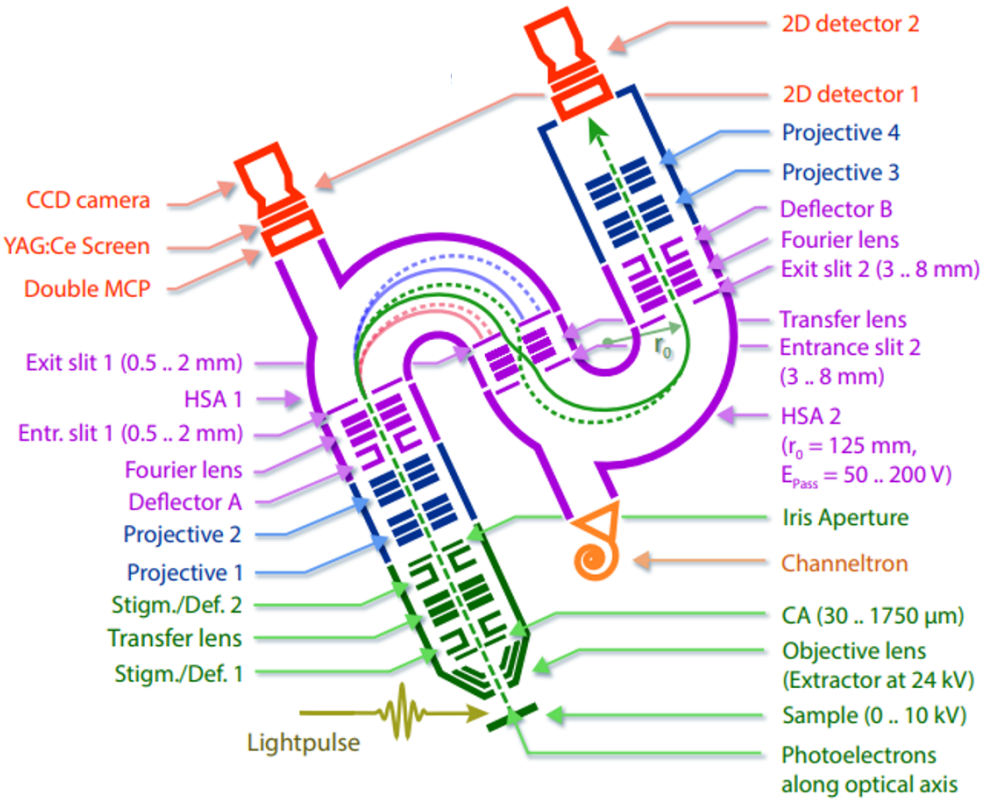

Figure 3.19: Schematic illustration of the experimental setup in NanoESCA as an example of an energy-filtered photoemission microscope. Image adapted from [130].

Figure 3.19(a) presents schematic diagram of the NanoESCA in case of the energy-filtered PEEM mode, which consists of objectives, projective lenses, two hemispherical analyzers (HSAs), and 2D image detectors. In this mode, the electrons enter the double hemispherical after passing the first optical column. The first hemisphere separates electron by kinetic energy, where only photoelectrons with certain kinetic energies are allowed to pass through the filter. The second hemisphere is used to compensate the (spherical) aberrations for high spatial resolution image. By adjusting the projection lens settings, the microscope can switch between real-space and momentum-space imaging, achieving spatial resolution of less than 150 nm and energy resolution of better than 70 meV [130]. In this study, both the real space and the k-space imaging are employed to perform the work function mapping and the band structure measurement, respectively.

Besides, this synchrotron light source has an energy range from 40 to 1000 eV with high photon flux density. It can produce linear polarised and circular polarised light. The beam spot is approximately 15-20 μm. The small beam size enable the measurement of the small domains and terraces in flakes or layered-materials.

In this thesis, the NanoESCA beamline was utilized to identify the presence of different terraces in $MnBi_6Te_{10}$ bulk crystal after cleavage and perform the circular dichroism photoemission studies on corresponding terraces. Detailed measurement results are presented in section 7.1.1 and 7.1.3.

4 Current Challenges in the field of Topological Insulator

Commentary: *This chapter presents a literature review on topological insulators, with a particular focus on current challenges in the field. The content has been compiled and developed by the author. The first section, Material Challenges, provides a review of both two-dimensional and three-dimensional topological insulators. Images included in this section have been taken from relevant sources, with proper citations provided within each caption.*

The second section, Growth Challenges, is based on both relevant literature and corresponding experimental evidence. The thin film samples discussed in this section were grown by the author, with the exception of Fig. 4.11(a) and Fig. 4.11(c), which were grown by Max Vaßen-Carl and Dr. Abdur Rehman Jalil, respectively. All TEM data acquisition, analysis and the preparation of TEM figures in this section were carried out by the author in close discussion with Dr. Abdur Rehman Jalil. The growth experiments were conducted at PGI-9, and sincere gratitude is extended to PGI-9 for providing the opportunity to perform these experiments. The TEM images presented in this chapter were collected at the Ernst Ruska Centre (ERC), and the author gratefully acknowledges ERC for access to their facilities.

During the last decades, topological insulators (TI) have become a popular field of research due to their exotic surface states and potential for advanced applications via Majorana zero modes in TI-superconductor (SC) hybrid nanostructures [3, 131, 132] including topological antiferromagnetic spintronics [133], and fault tolerant quantum computation [12, 14]. Despite significant progress, several challenges still remain for 2D and 3D TIs from the materials perspective. First of all, the material choice of 2D TI is limited and in most cases, it is difficult to obtain stable 2D TIs. Major issue for 3D TI is to find the optimal material system that exhibits the Dirac point (DP) and the Fermi level within the bandgap. Another challenge is the presence of charged fluctuations in TIs and the resulted charge puddles in the system, which limits the device application of TIs. These material-related challenges will be addressed in section 4.1, whereas the growth-related challenges will be discussed in section 4.2.

4.1 Material Challenges

4.1.1 2D Topological Insulator

With the theoretical prediction of the quantum spin Hall effect in graphene by Kane and Mele in 2005 [6], HgTe/CdTe quantum wells have been subsequently suggested by Hughes and Zhang [7] as the promising candidate for the 2D TI. Within the following year, the first experimental realization of a 2D TI was achieved using HgTe/CdTe quantum well structures by Molenkamp's group in Würzburg [8].

The first discovery of this 2D TI is a milestone in the understanding of topological phases of matter and opens up new paths for for technological purposes in the field of quantum spintronics and topological quantum computation. However, HgTe has a small bandgap (typically in the range of 10 - 30 meV [134]). Besides, it can not be annealed above 70 °C, which restricts its compatibility with standard device fabrication processes [135]. These limitations make HgTe unsuitable for integration with conventional devices.

In 2017, bismuthene[1] on the SiC substrate has been proven to exhibit similar topologically protected edge states at room temperature [136]. Compared to HgTe/CdTe, significant improvements in room-temperature stability of bismuthene further expands the potential applications of 2D TIs. However, the growth of bismuthene is particularly challenging due to its ultra-thin nature, as it consists of a single atomic layer of bismuth.

Bismuth as a bilayer has also been demonstrated to be a 2D TI [137]; however, with its thickness of only 0.4 nm and prone to surface oxidation, the growth is also challenging. The question arises how can this thickness limit be increased to realize the 2D TI. A theoretical proposal of $Bi_{1-x}Sb_x$ alloy indicates that by reducing the thickness of $Bi_{1-x}Sb_x$ (when x = 0.04 – 0.07) alloy to approx. 4 nm, the thin film starts to show 1D edge state. The thickness requirement for $Bi_{1-x}Sb_x$ (BiSb) to achieve the 2D regime is more relaxed compared with 1 nm or even thinner in case of Bi layers, thus providing a feasible platform for the topological device study.

Meanwhile, Bi orthorhombic phase with the thickness of 4 monolayers has also been identified as a 2D TI by Lu. et al [138]. Moreover, a recent study [17] predicts that Bi orthorhombic thin films with the thickness below 9 nm are in the topological regime, which further increases the thickness limit. This topic will be discussed in the second section of Chapter 5.

4.1.2 3D Topological Insulator

While 2D TIs face significant challenges in realizing suitable material systems, 3D TIs extend the challenges with the manipulation of the surface states and the presence of charged impurities. To enhance the relative transport contribution of topological surface states (TSS) in 3D TI, there are two requirements which need to be fulfilled.

- The bulk gap should be large enough.

[1] Bismuthene is a monolayer of bismuth, analogous to graphene.

- The Fermi level and the Dirac point should be within the bulk gap.

With the discovery of a class of binary TIs, i.e., Bi_2Te_3, Bi_2Se_3 and Sb_2Te_3 in 2008, researchers have been trying to explore and enhance the relative transport contribution of the TSS within the Dirac cone [27]. However, the three aforementioned 3D TIs suffer from the intrinsic defects in the materials. Sb_2Te_3 exhibits the intrinsic antisite defects that act as acceptors, leading to the p-type doping with the Fermi level in the bulk valence band (BVB). For Bi_2Te_3, the Fermi level is positioned in the bulk conduction band (BCB) due to Te vacancies that act as donors, and the Dirac point is buried deep in the "M" shape valence band pocket. Bi_2Se_3 is also a n-type materials with the Fermi level in the BCB due to the presence of selenium vacancies [139, 140]. The band structure of these three materials has already been demonstrated in the experiment and theoretical calculation, as shown in Figure 4.1. Crystal imperfections, in particular vacancies and antisites, are responsible for increased carrier density observed in the transport measurement [141]. Therefore, the n-type or p-type doped TI crystals exhibit metallic behavior. The measured conduction behavior in these materials is a mixture of the bulk and surface conduction, with the bulk contribution being the dominant, since the surface state only accommodates a small number of carriers [142].

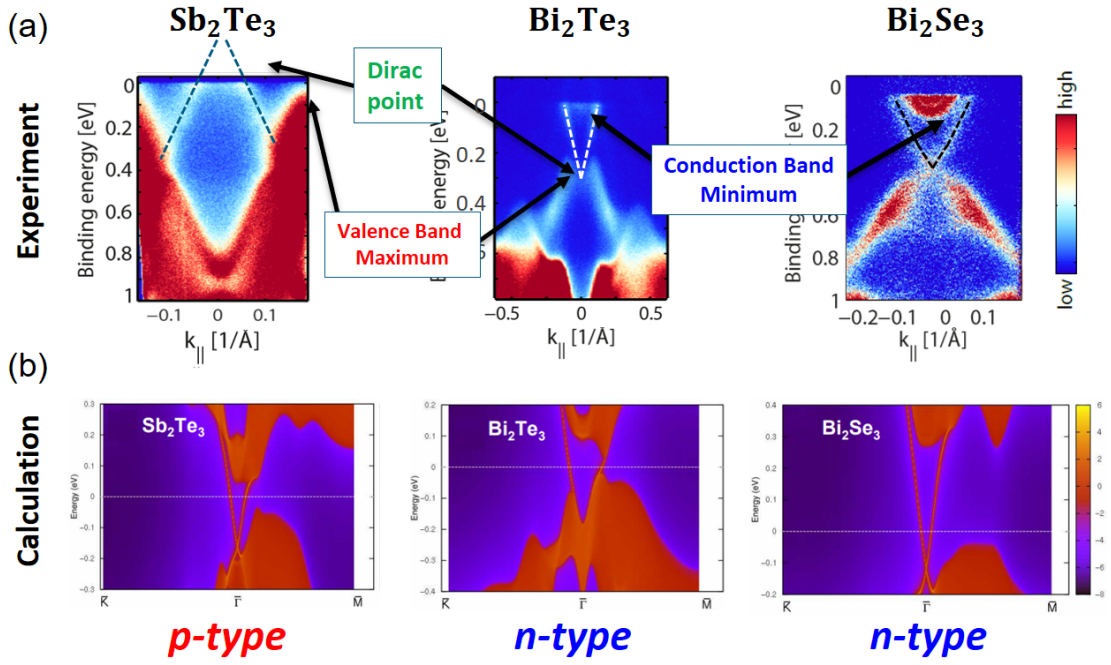

Figure 4.1: (a) Experimental ARPES measurement on Sb_2Te_3, Bi_2Te_3 and Bi_2Se_3 along $\overline{\Gamma M}$ direction showing the corresponding band structure and Dirac cone. ARPRS measurement in PGI-6 ARPES lab. (b) First-principle calculation of the surface electronic structure showing topological surface states of the three materials at $\overline{\Gamma}$ point, images taken from [27].

A material that fulfills the above-mentioned two requirements is named as the bulk insulating TI. However, the application of TIs to a wide range of devices requires a way

to intentionally manipulate the properties of the Dirac carriers while keeping the bulk sufficiently insulating [143].

- One of the approaches is applying gate voltages. Researchers have successfully manipulated the surface states in Bi_2Se_3 nanoribbons by gating the device [144]. However, this method has a higher requirement to the growth quality due to the high intrinsic defects in TIs.

- Another way is to alloy with additional element to the system ("chemical tuning"), which could also tune the Fermi level into the bulk gap and even to the Dirac cone. Since 2010, scientists have been trying to alloy Sb into Bi_2Te_3, forming the $(Bi_xSb_{1-x})_2Te_3$ alloy [145]. By controlling the concentration of Sb, the Dirac point can be shifted with respect to the Fermi energy E_F, allowing for reaching the bulk insulating state. As shown in Fig. 4.2(a), the Fermi level is shifted continuously downwards from the bulk conduction band (BCB) to bulk valence band (BVB) via a bulk insulating state (Sb = 75 %) while increasing the concentration of Sb.

However, while introducing the dopants into the system, the Coulomb disorder i.e., randomly distributed ionized acceptors and donors defects, can not be avoided. These randomly distributed charges (every 20 to 30 nm) in space create random potential fluctuations as large as the TI bulk gap. As shown in Fig. 4.2(b), the large fluctuations in the random potential of acceptors and donors will bend the conduction and valence bands edges and in some places bring them to the Fermi level, thereby creating electron and hole puddles that nonlinearly screen the random potential [139, 148]. Recently, Ando's group found that the length scale of the fluctuations, λ ranges from 13 to 54 nm [149]. These charge puddles will effectively reduce the resistivity, as the electron and holes can hop between puddles, thus reducing the activation energy of the bulk transport [146]. These charged impurities are detrimental to the performance of a Majorana bound states (MBS) device [150]. Therefore, how to avoid or improve the puddles in the compensated system has been a target from material perspective in this research field for a long time.

Doping Sb to Bi_2Se_3 instead of Bi_2Te_3 can improve the puddle issue, as Bi_2Se_3 have a much larger bandgap (c.a. 300 meV [151]) compared with Bi_2Te_3 (c.a. 171 meV [152]). The Fermi level can also be moved into the gap by adjusting the Sb concentration [145]. Due the larger bandgap, the random potential fluctuations caused by the charge impurities can be suppressed within the TI bulk insulating gap, which will hopefully reduce or eliminate the charge puddles. However, the crystal structure of Sb_2Se_3 is not rhombohedral but orthorhombic. Once the Sb content reaches a certain level, Sb_2Se_3 forms and segregates within the films, which does not allow the optimal growth of the pure $(Bi_xSb_{1-x})_2Se_3$ epilayers. This phenomenon has already been observed in the quaternary alloy $Bi_{2-x}Sb_xTe_{3-y}Se_y$ (BSTS) as shown in Fig. 4.2(c) [147].

As already discussed, it is critical to bring the Fermi level into the gap. However, the significant puddle effect in the BST leads to the band bending issue, which does not allow the Fermi level within the gap all the time. Therefore, it is important to search the suitable new material platforms. Another possibility is that the p-type dopant Sn could replace the Sb, forming the Sn-based Bi_2Te_3 alloy. In this case, unlike the conventional

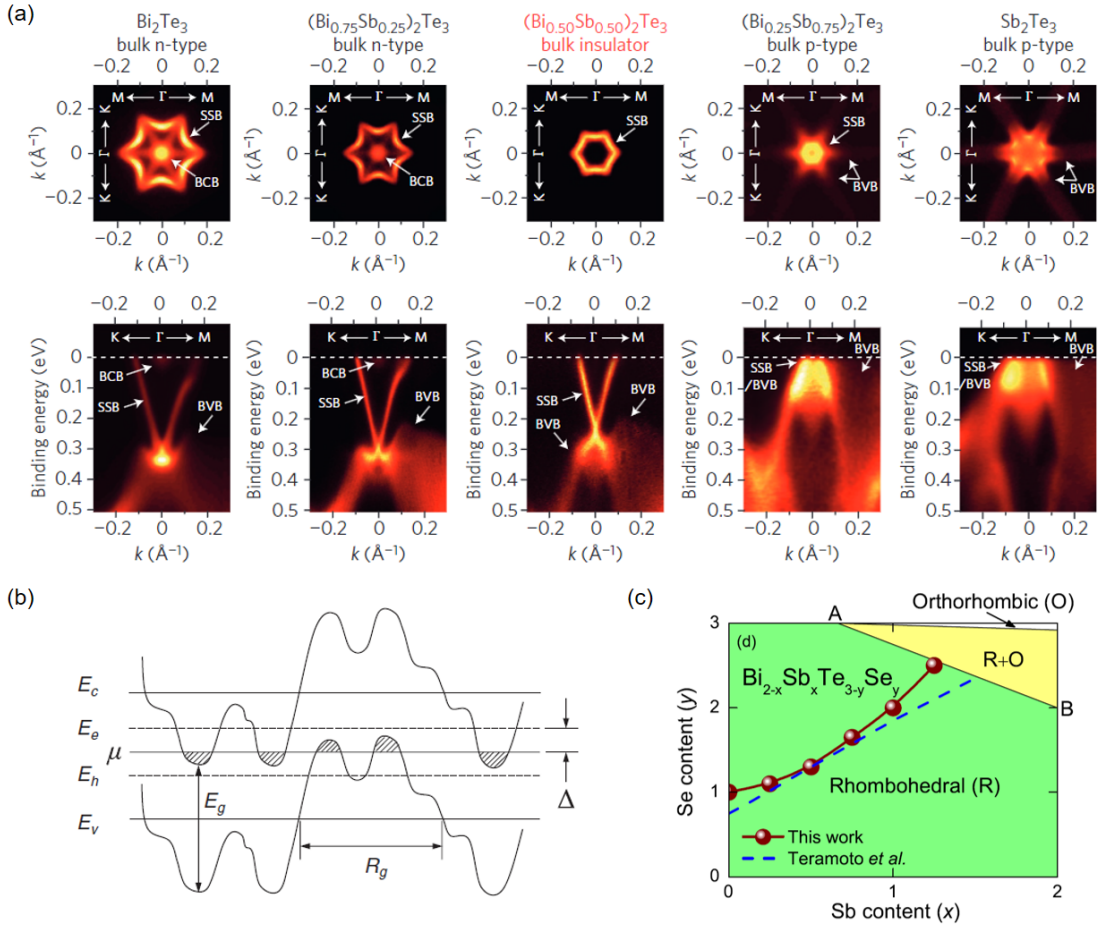

Figure 4.2: (a) ARPES Fermi surface maps (top row) and band dispersions along $K-\Gamma-M$ (bottom row) directions for bulk single crystals with nominal compositions of Bi_2Te_3, $(Bi_{0.75}Sb_{0.25})_2Te_3$, $(Bi_{0.50}Sb_{0.50})_2Te_3$, $(Bi_{0.25}Sb_{0.75})_2Te_3$ and Sb_2Te_3. Image taken from [145]. (b) Energy diagram of a completely compensated TI with band gap E_g. E_c and E_v are the unperturbed conduction and valance band, μ corresponds to the Fermi level, E_e and E_h in dashed lines are the percolation levels for electrons and holes. Puddles occupied by carriers are shaded. Image taken from [146]. (c) Composition structure diagram of the BSTS system. Image taken from [147].

quintuple layer structure in BST alloy, Sn-based Bi_2Te_3 alloy could form mutilayer structures according to the Sn content, such as septuple layers or 9-atomic layers. Besides, since Sn is a superconductor, forming Sn-based electrodes on a Sn-based TI alloy will hopefully facilitate the formation of high-quality and epitaxial interfaces, as Sb tends to diffuse heavily into the interface with the superconductor [153]. To explore this material system and its potential for further hybrid devices, systematic investigation of its growth is conducted and will be introduced in Chapter 6.

As far as the 2D TIs are concerned, a way to relate a 3D TI to a 2D TI is through the magnetic topological insulators (MTIs). By incorporating Mn into Bi_2Te_3 forms the MTI, i.e. $(MnTe)_m(Bi_2Te_3)_n$ based heterostructure, consisting of layers of alternating MnTe and Bi_2Te_3. As introduced in 2.6, MTIs are a type of 3D TI that exhibit a single spin channel along the edge. Different from the helical edge states in 2D TI, the single spin channel is locked to the magnetic moment in MTI [31]. This unique property paves the way for a new generation of low-energy quantum electronic and spintronic devices. The corresponding experimental exploration of the $MnBi_6Te_{10}$ crystal is discussed in Chapter 7.

As only certain TI materials in this field are currently available, it is important to focus on improving the their quality until more physical materials are discovered.

4.2 Growth Challenges

As introduced in Chapter 2, 3D TIs have topologically protected conductive surface states with non-degenerated spins [154]. By reducing the sample size, the contribution of the conductive surface states is enhanced due to the enhanced surface-to-bulk ratio. Therefore, nanoscale structures including ultra-thin films and nanowires/nanoribbons of the topological insulator materials are the promising candidates for the Majorana bound states (MBS) devices [155, 156].

The realization of the topological devices has encountered many challenges, as these devices should be reliable[2], reproducible, adaptable[3] across different dimensions (from micro to nanoscale) and scalable[4]. The challenges induced by the substrate and encountered during the growth will be discussed in the following sections.

4.2.1 Substrate Influenced Challenge

There are several methods to produce nano-structures for the device fabrication. This sections will introduce various approaches to obtaining nanoscale materials both with and without the substrate, along with their respective advantages and disadvantages. For device applications, the materials should be in the form of nanowires.There are different

[2]The physical and electronic properties should be preserved throughout the fabrication process.

[3]The platform should be able to provide structures with a wide range of dimensions, from micro to nanoscale.

[4]The platform should be able to provide structures of the desired dimensions and support fabrication processes, e.g. lithography.

ways to achieve nanowire. One approach is to directly produce nanowires and integrate them into the structures, while others combine thin films with lithography techniques to fabricate devices.

4.2.1.1 Nanowire

Nowadays, most of the nanowires are produced utilizing the vapour–liquid–solid (VLS) mechanism [157–159]. VLS nanowires have the best quality of TI compared with the other methods [155, 160, 161]. However, this approach lacks control over dimensions and reliability due to the difficulty in achieving surface passivation. Additionally, VLS nanowires are limited in application because they are neither adaptable nor scalable for complex architecture.

4.2.1.2 Ultra-thin film

To produce the ultra-thin films, exfoliation and molecular beam expitaxy (MBE) are common approaches.

- **Exfoliation**: For the layered topological insulator, e.g. Bi_2Te_3, single or few quintuple layer flakes can be obtained by exfoliation from the bulk crystal. This method can preserve the surface states in a controlled exfoliated environment. However, the reliability can not be guaranteed when the flakes are fabricated into nano-devices due to challenges in lithography and etching. Similar issues arise with dimensionality and scalability.
- **MBE**: As introduced in section 3.1, MBE is a powerful technique to produce high quality TI thin films, which are desirable for the device applications. Compared to exfoliation, MBE has the advantages of large area growth and the controllable stoichiometry of TIs. Furthermore, among other deposition approaches including sputtering [162], CVD [163], and physical vapor deposition (PVD) [164], MBE offers the best control of the film quality and thickness [165], enabling the high quality single crystal growth with high homogeneity. MBE is thus selected in this study to produce various thin films on the Si(111) substrate.

With the same optimized parameters, epilayers can be reproduced via MBE. Besides, the selective area epitaxy (SAE) developed using a pre-patterned substrate can produce high quality nanostructures within MBE, offering reliable, dimensionally controllable and scable nanostructures. This study mainly focuses on epitaxial growth of planar films, where the optimized thin films serve as the foundation for the future implementation of SAE.

During the MBE growth investigation, various types of defects are observed in the TI films, which is a significant challenge for their device application. During the growth, intrinsic defects in TIs are unavoidable due to the nature of the material, while the extended defects can be minimized by optimizing the growth parameters and reducing the growth rate. Detailed information of the defects is introduced in the next section.

4.2.2 General Defects

During the MBE growth, the topological epilayer starts to nucleate as a sublayer island with the height of 0.35 - 0.45 nm, as reported in references [166, 167]. The vdW interactions enable these islands to float on the passivated Si (111) surface, allowing them to grow and coalesce to form a closed layer. However, the presence of the Ehrlich–Schwoebel barrier[5] during the initial growth limits the mobility of the adatoms to cross a step edge from top to the bottom and form the closed film, which can be overcome by applying thermal energy to the adatoms. Besides, it has been observed that the atoms have higher mobility on a closed film compared to the Si(111) surface [169]. Therefore, the growth mode switches from island growth to Frank–van der Merwe (FM) growth[6] and then follows the 2D step flow after reaching a critical thickness of approx. 4 nm [166]. Hence, the ratio of the incoming adatoms flux (determined by the source temperature) and the thermal energy provided by the substrate (substrate temperature) is the critical factor that influence the film quality.

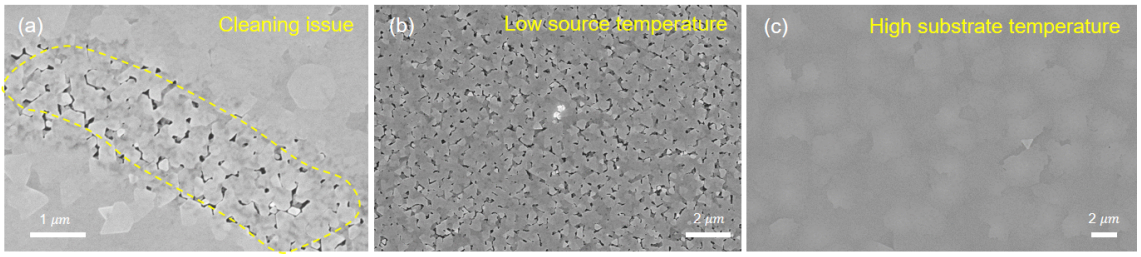

Figure 4.3: SEM images representing the Bi_2Te_3 epilayer surface imperfections in (a) due to the cleaning issue during the substrate cleaning process, (b) because of the low Bi source temperature, (c), which has an improved surface but with domains due to the slightly higher substrate temperature.

Figure 4.3 presents three SEM images illustrating three situations of epilayers with high density defects. The defect region in (a) results from substrate cleaning issues (refer to Table 3.1), while (b) and (c) indicate defect regions due to the insufficient flux to fill the gaps in the film and slightly too high thermal energy provided by the substrate, respectively. This illustrates how improper growth parameters induce various types of defects. The primary defects observed in this study are explained and analyzed in detail in the following sections.

4.2.2.1 Domains

Domains are the most common defects observed in TI films grown on the Si(111) substrate, including the rotational twin domains [170] and non-twinning domains (grains) [171].

[5] Ehrlich–Schwoebel barrier [168] refers to an potential barrier that atoms must overcome when moving from a higher terrace to a lower terrace of an island on a crystal surface.

[6] layer by layer growth

Chalcogenide 3D TIs exhibit a trigonal structure with a 3-fold rotational symmetry of 120°, whereas the Si(111) substrate has a hexagonal surface with a 6-fold rotational symmetry of 60°. When TI grows on the Si(111) substrate, initial crystalline has a 60° rotational freedom to align with the substrate, which leads to the rotational domains at the starting layer of the growth [22]. In 3D TI, domains with 60° rotational off axis are referred to as "twin domains" [172], while the domains with other rotational misalignment are known as "non-twinning domains" or grains [171].

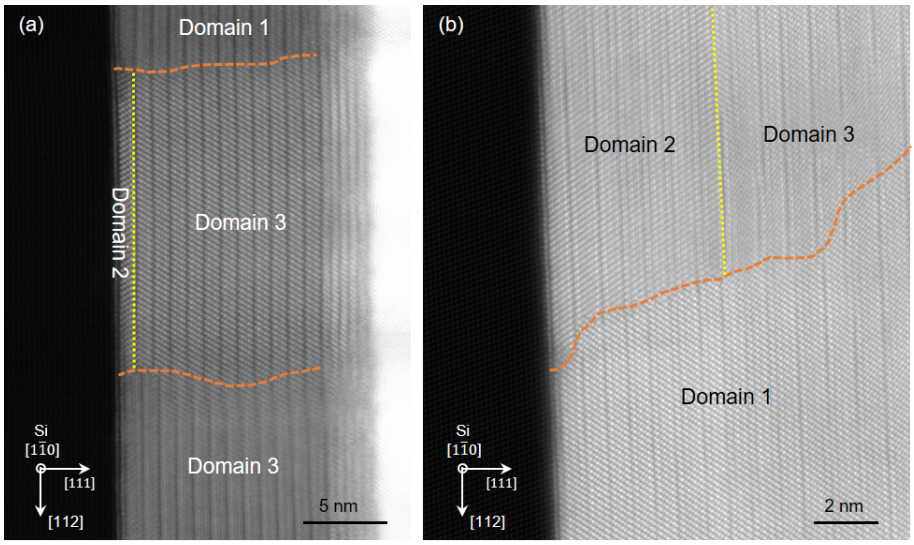

Figure 4.4: STEM-HAADF images acquired along Si[1$\bar{1}$0] projection containing grains/non-twinning domains. (a) BST epilayer grown exhibits high defect density with grain boundaries (orange line) and also translational shear faults (yellow lines, will be discussed later) as well. (b) $Sn_2Bi_2Te_5$ epilayer exhibits high defect density with similar defects.

During the growth, when two islands with the layers of different spatial arrangement in TI merge together, the atoms in the layers will rearrange themselves to form the epitaxial film. When the merged islands have different rotational alignment, domains can form depending on the growth rate. Figure 4.4 depicts the existence of grain/non-twinning domains in TI epilayers, which can easily form under high growth rate. The presence of domains in the epilayer are usually accompanied by another defect known as the translational shear fault (TSF) as shown in both (a) and (b), which will be discussed in the following section 4.2.2.2.

The 60° twin boundary is revealed by the STEM analysis in Fig. 4.5. The interface of the domain boundary is clearly visible within the marked red box, where the atomic structure is mirrored relative to the domain boundary, highlighting the symmetry across the domain interface. The twin domain is found to be collinear with either Si(311) or Si(220)[7], as reported in [173, 174]. It has been observed that the domain aligned with Si(311) is the dominant one for all the TI thin films grown by MBE [173, 174]. As shown Fig. 4.5(c), the twin domain persists for 2 QLs before being annihilated by the domain collinear with

[7]The atomic representations of Si(311), Si(220) and Si(111) are presented in Fig. A1.4

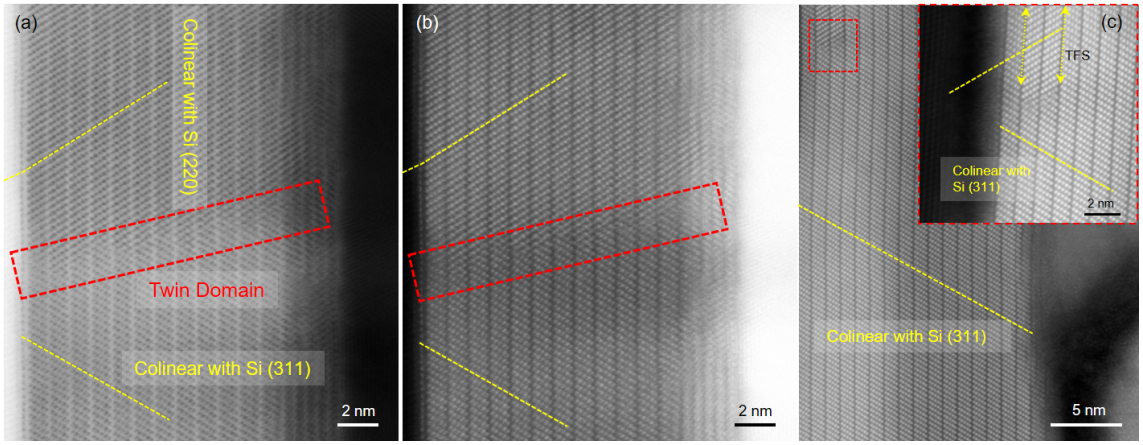

Figure 4.5: STEM images acquired along Si[1$\bar{1}$0] projection of the BST epilayer representing twin domains. (a) BF image depicting rotational twin domain through the entire layer, the orientations of the twin domains are indicated by the yellow dotted lines, (b) the corresponding contrast-inverted HAADF image with same information, (c) HAADF image showing the twin domain in a small region of the epilayer, with the magnified twin domain displayed on the upper right.

Si(311), which dominates the rest of the layer. By reducing the growth rate, the twin domain can be effectively suppressed [22].

4.2.2.2 Stacking Fault

Stacking fault is a planar defect that occurs when the periodicity arrangement of atoms is interrupted during the growth. It widely exist in vdW-based layered materials [175–177].

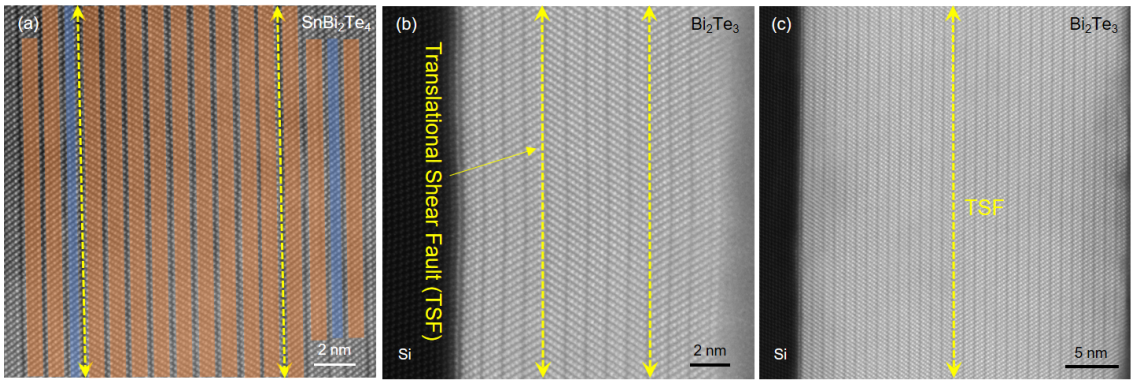

Figure 4.6: STEM-HAADF images acquired along Si[1$\bar{1}$0] projection of $SnBi_2Te_4$ epilayer in (a), where the QL is marked with blue-colored box and SL is marked with orange-colored box, depicting the stacking fault of the material; and of Bi_2Te_3 epilayers prepared with (b) high and (c) moderate growth rate, indicating the presence of translational shear faults (TSFs).

A conventional stacking fault has disordered stacking sequence within a crystallographic cell. As displayed in Fig. 4.6(a), the appearance of the quintuple layers in the $SnBi_2Te_4$

thin film, where a cell comprises of 3 septuple layers (This will be discussed in Chapter 6 in detail), indicates the presence of a stacking fault. Besides, different from the normal stacking fault, the translational shear fault (TSF) [178, 179] changes the angular order, which is a combination of the out-of-plane mirroring along with the shift operation parallel to the fault. TSF is mostly resulted from a crystallographic shear at the vdW gap [179, 180]. As shown in Fig. 4.6(b) and (c), TSFs with the stacking configurations across the vdW gap plane are observed (marked with the yellow dashed line). Both normal stacking fault and TSF can be suppressed by reducing the growth rate during the MBE growth.

4.2.2.3 Antiphase domain and screw dislocation

Antiphase domain and screw dislocation are the interlayer structural defects that can arise due to the imperfection of the substrate surface.

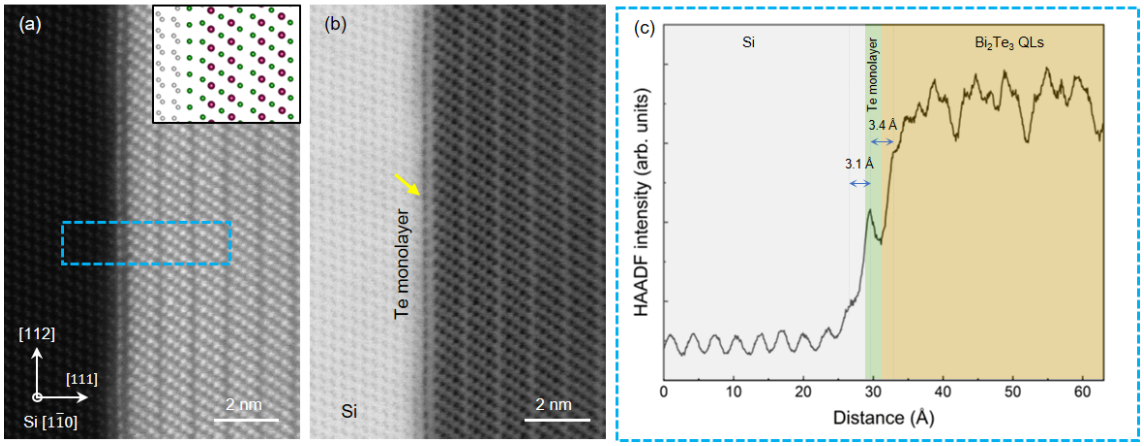

Figure 4.7: STEM images acquired along Si[1$\bar{1}$0] projection of a 3D TI epilayer grown on Si(111) substrate, indicating the defect-free interface. (a) HAADF image, (inset) the atomic model. (b) BF image. (c) An area-profile with the atomic intensity obtained from the blue box in (a), showing that the distance between the Si and Te monolayer is 0.31 nm while the distance between Te atoms across the vdW gap is 0.34 nm.

The ideal Si(111) substrate surface is atomically flat without any defects, which facilitates the vdW epitaxy growth. As shown in Fig. 4.7, an atomically flat interface between the TI epilayer and Si substrate acquired from a region where the Si(111) surface is passivated by a monolayer of Te atoms. From the area profile in (c), the distance between the Te monolayer and the first Te atom in the QL is measured to be 3.40 ± 0.02 Å, indicating the presence of the weak vdW interaction. This conclusion is supported by the fact that covalent bond length in Te-based compounds is always in the range of 2.4 - 3.1 Å [181].

However, the Si(111) wafer suffers from the miscut angle ranging from 0.1° to 5°, which can't be avoided. This miscut results in the formation of periodic step edges (appearing approx. every 45 to 450 nm) with a height of 0.39 nm. In Te-based TIs, such as Bi_2Te_3, the atomic layer sequence is Te_{out}-Bi-Te_{in}-Bi-Te_{out}. The distance between the outermost Te_{out} to innermost Te_{in} within a single quintuple layer is approx. 0.43 nm, which closely

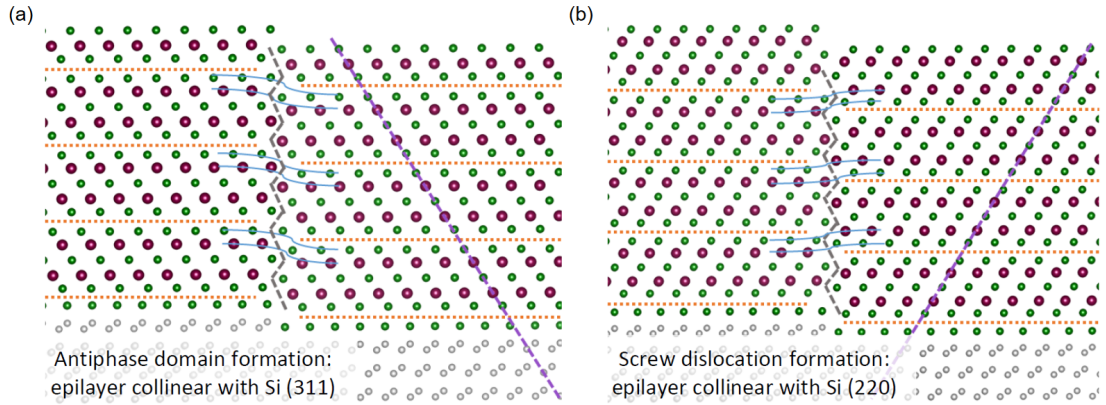

Figure 4.8: 2D atomic model of Bi_2Te_3 growth on Si(111) substrate, viewed along Si[$1\bar{1}0$] projection. Here are two possible types of structural defect formed at the Si step edge. (a) Antiphase boundary, when the epilayer is collinear with the Si(311) facet and encounters the Si step edge, it rearranges atoms without any antisite defects or atomic layer swapping, thus forming an antiphase domain. The antiphase boundary is marked with the yellow dashed lines. (b) Screw dislocation, when the epilayer is collinear with Si(220) facet and encounters the Si step edge, it forms antisite defects to swap the atomic layer of Bi and Te, thus generating the screw dislocation. Image taken from Dr. Abdur Rehman Jalil's PhD thesis [22].

matches the height of the Si step edges on the Si(111) substrate. Therefore, structural defects are generated at the Si step edges during the growth of 3D TIs.

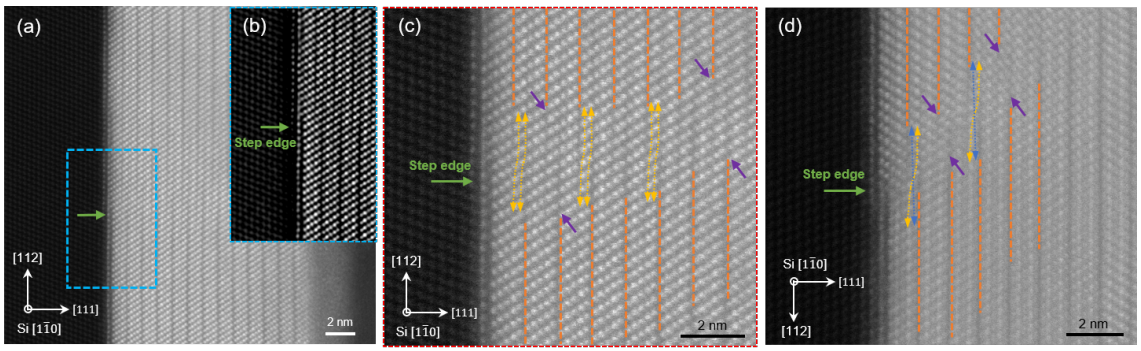

Figure 4.9: STEM images acquired along Si[$1\bar{1}0$] projection at the cross section of Bi_2Te_3 epilayer with Si step edge regions. (a) HAADF images showing the Si step edge (highlighted in the blue box) marked with the green arrow. The bandpass-filtered image is depicted in (b), which provides a clearer view of the Si step edge, enhancing the visibility of the structure. (c) Magnified HAADF image obtained from (a), where the epilayer is collinear with Si(311) and the layer rearranges themselves without antisite defect, thus forming the antiphase boundary. (d) HAADF image indicating the presence of screw dislocation due to the Si step.

Three possibilities can occur at the step edges, two of which are illustrated in the atomic models in Fig. 4.8. The presence of Si steps shifts the films at the top terrace relative to the bottom terrace, leading to a mismatch of the layer sequences on the top and bottom terrace. As depicted in Fig. 4.8(a), when the dominant domain is collinear with Si(311),

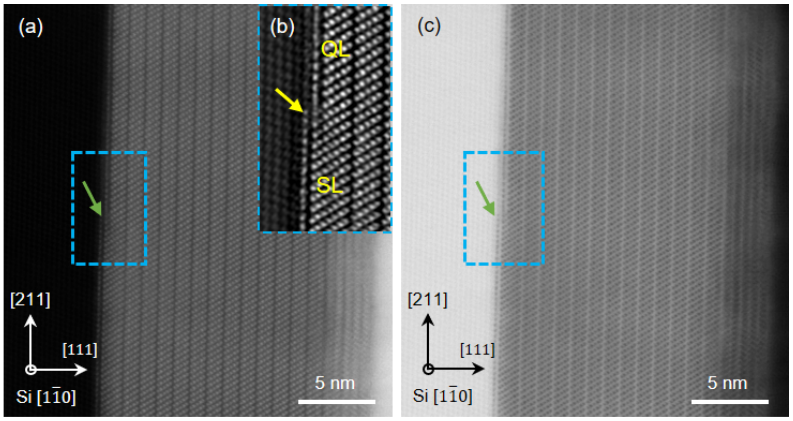

Figure 4.10: STEM images acquired along Si[1$\bar{1}$0] projection of BST epilayer, indicating the appearance of Si step edge. (a) HAADF image depicting the Si step edge (green arrow) in the blue box. The magnified bandpass-filtered image from the blue box is shown in (b), which gives better visibility of atoms. There is neither an antiphase domain nor screw dislocation formation, rather than a SL instead of a QL. The growth of a SL compensates the lower Si step, thus enabling the further growth of the QL of BST. (b) BF image of (a) represents the same information with the inverted contrast.

the five layers within a quintuple layer across the domain boundary (indicated by the gray dashed line) follow the blue lines in (a). In this configuration, the Bi layer merge with Bi layer and the Te layer merge with Te layer, resulting in the formation of an antiphase domain. When the dominant domain is collinear with Si(220), the five layers within a quintuple layer across the domain boundary (indicated by the gray dashed line) follow the blue lines in 4.8(b). In this case, the Bi layer merges with the Te layer and vice versa, leading to the formation of a screw dislocation.

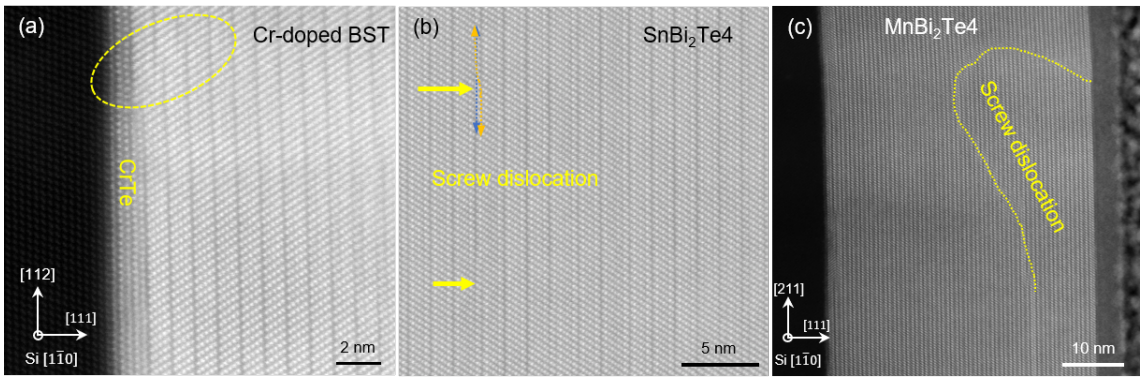

Figure 4.11: STEM-HAADF images acquired along Si[1$\bar{1}$0] projection of 3D TI epilayers, indicating the appearance of screw dislocation (a) due to the formation of the CrTe alloy in the starting phase of the Cr-doped BST growth, or due to the high grow rate/non-proper growth parameters that leads to the screw dislocations in small scale (b), in large scale in (c), marked with the yellow dashed line, respectively. The samples shown in (a) and (c) were grown by Max Vaßen-Carl and Dr. Abdur Rehman Jalil in PGI-9, respectively.

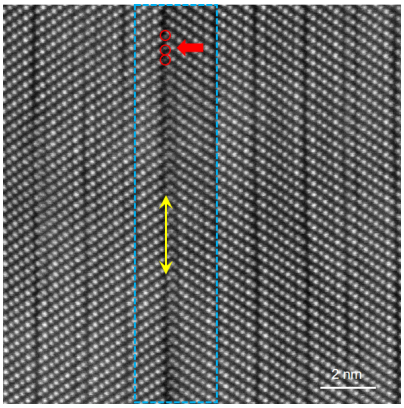

Figure 4.12: Intercalation of the adatoms. HAADF image acquired in the defect region in $Sn_2Bi_2Te_5$ epilayer depicting intercalated adatoms (red circles) at the TSF (yellow arrow) in the highlighted region (blue box).

During the STEM investigation, the Si step edges are observed in the TI epiplayers, as shown in Fig. 4.9(a) and (b). Additionally, the antiphase domain and the screw dislocation caused by step edges are presented in Fig. 4.9(c) and (d), respectively.

Another possibility is displayed in Fig. 4.10, where a septuple layer grows at the lower terrace of the Si step instead of the quintuple for the BST thin film, thus compensating the height difference at the Si step edge. The septuple layer is demonstrated to be the $(Bi_xSb_{1-x})_4Te_3$ in Dr. Abdur Rehman Jalil's thesis in [22].

Apart from the Si step edge, the screw dislocation can also form in the films under other circumstances. Examples are shown in Fig. 4.11, where the improper growth parameters result in screw dislocations in partial regions (b) or large scale (c).

In general, structural defects including the domains and stacking faults can be reduced by lowering the growth rate. However, the antiphase and screw dislocation formed at the Si step edges are challenging to eliminate. By utilizing the Si wafers with a smaller miscut angle, the density of the step edge defects can be decreased.

4.2.2.4 Point Defects

The point defects consist of vacancies, antisites defects, and interstitial defects [24]. Due to the low dimension of these defects, identifying all of them in TI films is a significant challenge.

- **Vacancy**: Vacancy defects refer to the absence of the atoms from the lattice sites they normally occupy, which leads to the unsaturated bonds and potentially higher carrier concentration [182, 183]. For example, in Bi_2Te_3, Te vacancies (V_{Te}) act as charged donors [184, 185], which shift the Fermi level into the conduction band at high concentration, resulting in the n-type feature of Bi_2Te_3 [185, 186].

- **Antisite defect**: When two different elemental atoms exchange their lattice sites with each other, antisites defects are formed in the film [182, 187, 188]. Different from Bi_2Te_3, Sb_2Te_3 suffers from the Sb_{Te} antisite defects due to the similar atomic radii of Sb (1.38 Å) and Te (1.33 Å) [189] as well as the lower antisite formation energy compared to Bi_{Te} [190, 191]. When Sb occupies the position of Te, it satu-

rates the bonds with neighboring Te atoms with an electron deficiency that acts as a hole. Therefore, the Sb_{Te} antisite defects serve as p-type dopant.

- **Interstitial defect**: The interstitial defect is a point defect that arises when the adatoms are embedded in the deformed crystals instead of the conventional lattice positions, which will increase the carrier concentration [24, 192]. These interstitial atoms are usually accommodated within the structural defects including rotational domain, stacking fault, TFS, antiphase domain and screw dislocation. An example is displayed in Fig. 4.12, where the atoms are intercalated between a TSF. This type of defect can be avoided by the defect-free growth with modified growth parameters.

In general, vacancies and antisites defects are intrinsic defects in TI films, which cannot be entirely eliminated, while the density of interstitial defects can be reduced by optimizing the growth conditions.

5 Phase-Selective Epitaxy of Trigional and Orthorhombic Bismuth Thin Films

Commentary: *This chapter addresses the growth and structural characterization of the trigonal and orthorhombic phases of bismuth. Previous studies have indicated that the pure phases of trigonal and orthorhombic bismuth have not yet been successfully synthesized. To differentiate between these two phases and to investigate their structural relationship, the growth-related tasks were divided between the author and Dr. Abdur Rehman Jalil.*

In this work, the MBE growth of trigonal and polycrystalline bismuth thin films was performed by the author, while the epitaxial layers exhibiting the orthorhombic phase were grown by Dr. Abdur Rehman Jalil. Structural characterization was primarily carried out by the author, including almost all TEM investigations (with the exception of a single image, located at the top right of Fig. 5.19(c), which was provided by JinHee Bae), as well as SEM, XRR, and XRD measurements. RSM and Phi scan data were contributed by Dr. Abdur Rehman Jalil. Data analysis was shared equally between the author and Dr. Jalil, with the author conducting approximately 50% of the analysis under his guidance, and the remaining work being completed collaboratively.

This chapter includes research conducted in collaboration with PGI-9, which has been published in ***Nanomaterials*** *[17], 2023. The author would like to express sincere gratitude to PGI-9 for the opportunity to perform growth, SEM, and XRD experiments under the supervision of Dr. Abdur Rehman Jalil, and to the Ernst Ruska Centre (ERC) for providing access to their facilities for the TEM investigations.*

Allotropes are different structural forms of the same chemical elements in the same physical state, arising from variations in how the atoms are bonded [25]. Although composed of the same type of atoms, allotropes often exhibit distinct physical and chemical properties. Allotropes exist in various materials, such as carbon [193], sulfur [194], or phosphorus [195]. In case of bismuth, it naturally only exists in the trigonal (001) phase. However, in the past few decades, various studies on bismuth have revealed the presence of allotropes in other phases, including the trigonal (012) phase, orthorhombic phase and black phosphorus phase [196]. In this chapter, the trigonal phase is denoted as the Bi_{TRIG}, while the orthorhombic phase is referred to as Bi_{ORTH}.

As introduced in Chapter 4, thin Bi films (<1 nm) of Bi_{TRIG}(001) and Bi_{ORTH} (within 4 monolayers) phases exhibit a quantum spin hall (QSH) phase, rendering them 2D topological insulators [137, 197, 198]. In addition, the theoretical model from Lu et al.

[138] indicates that Bi_{ORTH} can be topological under certain circumstances. Besides, in 2018, higher-order topological states have been observed in bulk bismuth in Bi_{TRIG} phase, where the topological states emerge along the lower dimensional edges, referred to as hinge states [44]. This chapter will focus on the realization of the 2D TIs with the growth exploration of various bismuth allotropes.

Since last two decades, the growth of Bi_{TRIG} and Bi_{ORTH} thin films has been conducted on various substrates, such as HOPG [138, 199], sapphire [200], InP (111) [198], glass [201], mica [202], and extensively on Si (111). While growing on Si (111) substrates, all reported growths were performed on either $\sqrt{3} \times \sqrt{3}$ - β [203, 204] or 7 $\times$ 7 [196, 205, 206] reconstructed surfaces.

Until now, researches are still unable to grow the $Bi_{TRIG}(001)$ and Bi_{ORTH} phases separately during the investigation, and they have been struggling to produce high-quality, coalesced thin films. Besides, achieving a thickness of the thin films below 1 nm remains a significant challenge, which makes it impossible to provide the desired crystals for exploiting Bi-based 2D TIs in technological applications for quantum spintronics and topological quantum computation. Therefore, realizing ultra- thin, high-quality and phase-pure growth of Bi_{TRIG} and Bi_{ORTH} phases is of crucial importance. The main question addressed in this chapter is how to grow the thin films phase-selectively.

In this work, a comprehensive and systematic study together with the thickness-dependent growth of the pure phase $Bi_{TRIG}(001)$ thin films has been performed, where the high-quality $Bi_{1-x}Sb_x$(BiSb) is also achieved by doping Sb 4% - 7% into the the Bi_{TRIG}, as discussed in section 5.1. Furthermore, pure phase Bi_{ORTH} allotrope has been realized as discussed in section 5.2. During investigations of Bi thin films, not only the $Bi_{TRIG}(001)$ and Bi_{ORTH} phases, but also the $Bi_{TRIG}(102)$ phase has been observed.

An overview of crystal structure, depicting the top and cross-sectional side-views of all attained allotropes of bismuth in this work, is presented in Fig. 5.1. (BiSb has the same crystal structures as all the Bi allotropes in Fig. 5.1.)

As shown in Fig. 5.1(d) and (g), the top surface looks similar for $Bi_{TRIG}(012)$ and Bi_{ORTH}. Most of the reported characterizations are based on top-surface investigations, including STM/STS [138, 196, 200, 204, 207], AFM [199] and LEED [205, 208], making it challenging to differentiate between these two allotropes. By conducting in-depth structural investigations on both single- and polycrystalline epilayers, our study offers a comprehensive understanding of domain alignment in different phases, effectively resolving ambiguities in distinguishing between $Bi_{TRIG}(102)$ and Bi_{ORTH} phases.

Besides, structural characterization using XRD techniques and STEM analysis provides a comprehensive understanding of phase segregation, phase stability and phase transformation in various Bi thin film allotropes. Interestingly, with well controlled thickness, the orthorhombic phase can be tuned into the topological regime, which can be potentially employed for the application in the quantum computing and spintronics.

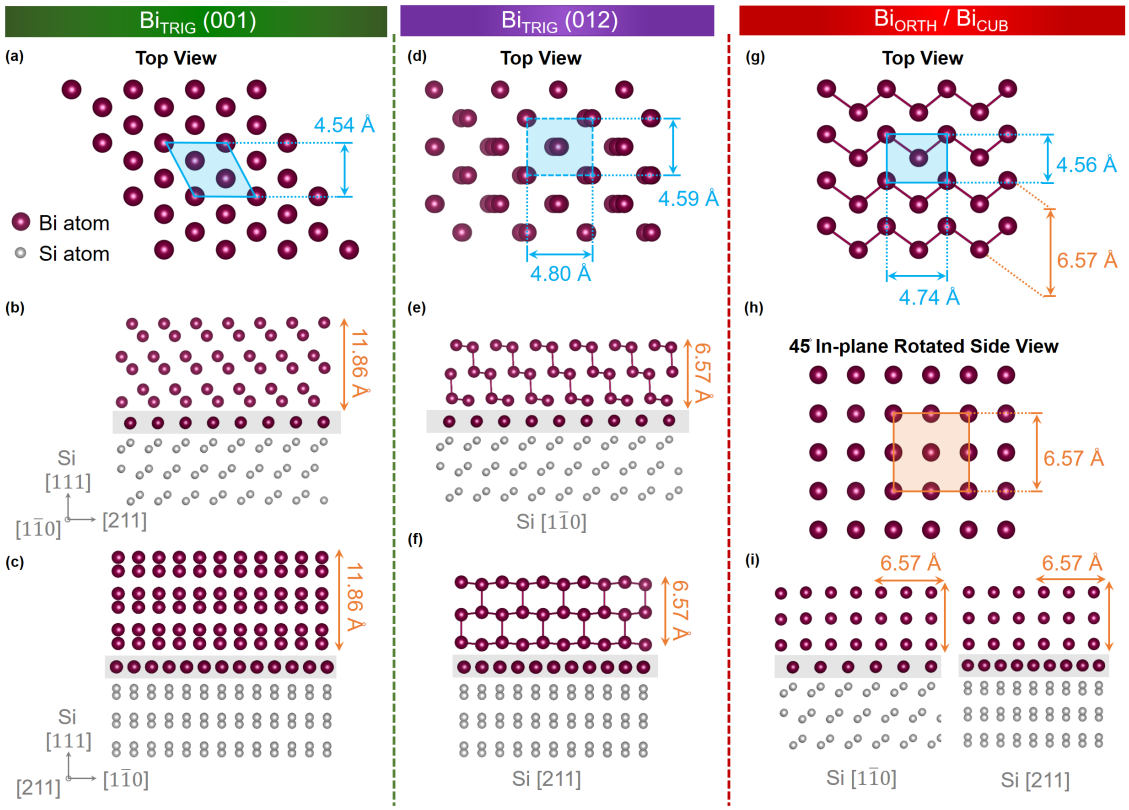

Figure 5.1: Crystal structure illustrations of bismuth nanofilm allotropes. (a) Top surface view of $Bi_{TRIG}(001)$ where the blue region highlights the 2D in-plane lattices. Cross-sectional side view of one unit cell thick epilayer of $Bi_{TRIG}(001)$ along (b) Si[1$\bar{1}$0] and (c) Si[211] projections. (d) Top surface view of Bi_{TRIG} (012) orientation with two monolayer thick film, and cross-sectional side view of one unit cell thick epilayer of $Bi_{TRIG}(012)$ along (e) Si[1$\bar{1}$0] and (f) Si[211] projections. (g) Top surface view of Bi_{ORTH} phase, (h) side view at 45°-rotated plane, (i) cross-sectional side view of one unit-cell thick epilayer of $Bi_{ORTH}(010)$ along Si[1$\bar{1}$0] and Si[211] projections. Image taken from [17].

5.1 Growth of Bi/BiSb Thin Films on Si (111) Substrate

To achieve smooth, high-quality Bi films using MBE, it is essential to determine the optimal growth parameters, i.e. the growth temperature (T_{sub}) and the thin-film growth rate (R_{TF}). This section will focus on the growth realization and optimization of the Bi_{TRIG} phase and BiSb thin films.

5.1.1 Growth Optimization of Bi_{TRIG} Phase

To achieve the Bi_{TRIG} (001) phase, Bi films are initially grown across a T_{sub} range from -20 °C to 80 °C (in steps of 5 °C) while keeping the R_{TF} = 10 nm/h. The R_{TF} is maintained by adjusting the temperature of the Bi effusion cell. After obtaining the series of grown thin films, SEM is used to analyze the morphology of the films, while XRD techniques characterize the crystal properties.

XRR scans reveal the thickness and roughness of each film, showing that lower growth temperatures result in smoother surfaces, whereas the roughness increases significantly with the increasing T_{sub}, as depicted in Figure 5.2(a).

Besides, XRD provides the qualitative investigations of Bi_{TRIG} (001) crystals with the rocking curve (RC) analysis of the Bi_{TRIG} (0003) peak. As shown in Fig. 5.2(a), the investigated temperature zones are highlighted in grey, orange, white, green and red color, respectively. The crystal evolution is introduced as follows:

- **Amorphous zone:** In this zone, Bi films are prepared between -20 °C and 0 °C which are either amorphous or partially crystalline.
- **High defect density zone:** In this zone, the films prepared between 0 °C and 15 °C start to crystallize in Bi_{TRIG}(001) phase; however, these films exhibit a poor crystal quality with RC-FWHM values above 900 arcseconds.
- **Transition zone:** In this zone, a continuous improvement in crystal quality is observed between 15 °C and 35 °C with RC values approaching 300 arcseconds.
- **Optimum zone:** In this zone, the films prepared between 35 °C and 50 °C are observed to have the best crystal quality, where RC values are below 200 arcseconds.
- **Deformation zone:** When T_{sub} > 50 °C, epilayers starts to degrade in crystal quality again, as the RC values increase, and the crystal transforms into polycrystalline. The transformation occurs due to the increased density of point and structural defects, since epilayers become increasingly thermally unstable at higher T_{sub}.

According to the obtained "optimum zone" in Fig 5.2 (a) during the growth exploration, thin films grown at T_{sub} = 40 °C have the best crystal quality. T_{sub} = 40 °C is therefore selected as the optimum T_{sub} for all future growths of the Bi_{TRIG}(001) phase. To find out the optimum R_{TF}, a similar series of growths are performed under R_{TF} = 15 nm/h, which is illustrated in Fig 5.2 (b).

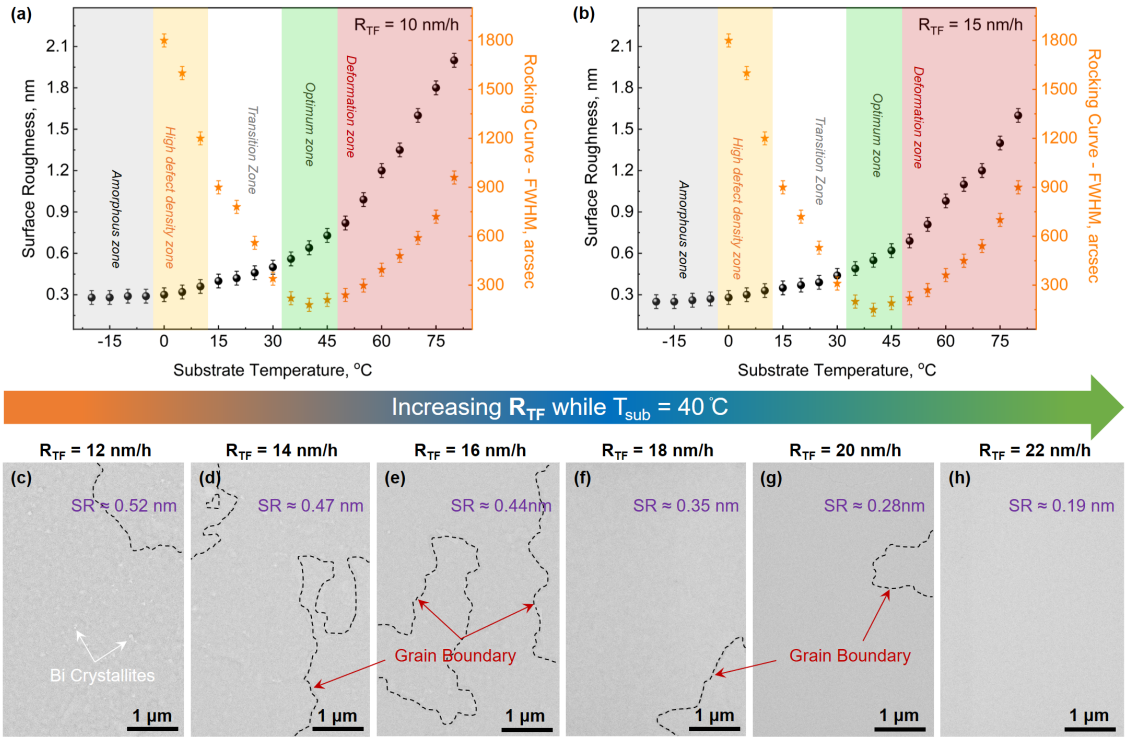

Figure 5.2: Identification of optimum growth parameters of the Bi_{TRIG}(001) phase. Temperature-dependent changes in surface and crystal quality of Bi_{TRIG}(001) epilayers from -20 °C to 80 °C prepared with (a) R_{TF} = 10 nm/h, (b) R_{TF} = 15 nm/h. SEM images of Bi_{TRIG} (001) epilayer prepared at T_{sub} = 40 °C with R_{TF} increasing from (c) 12 nm/h via (d) 14 nm/h, (e) 16 nm/h, (f) 18 nm/h, (g) 20 nm/h to (h) 22 nm/h. Image taken from [17]. Images were processed in collaboration with Dr. Abdur Rehman Jalil.

Compared to R_{TF} = 10 nm/h, both features, i.e., the surface and crystal quality improve at R_{TF} = 15 nm/h, as displayed in Fig. 5.2(b), indicating a higher probability to obtain optimum growths at R_{TF} > 15 nm/h. To determine the optimum R_{TF}, several Bi_{TRIG}(001) epilayers are prepared by gradually increasing R_{TF} in steps of 2 nm/h from 10 nm/h to 30 nm/h, while maintaining T_{sub} at 40 °C.

Figure 5.2(c)-(h) depict the corresponding changes in surface morphology with SEM images of the R_{TF} series (from 12 nm/h - 22 nm/h), where a substantial improvement in the surface quality of the epilayers is observed with increasing R_{TF}. With the increase of the R_{TF}, not only do the Bi crystallites at lower R_{TF} disappear, but also the average grain size increases significantly (marked by the black dashed lines in the SEM series images). With all the R_{TF} investigated, the best films are obtained at R_{TF} = 22 nm/h, which is therefore chosen as the optimum R_{TF}.

With aforementioned optimum R_{TF} and T_{sub}, several epilayers of different thicknesses are prepared to ensure the growth reproducibility. Detailed structural characterizations via XRD are performed to evaluate the lattice parameters of Bi_{TRIG} epilayers.

- **XRR:** Figure 5.3(a) shows the measured and simulated XRR curves of a 15.5 nm

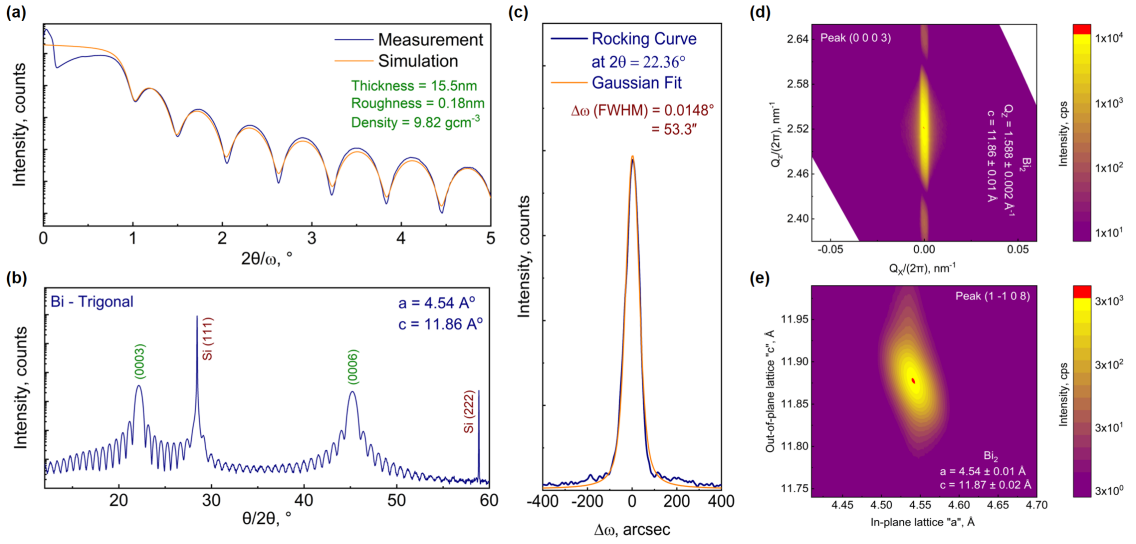

Figure 5.3: XRD characterization of Bi_{TRIG}(001) epilayer prepared at the optimal growth parameters. (a) Measured and simulated XRR curves providing information about the thickness and roughness of the epilayer, (b) XRD $\theta/2\theta$ scan confirms the single crystallinity, (c) Rocking curve acquired at Bi_{TRIG}(0003) peak, (d) symmetric RSM across Bi_{TRIG} peak to evaluate the out-of-plane lattice parameter and to identify the presence of any tilted grains and (e) asymmetric RSM across $Bi_{TRIG}(1\bar{1}08)$ peak to evaluate the in-plane lattice parameters. Image taken from [17]. Images were processed in collaboration with Dr. Abdur Rehman Jalil.

thick thin film. The fitting parameters indicate the ultra-smooth surface, with measured roughness even better than that of the Si(111) substrate itself (usually 0.3 nm), which is unusual in MBE growth. Typically, when growing layered materials such as Bi_2Te_3 and Sb_2Te_3 on a Si substrate, the unavoidable step heights of Si(111) lead to the formation of extended structural defects, such as antiphase domains and screw dislocations, as discussed in Chapter 4. In case of Bi_{TRIG}, the material is arranged in vertically stacked bilayers and the height of a single bilayer (3.9 Å) (three bilayers with 11.86 Å in Fig. 5.1) matches almost perfectly with the Si step-edge height (3.87 Å) [22, 209]. Therefore, the bilayer can insert itself at the step edge on the substrate, neutralizing the formation of extended defects, thus resulting in an improved crystal and surface quality of the epilayer.

- **XRD:** Figure 5.3(b) represents the XRD $\theta/2\theta$ scan, confirming the single crystalline behavior of the Bi_{TRIG}(001) epilayer. The presence of thickness oscillations up to 60° in the diffraction pattern is attributed to the ultra-smooth surface.

- **RC:** Figure 5.3(c) depicts the measured RC and the corresponding Gaussian fit, yielding the FWHM value of 53 ± 10 arcseconds, which is the best value ever reported in the MBE-grown Bi-based material systems.

- **RSM and aRSM:** Figure 5.3(d) presents a symmetric map across the Bi_{TRIG}(0003) peak. The measured value provided $Q_Z = 2\pi$ (2.529) ± 0.002 nm^{-1} = 1.588 ± 0.002

$Å^{-1}$, where the corresponding out-of-plane lattice "c" = 11.86 ± 0.01 Å, calculated from the equation (3.3). The asymmetric RSM in Fig. 5.3(e) utilized ($1\bar{1}08$) peak to probe the in-plane structure, where the in-plane lattice a = b = 4.54 ± 0.01 Å, calculated from equation (3.2) in section 3.3.1.1.

5.1.2 Thickness-dependent Growth of Bi_{TRIG} thin film

According to the literature [210–212], the topological properties of the BiSb thin film is highly affected by the film thickness. Initially, to investigate the influence of the thickness, a thickness-dependent epitaxy of pure $Bi_{TRIG}(001)$ phase was performed to ensure the feasibility of controlling the thickness of BiSb thin films.

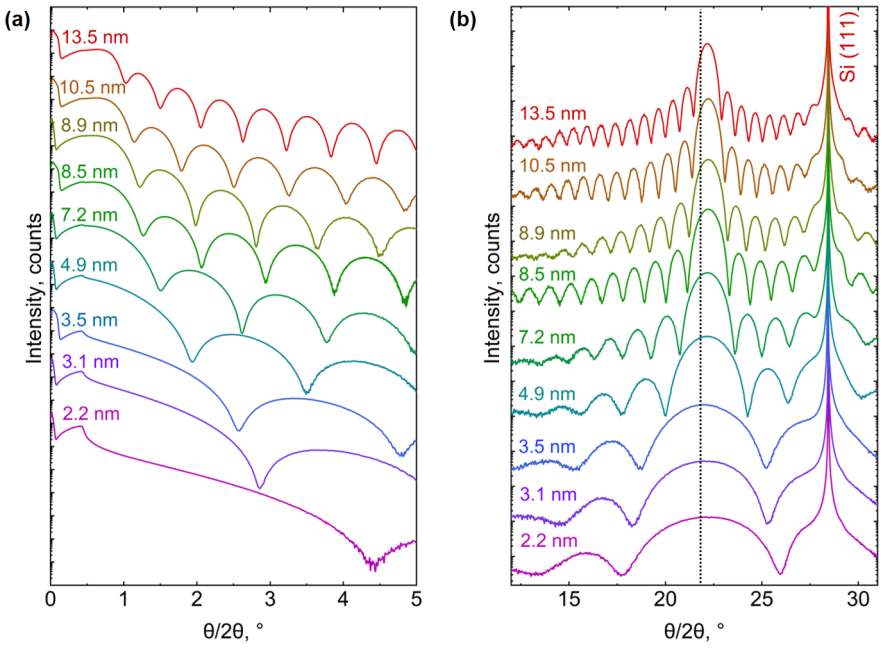

Figure 5.4: Thickness series of the $Bi_{TRIG}(001)$ phase. (a) XRR-measured curves of epilayers ranging in thickness from 2.2 nm to 13.5 nm, whereas (b) depicts the corresponding diffraction patterns.The dotted black line in (b) indicates a slight shift in the out-of-plane lattice parameter due to thin-film effect. Image taken from [17]. Images were processed in collaboration with Dr. Abdur Rehman Jalil.

$Bi_{TRIG}(001)$ epilayers ranging in thicknesses from 2.2 nm to 13.5 nm are prepared under the optimum values of the growth parameters (T_{sub}, R_{TF}) = (40 °C, 22 nm/h). Figure 5.4 represents the XRD characterization of the $Bi_{TRIG}(001)$ thickness series, where (a) depicts XRR curves, and (b) depicts the corresponding diffraction patterns. Figure 5.4(b) indicates that all epilayers exhibit pure phase $Bi_{TRIG}(001)$, with the absence of the peaks for other phases. The black-dotted line highlights a shift in the out-of-plane lattice constant due to the scaling effect, which has already been reported for GeTe, where a decrease in film thickness of GeTe can lead to an expansion of the out-of-plane lattice parameter [213].

5.1.3 Growth Realization of BiSb Thin Films

In previous investigations, we have achieved reproducible and high quality growth of pure $Bi_{TRIG}(001)$ thin films, where the thickness has been controlled by the growth rate and duration. As mentioned in section 4.1, when adding a certain amount of Sb to the films, their topological properties are influenced by the thickness of the thin film. In this section, Sb is successfully incorporated into the film and the thickness-controlled growth is demonstrated in Fig. 5.5.

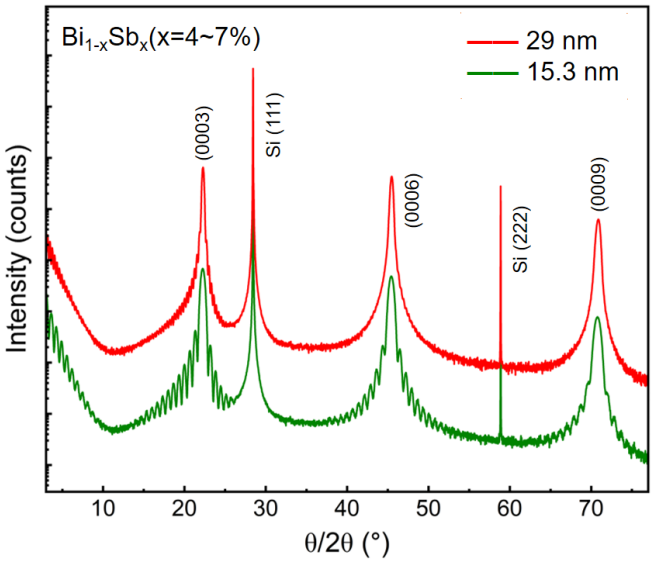

Figure 5.5: XRD $\theta/2\theta$ scan of BiSb samples with different thicknesses. Here, Sb was alloyed into Bi with the content between 4% to 7%. The growth rate of Bi is 22 nm/h, while that of Sb is 1 nm/h. The growth duration for the epilayer at the top (red) and bottom (green) is 75 minutes and 40 minutes, resulting in sample thicknesses of 15.3 nm and 29 nm, respectively. Data provided by Dr. Abdur Rehman Jalil, plotted and analyzed by the author.

During the BiSb growth, the growth rate of Bi is kept at the optimum growth value for Bi_{TRIG} (22 nm/h), while Sb flux rate is adjusted to 1 nm/h. Therefore, the overall growth rate is 23 nm/h. With the corresponding flux settings, Sb content in the grown thin films can be controlled between 4% and 7%. The XRD investigation of the two epilayers grown with the same flux but different duration is presented in Fig. 5.5.

In general, it is feasible to incorporate a small proportion of Sb into Bi thin films while preserving the crystal quality of the epilayer. The thickness of BiSb can be precisely controlled, as demonstrated by these preliminary results. In the future, BiSb epilayers with thicknesses below 4 nm will be grown and fabricated into devices to investigate the 1D topological edge state.

5.2 Growth Transformation towards Bi_{ORTH} Phase

As discussed in the last section, we have obtained ultra-smooth, high-quality pure single crystalline $Bi_{TRIG}(001)$ and BiSb thin films with well controlled thickness. However, an additional phase (Bi_{ORTH}) phase is also observed during the pure Bi growth process. What is the relationship is between $Bi_{TRIG}(001)$ and Bi_{ORTH} phase, remains to be discovered. This section will unveil the mystery of the Bi_{ORTH} and how the phases relate to each other in growth.

5.2.1 Growth Optimization of Bi_{ORTH} Phase

As stated in Fig. 5.2, the crystal goes into polycrystalline state when $T_{sub} > 50$ °C. Preliminary XRD investigations indicated that the polycrystalline consists of either $Bi_{TRIG}(012)$ or Bi_{ORTH} phase (as both phases exhibit identical out-of-plane lattices), together with the $Bi_{TRIG}(001)$ phase. As indicated in Fig. 5.2, the crystal quality of the $Bi_{TRIG}(012)$ phase initially improves to the best value and then decreases with the increase of T_{sub}. To explore the Bi_{ORTH} phase, a systematic growth with stepwise increased T_{sub} is carried out.

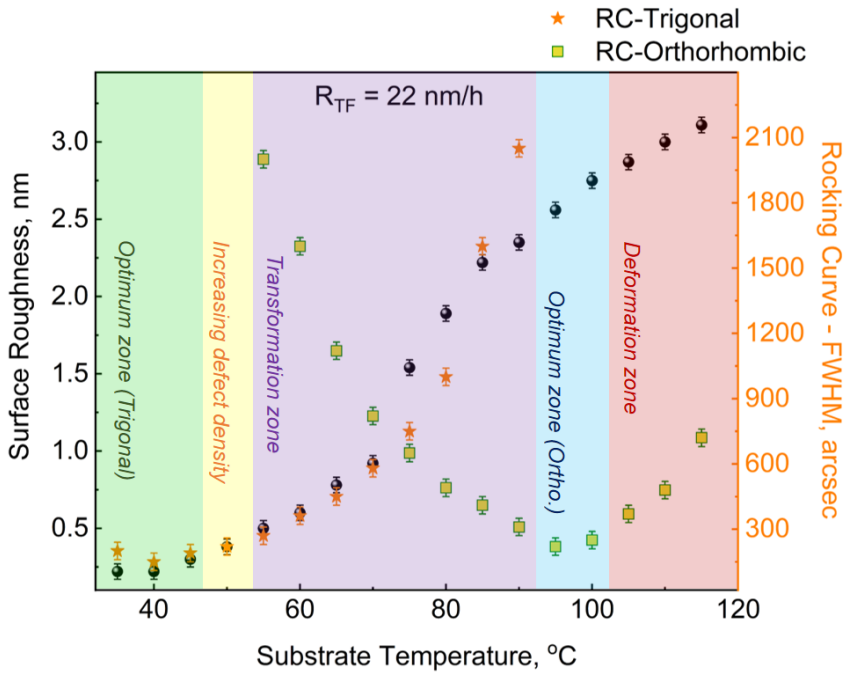

Figure 5.6: Structural transformation map from $Bi_{TRIG}(001)$ to $Bi_{ORTH}(010)$ phase in Bi epilayers. Temperature-dependent changes in surface roughness (indicated by black data points) and crystal quality of Bi epilayers prepared at 40 °C $\leq T_{sub} \leq$ 120 °C, R_{TF} = 22 nm/h, result in continually changing structures from $Bi_{TRIG}(001)$ to $Bi_{ORTH}(010)$ phase via polycrystalline states. Image taken from [17]. Images were processed in collaboration with Dr. Abdur Rehman Jalil.

Keeping R_{TF} = 22 nm/h (optimum value adopted for the $Bi_{TRIG}(001)$ phase), a series of growths are conducted, with the T_{sub} has been gradually (in steps of 5 °C) increased from

40 °C to 120 °C. The structural investigations and the summary of the acquired results are illustrated in Fig. 5.6.

Based on Fig 5.2(a), Fig. 5.6 extends the T_{sub} range up to 120 °C. Similar to Fig 5.2(a), the investigated temperature zones are highlighted in green, yellow, purple, blue and red color, respectively.

- **Optimum (trigonal) and increasing defect density zone (35 °C $\leq T_{sub} \leq$ 55 °C):** These two zones are the corresponding zones where $Bi_{TRIG}(001)$ phase has the best crystal quality and the crystal quality starts to degrade as discussed in section 5.1.1.
- **Transition zone (55 °C $\leq T_{sub} \leq$ 95 °C):** In this zone, Bi_{ORTH} starts to emerge in the epilayer, forming the polycrystalline layers (containing both $Bi_{TRIG}(001)$ and Bi_{ORTH} phases). With the increase of T_{sub}, the ratio of Bi_{ORTH} phase rises while the fraction of $Bi_{TRIG}(001)$ phase drops down. Meanwhile, the crystal quality of Bi_{ORTH} also gets improved with increased T_{sub}.
- **Optimum zone (Orth.) (95 °C $\leq T_{sub} \leq$ 105 °C):** In this region, the pure phase of the Bi_{ORTH} crystallize. Although the surface quality of acquired Bi_{ORTH} epilayer is not ideal, the crystal quality is acceptable, with the FWHM value of the $Bi_{ORTH}(020)$ peak reaching below 300 arcseconds.
- **Deformation zones (T_{sub} > 105 °C):**In this zone, the crystal starts to degrade again.

The diffraction patterns of the epilayer grown at several key T_{sub} points (40 °C - 100 °C) is presented in Fig. 5.7(a), while the corresponding surface morphology is visualized via SEM images in Fig. 5.7(b)-(g).

As shown in Fig. 5.6(a), an abrupt change in crystal structural is observed within "transformation zone" between 70 °C and 80 °C. Between 70 °C and 80 °C the intensity of the Bi_{TRIG} (0003) peak decreases and Bi_{ORTH} (020) peak increases. This phenomenon is supported by SEM images in Fig. 5.7(b)-(g), where a relatively smooth and almost fully coalesced layer at 70 °C is suddenly converted into rough and randomly ordered crystals at 80 °C.

In addition, although single crystalline Bi_{ORTH} is achieved at the T_{sub} = 100°C as indicated in Fig. 5.6, the corresponding surface morphology shown in Fig. 5.7(g) is still rough. To optimize the surface roughness, the R_{TF} is increased from 22 nm/h to 32 nm/h (similar to the optimization exploration of the $Bi_{TRIG}(001)$ phase). The corresponding morphological changes can be visualized in the SEM images in Fig. 5.8(a)-(f). As the R_{TF} increases, defects on the surface are significantly reduced, and fully coalesced films are successfully achieved as displayed in Fig. 5.8(f).

XRD-based structural characterizations are performed on the best acquired film at R_{TF} = 32 nm/h.

- **XRD:** The diffraction pattern is plotted in Fig. 5.8(g), which indicates the single crystallinity of the Bi_{ORTH} phase.

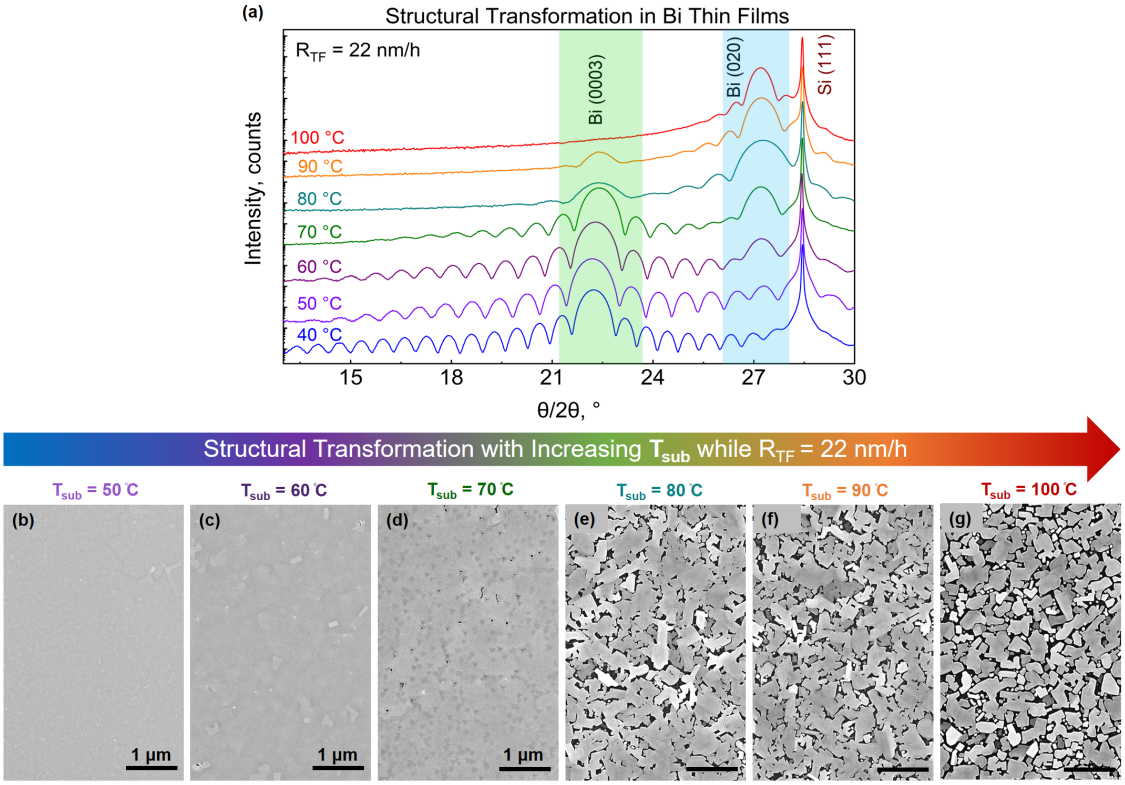

Figure 5.7: Structural transformation in Bi epilayers. (a) Corresponding diffraction pattern at selected T_{sub} indicates the continually reducing and enhancing contributions of Bi_{TRIG}(001) and Bi_{ORTH}(010) phases, respectively. Bi_{TRIG} (0003) and Bi_{ORTH} (020) peak regions are highlighted with green and blue, respectively. (b)-(g) indicate the corresponding morphological variations via SEM images with epilayers prepared at T_{sub} from 50 °C to 100 °C. Image taken from [17]. Images were processed in collaboration with Dr. Abdur Rehman Jalil.

- **RC:** The RC measurement at the Bi_{ORTH} (020) peak is depicted as an inset in Fig. 5.8(g). It provides the FWHM value of 58 ± 10 arcseconds, which is comparable to the crystal quality of the Bi_{TRIG} (001) in Fig. 5.3(c).
- **RSM:** The symmetric RSM is acquired at the Bi_{ORTH}(020) peak and depicted in Fig. 5.8(h). The measured value provides $Q_Z = 2\pi$ (3.406) ± 0.002 nm^{-1} = 1.914 ± 0.002 $Å^{-1}$, resulting in an out-of-plane lattice b = 6.57 ± 0.01 Å. This value is in good agreement with earlier reported results on Si(111) substrates [196, 208, 214].

Therefore, the single crystal Bi_{ORTH} phase with the best crystal quality can be obtained at T_{sub} = 100°C, R_{TF} = 32 nm/h.

5.2.2 Thickness-dependent Growth of Bi_{ORTH} thin film

Through the systematic investigation of the growth parameters in last section, high quality single crystal Bi_{ORTH} phase has been successfully achieved. Previous studies have confirmed that the Bi_{ORTH} phase emerges in the early stages of growth as crystallites on

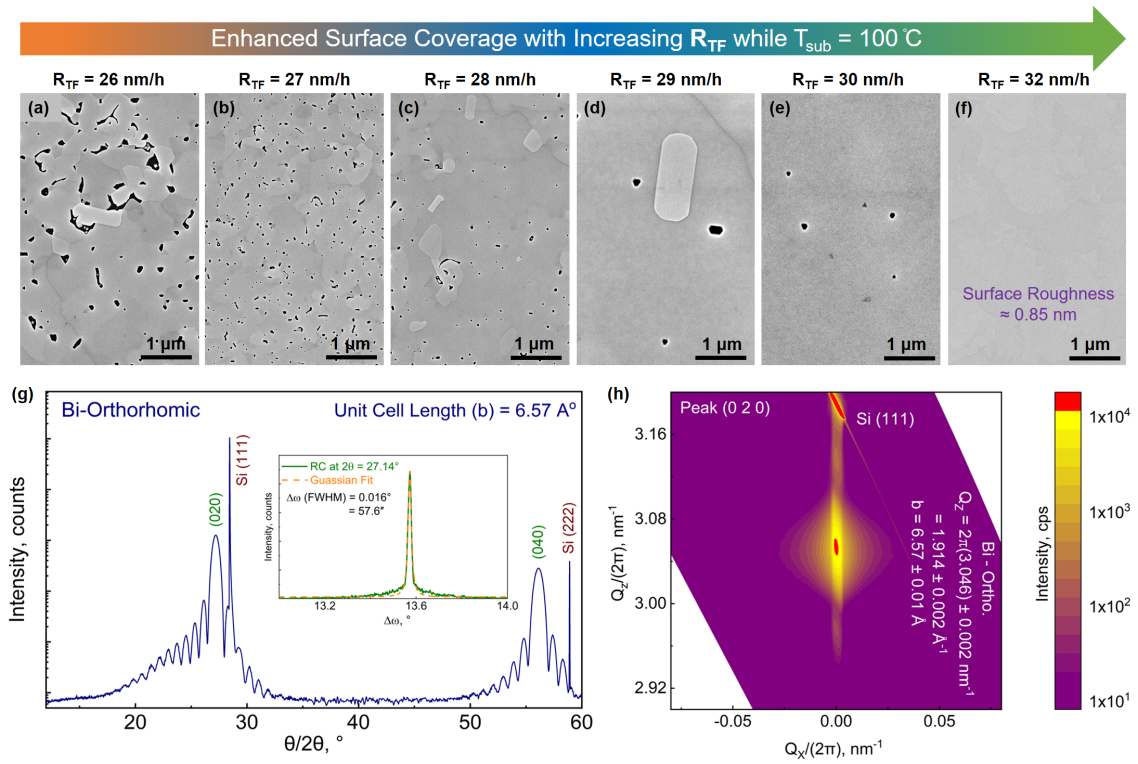

Figure 5.8: Growth optimization and structural characterization of Bi_{ORTH} epilayers. SEM images represent continually improving surface coverage when the epilayers are prepared with (a) R_{TF} = 26 nm/h, (b) 27 nm/h, (c) 28 nm/h, (d) 29 nm/h, (e) 30 nm/h and (f) 32 nm/h while T_{sub} is kept at 100°C. (g) Diffraction pattern of Bi_{ORTH} epilayer prepared at 32 nm/h, (inset) rocking curve acquired at Bi_{ORTH} peak, (h) symmetric RSM acquired at Bi_{ORTH} peak, providing information about the out-of-plane lattice parameters and confirming high crystal quality of the Bi_{ORTH} epilayer. Image taken from [17]. Images were processed in collaboration with Dr. Abdur Rehman Jalil.

various substrates, including Si(111), Al_2O_3(0001), and highly oriented pyrolytic graphite (HOPG) [199, 200, 215]. These reports demonstrated that the Bi_{ORTH} phase remains stable in ultra-thin films up to four monolayers (4 ML), approximately 1.3 nm thick. However, as the layer thickness increases (but remains below 8–10 ML, or about 3.5 nm), Bi_{ORTH} starts to transition into the Bi_{TRIG}(001) phase. Any film thicker than 3.5 nm has been observed to crystallize only in Bi_{TRIG}(001) phase. These findings are supported by the corresponding theoretical modelling and simulations [196, 207, 216]. However, the results presented in this section, mostly contradict the aforementioned reports, where the epitaxial growth of the Bi_{ORTH} phase with different thicknesses is achieved independently from the Bi_{TRIG}(001) phase, as depicted in Fig. 5.4.

To investigate whether the phase changes with varying film thickness, a systematic epitaxy of the Bi_{ORTH} phase is performed using optimized growth parameters (T_{sub}, R_{TF}) = (100 °C, 32 nm/h). The thicknesses of the grown epilayers range from 1.6 nm to 13.6 nm. Symmetric RSMs are performed at the Bi_{ORTH}(020) peak of these epilayers. The results

are summarized in Fig. 5.9.

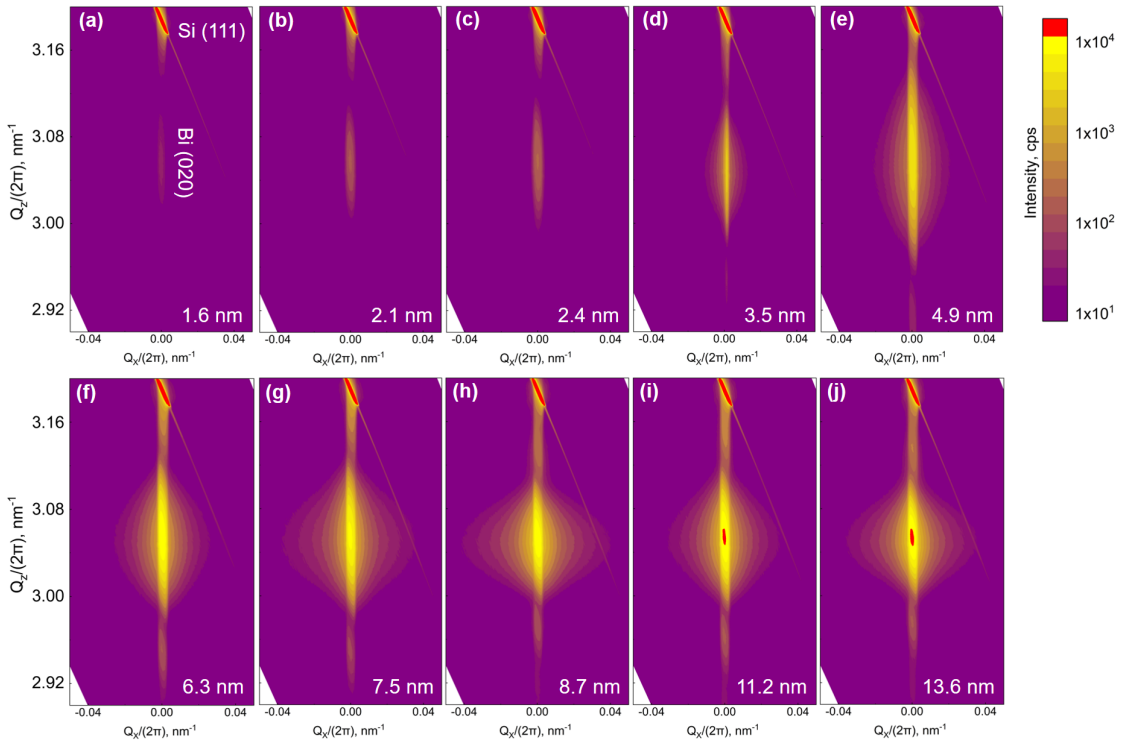

Figure 5.9: Thickness series of the Bi_{ORTH}(010) phase. The presence of a high-intensity Si (111) peak in vicinity of the Bi_{ORTH} (020) peak does not facilitate the analysis of thin films via diffraction pattern; however, it can be adopted as a reference in a symmetric RSM. Various symmetric RSMs of Bi_{ORTH} epilayers are acquired at the (020) peak, while the epilayer thickness is varied from (a) 1.6 nm to (b) 2.1 nm, (c) 2.4 nm, (d) 3.5 nm, (e) 4.9 nm, (f) 6.3 nm, (g) 7.5 nm, (h) 8.7 nm, (i) 11.2 nm and (j) 13.6 nm. Image taken from [17]. Images were processed in collaboration with Dr. Abdur Rehman Jalil.

As shown in Fig. 5.9(e)-(j), Bi_{ORTH} (020) peak is present in the grown epilayers when the film thickness $\geq$ 3.5 nm, suggesting that the Bi_{ORTH} epilayers can be grown phase-segregated. This observation also indicates that the layer thickness has no direct relationship to the phase transformation.

Nevertheless, it is crucial to identify potential factors that may have contributed to the thickness-dependent phase transformation of Bi_{ORTH} in previous studies. Compared to earlier reports, the key differences in this work are the substrate surface and the selection of growth parameters.

- **Substrate surface:** All growths in this work are performed on conventional Si(111) 1×1 surfaces passivated by a monolayer of Bi, whereas previous studies utilized Si(111) $\sqrt{3} \times \sqrt{3}$ or 7×7 reconstructed surfaces, which may have influenced the starting phase of the Bi films.

- **Growth parameters:** This work explores and implements the phase-dependent

optimal growth parameters to ensure the phase purity of the epilayer during growth, which has never been done before.

Different from previous studies, the thickness-dependence phase transformation from Bi_{ORTH} into Bi_{TRIG} is not observed. However, a continuous shift in its lattice parameters is detected. Figure 5.9 indicates a slight change in the out-of-plane lattice with the increasing the epilayer thickness, while significant changes occur in the in-plane structure of Bi_{ORTH}. The behavior of the in-plane lattices will be discussed in detail in the following section.

5.2.3 Lattice Evaluation of Bi_{ORTH}

To investigate the evolution of the in-plane structure of Bi_{ORTH} with varying thicknesses, asymmetric RSMs are performed on the thin films with different thicknesses to evaluate the 2D in-plane lattices of Bi_{ORTH}. The asymmetric RSMs are conducted at the Bi_{ORTH} $(15\bar{1})$ peak, which is in-plane rotated by 45°. The corresponding RSMs are displayed in Fig. 5.10.

As shown in Fig. 5.10(a), dual diffraction peaks appear as expected, due to the nonequivalent in-plane lattice value in orthorhombic structure. According to this asymmetric RSMs acquired at the Bi_{ORTH} $(15\bar{1})$ peak, the in-plane lattice parameters are found to be 4.49 ± 0.02 Å and 4.81 ± 0.02 Å, respectively. The measured lattices are in close agreement with reported values of Bi_{ORTH} on HOPG [138, 215, 217], but they differ slightly from reported values acquired on Si(111) [196, 207, 208, 214, 216]. By analyzing the RSM in Fig. 5.10(a), it can be seen that two in-plane lattice parameters are unequal, with a difference of Δd = 0.32 Å. Moreover, a subtle difference along the z-direction of two peaks is observed, with a measured value of Δh = 0.09 Å, which can be related to buckling[1] [138, 199, 207]. $Bi_{TRIG}(012)$ is a phase known to exhibit strong buckling, whereas in Bi_{ORTH}, the strain relaxes within the crystal, leading to the reduction of the buckling height. In this study, the measured buckling height of 0.09 Å confirms the relaxed state of Bi_{ORTH} compared to the $Bi_{TRIG}(012)$ phase [138, 196, 199].

When the 45° in-plane rotated Bi_{ORTH} lattice is projected onto Si$[1\bar{1}0]$ and Si[211] planes, it forms a pseudo-cubic sub-lattice with the matched out-of-plane lattice, as depicted in Fig. 5.1(g)-(i). Based on the values calculated by the Pythagorean theorem with equations 5.1-5.3 and the matching out-of-lattice parameters, Bi in the pseudo-cubic structure (Bi_{cub}) is estimated to arrange with $a \approx b \approx c \approx 6.58$ Å.

$$a_{CUB} = \sqrt{a_{ORTH}^2 + c_{ORTH}^2} \tag{5.1}$$

$$a_{CUB-8nm} = \sqrt{4.49^2 + 4.81^2} \approx 6.58 \tag{5.2}$$

[1] Buckling is a strain-induced deformation in a crystal and can be described as the height difference between two atoms of the same monolayer.

$$a_{CUB-25nm} = \sqrt{4.57^2 + 4.74^2} \approx 6.58 \tag{5.3}$$

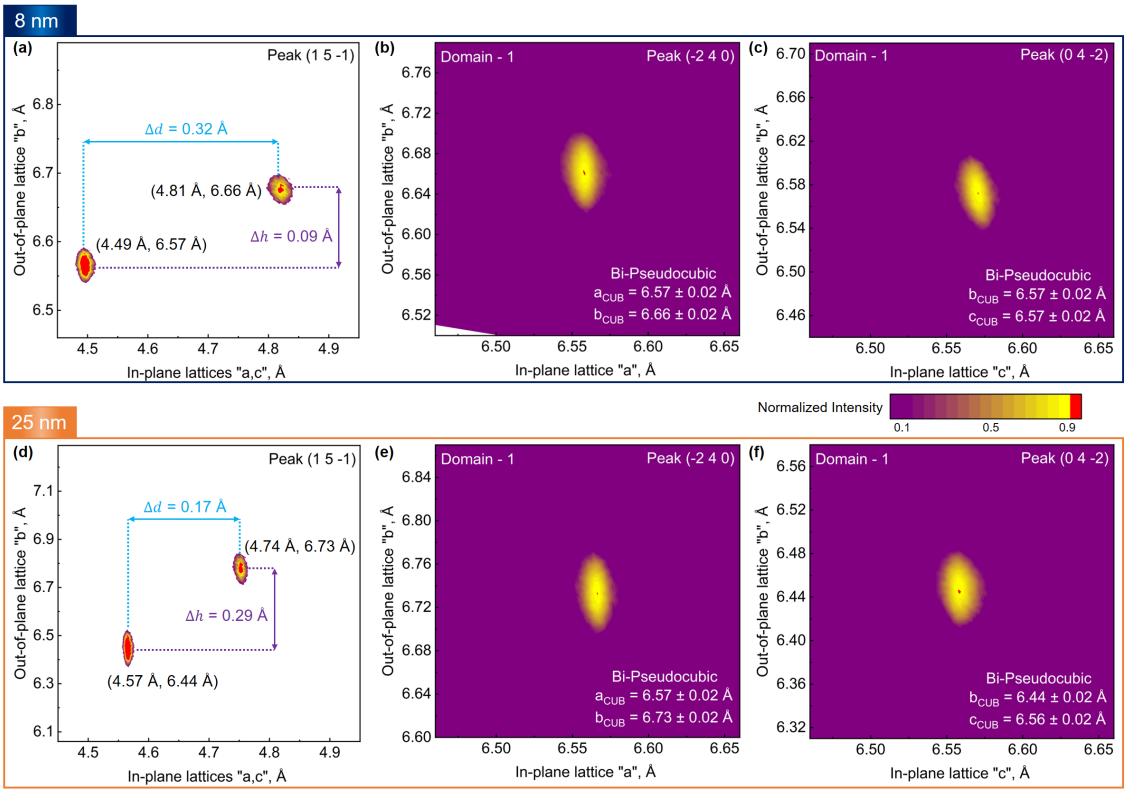

Figure 5.10: Evaluation of in-plane lattice parameters of the Bi_{ORTH}(010) epilayers via asymmetric RSM. (a) A map acquired at the Bi_{ORTH} $(15\bar{1})$ peak in an 8.4 nm thick epilayer, where Δd represents the difference in length between in-plane lattices while Δh represents buckling, i.e., high difference between Bi atoms of the same monolayer; the 45° in-plane rotation led to the formation of pseudo-cubic sub-lattice, and the acquired maps at the Bi_{CUB} $(\bar{2}40)$ and the Bi_{CUB} $(04\bar{2})$ peaks are represented in (b) and (c), respectively. Similar measurements are performed in a 25 nm thick epilayer at (d) Bi_{ORTH} $(15\bar{1})$, (e) Bi_{CUB} $(\bar{2}40)$ and (f) Bi_{CUB} $(04\bar{2})$ peaks, where a difference in buckling height in (d) is observed to enhance from 0.09 Å to 0.29 Å. Image taken from [17]. Images were processed in collaboration with Dr. Abdur Rehman Jalil.

Adopting Bi_{CUB} parameters, the asymmetric RSMs at the high-intensity asymmetric peaks i.e. Bi_{CUB} $(\bar{2}40)$ and Bi_{CUB} $(04\bar{2})$ peaks, are successfully acquired, as shown in Fig. 5.10 (b) and (c) respectively. The difference in the out-of-plane lattice constant (b_{CUB}) obtained in the two peaks can be directly linked to the buckling height (Δh = 0.09 Å), as indicated in Fig. 5.10 (a).

Further RSM investigations reveal that the thickness plays a critical role in the structural arrangement of the Bi_{ORTH} lattice. RSM acquired at Bi_{ORTH} $(15\bar{1})$ peak for a 25 nm thick epilayer are depicted in Fig. 5.10(d), where the in-plane lattice parameters are determined to be 4.57 ± 0.02 Å and 4.74 ± 0.02 Å, respectively. A slight shift in both in-plane lattice

parameters is observed, with the difference (Δd) between them reduced from 0.32 Å to 0.17 Å. Moreover, when the layer thickness is increased from 8 nm to 25 nm, the buckling height (Δh) is witnessed to enhance three times from 0.09 Å to 0.29 Å, revealing the increased strain in the Bi_{ORTH} films.

An interesting observation is that no thickness-dependent change in the in-plane lattices of Bi_{CUB} is detected, as the projected values of both sets of orthorhombic lattices at 8 nm and 25 nm are almost identical (Equation 5.2 and 5.3). In general, Bi_{ORTH} and Bi_{CUB} are two different representations of the same crystal structure in this case, as shown in Fig. 5.1(g)-(i).

The acquired lattices in the 25 nm-thick Bi_{ORTH} epilayer are found to be in close agreement with earlier reports on Si(111), although the buckling height is still much smaller than the reported value of 0.5 Å [196, 207, 208, 214, 216].

5.2.4 Buckling and Topology of Bi_{ORTH}

From the last section, the in-plane lattice investigation of Bi epitaxial growth has revealed the thickness-dependent properties of the Bi_{ORTH} epilayer. Different from the shifted out-of-planes lattice at different thickness in Bi_{TRIG} phase (due to the scaling effect), a shift in the in-plane lattice parameters is also observed in the Bi_{ORTH} phase. The variation in the in-plane lattice is demonstrated to be related to the evolution of the buckling height with respect to the film thickness. The trend of buckling height dependence on the thickness of Bi_{ORTH} layer is summarized in Fig. 5.11(a).

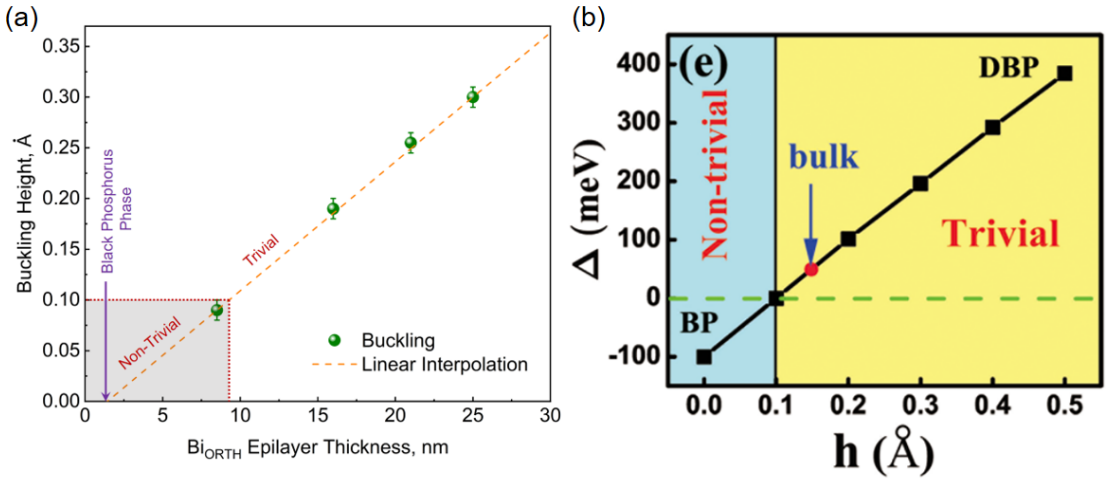

Figure 5.11: Buckling height vs. topology in the Bi_{ORTH} epilayers. (a) Linear interpolation of thickness-dependent acquired values indicate that the buckling height in Bi_{ORTH} epilayers should reach zero, which would allow the realization of the black-phosphorus-like phase of Bi (Bi_{BP}). Image taken from [17], processed in collaboration with Dr. Abdur Rehman Jalil. (b) Theoretical model which indicates any Bi_{ORTH} epilayer hosting the buckling height $\leq$ 0.1 Å must exhibit topology, and thus, all Bi_{ORTH} epilayers with thickness $\leq$ 9 nm are predicted to exhibit non-trivial attributes. Image taken from [138].

Besides, it has been observed by Lu et al. [138] that the buckling height has a significant influence on the topological properties of Bi_{ORTH}. Epilayers with a buckling height ≤ 0.1 Å exhibit non-trivial topology, whereas an increase in buckling height leads to a transition to a trivial phase, as illustrated in Fig. 5.11(b) [138].

Based on Fig. 5.11(b), the Bi_{ORTH} epilayers prepared in this work with thickness ≤ 9 nm are expected to exhibit non-trivial topology. which was only true for approx. 1.3 nm thick epilayers in all earlier studies. It facilitates the realization of Bi_{ORTH}-based quantum devices, as achieving fully coalesced 9 nm-thick epilayers is less challenging compared to 1.3 nm.

However, the increasing buckling height in the epilayer suggests that after a certain thickness, the Bi_{ORTH} epilayer becomes unstable and tends to cross the limit of quantum confinement, transforming into the $Bi_{TRIG}(001)$ phase. This hypothesis is verified by the growth of a 45 nm-thick Bi_{ORTH} epilayer, which exhibits a polycrystalline phase containing both Bi_{ORTH} and the $Bi_{TRIG}(001)$ structures. This observation indicates that the maximum stable thickness of the Bi_{ORTH} phase lies between 30 nm (depicted in Fig. 5.16 and 5.18) and 45 nm.

Moreover, 5.11(b) suggests that the black-phosphorus phase of Bi (Bi_{BP}) exhibits zero-buckling. With the linear interpolation in Fig. 5.11(a), the Bi_{BP} phase can be realized only when the epilayer thickness is below 1.32 nm. As the thinnest Bi_{ORTH} epilayer achieved in this study is 1.63 nm, the Bi_{BP} phase is not observed in this work.

5.3 Domain Alignment of Bi Nanofilm Allotropes

As described in the last two sections, the Bi_{TRIG} and Bi_{ORTH} phase have been successfully grown as separated, pure phases. Questions regarding how these two phases align themselves on the Si(111) substrate and what occurs during the transition process from the Bi_{TRIG} to the Bi_{ORTH} phase arise, which will be explored in detail in this section.

To understand the in-plane alignment of the two allotropes with respect to the substrate, the rotational symmetry of the lattices is investigated with the ϕ-scanning. Figure 5.12 represents detailed information on the domain alignment of various Bi phases.

Theoretically, a trigonal lattice exhibits 3-fold rotational symmetry. When a trigonal crystal grows on a hexagonal surface, e.g., Si(111) surface, the crystal may develop 60° in-plane rotated domains. This phenomenon is observed in $Bi_{TRIG}(001)$ epilayers, as depicted in Fig. 5.12(a). The top figure in (a) presents a 3D pole-figure map on the Bi_{TRIG} $(1\bar{1}02)$ peak[2], which shows all domains that exist in the epilayer. It is evident that the epilayer contains twin domains, characterized by 60°-rotated orientations. The twin domains are also visually represented by the two 60°-rotated colored triangles within the pole-figure map. Moreover, one of the domains (orange colored triangle) is observed to be collinear with the substrate peaks, corresponding to the 60°, 180°, and 300° marks in the map. The bottom figure in (a) is a 2D cut ϕ-scan at $\chi = 55.7°$ from the top pole-figure map. As shown in the ϕ-scan, one of the domains is collinear with of the Si(220) facet,

[2]This peak is chosen due to its highest diffraction intensity.

while the other one aligns with the Si(311) facet. According to the intensity, the ratio of the two rotated domains is approx. 1:5. The unequal domain ratio suggests that one domain is suppressed under optimized growth conditions, with the domain collinear with Si(220) being preferentially favored.

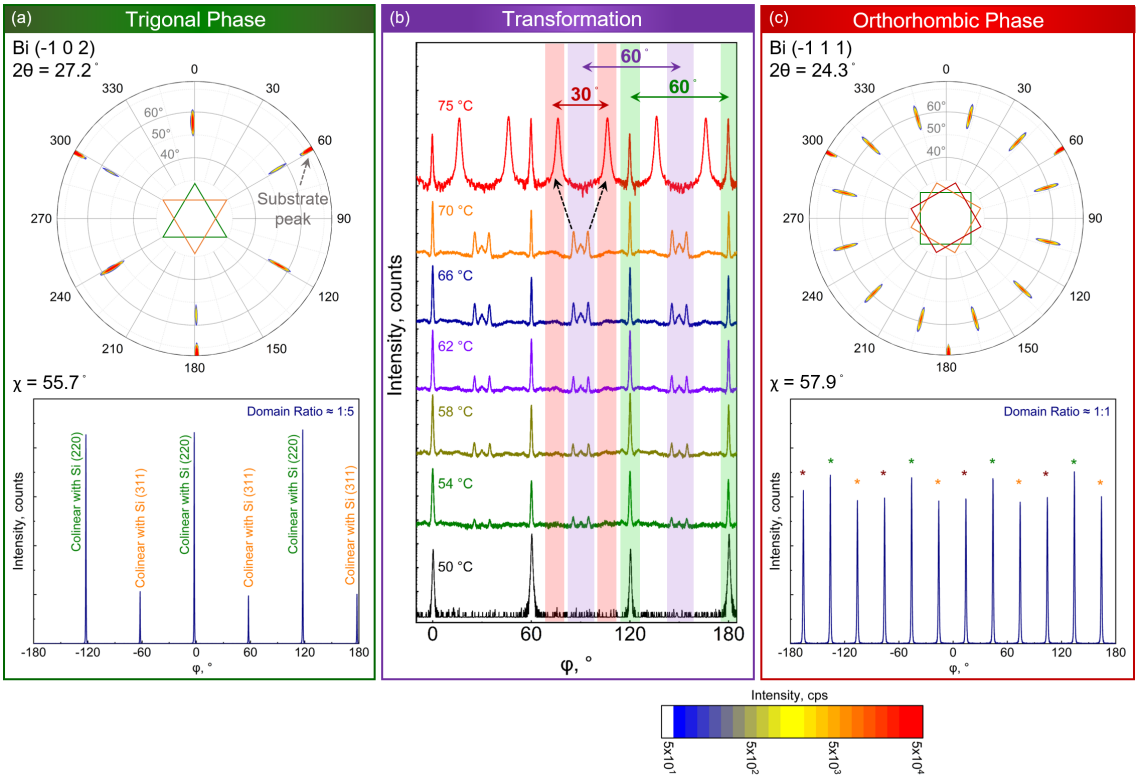

Figure 5.12: Domain analysis of Bi nanofilm allotropes and their alignment with respect to the substrate. (a) Analysis of the $Bi_{TRIG}(001)$ epilayers performed by probing the $(1\bar{1}02)$ peak. (Top) A pole-figure map representing six distinct peaks originating from two 60° in-plane rotated trigonal domains. (Bottom) The ϕ-scan, a 2D cut at χ= 55.7°, (b) A series of ϕ-scans representing temperature-dependent structural transformation in Bi epilayers. The emergence of three-pointed distinct peaks is found to be related to the $Bi_{TRIG}(012)$, whereas the transformation of those three-pointed peaks into 12 distinct peaks is an indication of the orthorhombic crystal structure. (c) Analysis of the $Bi_{ORTH}(010)$ epilayers conducted via probing $(\bar{1}11)$ peak. (Top) A pole-figure map representing 12 distinct peaks originating from three 30° in-plane rotated orthorhombic domains highlighted with district colored and rotated squares. (Bottom) The ϕ-scan, a 2D cut at χ= 59.9°, provides information about the relative presence of domains in the epilayer. Each peak is marked with a color that corresponds to the associated domain. Image taken from [17]. Images were processed in collaboration with Dr. Abdur Rehman Jalil.

Previously in section 5.2.1, it has been discovered that the crystal enters "transformation zone" when the T_{sub} > 50 °C. The corresponding in-plane transition of the domains is demonstrated through a series of ϕ-scans of the epilayers prepared at T_{sub} = 50 - 75 °C, as shown in Fig. 5.12 (b). The transition occurs in following stages:

- **T_{sub} = 50°C:** ϕ-scan exhibits 60°-periodicity peaks, indicating the pure phase of

$Bi_{TRIG}(001)$. The 60°-rotated domains of $Bi_{TRIG}(001)$ are highlighted in the green-colored regions.

- **T_{sub} = 54 - 75 °C:** Starting from T_{sub} = 54 °C, distinctive three-pointed peaks start to appear between Bi_{TRIG} peaks in the initial stage. These peaks exhibit a 60° periodicity, highlighted in the purple-colored zone in Fig. 5.12(b). The exotic three-pointed peaks positioned between Bi_{TRIG} peaks have a 30° offset with the substrate collinearity. Along with the appearance of three-pointed peaks in the ϕ-scan, a diffraction peak at 2θ = 27.2° starts to emerge in Fig. 5.7(a), suggesting that these two phenomena are related with each other. Moreover, the 60° periodicity of the newly appeared three-pointed peaks indicates that they cannot originate from the Bi_{ORTH} phase (since the ϕ-scan of the Bi_{ORTH} phase exhibits 12 peaks with 30° periodicity, as shown in (c)) and must be associated with the $Bi_{TRIG}(012)$ orientation, as the $Bi_{TRIG}(012)$ also has the characteristic diffraction peak at 2θ = 27.2°. This assumption still requires further investigation. As T_{sub} increases, it is observed that the relative intensity of these distinctive three-pointed peaks increases until T_{sub} reaches 70 °C.

- **T_{sub} = 70 - 75 °C:** When the T_{sub} > 70 °C, the three-pointed peaks split into two peaks that are 30° apart from each other and ± 15° shifted from the the original peak position, as shown in the black-dotted arrows in Fig. 5.12(b). This in-plane transition results in the formation of 12 peaks that exhibit 30° periodicity, along with six peaks originating from the $Bi_{TRIG}(001)$ phase, as displayed in the ϕ-scan of the epilayer prepared with T_{sub} = 75 °C. During this process, the morphology of the crystal changes significantly, as displayed in Fig. 5.7(d)-(e). The appearance of 12 distinct peaks with 30° periodicity is a signal of cubic-like structures when aligned on a hexagonal surface [218]. Therefore, this in-plane transition stage can be associated with the appearance of the Bi_{ORTH} phase.

- **T_{sub} = 75 - 95 °C:** As T_{sub} increases further, the peaks originating from the Bi_{TRIG} gradually diminish, while the 30° periodic Bi_{ORTH} peaks are observed to increase in intensity until T_{sub} reaches 95 °C.

- **T_{sub} > 95 °C:** When T_{sub} > 95 °C, epilayers are observed to crystallize in pure Bi_{ORTH} phase..

Figure 5.12(c) depicts a 3D pole-figure map (top) of the Bi_{ORTH} epilayer acquired by probing $(\bar{1}11)$ peak, along with a 2D cut ϕ-scan (bottom) at 2θ = 57.9°, confirming the presence of only 12 in-plane peaks. As the orthorhombic structure exhibits four-fold rotational symmetry, the alignment of domains in the epilayer is illustrated using three distinct colored square boxes, each rotated by 30° and positioned within the pole-figure map. The three domains are identified by the three colored peaks in the bottom 2D cut ϕ-scan, where composition of each domain is similar, indicated from comparable peak intensities. During the first and second in-plane transitions in Fig. 5.12(b) at 54 °C and 75 °C, respectively, the non-collinearity of the crystal peak with respect to the substrate was explained. Here, the three Bi_{ORTH} domains exhibit a 15°, 45°, and 75° offset with respect to the substrate peak, respectively.

5.4 Atomic-scale Structural Characterization via STEM

Since domain alignment of different allotropes of Bi on the hexagonal Si substrate is revealed in the last section, STEM is further introduced to investigate different Bi phases and their interfaces with the Si substrate. The lamellae for TEM investigation are prepared by the FIB system "FEI Helios Nanolab 600i". Before inserting into the microscope, plasma cleaning was carried out to remove the surface contamination of the lamella. STEM measurements are performed with "FEI Titan G2 80-200 ChemiSTEM" microscope, which is equipped with a spherical aberration probe “Cs” corrector (CEOS DCOR) and the dark/bright-field detectors. STEM-HAADF and -BF images are acquired at 200 kV.

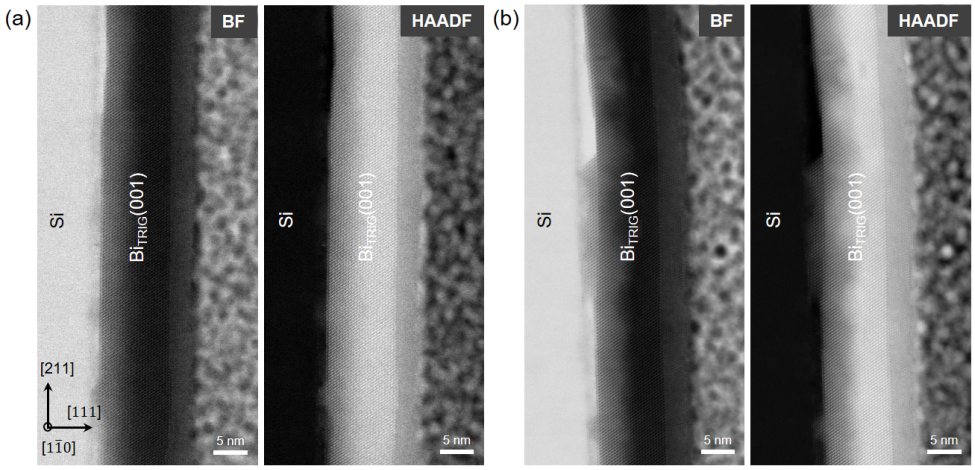

Figure 5.13: STEM images acquired along Si[1$\bar{1}$0] projection, indicating the effect of image acquisition time on the Bi$_{TRIG}$(001) epilayers. The average acquisition time in (b) is higher than (a). The damaged regions in (b) are the confirmation of Bi instability under prolonged electron beam exposure.

Epilayers from three distinct phases, including the $Bi_{TRIG}(001)$, $Bi_{ORTH}(010)$, and a polycrystalline phase (acquired at T_{sub} = 70 °C) containing both $Bi_{TRIG}(012)$ and Bi_{ORTH} orientations are selected. Lamellae at the cross-sections of each epilayer along Si [1$\bar{1}$0] and Si [211] are extracted.

Due to the low melting point of Bi (271 °C), lamella extraction and high-resolution STEM image acquisition from this material is challenging. During the STEM investigation, it has been observed that the lamella became amorphous, with a heavily deformed interface between Bi and the substrate. Besides, Bi oxidizes rapidly when exposed to the atmosphere. The fully amorphized films are shown in Fig. A2.2 in the Appendix.

Moreover, to analyse the impact of image acquisition and electron beam illumination time, examples are summarized in Fig. 5.13 and 5.14. In the case of either extending the image acquisition time or increasing the beam illumination time in the same region of the specimen, the interfaces between the Si substrate and the Bi epilayer were damaged,

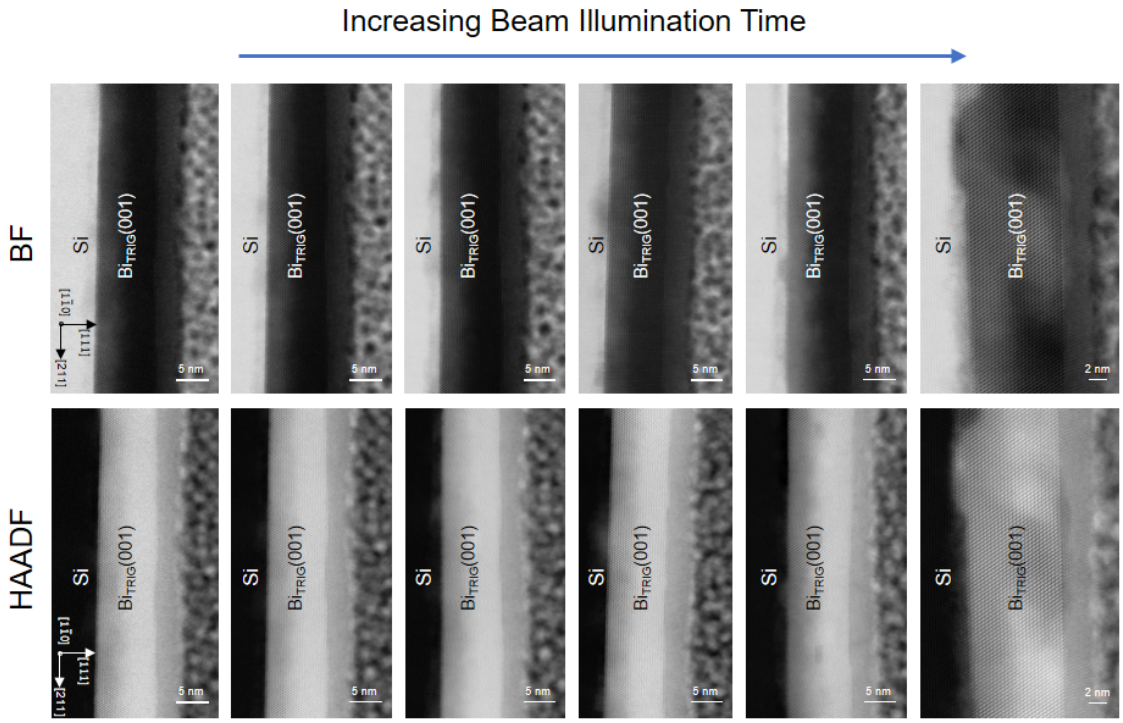

Figure 5.14: STEM images acquired along Si[1$\bar{1}$0] projection, representing the continual structural damage of Bi epilayer with increasing electron beam illumination time. The interface between Bi and Si is observed to be the most affected region. The acquisition time remains constant across all images.

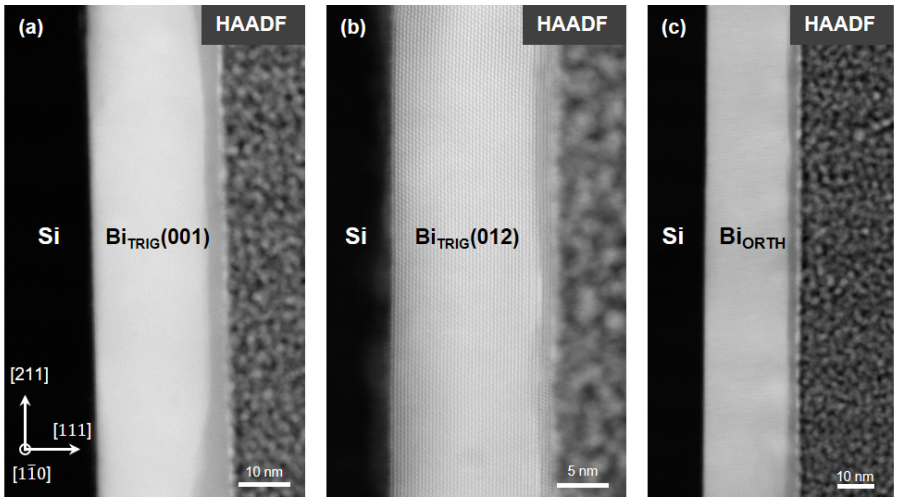

Figure 5.15: STEM-HAADF images of Bi$_{TRIG}$(001), Bi$_{TRIG}$(012) and Bi$_{ORTH}$(020) epilayers, acquired along Si[1$\bar{1}$0] projection, confirming the large grain sizes and high crystal quality of the epilayers.

where the Bi melted into the substrate. This phenomenon makes it particularly challenging to conduct further investigations. By carefully fabricating lamellae at low energies in FIB and minimizing the suitable exposure time under the focused electron beam during STEM measurement, structural investigations have been successfully performed.

During the STEM investigation, large grain size of different allotropes is observed, which has never been reported so far. As displayed in Fig. 5.15, the grain size of $Bi_{TRIG}(003)$, $Bi_{TRIG}(012)$, $Bi_{ORTH}(010)$ can reach hundreds nanometers within the films, demonstrating high quality growth of these phases, which has been achieved through optimized growth parameters in this study. High-resolution STEM images of each phases are summarized in Fig. 5.16, 5.17 and 5.18.

Figure 5.16 depicts overview HAADF images of the $Bi_{TRIG}(001)$ epilayer along $Si[1\bar{1}0]$ projection. An atomically sharp interface between Bi_{TRIG} and Si(111) can be visualized in Fig. 5.16(b) and (c), depicting HAADF and BF images, respectively. Before the periodic stacking of Bi bilayers starts, a monolayer of Bi is observed, which passivates the dangling bonds at the Si(111) surface. It affirms the formation of 1×1-Bi surface, a 2D sheet of Bi that serves as a seed layer for epitaxial growth of $Bi_{TRIG}(001)$. A magnified HAADF image of the central region (away from the interface), is depicted in Fig. 5.16(d), confirming the high structural quality of the epilayer without the appearance of any extended defects. The measured lattice values from the highly magnified image (e) and (f) are in perfect agreement with the theoretical value in Fig. 5.1.

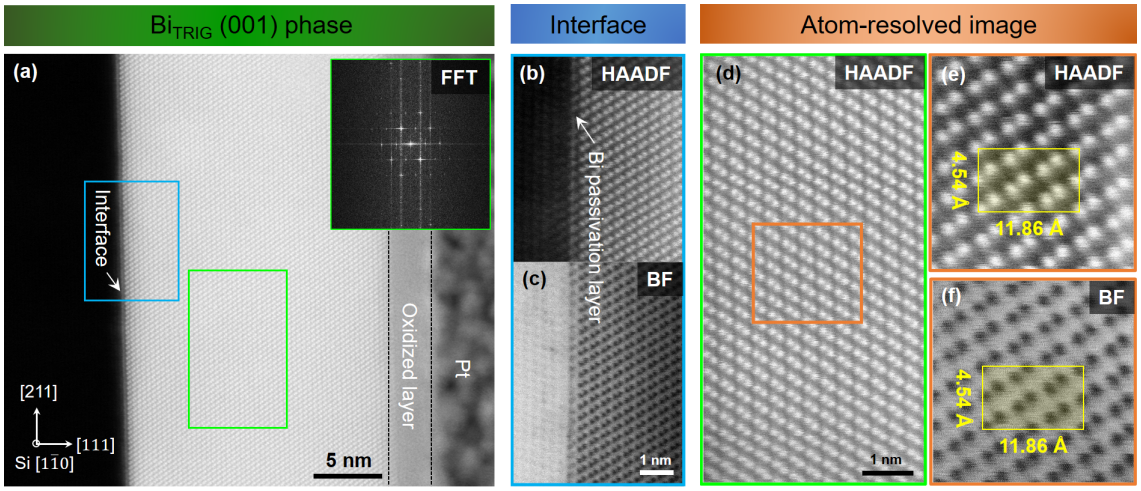

Figure 5.16: STEM investigation of $Bi_{TRIG}(001)$ phase. (a) A cross-sectional HAADF image of $Bi_{TRIG}(001)$ epilayer acquired along $Si[1\bar{1}0]$ projection. The magnified region at the interface can be visualized via (b) HAADF and (c) BF images, respectively. The central marked region is further magnified and depicted in (d), where the periodic stacking of Bi bilayers can be seen in (e) and (f). Image taken from [17].

During the investigation of polycrystalline epilayers, the presence of the $Bi_{TRIG}(102)$ oriented crystals, as indicated during the domain alignment analysis in Fig. 5.12(b), is observed and successfully captured. A HAADF image focusing on the $Bi_{TRIG}(012)$ oriented grain is depicted in Fig. 5.17(a), while a low-pass filtered, magnified image of the central

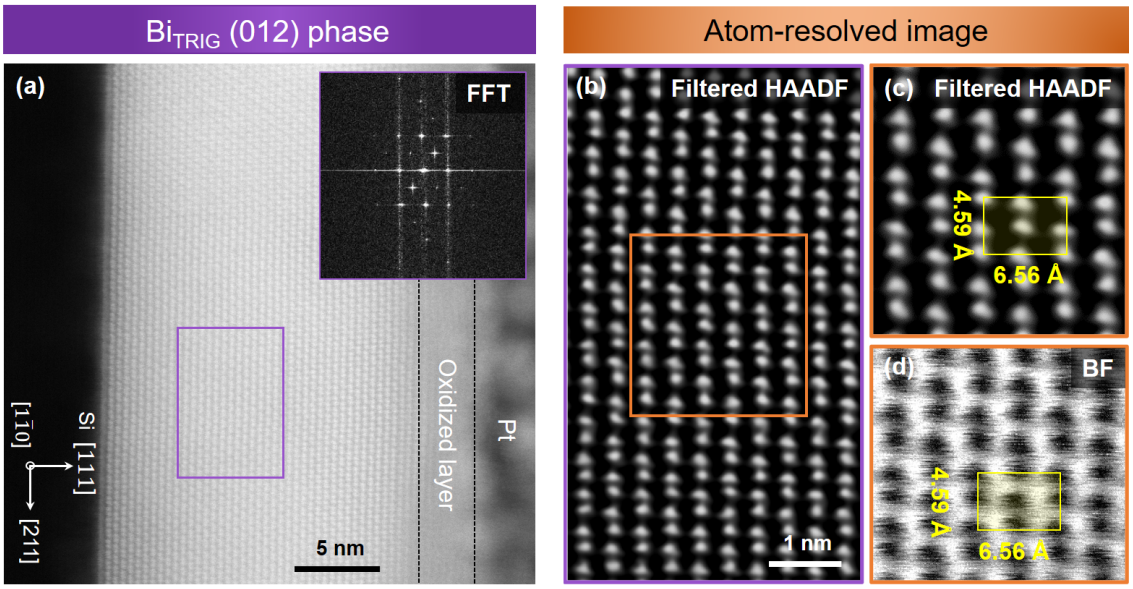

Figure 5.17: STEM investigation of Bi$_{TRIG}$(012) phase. (a) A HAADF image of Bi$_{TRIG}$(012) grain in a polycrystalline epilayer acquired along Si[1$\bar{1}$0] projection. The central marked region is magnified, filtered (band-pass) and depicted in (f), where the puckered structures of Bi atoms along with a strong buckling between puckered atoms can be perceived. Image taken from [17].

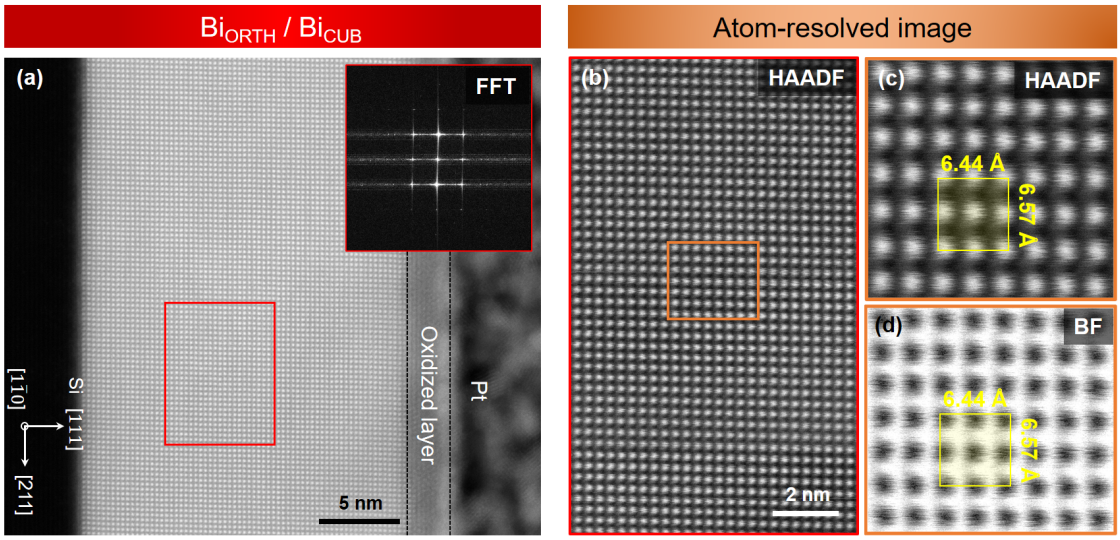

Figure 5.18: STEM investigation of Bi$_{ORTH}$(010) phase. (a) A HAADF image of Bi$_{ORTH}$(010) epilayer acquired at the cross-section along Si[1$\bar{1}$0] projection. The domain is observed to be 2° in-plane rotated with respect to the substrate, which does not allow acquisition of atomically resolved images at the interface. The central highlighted region is magnified and depicted in (h), where the pseudo-cubic structure of Bi sub-lattice is evident. Image taken from [17].

region is depicted in Fig. 5.17(b). Figure 5.17(b) indicates the strong buckling between the Bi atoms in Bi$_{TRIG}$(012) phase. Atomic distance measurements via line profiles of the HAADF image have revealed the buckling height to vary between 0.43 ± 0.02 Å and 0.48

± 0.02 Å in a $Bi_{TRIG}(012)$ monolayer. The difference between various measured values at different positions in the acquired image can be linked to localized changes in the tilt angle, as the lamella is observed to be strongly bent due to the curtain effect imposed by the deposited Pt layer during FIB process, as seen in Fig. A1.2 in the Appendix.

Figure 5.18(a) represents a HAADF image acquired at the cross-section of a Bi_{ORTH} epilayer along Si[1$\bar{1}$0] projection. This image reveals an apparently relaxed and periodic stacking of the Bi monolayer, arranged in a cubic-like structure. An atomically sharp and clean interface between the substrate and Bi_{ORTH} epilayer is clearly visualized. As established during XRD investigations, the unique alignment of the Bi_{ORTH} crystals with a 45° in-plane offset with the Si(111) substrate facilitates the formation of a pseudo-cubic sub-lattice. A magnified HAADF image depicted in Fig. 5.18(b) represents the Bi_{CUB} structure, with the in-plane and the out-of-plane lattices measured to be 6.57 ± 0.02 Å and 6.44 ± 0.02 Å, respectively. The acquired values from STEM are in good approximation with XRD acquired lattices, as indicated in Fig. 5.10(d)-(f).

The oxidation layer can be observed above Bi thin film due to the fast surface oxidation of Bi in the atmosphere, as shown in Fig. 5.16(a), Fig. 5.17(a), and Fig. 5.18(a).

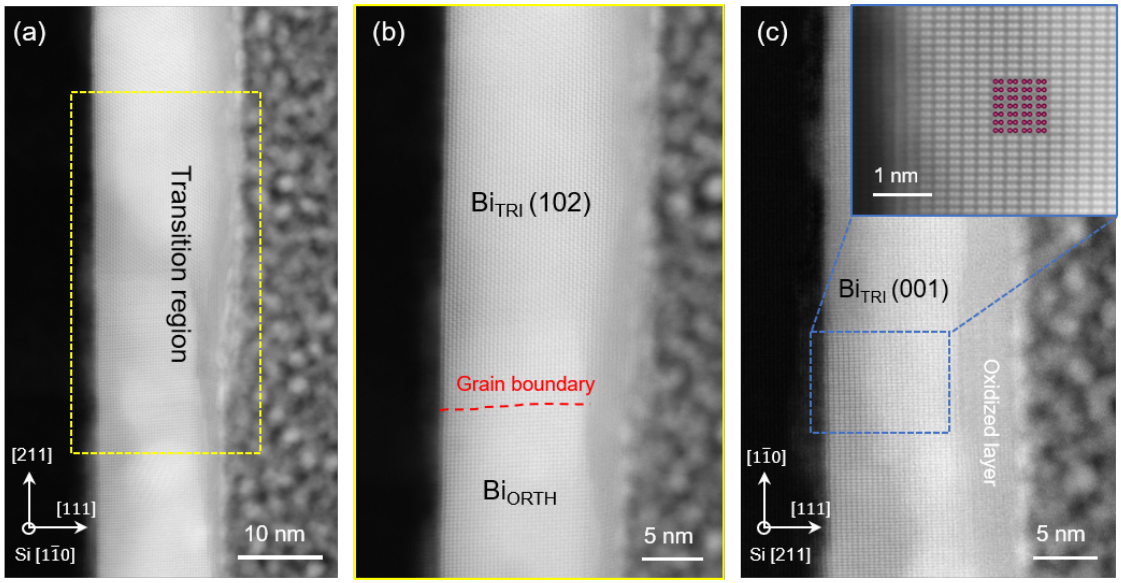

Figure 5.19: STEM-HAADF images of (a) co-existence region of Bi_{TRIG} and Bi_{ORTH} phases, (b) further magnification of the yellow box in (a), (c) 30°-rotated $Bi_{TRIG}(001)$ phase, with the atomic resolution image on the top right. The atomic model from the literature [219] fits the atomic arrangement perfectly. The image in the top right of (c) was provided by JinHee Bae.

Furthermore, the transition region and the other orientation of $Bi_{TRIG}(001)$ phase are also detected in the grown epilayer, as shown in Fig. 5.19. As mentioned in 5.3, $Bi_{TRIG}(012)$ serves as the transition phase during the evolution from $Bi_{TRIG}(001)$ to Bi_{ORTH} phase. A polycrystalline phase grown at T_{sub} = 70 °C including $Bi_{TRIG}(012)$ and Bi_{ORTH} phases, is shown in Fig. 5.19(a). The grain boundary between the two phases is highlighted with the red dashed line in Fig. 5.19(b), which is the magnified from the transition region from the yellow box in (a). Moreover, the in-plane rotated $Bi_{TRIG}(001)$ phase is also observed

during the investigation of another specimen, as displayed in Fig. 5.19(c). The bilayer stacks of Bi are rotated 30° compared to the orientation in Fig. 5.16, projecting along Si[211]. This atom arrangement corresponds to the atom model shown in Fig. 5.1(c).

5.5 Summary

In this chapter, we have demonstrated the high-quality growth of Bi thin films of various phases and BiSb thin film with desired thickness via MBE on Si(111) 1×1 surfaces.

Firstly, the growth parameters for the trigonal phase, i.e., $Bi_{TRIG}(001)$, were optimized to T_{sub} = 40 °C and R_{TF} = 22 nm/h, with the rocking curve as sharp as 53 ± 10 arcseconds. By applying the optimum growth condition of $Bi_{TRIG}(001)$, the corresponding series of thickness is obtained at each growth time. Sb is then added to the thin film forming BiSb (Sb = 4%) alloy, where the high quality growth of BiSb thin film is also achieved.

While increasing the substrate temperature from T_{sub} = 40 °C to 95 °C, a structural transformation of the Bi epilayers into the orthorhombic $Bi_{ORTH}(010)$ phase was observed. After optimizing the crystal quality of the $Bi_{ORTH}(010)$ phase to a rocking curve value of 58 ± 10 arcseconds, ϕ-scans of various growth series were performed to reveal the dynamic transformation between the Bi trigonal and orthorhombic phases with respects to T_{sub} and R_{TF}. Strikingly, it was found that the six-fold symmetry of the twinned trigonal phase, i.e., $Bi_{TRIG}(001)$, transforms partly into an intermediate phase before fully turns into the orthorhombic phase. The observed intermediate phase with its characteristic three-pointed peaks was identified as the $Bi_{TRIG}(012)$ phase.

During the following STEM investigation, all three phases including the intermediate $Bi_{TRIG}(012)$ phase were observed from 3 lamellae with each individually optimized growth parameters, where the domain size of $Bi_{TRIG}(001)$ and $Bi_{ORTH}(010)$ phases are up to hundreds nanometers, thus confirming the high quality growth of the two pure phases. It is also for the first time that the atomic arrangement of the three phases is clearly demonstrated in the high resolution STEM images, indicating the existence of Bi_{ORTH} phase instead of Bi_{BP} phase reported in the previous literature. The lattice parameters extracted from the high resolution imaging are in good agreement with the values measured from the XRD study and in the reported literature.

Besides, the buckling height in phase-pure $Bi_{ORTH}(010)$ thin films was investigated, as it was proposed that the amount of buckling determines the topological class to which the Bi crystal belongs to. It was found that the buckling height increases with the increase of epilayer thickness. Different from earlier study, the maximum thickness of phase-pure $Bi_{ORTH}(010)$ before transforming into $Bi_{TRIG}(001)$ was found to be 30 nm instead of 1.3 nm reported previously as the critical height. The enhanced maximum thickness observed in our study enables the exploration of the topological phase in $Bi_{ORTH}(010)$, which has been predicted to be present in thin films when the thickness under 9 nm.

In the future, BiSb thin film alloy with the thickness below 4 nm will be grown and fabricated into topological devices to investigate its 2D topological properties. Besides, based on the topological and phase transition properties, Bi_{ORTH} thin film can also potentially be used in the field of quantum topology when its thickness less than 9 nm. In general,

this phase-selective growth study of Bi thin films in different allotropes offers a promising path to the novel topological and neuromorphic applications.

6 Stoichiometry Growth of SnBiTe Family and Structural Characterization

Commentary: *This chapter presents the growth and structural characterization of three stoichiometries from the $Sn_xBi_yTe_z$ series. The MBE growth of SnBT-124, SnBT-147, and SnBT-225 thin films was carried out by the author. Structural characterization, including all TEM investigations and XRR/XRD measurements, was also performed by the author. Reciprocal space mapping (RSM) data for in-plane lattice analysis were provided by Dr. Abdur Rehman Jalil.*

To assess the surface morphology and roughness of the thin films, atomic force microscopy (AFM) measurements were conducted by Dr. Nisha Shahi upon the author's request. Furthermore, transport measurements to examine the electrical properties of the SnBT-147 thin film were performed by Jonas Buchhorn (PGI-9). With the exception of the figures related to transport measurements, all figures were prepared and all data analyses were conducted by the author, with guidance and support from Dr. Abdur Rehman Jalil.

As introduced in section 2.7, the topological phase of a material can be transformed into another topology by tuning the stoichiometry. Stoichiometric variation allows the realization of various compositional alloys consisting of "base" (topological) and "additive" (trivial) heterostructures. By controlling the relative composition of "base" and "additive", the electronic band structure of the alloy can be engineered.

This chapter is dedicated to study the $Sn_xBi_yTe_z$ material series, where Bi_2Te_3 acts as the "base" and Sn acts as the "additive" material. While incorporating Sn into Bi_2Te_3, Sn tends to be alloyed with Te, forming the SnTe in the material system. Therefore, this system can also be interpreted as $(SnTe)_m(Bi_2Te_3)_n$ based heterostructures. Since Bi_2Te_3 is an n-type topological insulator and Sn acts as a p-type dopant, by merging Bi_2Te_3 and Sn together, the position of the Fermi level with respect to the topological surface states (TSS) in TI can be tuned [220]. Moreover, as indicated in Section 2.7, with the increase of Sn content, the strength of the SOC decreases, so that the inverted bandgap also decrease until it reaches a critical point of 0 eV, where the material becomes a semimetal.

Some of the stoichiometries in $Sn_xBi_yTe_z$ have already been reported to have outstanding thermoelectric properties [221–223]. They possess van der Waals (vdW) heterostructures with a periodic stacking order of layers, which can be altered by varying the content of Sn and Bi. Upon changing the stacking order of the layers, not only the thermoelectric properties [222, 223], but also the topological phase transition phenomenon [224] and transport properties are expected to be affected. Therefore, understanding the relationship

between structural transformations, topology and transport phenomenon is crucial for the development of next-generation electronic and spintronic devices.

Moreover, $Sn_xBi_yTe_z$ alloys are also well-known for the phase change characteristics (PCM). According to the crystallography, these alloys undergo a structural transformation from trigonal structure (Bi_2Te_3) to cubic structure (SnTe) with the addition of SnTe.

In recent years, the growth of $Sn_xBi_yTe_z$ alloys has been performed as bulk crystals [225–227] by heat treatment method [227] and Bridgman's method [226], and as thin films [220, 221, 228] by chemical syntheses [221], CVD [228], and MBE [220]. However, large-scale high-quality thin film growth with different stoichiometries in the series has not yet been achieved. Furthermore, the most of reported topological characterizations are based on the DFT calculations [227, 229, 230]. Systematic ARPES experiments and transport measurements for high quality grown thin films are still at large.

In this chapter, the epitaxial growth of three distinct stoichiometries i.e. $SnBi_4Te_7$, $SnBi_2Te_4$, $Sn_2Bi_2Te_5$ is conducted on Si(111) substrates via MBE, where high crystal quality thin film growth is achieved for each composition. Transformations between different stoichiometries are systematically investigated in this study. For structural characterization, XRD technique provides a comprehensive understanding of the crystal quality of the grown thin films and helps to determine the corresponding stoichiometry. STEM analysis conveys detailed information about the crystallinity and atomic arrangements of the stacking order in the thin films.

Besides, magneto-transport measurements have been performed on the $SnBi_4Te_7$ thin films with different thicknesses, indicating the presence of weak anti-localization in the material.

6.1 Introduction

6.1.1 $(SnTe)_m(Bi_2Te_3)_n$ nomenclature and layer architecture

The stoichiometric state $Sn_xBi_yTe_z = (SnTe)_m(Bi_2Te_3)_n$ can be simplified as SnBT-xyz. The values of (x,y,z) represent the atomic content, while the values of (m,n) are the relative distributions of SnTe and Bi_2Te_3 in a unit cell. The relation between the layer size and unit cell can be determined by evaluating whether (x+y+z) or (m+n) is a multiple of 3.

Key members of SnBT stoichiometric series along with their layer stacks in a unit cell are depicted in Fig. 6.1.

6.1.2 Epitaxy and structural characterization

An overview of the MBE-growth of $Sn_xBi_yTe_z$ stoichiometric alloy is listed in table 6.1, where m and n indicate the total number of SnTe and Bi_2Te_3 in a unit cell respectively. The increasing number of SnTe in a unit cell raises the relative content of Sn in the alloy. The out-of-plane lattice constant "$c_{predicted}$" is calculated using the equation 6.1. $c^{'}$ and

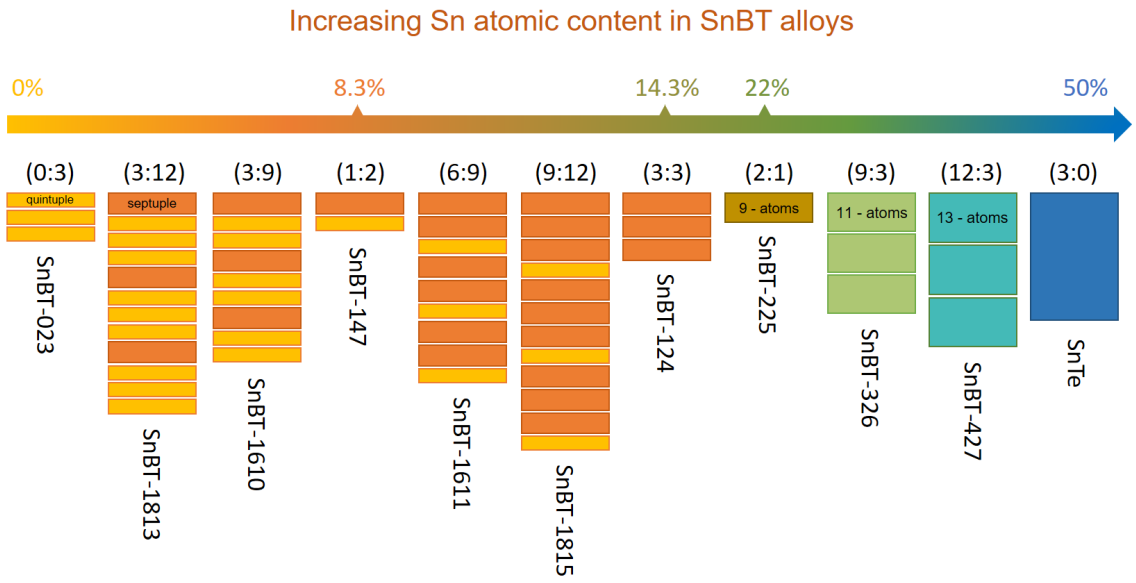

Figure 6.1: An overview of the unit cells of SnBT = $(SnTe)_m(Bi_2Te_3)_n$, showing the main stoichiometric series together with their stacking sequences. Different colors of various blocks represent different layer structures. With the increase of the atomic fraction of Sn, yellow, orange, brown, green and indigo represent the quintuple layer (QL), septuple layer (SL), 9-atomic, 11-atomic and 13-atomic layer stacking respectively, while the blue means the non-stacked structure of SnTe.

c'' are the unit length of Bi_2Te_3 = 30.48 Å, and SnTe(111) = 10.95 Å [1] respectively.

$$c_{predicted} = \frac{1}{3}(mc' + nc'') \tag{6.1}$$

Besides, all alloys are investigated by STEM, and the lattice constant parameters together with the stacking sequence are obtained from the STEM investigation.

Here, it is important to note that a unit cell of $SnBi_2Te_4$ consists of three SLs. The reason behind it is that the trigonal lattice should possess a periodic arrangement of atoms (ABC-ABC stacking) in one unit cell. For $SnBi_2Te_4$, each SL serves as a characteristic unit containing 7 (x+y+z = 1+2+4 =7) atomic layers. This structure does not allow the ABC-ABC stacking, since 7 is not a multiple of 3. Therefore, a SL should repeat itself 3 times with 21 atomic layers to ensure the periodicity of the stacking order for a unit cell. Similarly, as presented in Chapter 5, the unit cell of Bi_{TRIG} consists of 3 bilayers containing 6 atoms, as shown in Fig. 5.1(b)-(c). However, $SnBi_4Te_7$ and $Sn_2Bi_2Te_5$ do not suffer from this issue, since (x+y+z) = (1+4+7) = 12/(x+y+z) = (2+2+5) = 9 are multiple of 3, the two stoichiometric states consist of periodic stackings of (QL+SL)/9-atomic layers with individual layers that act as a unit cell.

[1] The original crystal structure of SnTe is cubic with the lattice constant 6.32 Å. However, when grown on the hexagonal Si(111) substrate surface, SnTe tends to orient itself along the (111) facet. Therefore, the oriented crystal structure is hexagonal with the lattice constant $\sqrt{3} \times 6.32$ = 10.95 Å.

Table 6.1: An overview of SnBT stoichiometric alloys prepared via MBE. For each state the relative contents of individual elements i.e. Sn, Bi and Te, the number of individual layers of SnTe and Bi_2Te_3 in a unit cell, the out-of-plane predicted ($c_{predicted}$) and measured (c_{actual}) lattice constant together with the in-plane (a_{actual}) lattice constants from XRD are listed.

$Sn_xBi_yTe_z$	m	n	comments	Sn (%)	Bi (%)	Te (%)	$c_{predicted}$ (Å)	c_{actual} (Å)	a_{actual} (Å)
Bi_2Te_3	0	3	Reference	0	40	60	30.47	30.46	4.38
$SnBi_4Te_7$	1	2	QL-SL stacks	8.33	33.33	58.33	23.96	24.01	4.40
$SnBi_2Te_4$	3	3	Mutiple of 3	14.29	28.57	57.14	41.42	41.48	4.42
$Sn_2Bi_2Te_5$	2	1	9-atom stacks	22.22	22.22	55.56	17.46	17.60	4.4
SnTe	3	0	cubic	50	0	50	10.95	-	-

The corresponding atomic models for $SnBi_4Te_7$, $SnBi_2Te_4$, $Sn_2Bi_2Te_5$ from top view and side view are shown in Fig. 6.2.

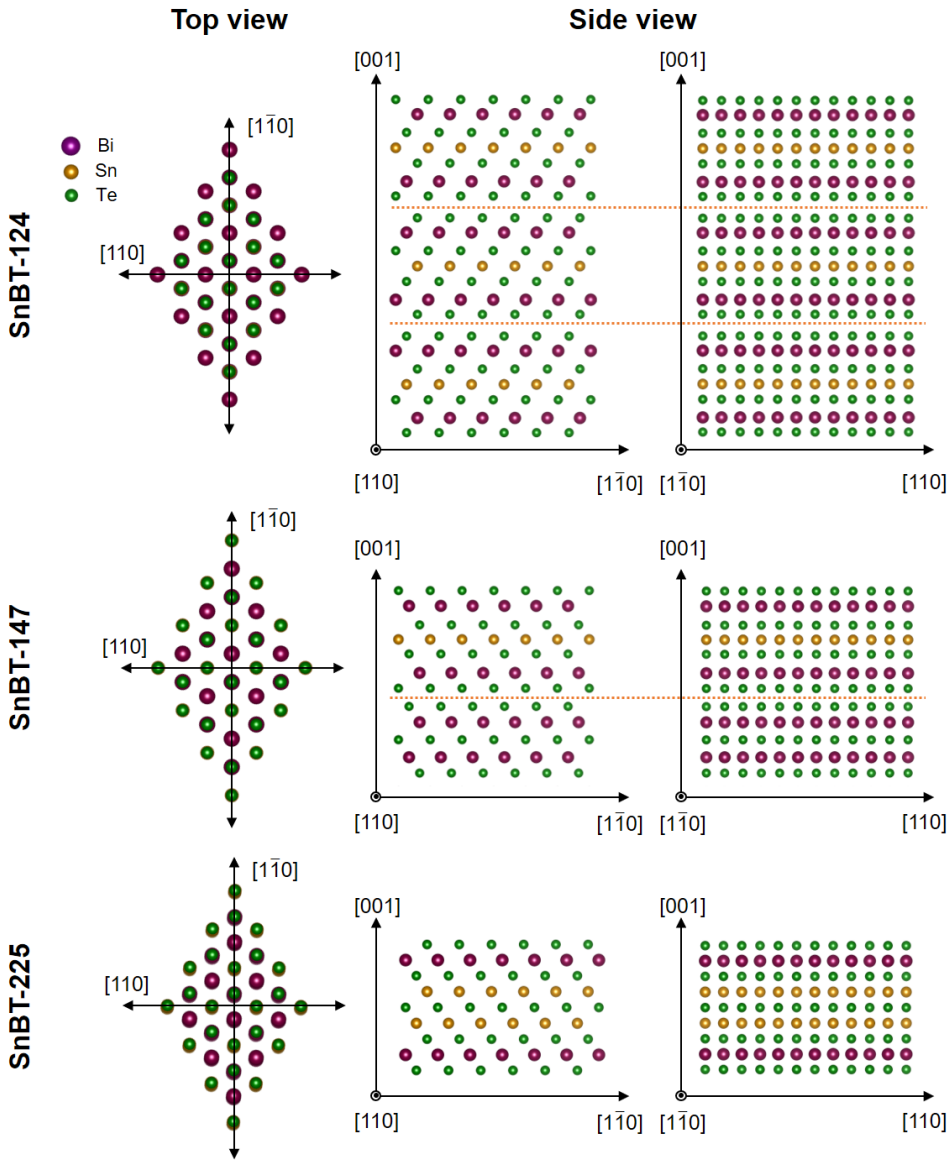

Figure 6.2: Atomic models representing the unit cell of SnBT-124, 147 and 225 from top to bottom, with the layer sequence projected along [110], [1$\bar{1}$0] and [001]. Dark red, yellow and green represent Bi, Sn and Te respectively. SnBT-124 has the unit cell with the building blocks of 3 septuple layers (SL), 147 has the alternative building blocks of a quintuple layer and a septuple layer (QL+SL), where 225 consists of the building block of a 9-atomic layer. Dotted orange lines indicate vdW gaps inside the materials.

6.2 Epitaxial growth of SnBT series

Different from the growth of the single element Bi introduced in Chapter 5, the stoichiometric growth of SnBT ternary alloys requires additional tuning of of the source fluxes, which are determined by the corresponding source temperatures.

6.2.1 Growth parameter exploration of SnBT series

Before starting the growth of SnBT series, it is crucial to optimize the growth conditions for the base material, Bi_2Te_3. According to Jalil's PhD thesis [22], the best quality of the Bi_2Te_3 thin films were achieved using substrate temperature T_{sub} = 300 °C, Bi source temperature T_{Bi} = 482 °C and Te source temperature T_{Te} = 325 °C. In Addition, based on previous investigation of the GST series alloy in [22], the temperature of Te will be maintained at 325 °C, while the Sn/Bi flux ratio and the substrate temperature will be systematically adjusted to engineer the stoichiometry in the SnBT series.

Following the successful growth Bi_2Te_3 thin films, Sn will be added to the film to prepare SnBT-124 alloy first. However, since Sn tends to segregate at high temperature, T_{sub} should be reduced to incorporate the Sn more homogeneously. Therefore, the T_{sub} is lowered to 240 °C and high quality SnBT-124 thin film was obtained at T_{Sn} = 995 °C, T_{Bi} = 482 °C, and T_{Te} = 325 °C. Through the film quality optimization process, the substrate temperature of 240 °C was identified as optimal and was subsequently employed for all further epitaxial growth experiments.

By lowering the T_{Sn} to 970 °C, a high quality SnBT-147 thin film was successfully acquired, whereas increasing the T_{Sn} to 1020 °C led to the high quality SnBT-225 thin film. The other growth parameters for both SnBT-147 and SnBT-225 thin films remained the same as those used for the SnBT-124 epitaxial layer. The Bi/Sn flux ratio was effectively controlled by adjusting the T_{Sn}, enabling the precise stoichiometric tuning of the films.

The corresponding growth parameters are summarized in Table 6.2.

Table 6.2: Growth parameters of Bi_2Te_3,SnBT-147, SnBT-124 and SnBT-225.

Material	T_{sub} (°C)	T_{Bi} (°C)	T_{Te} (°C)	T_{Sn} (°C)
Bi_2Te_3	300	482	325	-
SnBT-147	240	482	325	970
SnBT-124	240	482	325	995
SnBT-225	240	482	325	1020

The structural characterization of the obtained three stoichiometries, i.e. SnBT-124, SnBT-147 and SnBT-225 thin films are introduced in the following sections.

6.2.2 Structural characterization of the SnBT-124 thin film

The stoichiometric state SnBT-124 contains 14.28 % Sn atomic fraction. It has the unit cell of (m:n) = (1:1), where the SnTe block merge with the QL, forming the septuple layer (SL). A complete unit cell exhibits three SLs, consisting of (m:n) = (3:3). SnBT-124 has a rhombohedral (R) crystal structure with the space group 166 (R-3m) and the unit cell length $c_{predicted}$ = 41.65 Å.

The high quality epitaxial film of SnBT-124 was achieved and characterized by XRD. Figure 6.3 displays the XRD $\theta/2\theta$ scan of a 46 nm thick epilayer of SnBT-124 with the

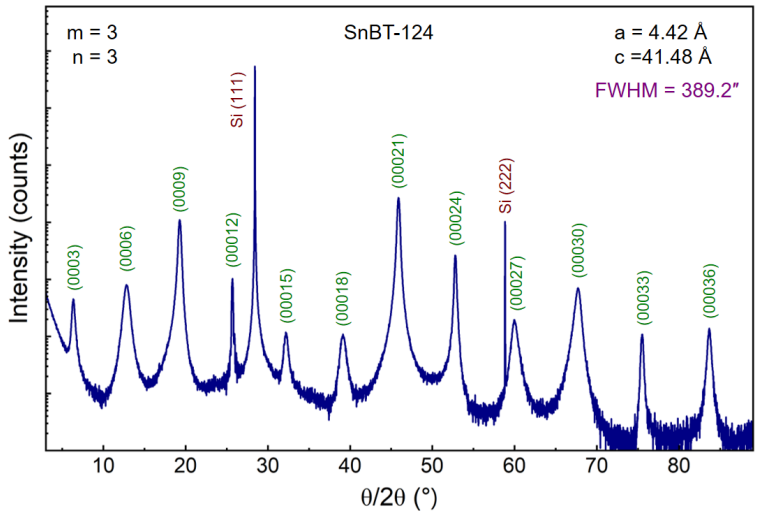

Figure 6.3: XRD $\theta/2\theta$ scan of SnBT-124 epilayer, consisting of (m:n)=(3:3), with the unit cell length c = 41.48 ± 0.01 Å, $\Delta\omega$ scan indicates the FWHM = 389.2 arcseconds, obtained at 2θ = 45.89° at (000 21) peak.

growth rate R_{TF} = 23 nm/h. Based on XRD $\theta/2\theta$ scan, the out-of-plane lattice constant can be evaluated through Bragg diffraction with equation 6.2 (based on the equation 3.1 from the Chapter 3). The relation between the diffraction index (n) and sin(θ_n) is plotted in Fig. 6.4(a), where the θ_n is the angle of incidence corresponding to the particular diffraction index [231]. According to Fig. 6.4(a), the unit cell length $c_{actual(XRD)}$ = 41.55 Å, which is slightly deviated from the $c_{predicted}$ = 41.65 Å.

$$sin\theta = \frac{n\lambda}{2c} \tag{6.2}$$

To obtain the in-plane unit cell parameter, asymmetric RSM is performed at the (1 $\bar{1}$ 0 28) peak, as displayed in Fig. 6.4(b), providing the $c_{actual(RSM)}$ = 41.48 ± 0.05 Å, $a_{actual(RSM)}$ = 4.42 ± 0.02 Å. The values obtained from RSM confirm that the slight derivation between the actual and predicted unit cell length is not an artifact. This discrepancy can be attributed to the high growth rate of the thin film, which may induce defects within the films. The structural quality of epilayer is evaluated via RC ($\Delta\omega$) analysis, which yields the FWHM of 389.2 arcseconds.

To investigate the surface morphology of the grown thin film, AFM measurements were performed on the same SnBT-124 epilayer. Figure 6.5 presents two AFM images at different magnifications, along with two height line profiles corresponding to a relatively large and a small grain on the sample surface in each image. From these measurements, the averaged surface roughness is determined to be less than 3 nm. In addition, line profiles further reveal that the height differences between different islands vary across the sample surface.

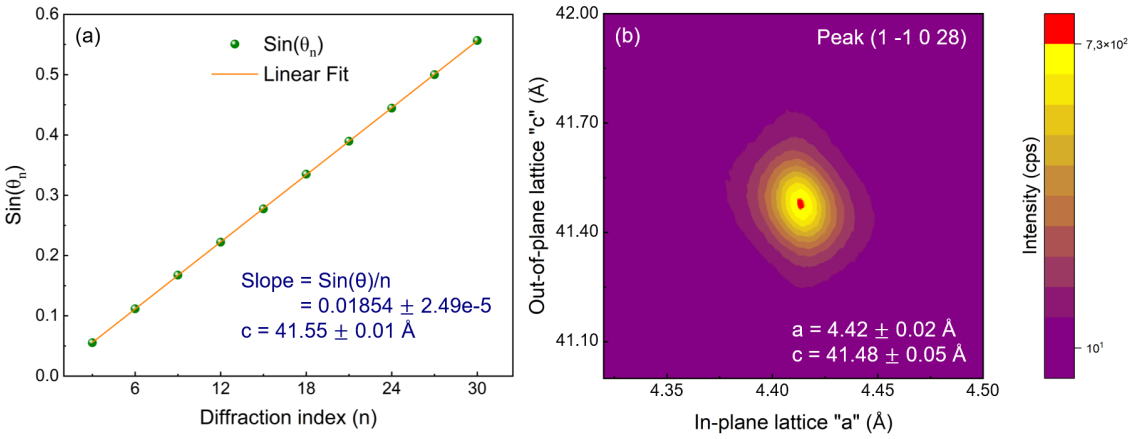

Figure 6.4: Lattice parameters analysis of SnBT-124 via XRD. (a) Evaluation of unit cell length "c" according to Bragg diffraction by XRD $\theta/2\theta$ scan. The plot depicts the relation between diffraction index (n) and incidence angle (θ_n). (b) Asymmetric RSM of SnBT-124 acquired along the (1 $\bar{1}$ 0 28) peak, providing the in-plane and out-of-plane lattice constant. RSM measurement performed by Dr. Abdur Rehman Jalil.

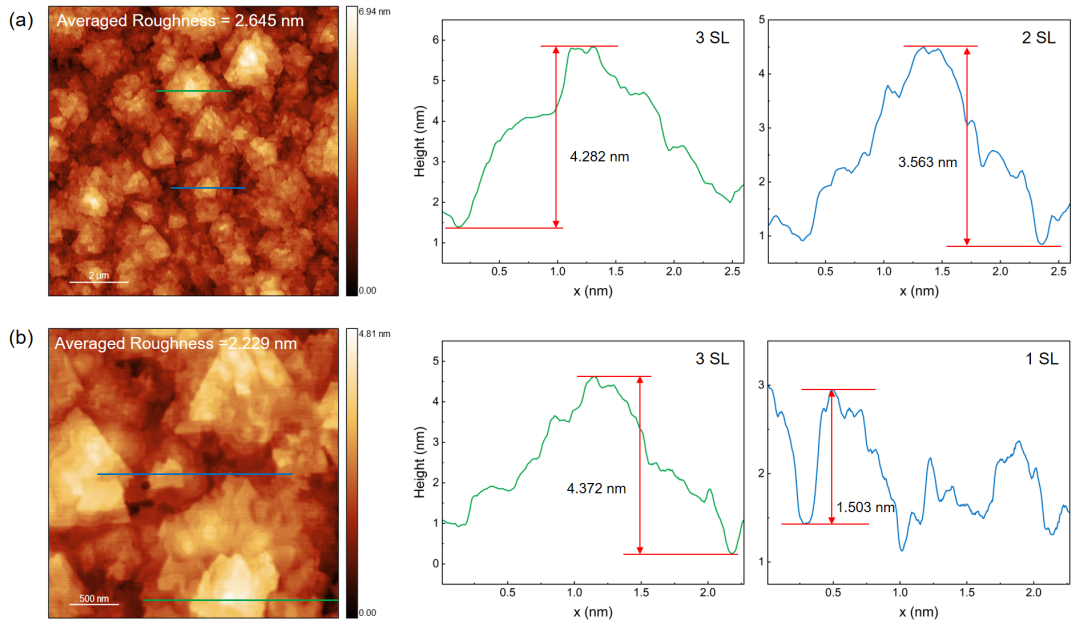

Figure 6.5: AFM images of SnBT-124 sample with low and high magnification. (a) Low magnification image, where the averaged roughness is 2.645 nm. Two line scans of the surface morphology in two positions are demonstrated in (b) and (c) with green and blue respectively. The corresponding height difference is 4.282 nm and 3.563 nm. (d) High magnification image, where the averaged roughness is 2.229 nm. Two line scans of the surface morphology in two positions are demonstrated in (e) and (f) with green and blue respectively. The corresponding height difference is 4.372 nm and 1.814 nm. AFM measurement performed by Dr. Nisha Shahi.

6.2.3 Structural characterization of the SnBT-147 thin film

The stoichiometric state SnBT-147 contains 8.33% Sn atomic fraction. It has the unit cell of (m:n) = (1:2) with the stacking order of QL+SL. Since the Sn content in this component is lower than that of SnBT-124, the Sn flux should be reduced. The transformation process from SnBT-124 to SnBT-147 is demonstrated by XRD scans of each growth, as illustrated in Fig. 6.6(a).

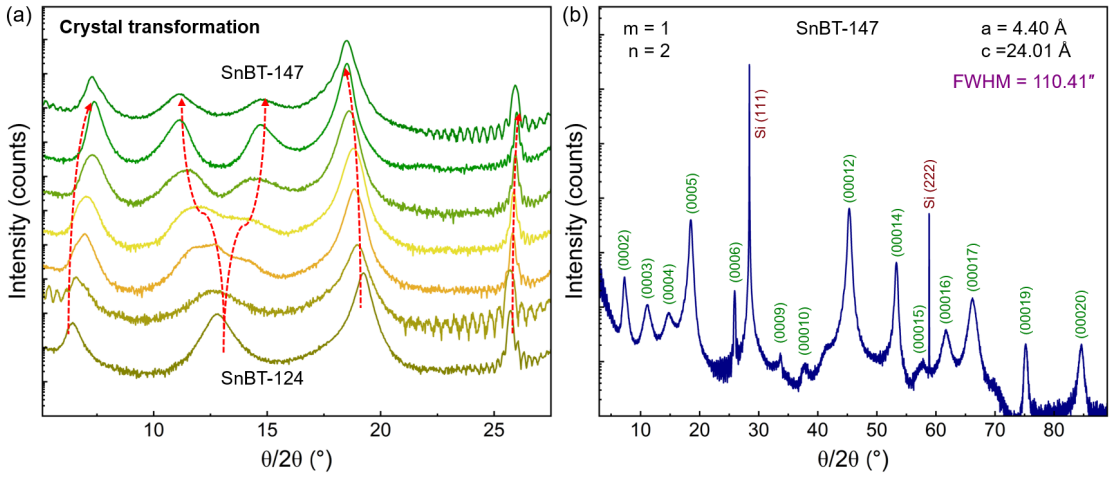

Figure 6.6: Structural transformation from SnBT-124 to SnBT-147. (a) XRD $\theta/2\theta$ scans of the growth transformation from SnBT-124 to SnBT-147 epilayer. The characteristic peak (000 6) at 2θ = 12.83° for SnBT-124 is observed to gradually broaden and then split into two peaks with the increase of Bi content and decrease of Sn content. With the further increase the divided peaks can be observed to move in the opposite directions (better visibility with the red arrows). The two splited peaks are the characteristic peak (000 3) and (000 4) for SnBT-147. (b) XRD $\theta/2\theta$ scan of SnBT-147 epilayer, consisting of (m:n)=(1:2), with the unit cell length c = 24.01 ± 0.01 Å, $\Delta\omega$ scan indicates the FWHM = 110.41 arcseconds, obtained at 2θ = 45.33° at (000 12) peak.

As shown in Fig. 6.6(a), the bottom XRD scan is from pure phase of SnBT-124 epilayer, while the top scan is from pure phase of SnBT-147 epilayer. The XRD scans, displayed from bottom to top, indicate the decreased Sn content in the epilayer. Moreover, the second characteristic peak (000 6) of SnBT-124 is observed to split into two distinct peaks, which subsequently shift in opposite directions. The two divided peaks correspond to the characteristic peaks (000 3) and (000 4) of SnBT-147. Additionally, during the transformation process to SnBT-147, the first peak (000 3) and the fourth peak (000 12) of SnBT-124 are slightly shifted to the right, while the third peak (000 9) moves in the left, as indicated by the red arrows inside figure. With fine tuning of the flux and Sn, a high-quality single-crystal SnBT-147 thin film was successfully obtained, where its XRD characterizations are depicted in Fig. 6.6(b) and Fig. 6.7.

Figure 6.6(b) displays the XRD $\theta/2\theta$ scan of a 27.4 nm thick epilayer of SnBT-147 with the growth rate R_{TF} = 13.7 nm/h. The relation between the diffraction index (n)

and Sin(θ_n) is plotted in Fig. 6.7(a). Using calculation based on Bragg's law, the out-of-plane lattice constant is determined to be $c_{actual(XRD)}$ = 24.03 ± 0.01 Å, which is in close agreement with the $c_{predicted}$ = 23.96 Å. Besides, asymmetric RSM is performed at the (1 $\bar{1}$ 0 16) peak, as shown in Fig. 6.7(b), providing the $c_{actual(RSM)}$ = 24.01 ± 0.01 Å and $a_{actual(RSM)}$ = 4.40 ± 0.01 Å, which affirms the agreement between experimental and theoretical value. The structural quality of epilayer is evaluated via RC ($\Delta\omega$) analysis, which yields the FWHM value of 110.41 arcseconds.

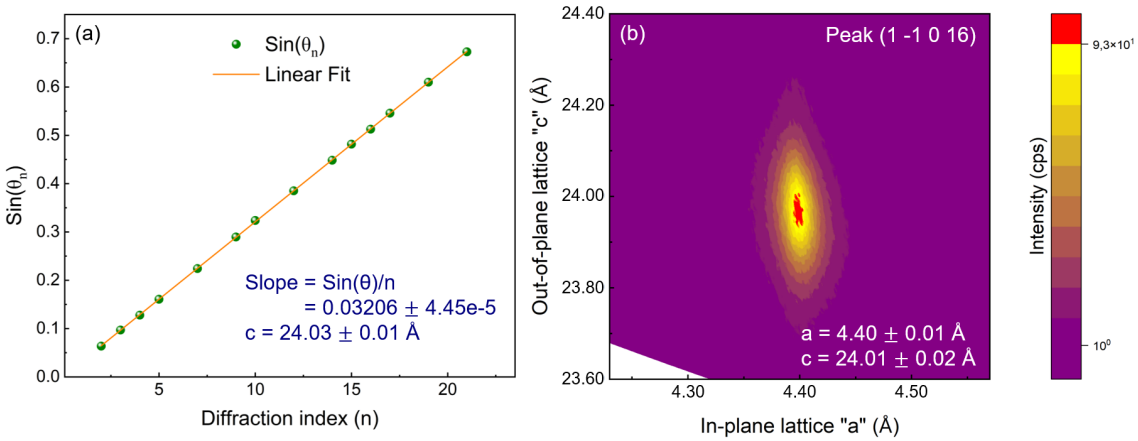

Figure 6.7: Lattice parameters analysis of SnBT-147 via XRD. (a) Evaluation of unit cell length "c" according to Bragg diffraction by XRD $\theta/2\theta$ scan. The plot depicts the relation between diffraction index (n) and incidence angle (θ_n). (b) Asymmetric RSM of SnBT-147 acquired along the (1 $\bar{1}$ 0 16) peak, showing that lattice constants "a" and "c" are in good agreement with theoretical value. RSM measurement performed by Dr. Abdur Rehman Jalil.

AFM measurements were performed on the same SnBT-147 thin film to evaluate its surface quality, with the results presented in Fig. A3.1 in the Appendix. Figure A3.1 depicts two AFM images at different magnifications, along with two height line profiles corresponding to a relatively large and a small grain on the sample surface in each image. From Fig. A3.1, the averaged surface roughness is approximate 3.5 nm. Besides, the line profiles indicate the height difference between the islands, indicating that the surface roughness varies at different grains and positions.

6.2.4 Structural characterization of the SnBT-225 thin film

The stoichiometric state SnBT-225 contains 22.22% Sn atomic fraction. It has the unit cell of (m:n) = (2:1) with the stacking order of 9-atomic layer. Compared with SnBT-124, the Sn content in SnBT-225 alloy is higher. Therefore, the Sn flux should be increased to achieve the desired composition of SnBT-147. The transformation process from SnBT-124 to SnBT-225 is demonstrated by XRD scans of each growth, as illustrated in Fig. 6.8(a).

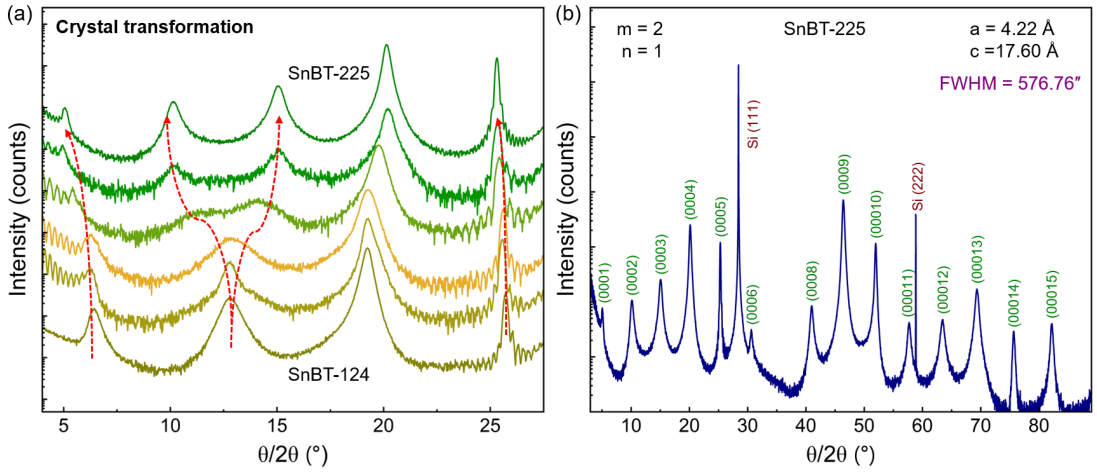

Figure 6.8: Structural transformation from SnBT-124 to SnBT-225. (a) XRD $2\theta - \theta$ scans of the growth transformation form SnBT-124 to SnBT-225 epilayer. The characteristic peak (000 6) for SnBT-124 is gradually broadened and then split into two peaks with the increase of Bi content and decrease of Sn content. With the further trend of Bi and Sn, the divided peaks can be observed to move in the opposite directions (better visibility with the red arrows). The two splited peaks are the characteristic peak (000 2) and (000 3) for SnBT-225. (b) XRD $\theta/2\theta$ scan of SnBT-225 epilayer, consisting of (m:n)=(2:1), with the unit cell length c = 17.6 ± 0.01 Å, $\Delta\omega$ scan indicates the FWHM = 576.76 arcseconds, obtained at 2θ = 46.42° at (000 9) peak.

As shown in Fig. 6.8(a), the bottom XRD scan is from pure phase of SnBT-124 epilayer, while the top scan is from pure phase of SnBT-225 epilayer. The XRD scans from bottom to top indicate the increased content of Sn. During the transformation process, the second peak characteristic peak (000 6) of SnBT-124 is observed to split into two peaks, which then shift in opposite directions. The two divided peaks correspond to the characteristic peaks (000 2) and (000 3) of SnBT-225. Besides, the first peak (000 3) and the fourth peak (000 12) of SnBT-124 are slightly shifted towards left direction, while the third peak (000 9) moves to the right, as indicated by the red arrows within Fig. 6.8(a). With fine tuning of the Sn flux, a high-quality single-crystal SnBT-225 thin film was successfully obtained. The corresponding XRD characterizations are depicted in Fig. 6.8(b) and Fig. 6.7.

Figure 6.8(b) displays the XRD $\theta/2\theta$ scan of a 55.86 nm thick SnBT-147 epilayer with the growth rate R_{TF} = 18.62 nm/h. The relation between the diffraction index (n) and Sin(θ_n) is plotted in Fig. 6.9(a), where the out-of-plane lattice constant $c_{actual(XRD)}$ = 17.60 ± 0.01 Å, which is in close agreement with the $c_{predicted}$ = 17.46 Å. Besides, asymmetric RSM conducted at the ($\bar{1}$ 1 0 12) peak is displayed in 6.9(b), providing the $c_{actual(RSM)}$ = 17.55 ± 0.05 Å and $a_{actual(RSM)}$ = 4.40 ± 0.02 Å, which affirms the agreement between experimental and theoretical value. The structural quality of epilayer is evaluated via RC ($\Delta\omega$) analysis, which yields the FWHM value of 576.76 arcseconds.

AFM measurements were performed on the same SnBT-225 thin film, with the results

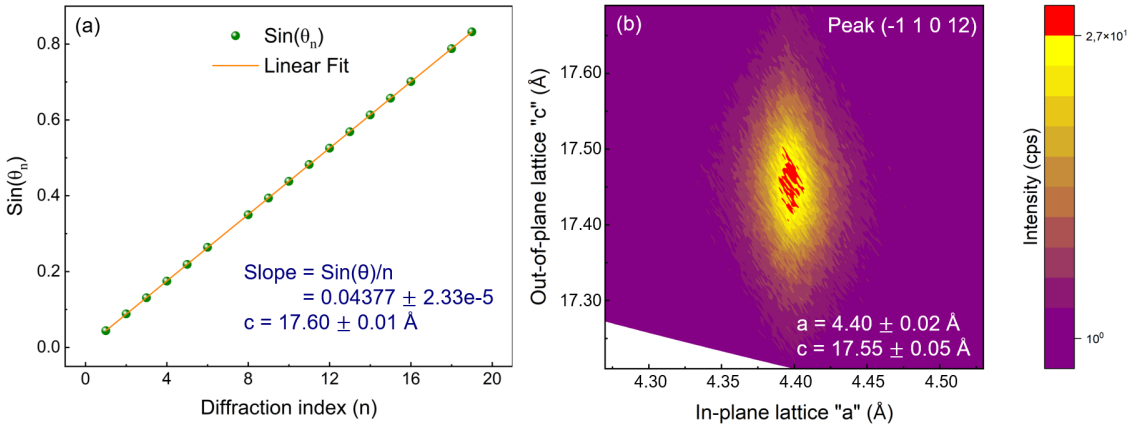

Figure 6.9: Lattice analysis of SnBT-225 via XRD. (a) Evaluation of unit cell length "c" according to Bragg diffraction by XRD $\theta/2\theta$ scan. The plot depicts the relation between diffraction index (n) and incidence angle (θ_n). (b) Asymmetric RSM of SnBT-225 acquired on the ($\bar{1}$ 1 0 12) peak, showing that lattice constants "a" and "c" are in good agreement with theoretical value. RSM measurement performed by Dr. Abdur Rehman Jalil.

presented in Figure A3.2 in the Appendix. Figure A3.2 depicts two AFM images at different magnifications, along with two height line profiles of a relatively large and a small grain on the sample surface in each image. From Fig. A3.2, the averaged surface roughness is approximate 2.5 nm.

6.3 STEM investigation of the SnBT thin films

6.3.1 Crystal Structure Analysis

After obtaining high quality single crystalline thin films of the three stoichiometries, corresponding lamellae are extracted for the following STEM investigation. STEM-HAADF images, acquired along Si[1$\bar{1}$0] and Si[211] projections, of the three alloys are presented in Fig. 6.10, 6.11 and 6.12, respectively.

Figure 6.5 displays the high-resolution HAADF images of the two projections along the Si substrate, indicating the SL stacking order of the SnBT-124 thin film alloy. The bandpass-filtered HAADF images are positioned at the top right of each HAADF image for better visibility of the atoms, where the atomic model of SnBT-124 aligns perfectly with the atomic arrangement in the image. The defect-free scanned area indicates the high growth quality of the obtained SnBT-124 thin film. Similarly, the high-resolution HAADF images from Fig. 6.11 and 6.12 demonstrate the QL+SL alternative stacking order and the 9-atomic layer stacking order, respectively. The corresponding atomic models fit perfectly into the atomic arrangement from the bandpass-filtered HAADF images, revealing the high quality of the SnBT-147 and SnBT-225 thin films.

In addition, Bi_2Te_3 and SnTe thin film specimens (grown by Dr. Abdur Rehman Jalil)

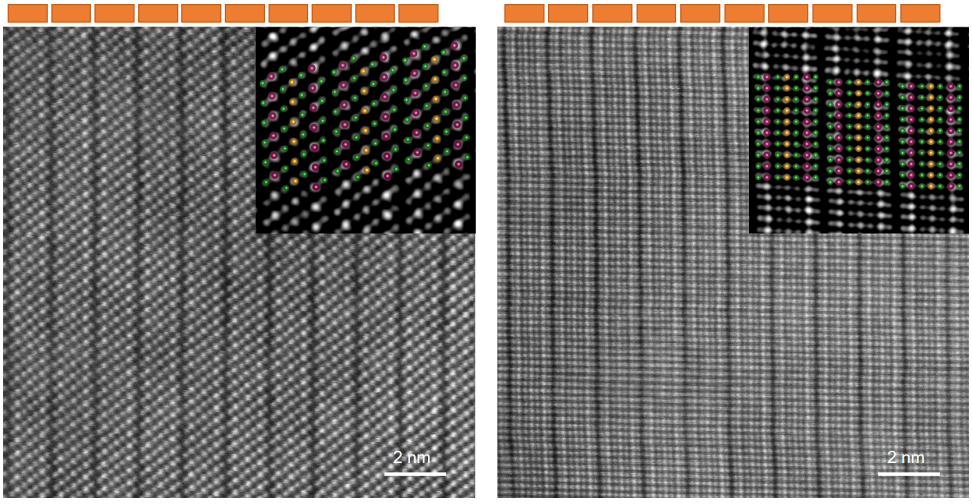

Figure 6.10: STEM-HAADF images acquired along the Si[$1\bar{1}0$] and Si[211] projections in the left and right respectively, representing the unit cells of SnBT-124. The arrangement of the unit cells in both projections in the HAADF images confirms SL stacking order. The bandpass-filtered HAADF images are shown on the top right of both images, where the atomic model of SnBT-124 could fit perfectly into the experimental atoms.

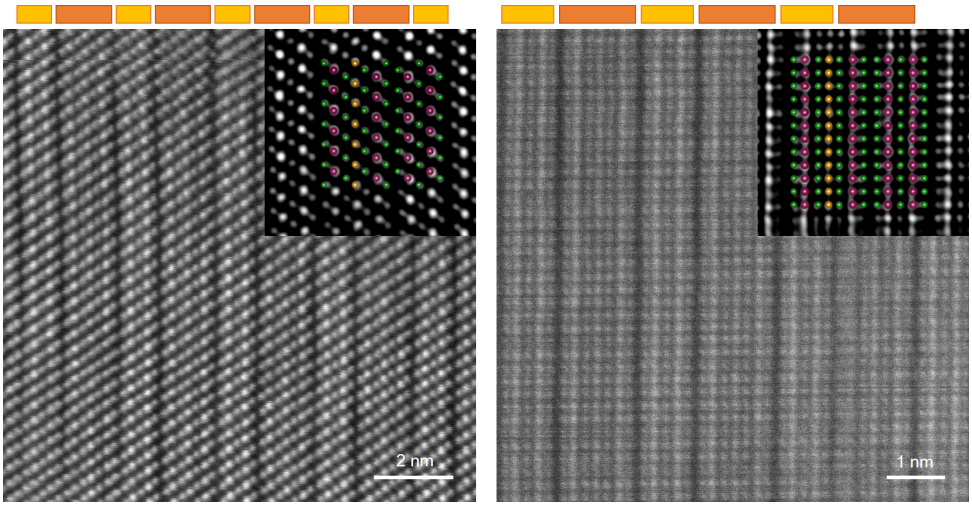

Figure 6.11: STEM-HAADF images acquired along the Si[$1\bar{1}0$] and Si[211] projections in the left and right respectively, representing the unit cells of SnBT-147. The arrangement of the unit cells in both projections in the HAADF images confirms QL+SL alternate stacking order. The bandpass-filtered HAADF images are shown on the top right of both images, where the atomic model of SnBT-147 could fit perfectly into the experimental atoms.

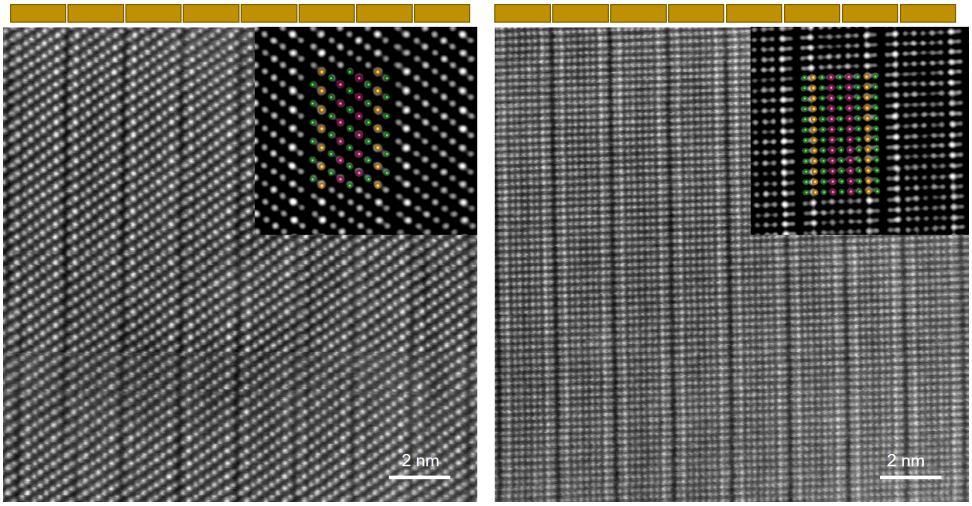

Figure 6.12: STEM-HAADF images acquired along the Si[$1\bar{1}0$] and Si[211] projections in the left and right respectively, representing the unit cells of SnBT-225. The arrangement of the unit cells in both projections in the HAADF images confirms 9-atomic layer stacking order. The bandpass-filtered HAADF images are shown on the top right of both images, where the atomic model of SnBT-225 could fit perfectly into the experimental atoms.

were also included during the STEM investigation. Figure 6.13 displays 5 components in the SnBT series, with the increase of the Sn content from Bi_2Te_3 (Sn = 0) to SnTe (Sn = 50%). The atomic-resolved images indicate that the layer stacking transitions from a trigonal structure (Bi_2Te_3) to a cubic structure (SnTe). It is noted that the crystal structure remains unchanged unless the concentration of Sn is larger than 22.22%, suggesting that the crystal transformation occurs at certain component between SnBT-225 and SnTe. To determine the precise Sn content in the critical transition crystal, further systematic growth experiments and investigations are required.

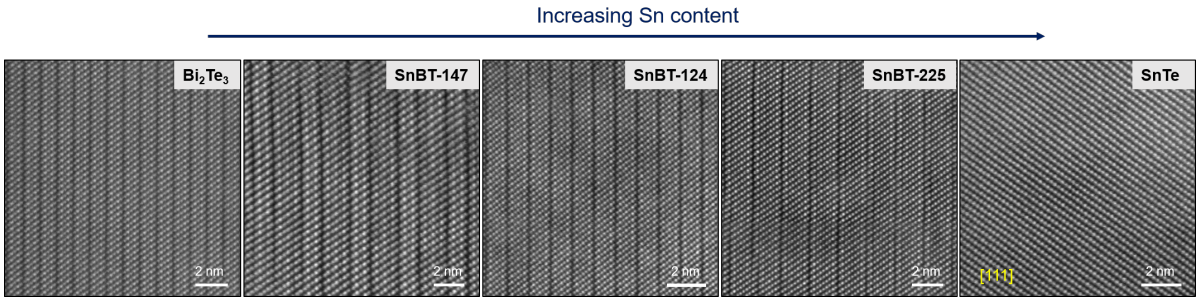

Figure 6.13: STEM-HAADF images of 5 alloys in SnBT series with the increase of the Sn content from left to right, where four of them are trigonal phase and SnTe is the cubic phase.

6.3.2 Bond length Analysis

Similar to Bi_2Te_3, SnBT-124, SnBT-147 and SnBT-225 exhibit vdW gaps between Te-Te atoms with different stacking orders. During the structural characterization of the three

components, the interlayer gap between Te-Te atoms and the projected bond length are measured from the obtained high resolution STEM images in Fig. 6.10, 6.11 and 6.12. The accuracy of the measured data can be confirmed with the evaluation of the angle of atomic arrangement in the crystal by Pythagorean Theorem, which is displayed in Fig. 6.14.

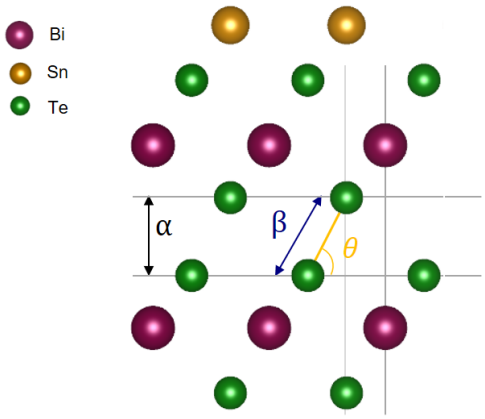

Figure 6.14: Atomic model representing (a) the vdW gap between a QL and SL in SnBT-124 as an example. α is the pristine vdW gap, β represents the projected bond length between neighboring Te atoms on both sides of the vdW gap while θ is the angle of the atomic arrangement based on the horizontal line.

Taken SnBT-124 as an example, the measured interlayer gap between the Te atoms in each SLs (α) = Pristine vdW gap = 2.55 ± 0.02 Å. The measured projected bond length (β) = 2.87 ± 0.02 Å. The angle of the atomic arrangement (θ) = $\mathrm{Sin}^{-1}(\alpha/\beta)$ = 62.68° ± 0.4°.

The overview of measured and calculated projected bond lengths and for the three stoichiometries are listed in Table 6.3.

Table 6.3: An overview of the measured structural parameters via STEM-HAADF line profiles, including the unit cell length (c_{actual}), vdW gaps sizes, the corresponding projected bond lengths and real bond lengths for the stoichiometric states of SnBT-124, SnBT-147 and SnBT-225.

Component	Interlayer stack	c_{actual} (Å)	Interlayer gap (Å)	Projected bond length (Å)	θ (°)
SnBT-124	SL	41.22 ± 0.02	2.55 ± 0.02	2.87 ± 0.02	62.68 ± 0.4
SnBT-147	QL+SL	23.62 ± 0.02	2.56 ± 0.02	2.91 ± 0.02	61.61 ± 0.4
SnBT-225	9-atomic layer	17.34 ± 0.02	2.51 ± 0.02	2.85 ± 0.02	61.73 ± 0.4

From Table 6.3, the interlayer gap, the projected bond length and the θ angle of the three stoichiometries are virtually identical, suggesting the closeness of the actual bond lengths among the three compounds.

Additionally, the measured out-of-plane lattice constants c_{actual} from STEM images of the three thin films align well with the predicted values presented in Table 6.1.

6.4 Transport Measurement

After achieving the high quality thin film of the SnBT series, magneto-transport studies were performed to characterize the electronic properties of the grown epilayer. Due to the time limitation, Hall measurements were only conducted on SnBT-147 thin films with different thicknesses.

6.4.1 Hall Effect

Hall effect originates from the deflection of the charge carriers driven by the Lorentz force when exposed to a magnetic field **B**, resulting in the Hall voltage. The generated Hall voltage is transverse to the electric current and the applied magnetic field perpendicular to the current [232]. Hall measurement is conducted to investigate the electronic characteristics of topological materials. Detailed experimental setup is displayed in Fig. 6.15 and theoretical background will be discussed in this section.

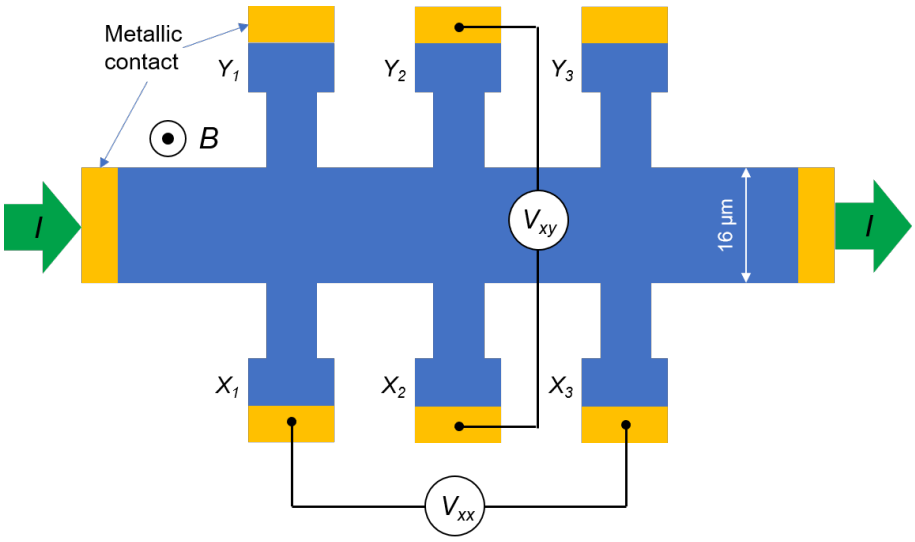

Figure 6.15: Schematic illustration of a 16 μm wide Hallbar with metallic contact as an example. X_1 and X_3 are the input longitudinal terminals with V_{xx} applied between the contacts. Hall voltage (V_{xy}/V_H) is measured between terminals X_2 and Y_2.

MBE-grown SnBT-147 alloy with different thicknesses were fabricated into Hall-bars with the width (W) of 16 μm. The lithography process and the corresponding transport measurements were conducted by Jonas Buchhorn from PGI-9. The summary of the performed measurements and the analysis with 10.6 nm-thick SnBT-147 are discussed below:

- The longitudinal resistance R_{xx} is measured between terminal X_1 and X_2, as displayed in Fig. 6.15. Figure 6.16(a) presents the temperature dependent magnetoresistance, measured at temperatures ranging from 1.25 K to 30 K. Figure 6.16(b) displays same measurement under lower magnetic fields of ± 1 T, indicating the weak anti-localization (WAL) effect. WAL is a quantum mechanical phenomenon,

which has already been observed in topological insulator samples [233–236]. This phenomenon arises from the interference of electron wave functions due to coherent backscattering, which enhances the electrical conductivity. It can be observed in the systems with strong spin-orbit coupling (SOC) through magnetoresistance measurements [237].

- The transverse voltage V_{xy} is measured between terminal X_2 and Y_2 according to Fig. 6.15, while the Hall resistance ($R_{xy} = R_H$) is plotted in Fig. 6.16(c). With equation 6.3 and 6.4, the the Hall constant (A_H) and the 2D charge carrier density (η_{2D}) are extracted, which is demonstrated in Fig. 6.16(d). The 3D carrier concentration (η_{3D}) can be calculated using equation 6.5. In addition, the phase coherence length (l_ϕ) and the mobility (μ), evaluated using equation 6.6 and 6.7 are depicted in Fig. 6.16(e)-(f).

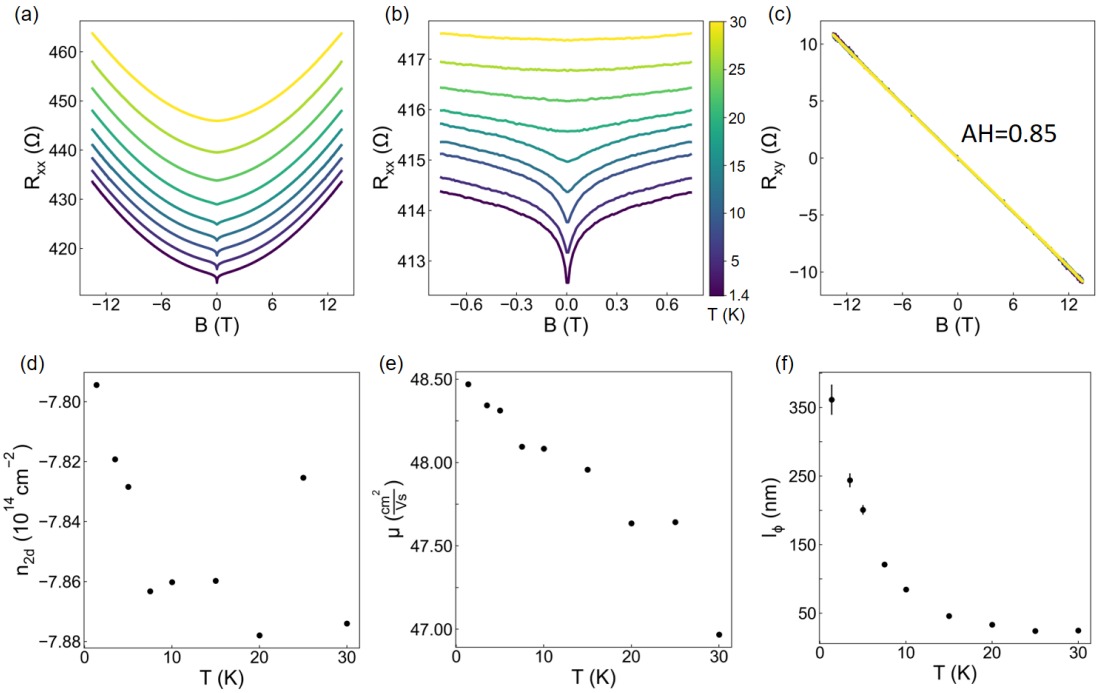

Figure 6.16: Hall measurements of SnBT-147 at constant voltage with varying the temperature. (a) Temperature dependent trend in longitudinal resistance (R_{xx}) vs. applied magnetic field (B). (b) Temperature dependent trend of weak anti-localization in R_{xx} at lower magnetic fields. (c) Hall resistance R_{xy} versus applied field. (d) 2D carrier concentration (η_{2D}); (e) mobility (μ); (f) phase coherence length (l_ϕ). Data and images provided by Jonas Buchhorn.

$$R_H = R_{xy} = \frac{V_H}{I_{xx}} = A_H \frac{B_z}{d}, \tag{6.3}$$

$$A_H = \frac{1}{\eta_{2D}}, \tag{6.4}$$

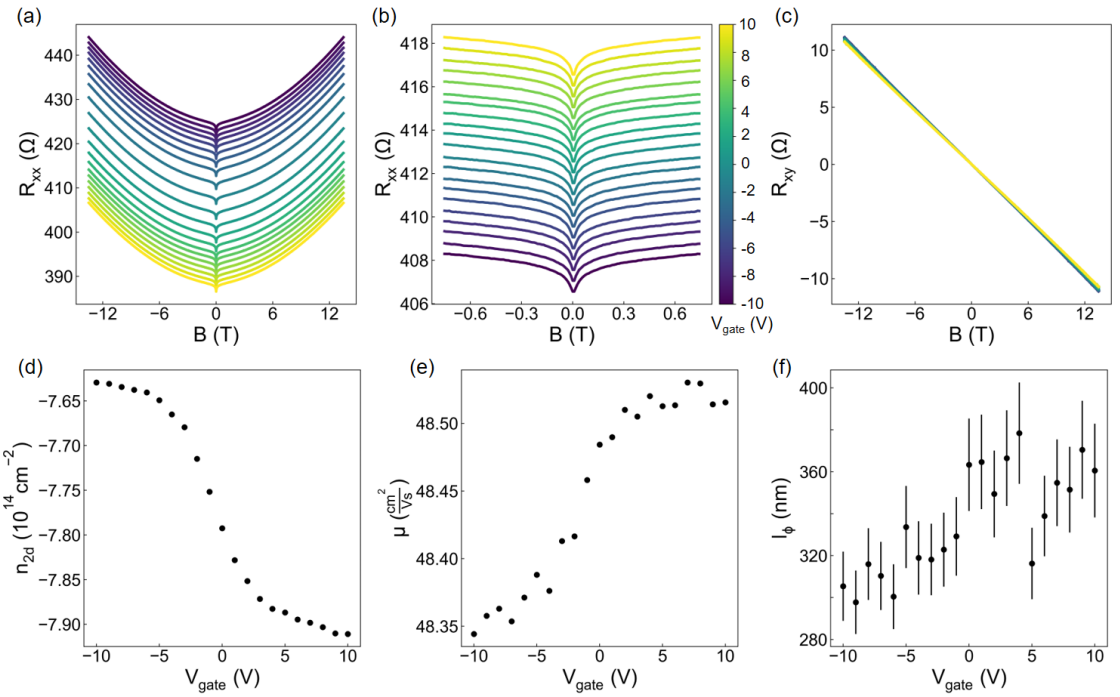

Figure 6.17: Hall measurements of SnBT-147 at constant temperature with varying the gate voltage. (a) Voltage dependent trend in longitudinal resistance (R_{xx}) vs. applied magnetic field (B). (b) Voltage dependent trend of weak anti-localization in R_{xx} at lower magnetic fields. (c) Hall resistance R_{xy} versus applied field. (d) 2D carrier concentration; (e) mobility; (f) phase coherence length. Data and images provided by Jonas Buchhorn.

R_H and V_H are the Hall resistance and Hall voltage, respectively. I_{xx} is the longitudinal current, B_z is the applied out-of-plane magnetic field, d is the thickness of the sample. A_H is the Hall constant, q is the universal charge.

$$\eta_{3D} = \frac{\eta_{2D}}{d}, \tag{6.5}$$

η_{2D} and η_{3D} are the 2D and 3D charge carrier density, respectively; d is the thickness of the thin film.

$$R_{sheet} = R_{xx}\frac{W}{L}, \tag{6.6}$$

W and L are the width and length of the Hallbar, respectively.

$$\mu = \frac{A_H}{R_{sheet}}. \tag{6.7}$$

In addition to the temperature-dependent magnetoresistance measurement, similar measurements with varying the gate voltage from -10 V to 10 V (in steps of 1 V) under 1.25

K of the same sample are displayed in Fig. 6.17(a)-(f). Furthermore, an additional sample of the same thickness and another sample with a thickness of 31.9 nm were investigated following the aforementioned process. The corresponding results from each sample are summarized in Table 6.4 and 6.5.

Table 6.4: The summary of the parameters extracted from Hall measurements with varying temperature of SnBT-147 thin films in different thicknesses. MR represents the percentage change in the magnetoresistance in R_{xx} between B = 0 T and B = 10 T.

Sample ID	Carrier	Thickness (nm)	η_{2D} $\times 10^{13} cm^{-2}$	η_{3D} $\times 10^{19} cm^{-3}$	l_ϕ (nm)	μ (cm^2/Vs)	MR @ 10T (%)	Comments
1	p-type	31.9	7.08	2.2	250	45.5	2.5	in-situ capped
2		10.6	3.3	3.1	71	69	9.5	
3		10.6	7.79	7.35	350	48.5	3.4	

Table 6.5: The summary of the parameters extracted from Hall measurements with varying gate voltage of SnBT-147 thin films in different thicknesses. MR represents the percentage change in the magnetoresistance in R_{xx} between B = 0 T and B = 10 T.

Sample ID	Carrier	Thickness (nm)	η_{2D} $\times 10^{13} cm^{-2}$	η_{3D} $\times 10^{19} cm^{-3}$	l_ϕ (nm)	μ (cm^2/Vs)	MR @ 10T (%)	Comments
1	p-type	31.9	6.8	2.1	285	45.2	3	in-situ capped
2		10.6	3.3	3.1	96	62	6.7	
3		10.6	7.6	7.2	380	48.5	3.1	

The measurements of SnBT-147 thin films indicate the p-type feature of this material system regardless of the thickness. It is observed that the properties of sample 2 and 3 differs significantly, although they were grown under identical parameters. The difference can be associated to the slight variation in the positioning on the growth holder, the cleanliness of the substrate (which might have potential contamination), and the overall defect density in the films.

Moreover, despite the high crystal quality of the thin films achieved via MBE, high carrier concentrations in Hall-bars are observed. The lowest carrier density is witnessed in the 31.9 nm thick film with approx. 2.1×10^{19} cm^{-3}, while the optimal range lies between 10^{17} - 10^{18} cm^{-3} [22]. The overall high carrier concentration can be attributed to the existing defects in the thin films. Figure 6.18 displays the common type of defects, including stacking fault, grain boundaries, translational shear fault and screw dislocations, which have already been discussed in detail in Chapter 4.

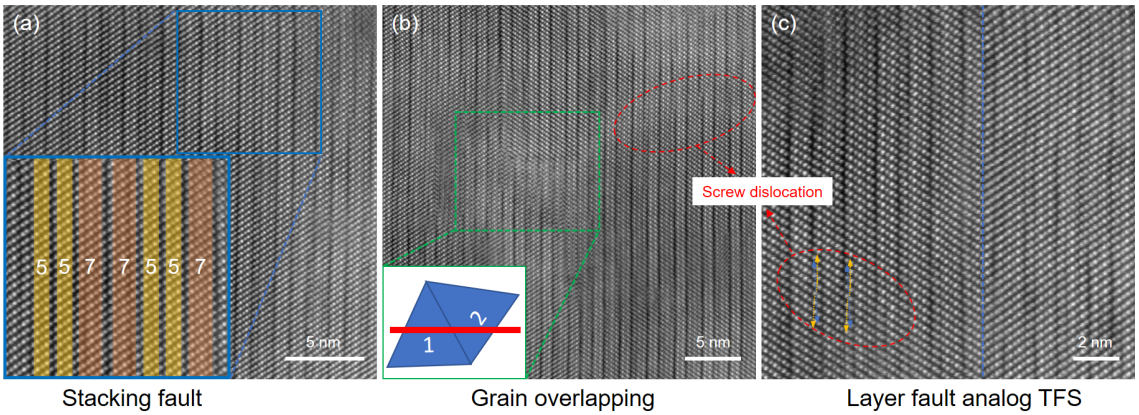

Figure 6.18: STEM-HAADF images indicating different types of defects found in the SnBT-147 thin film. (a) The stacking fault where the sequence follows QQLLQQL rather than the typical alternating Q+L layer structure. (b) Two overlapping grains, as illustrated in the diagram at the bottom left. (c) A layer fault analogous to translational shear fault (TFS) in the thin film. Additionally, screw dislocations are present in both (b) and (c).

6.5 Summary

In this chapter, the systematic single-crystal growth of SnBT-124, SnBT-147 and SnBT-225 thin films has been performed. Detailed XRD investigations indicate the high quality of the grown films and the measured lattice parameters are in good agreement with the predicted values.

During the growth investigations, the transformation process from SnBT-124 to SnBT-147 and SnBT-225 alloys has been demonstrated by the XRD $\theta/2\theta$ scans, where the characteristic peak (000 6) for SnBT-124 is split into either the two characteristic peaks (000 3) and (000 4) towards SnBT-147 alloy or the two characteristic peaks (000 2) and (000 3) towards SnBT-225 alloy. Besides, the first, third and fourth peaks of the SnBT-124 alloy in the XRD pattern are slightly shifted in the opposite directions during the transformation processes to the SnBT-147 and SnBT-225 alloys.

High resolution STEM-HAADF images display the defect-free atomic arrangements of the three components, confirming high quality growth and the correct stacking order of SL, QL+SL and 9-atomic layers in each alloy respectively. Additionally, by adding Bi_2Te_3 and SnTe to the SnBT series, the evolution of the stacking order within this series is clearly depicted by the STEM images. A crystalline transformation from the trigonal to the cubic structure is observed when the Sn content exceeds 22.22%, suggesting that the transformation may occur between SnBT-225 and SnTe. However, the precise point at which the crystal structure changes remains unrevealed.

In addition, SnBT-147 thin films with two different thicknesses were fabricated into Hall bars for further magnetoresistance investigation. The transport measurements of SnBT-147 indicates a p-type feature for these materials regardless of the thickness, with the WAL effect observed at low magnetic fields. The high carrier concentration might be due to the high defect density in the films, as indicated by the STEM images. Due to

the time limitation, the transport investigation for the other components is left for future exploration. Moreover, a deeper understanding of the correlation between the crystal structure and electronic band structure in the SnBT series require further studies with the angle-resolved photoemission spectroscopy.

7 ARPES investigation of Topological Insulator

Commentary: *This chapter presents the circular dichroism angle-resolved photoemission spectroscopy (CD-ARPES) measurements of $MnBi_6Te_{10}$ and ARPES measurements of (V-alloyed) $(Bi,Sb)_2Te_3$ (BST) thin films. The ARPES measurements on both the pristine and V-alloyed BST thin films were conducted by the author with the assistance of Mohammed Qahosh. The BST thin film was provided by Dr. Abdur Rehman Jalil, while the V-alloyed BST thin film was supplied by Dr. Steffen Schreyeck from the University of Würzburg.*

A portion of the CD-ARPES measurements was carried out at the NanoESCA beamline in Italy by members of Dr. Lukasz Plucinski's group, as the author was not present during that period. Additional CD-ARPES measurements were performed by Dr. Plucinski at PGI-6. The theoretical interpretation of the CD-ARPES results was subsequently developed by Dr. Plucinski through dedicated calculations. All figures were prepared and the data were analyzed by the author, with guidance and support from Dr. Plucinski's group, utilizing software tools developed in-house.

Circular dichroism (CD) is a phenomenon where the material system exhibits different responses against opposite helicities of the photons. Therefore, CD has been employed to study magnetic materials or those with strong spin-orbit coupling [238–240]. When CD is combined with angle-resolved photoemission spectroscopy (ARPES), the information is further enriched by investigating the CD in the angular distribution (CDAD) of the photoelectrons in the mapped band structure of the material [241–244]. More recently, this method has been used to study topological insulators with strong orbit coupling, i.e. Bi_2Te_3 [245, 246], Bi_2Se_3 [247, 248], and large CD has been observed from their helical Dirac states. However, the underlying physics for the observed CD is still under debate.

Nowadays, scientists relate the CD-ARPES signal to the orbital angular momentum (OAM) in the band structure, which is locked to the electron momentum in the opposite direction to the spin, experimentally [248–252] and with the first-principles calculation [248, 252, 253].

In this study, we will investigate one of the Bi_2Te_3 terminated terraces from the bulk $MnBi_6Te_{10}$ single crystal with CD-ARPES, trying to clarify the origin of the dichroic signal. High-resolution CD-ARPES measurements with circular polarized light on single-crystals of $MnBi_6Te_{10}$ were performed using a laser-based ARPES system ($h\nu$ = 6 eV) at at the Peter Grünberg Institute (PGI-6) in Jülich, equipped with MBS A-1 hemispherical energy analyzer with a deflector lens. Terrace-dependent CD-ARPES experiments were conducted at NanoESCA beamline with the μ-beam system.

Besides, the electronic band structure of the MBE-grown BST thin film (provided by Dr. Abdur Rehman Jalil from PGI-9, Forschungszentrum Jülich) and the V-alloyed BST thin film with Te capping (provided by Dr. Steffen Schreyeck from Würzburg university) have been successfully characterized with the ARPES system at PGI-6.

It is important to mention that three methods (introduced in Chapter 3) are implemented to preserve clean surfaces of corresponding bulk or thin film topological insulators to perform ARPES measurements.

- **Tape cleavage:** the bulk $MnBi_6Te_{10}$ sample is in-situ cleaved with scotch tape for the CD-AREPS measurement.
- **Vacuum transfer:** the MBE-grown BST thin film is vacuum transferred via the vacuum suitcase, ensuring an atomically clean surface. Therefore, the electronic band structure BST thin film is successfully captured by ARPES, where the Fermi level is tuned to the Dirac point by varying the composition of the doping material, facilitating potential applications in quantum computing and spintronics.
- **Post cleavage:** a post is attached to the Te-capped V-alloyed BST thin film surface with glue and then knocked off in-situ by the applied force. This process effectively removes the Te capping layer with the glue at the same time, enabling the ARPES measurement on this sample.

7.1 Circular Dichroism ARPES measurement of $MnBi_6Te_{10}$

Similar to $SnBi_6Te_{10}$ (SnBT-1610) shown in Fig. 6.1, the bulk $MnBi_6Te_{10}$ sample has the layer sequence of 1 SL ($MnBi_2Te_4$) + 2 QLs (Bi_2Te_3) with a unit cell comprising three of these sequences. Typically, when various types of layer stacking are present in materials, the cleavage will produce atomically flat terraces with different terminations. In the case of $MnBi_6Te_{10}$, two distinct quintuple layer Bi_2Te_3 terminations and one septuple layer $MnBi_2Te_4$ termination are expected to appear after the cleavage.

Since surface states are localized at the last few atomic lattice sites, understanding the different types of surface terminations in $MnBi_6Te_{10}$ crystal is of crucial importance. To visualize and distinguish these terminations, work function mapping and X-ray photoelectron spectroscopy (XPS) have been performed within the photoemission electron microscopy at NanoESCA beamline with E_{kin} = 40 eV to characterize the generated terraces after cleavage.

7.1.1 Material Characterization of $MnBi_6Te_{10}$

Here, the bulk $MnBi_6Te_{10}$ has been in-situ cleaved using the scotch tape at the beamline. Three types of termination should exist after the cleavage, as illustrated in Fig. 7.1(a). The results of the work function mapping and XPS measurement of the generated terraces are summarized in Fig. 7.1.

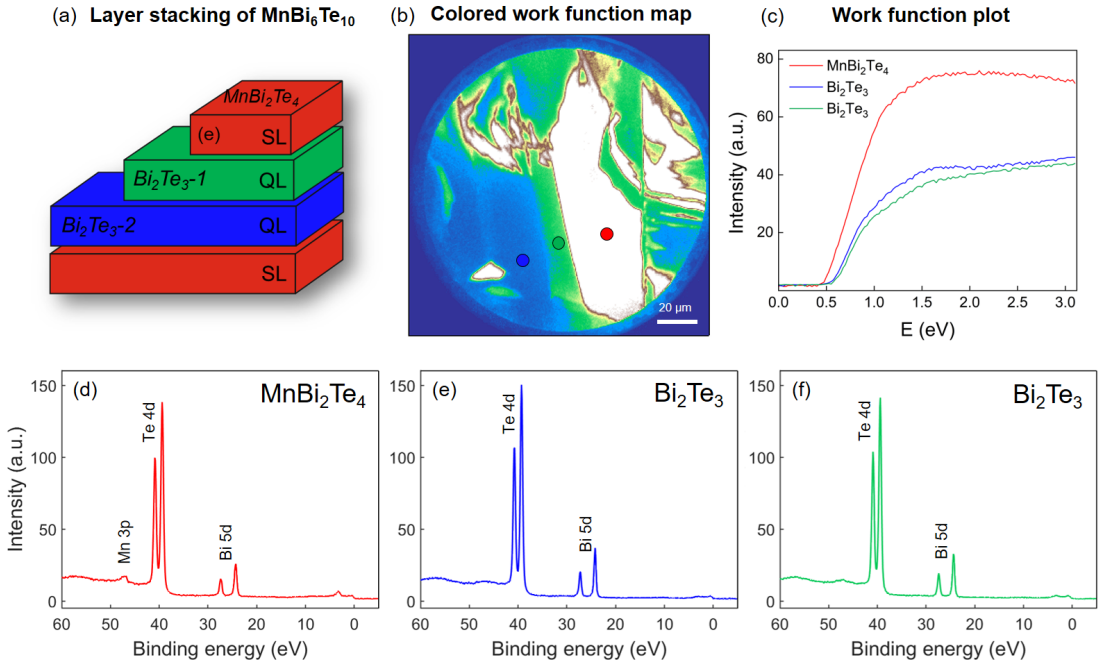

Figure 7.1: Terrace study of $MnBi_6Te_{10}$ with work function and XPS measurement. (a) Illustration of the three possible terminations in $MnBi_6Te_{10}$. (b) Colored work function mapping of the cleaved bulk $MnBi_6Te_{10}$ crystal, with different regions in three contrasts, indicating the presence of the three types of termination presented in (a). (c) Work function plots acquired from the three-colored regions in (b). As indicated from the three-colored circles in (b), the red plot is extracted from the white region, blue and green curves are from the same colored regions in (b) respectively. (d)-(f) XPS spectra acquired at the three-colored regions in (b) respectively. The peak appearing at approx. 47.5 eV in (d) is the characteristic peak of Mn 3p, indicating the presence of Mn in this terrace. Both (e) and (f) depict the XPS spetra of Bi_2Te_3 terraces, though the sequence of the two QLs remains unknown. Data collected at NanoESCA beamline by Dr. Lukasz Plucinski's group, plotted and analyzed by the author.

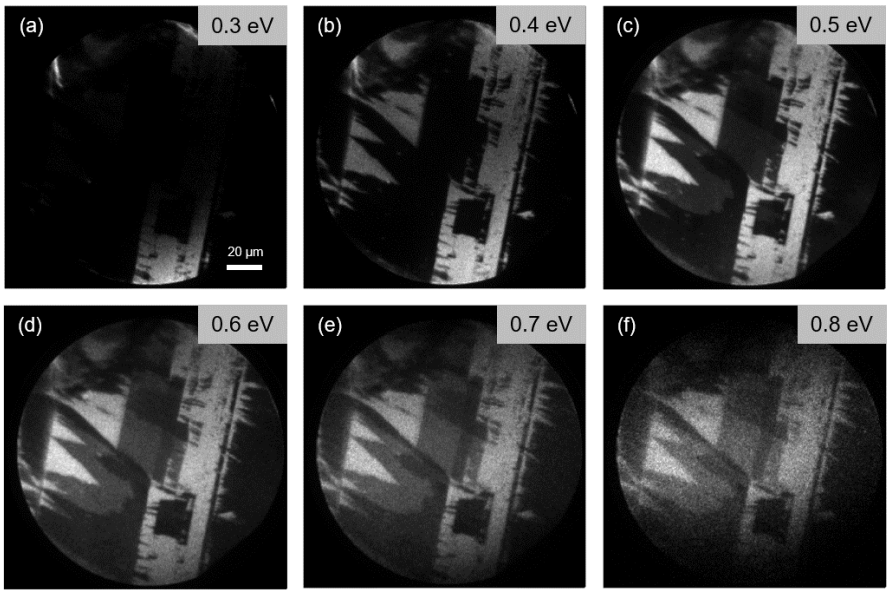

Figure 7.2: The Work function map under a series of binding energies from 0.3 eV to 0.8 eV (in steps of o.1 eV) fom (a) to (f). (c)-(e) indicate that there are clear boundaries between the three contrast (black/dark-gray/white). Data collected at NanoESCA beamline by Dr. Lukasz Plucinski's group, exacted and analyzed by the author.

Figure 7.1(b) shows the false colore work function map of the cleaved $MnBi_6Te_{10}$ crystal, where three regions exhibiting different contrasts are observed. The presence of the three contrast regions indicates the existence of the three possible terminations of $MnBi_6Te_{10}$, as depicted in Fig. 7.1(a). The corresponding work function plots of the three-colored regions shown in (b) indicate that the plots in blue and green are close but with a slight shift in energy, possibly referring to the two types of Bi_2Te_3 terraces, while the more intense is related to the $MnBi_2Te_4$ termination.

To further verify and determine the types of different terraces, XPS is then performed on the three regions. Figure 7.1(d)-(f) depict the XPS spectra of regions in accordance to those in (c). Since the Mn 3p characteristic peak is expected at around 47.2 eV [254], the appearance of the peak in (d) at approx. 47.5 eV indicates the presence of Mn in the white-colored terrace in (b). The doublet at around 40 eV corresponds to the characteristic peak of Te 4d (5/2 at 40.4 eV, 3/2 at 41.9 eV), while the doublet at around 25 eV is the characteristic peak of Bi 5d (5/2 at 23.8 eV, 3/2 at 26.9 eV). Therefore, the white-colored area in (b) corresponds to the $MnBi_2Te_4$ terrace, while the blue- and green-colored regions are the two types of Bi_2Te_3 terraces, as indicated by (e) and (f), which exhibit similar XPS spectra. According to the layer stacking series in Fig. 7.1(a), the sequence of the two QLs is different, where one being above and the other below the $MnBi_2Te_4$ SL, generating two different terraces. However, how to identify the two types of Bi_2Te_3 in $MnBi_6Te_{10}$ is still an open question, which requires further investigation.

Besides, work function maps acquired under a series of binding energy at a different position are demonstrated in Fig. 7.2, where the boundaries between the three different

contrasts in Fig. 7.2(c)-(e) are clearly visible, confirming the presence of the three terminations in $MnBi_6Te_{10}$.

7.1.2 ARPES Measurements at PGI-6

CD-ARPES measurements were conducted at Forschungszentrum Jülich and NanoESCA beamline using different geometries of the material.

The experimental photoemission geometry at PGI-6, Forschungszentrum Jülich is illustrated in Fig. 7.3(a). Figure 7.3(b) and (c) show ARPES maps of Bi_2Te_3 terrace at the Fermi level taken with left- and right-circularly polarized (LCP and RCP) light, respectively. The dichroism is already visible in (b) and (c), marked by the black arrows that indicate regions of higher intensity. Here, the CD magnitude is defined as the normalized difference:

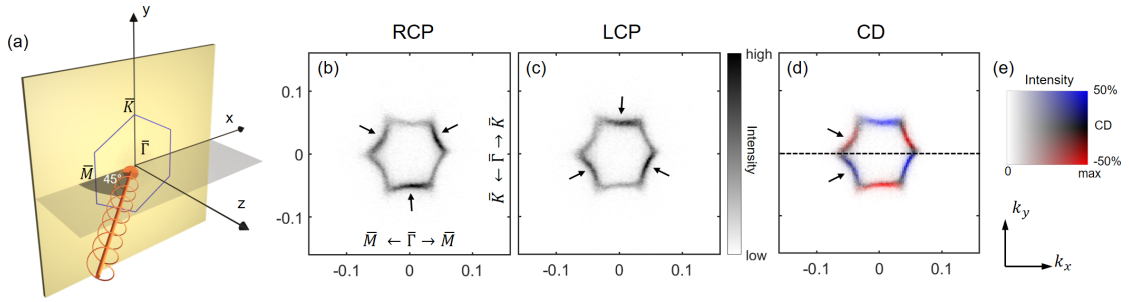

Figure 7.3: Experimental CD-ARPES with photon source energy hν = 6 eV on one of Bi_2Te_3 terraces of $MnBi_6Te_{10}$ crystal. ARPES system is cooled down to 5.1 K. (a) Experimental setup for the measurement. Light impinges on the sample surface within the $\overline{M}-\overline{\Gamma}-\overline{M}$ plane. (b), (c) ARPES maps from Bi_2Te_3 terrace at the Fermi level, taken with RCP and LCP light at 6 eV respectively. (d) CD-ARPES map obtained from (b) and (c), the maps use the color scale shown in (e). In this case, the reaction plane coincides with a mirror plane of the material, which is reflected in the CD-ARPES maps by the sign reversal upon reflection at the mirror plane. Data in (b)-(d) provided by Dr. Lukasz Plucinski, plotted and analyzed by the author.

$$CD = \frac{I_{LCP} - I_{RCP}}{I_{LCP} + I_{RCP}}, \tag{7.1}$$

I_{LCP}, I_{RCP} are the measured photoemission intensities with LCP and RCP light [250]. The CD map calculated using Eq. 7.1 is shown in Fig. 7.3(d), where the blue and red colors from the 2D colormap in (e) indicate opposite signs of the CD.

As shown in Fig. 7.3(d), the horizontal direction of CD-ARPES map is along the $\overline{M}-\overline{\Gamma}-\overline{M}$ direction while the vertical direction is along the $\overline{K}-\overline{\Gamma}-\overline{K}$ direction. It is noticed that the CD sign is reversed following the relation of CD(k_x, k_y) = -CD(k_x, -k_y), which indicates that the light incidence coincides with the mirror plane of the material. The phenomenon happens to the CD-ARPES map at different binding energies, ranging from the Fermi level to 0.25 eV, as shown in Fig. 7.4.

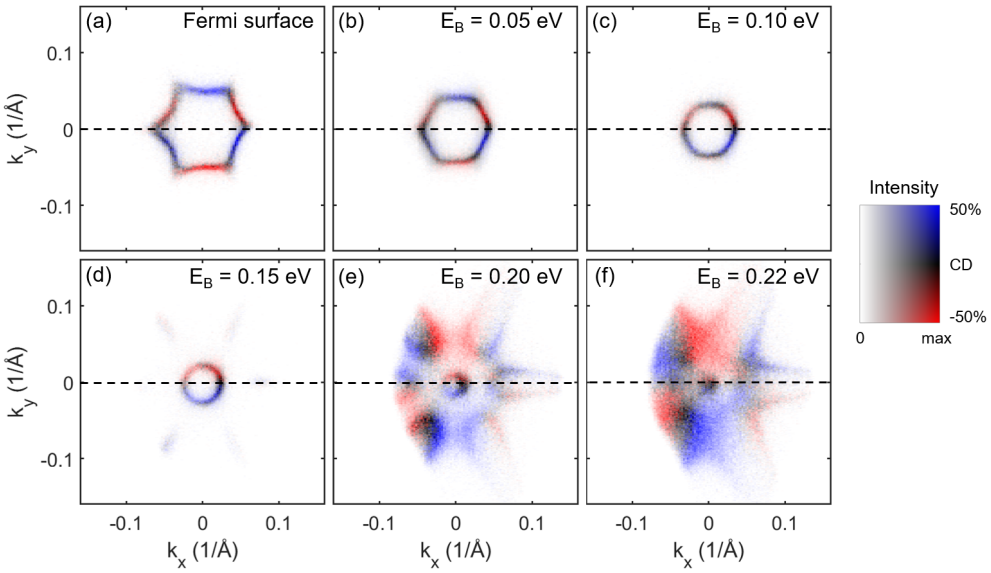

Figure 7.4: High-resolution CD-ARPES at different binding energies for the bulk MnBiTe sample, shown in (a)-(e) from the Fermi level to 0.20 eV (in steps of 0.05 eV) and at 0.22 eV in (f), in which the Dirac cone is located. All maps exhibit inverted CD spin with respect to the reaction plane, CD(k_x, k_y) = -CD(k_x, -k_y). Data provided by Dr. Lukasz Plucinski, plotted and analyzed by the author.

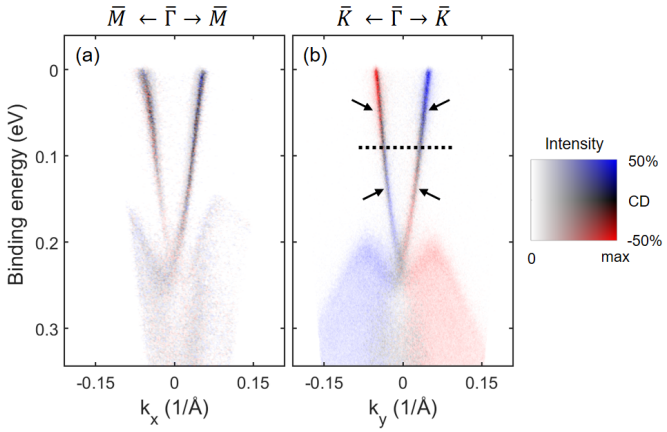

Figure 7.5: CD-ARPES cuts along $\overline{M} - \overline{\Gamma} - \overline{M}$ in (a) and $\overline{K} - \overline{\Gamma} - \overline{K}$ in (b) from the measurement results in Fig. 7.3. Data provided by Dr. Lukasz Plucinski, plotted and analyzed by the author.

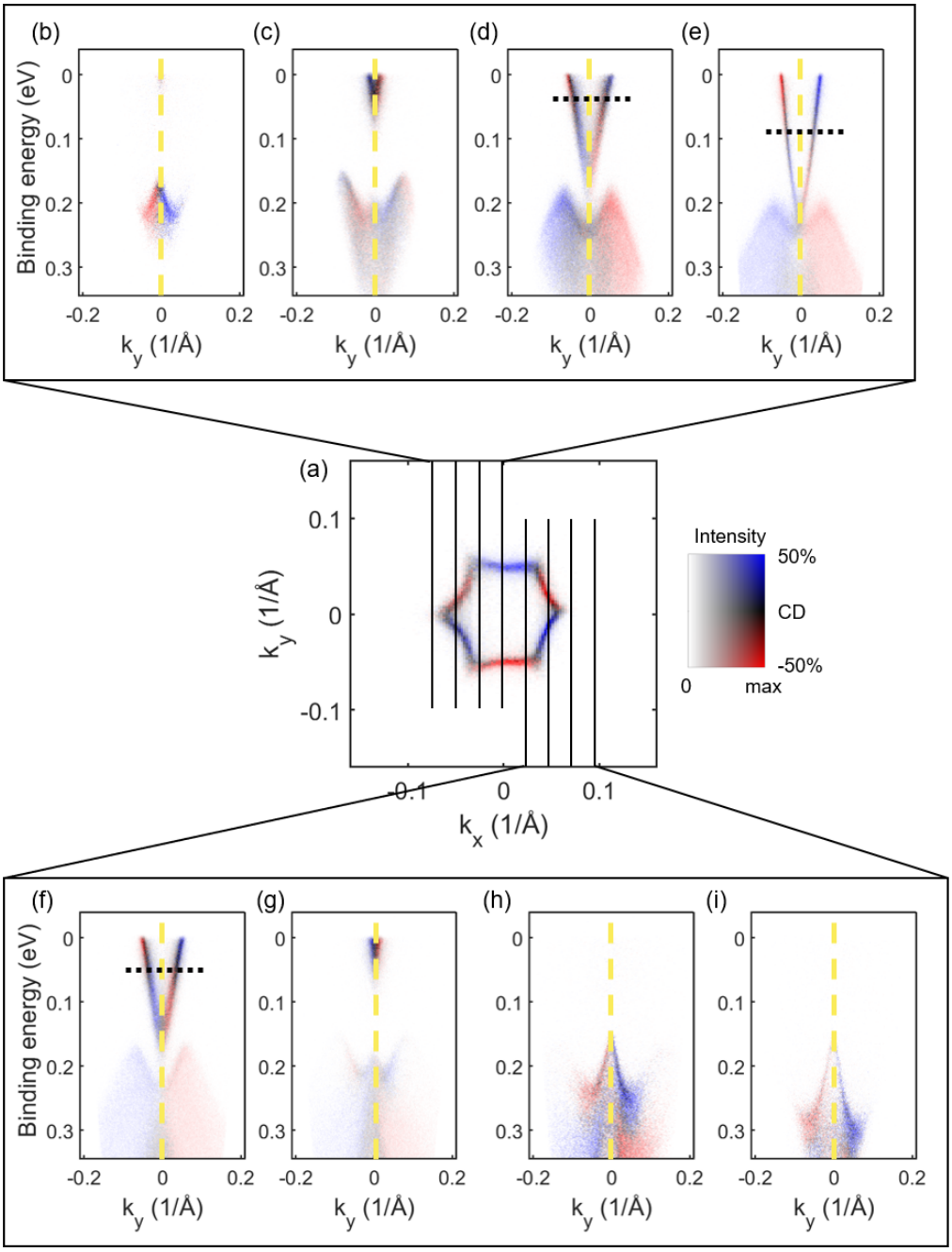

Figure 7.6: High-resolution CD-ARPES maps of different k_x cuts. (a) CD-ARPES energy cut at the Fermi level. (b)-(i) represent the corresponding CD-ARPES cuts along $\overline{K}-\overline{\Gamma}-\overline{K}$ at k_x = -0.72 Å^{-1}, -0.48 Å^{-1}, -0.24 Å^{-1}, 0 Å^{-1}, 0.24 Å^{-1}, 0.48 Å^{-1}, 0.72 Å^{-1} and 0.96 Å^{-1}, respectively. It is clearly observed that all E(k_y) spectra have the reversed CD sign over the yellow dashed line marked within the maps. Furthermore, the black dotted lines in (d)-(f) indicate the energy at which the CD sign is reversed. (Data provided by Dr. Lukasz Plucinski, plotted and analyzed by the author.)

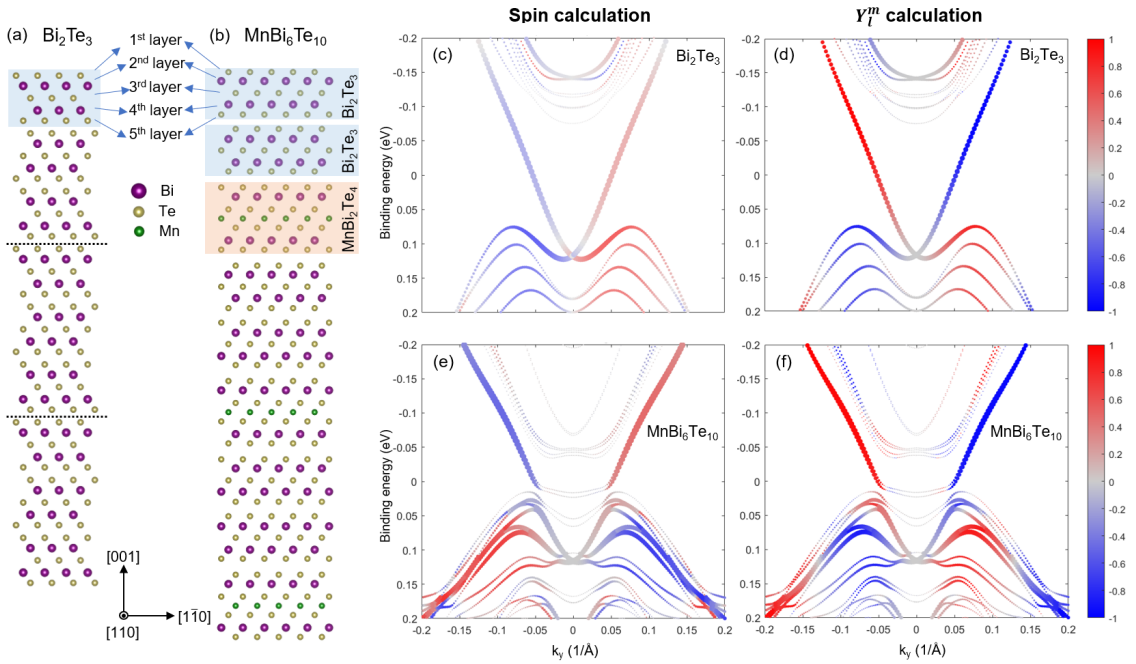

Figure 7.7: (a) The atomic model of three unit cells of pure Bi_2Te_3 crystal. (b) The atomic model of a unit cells of $MnBi_6Te_{10}$ crystal. (c)-(d) spin-polarized and Y_l^m calculation of Bi_2Te_3 slabs. (e)-(f) spin-polarized and Y_l^m calculation of the 2QL Bi_2Te_3-terminated $MnBi_6Te_{10}$ crystal (MBT) slabs. Data in (c)-(f) provided by Dr. Lukasz Plucinski, plotted and analyzed by the author.

Figure 7.5 presents the CD-ARPES cuts along $\overline{M}-\overline{\Gamma}-\overline{M}$ in (a) and $\overline{K}-\overline{\Gamma}-\overline{K}$ in (b) from the the same measurement. As expected, CD vanishes within the reaction plane, as shown in Fig. 7.5(a). As indicated in the $\overline{K}-\overline{\Gamma}-\overline{K}$ cut in Fig. 7.5(b), another sign reversal occurs across the black dashed line (at the binding energy approximately 0.1 eV). The latter sign reversal also appears in other k_x cuts, as displayed in Fig. 7.6. Similar phenomenon has been observed in the CD measurement on Bi_2Te_3 by Jung et al. [247] and in theoretical calculations by Mirhosseini and Henk [246]. As shown in Fig. 7.4, this phenomenon is related to the transition between the warped and circular Fermi surface.

To unveil the theory underlying these CD-ARPES results, theory calculations were performed using the atomic positions in the Bi_2Te_3 terrace from the pure Bi_2Te_3 and $MnBi_6Te_{10}$ crystal, respectively, as depicted in the atomic model in Fig. 7.7(a)-(b). The sequence of the calculated atomic layers follows the order: Te_{1st}-Bi_{2nd}-Te_{3rd}-Bi_{4th}-Te_{5th}.

Figure 7.7(c)-(f) show surface electronic band structures along $\overline{\Gamma K}$ for the 9 QL Bi_2Te_3 and for 2QL Bi_2Te_3-terminated $MnBi_6Te_{10}$ crystal (MBT) slabs. The $MnBi_6Te_{10}$ crystal slab contained 2 SL of $MnBi_2Te_4$ and 6 QL of Bi_2Te_3 in total. For spin-polarized calculation the size of the symbol is proportional to the weight at the surface-most Te atom, while the color refers to the out-of-plane spin polarization. For the orbital angular momentum (OAM) calculation, the difference between the weights on Te $5pY_1^{-1}$ and Y_1^1 are plotted[1]. Ferromagnetic coupling of the Mn local moments has been assumed in the the

[1] Y_l^m: spherical harmonics, l and m correspond to the azimuthal (or orbital), and magnetic quantum num-

MBT calculation and we performed two calculations with magnetization M = (001) and M = (00$\bar{1}$).

These two calculations have been averaged out in order to approximate the averaging over magnetic domains in the experiment, where the sample temperature was $\approx 10K$, therefore the sample could be expected to be in the magnetic state [256]. The calculations have been performed using the WIEN2k package [257], for the MBT calculations we used DFT+U with U = 5.3 eV on Mn 3d levels [258].

One can see pronounced similarities between the Bi_2Te_3 and MBT surface bands, in particular the Bi_2Te_3 topological surface state is present in the 2QL-terminated MBT, with only minor modifications. In the MBT calculation this band exhibit a local gap of $\approx$ 10 meV near the Fermi level, which is not observed in the experiment despite sufficient resolution. This suggests that either the actual gap is much smaller than predicted, or that the surface has been terminated with more than 2 QL of Bi_2Te_3.

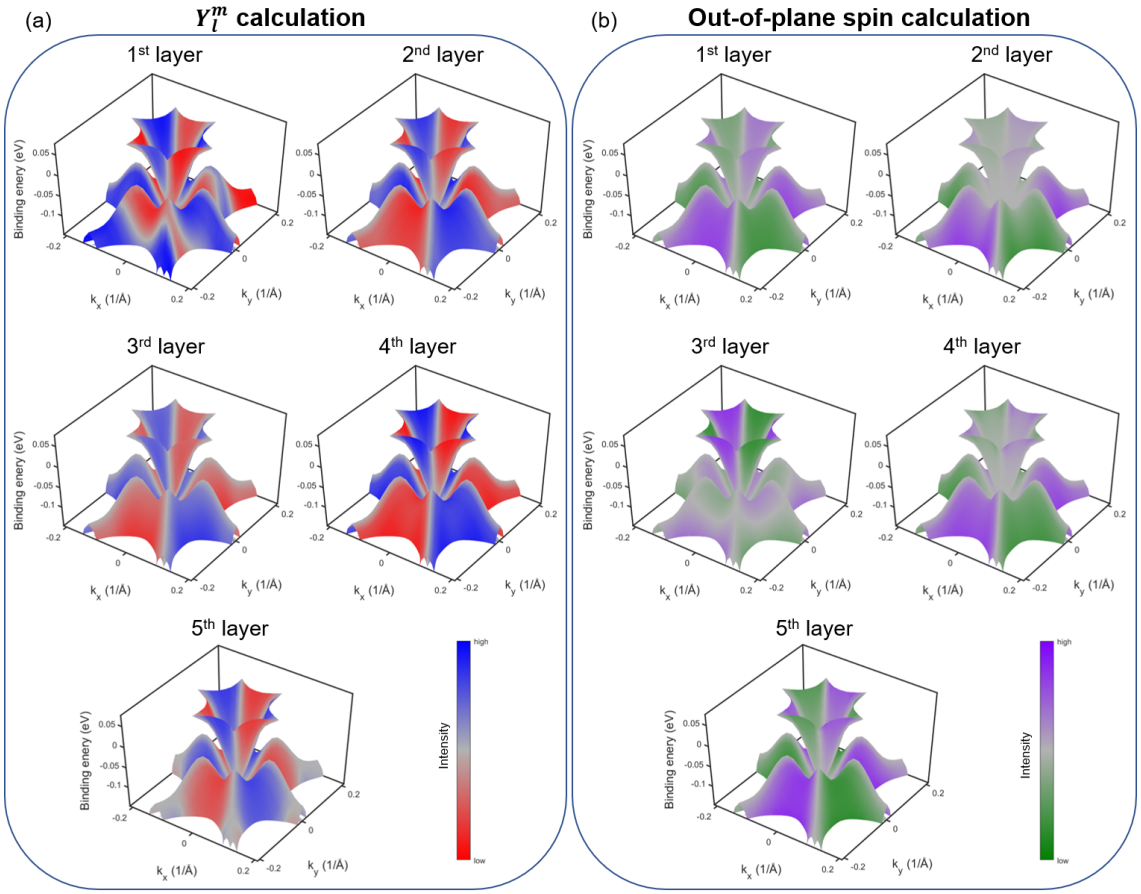

Figure 7.8: (a) Y_l^m calculation of the topmost five layers in the Bi_2Te_3 terrace in Fig.7.7(a); (b) Out-of-plane spin calculation of the topmost five layers in Bi_2Te_3 terrace in Fig.7.7(a), using WIEN2k theory. Data provided by Dr. Lukasz Plucinski, plotted and analyzed by the author.

Therefore, the Bi_2Te_3 slabs are employed for further calculations. The detailed results

bers. (e.g. Y_1^0 represents linearly polarized light, or Y_1^m represents circularly polarized light [255]).

of the Y_l^m and the out-of-plane spin calculations of the 5 atomic layers are presented in Fig. 7.8(a)-(b). Y_l^m quantization axis is set at $\theta = 45°$, which is aligned within the light incidence direction in the CD-ARPES experiment, as shown in Fig. 7.3(a). The Y_l^m sign in Fig.7.8(a) in the five layers is observed to remain consistent across all layers at the Fermi energy. However, as displayed in Fig.7.8(b), the direction of the out-of-plane spin in the third layer is reversed compared to the other four layers at the Fermi energy. The calculated spin results are in agreement with the calculations reported in [259].

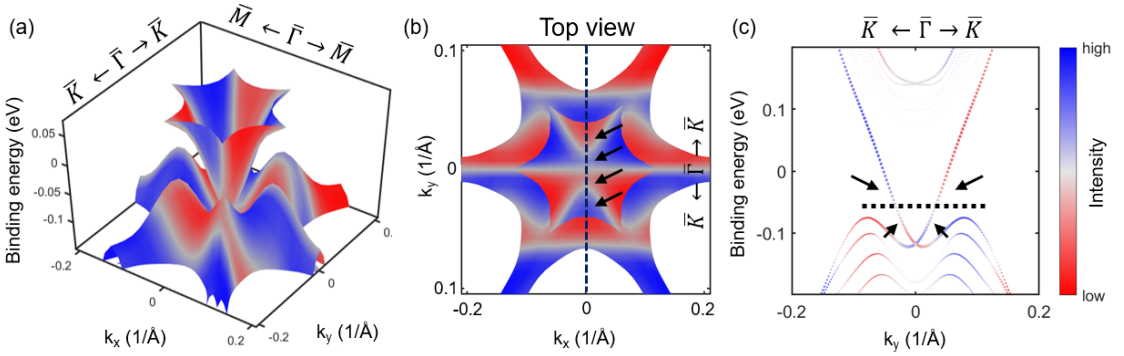

Figure 7.9: (a) Calculated Y_l^m of the first Te atom layer of the Bi_2Te_3 terrace. (b) Top view of the 3D calculation data. (c) CD-ARPES cut along $\bar{K} - \bar{\Gamma} - \bar{K}$ direction. Data provided by Dr. Lukasz Plucinski, plotted and analyzed by the author.

The inconsistency of the spin calculation across five layers indicates that the origin of the CD maybe attributed to the OAM, instead of the spin texture. Besides, it is also noticed that the Y_l^m calculation of the first Te atom layer differs from the other layers above and below the Dirac point. Detailed information of the Y_l^m calculation of the first Te atom layer is displayed in Fig. 7.9.

Figure 7.9(a) is the same calculation of the first Te layer as shown in Fig. 7.8(a), while (b) and (c) are the top view of the 3D data and the 2D cut along the $\bar{K} - \bar{\Gamma} - \bar{K}$ direction, respectively. As shown in Fig. 7.9(b), the CD sign is reversed not only following the relation of CD(k_x, k_y) = -CD(k_x, -k_y), but also within the warped structure above the Dirac cone along the $\bar{K} - \bar{\Gamma} - \bar{K}$ direction, indicated by the black arrows. In addition, the reversed CD sign can also be observed across the black dashed line in Fig. 7.9(c), indicated by the black arrows. This phenomenon is consistent with the experimental observation in Fig. 7.5(b). The agreement of the CD sign reversal above the Dirac cone observed in the experiment and the Y_l^m calculation suggests that the OAM of the first Te layer from the Bi_2Te_3 terrace contributes significantly to the CD signal in this material.

Most of the results obtained so far are consistent with the CD results of Bi_2Te_3 in the previous report [246, 247, 249, 250]. Additional CD-AREPS measurements are conducted on different terraces on the same $MnBi_6Te_{10}$ sample at the NanoESCA beamline, which enables the spatial resolution of 15 μm under PEEM mode. The corresponding results will be introduced in next section.

7.1.3 μ-ARPES Measurements at NanoESCA Beamline

The bulk $MnBi_6Te_{10}$ sample has been in-situ cleaved using the scotch tape and measured at the NanoESCA beamline. CD-ARPES results of one of the Bi_2Te_3 terraces and the $MnBi_2Te_4$ terrace are displayed in Fig. 7.10.

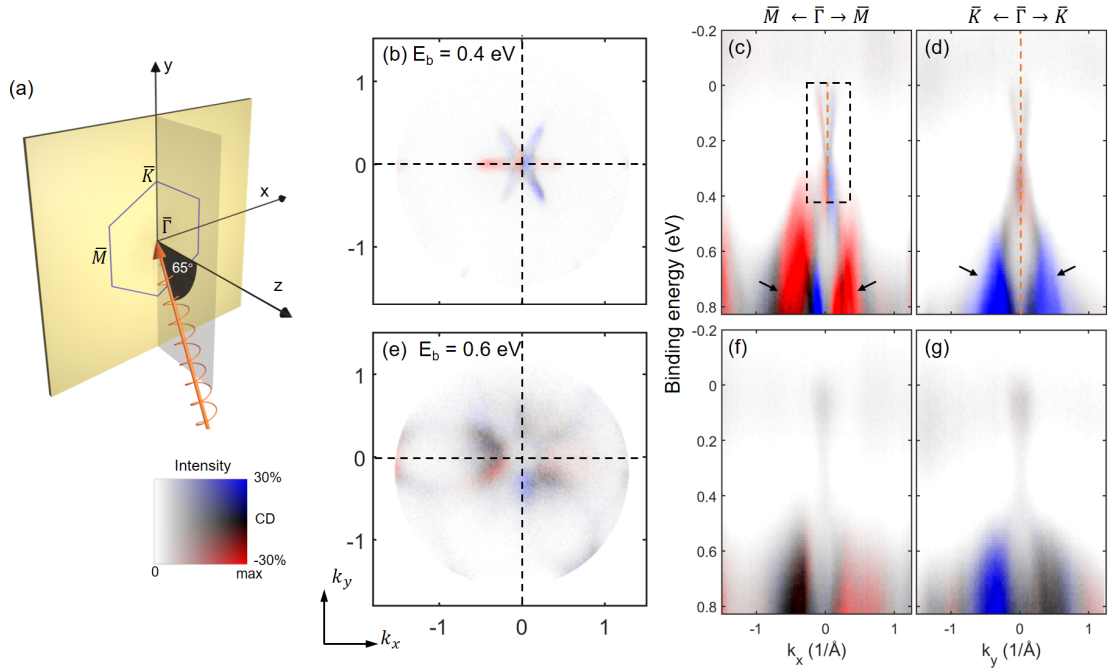

Figure 7.10: CD-ARPES at hν = 40 eV on one of the Bi_2Te_3 terraces and the $MnBi_2Te_4$ terrace. (a) Experimental setup for the measurement. Light incidents on the sample surface within the $\overline{K}-\overline{\Gamma}-\overline{K}$ plane. (b)-(d) are acquired from Bi_2Te_3 terrace, while (e)-(g) are acquired from $MnBi_2Te_4$ terrace of the $MnBi_6Te_{10}$ crystal. (b) CD-ARPES energy map at E_B = 0.4 eV of the Bi_2Te_3 terrace. The black dashed lines indicate the cut direction where the corresponding 2D cuts along $\overline{M}-\overline{\Gamma}-\overline{M}$ (c) and $\overline{K}-\overline{\Gamma}-\overline{K}$ (d). (e) CD-ARPES energy map of the $MnBi_2Te_4$ terrace at E_B = 0.6 eV. The black dashed lines indicate the cut direction with the corresponding 2D cuts along $\overline{M}-\overline{\Gamma}-\overline{M}$ in (f) and $\overline{K}-\overline{\Gamma}-\overline{K}$ in (g). (b)-(g) Data collected at NanoESCA beamline by Dr. Lukasz Plucinski's group, plotted and analyzed by the author.

Different from the experimental geometry in Fig. 7.3(a), the incident light lies within the $\overline{K}-\overline{\Gamma}-\overline{K}$ plane, which is not the mirror plane of the crystal. Therefore, the CD bands are non-symmetric in both $\overline{K}-\overline{\Gamma}-\overline{K}$ and $\overline{M}-\overline{\Gamma}-\overline{M}$ directions for Bi_2Te_3 terrace in (b), indicated also in corresponding E(k) cuts shown in (c) and (d). Figure 7.11 displays the CD-ARPES maps at different binding energies from the Fermi level to 0.7 eV, which also does not show any symmetric CD sign reversal along both directions.

Besides, as depicted in Fig. 7.10(e)-(g), the CD magnitude obtained from the $MnBi_2Te_4$ terrace is too low to clearly distinguish the dichroic features of the electronic bands. Same for the CD-ARPES maps at different binding energies in Fig. 7.12. Longer accumulation times in the experiment would be required to enhance the statistics.

Our CD-ARPES measurement of $MnBi_6Te_{10}$ has provided preliminary insights into the

dichrosim of the Bi_2Te_3 and $MnBi_2Te_4$ terrace. Further experimental and theoretical study are necessary to understand the physics of CD on different terraces in this material.

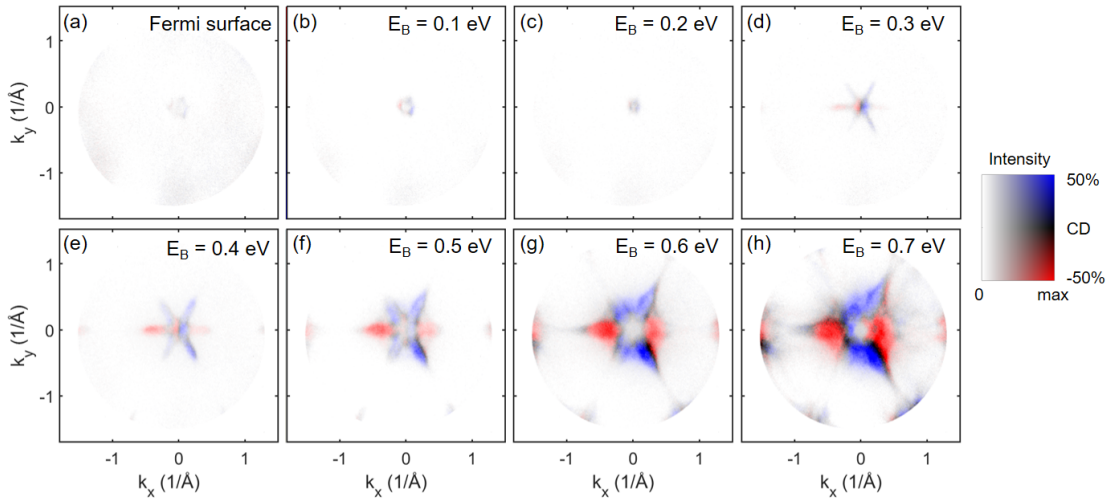

Figure 7.11: CD-ARPES at different binding energies from the Fermi level to 0.7 eV (in steps of 0.1 eV) on one of the Bi_2Te_3 terraces. Data collected at NanoESCA beamline by Dr. Lukasz Plucinski's group, plotted and analyzed by the author.

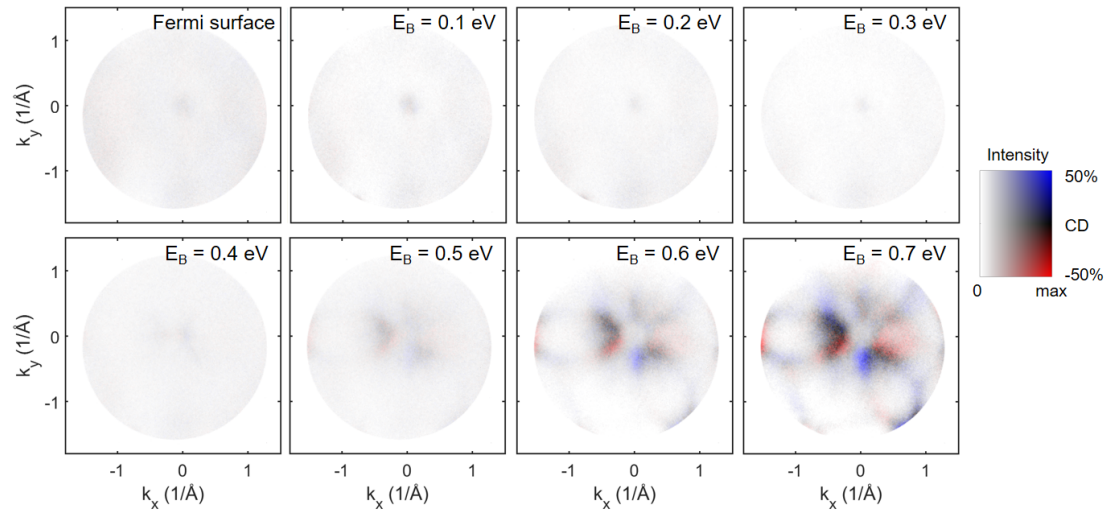

Figure 7.12: CD-ARPES at different binding energies from the Fermi level to 0.7 eV (in steps of 0.1 eV) on the $MnBi_2Te_4$ terrace. Data collected at NanoESCA beamline by Dr. Lukasz Plucinski's group, plotted and analyzed by the author.

7.2 ARPES Measurements of (V-alloyed) BST Thin Film

Different from bulk samples, there are two methods for thin film TIs to obtain a clean surface for ARPES measurement, which will be implemented in the following investigation of the MBE-grown (V-alloyed) BST thin films.

7.2.1 Vacuum Transfer of BST Thin Film

As introduced in Chapter 4, in order to manipulate the surface electronic structure of TIs, parental TI elements, such as Bi_2Te_3 or Sb_2Te_3 are merged together, forming a ternary alloy (BST). By varying the composition of Bi, the Fermi level and Dirac point (DP) position can be tuned for potential device application. Therefore, ARPES is employed to map the corresponding electronic band structure, in order to establish the Fermi level position in various films.

Here, the MBE-grown BST thin film is transferred using the vacuum suitcase into the ARPES chamber without exposure to the air.

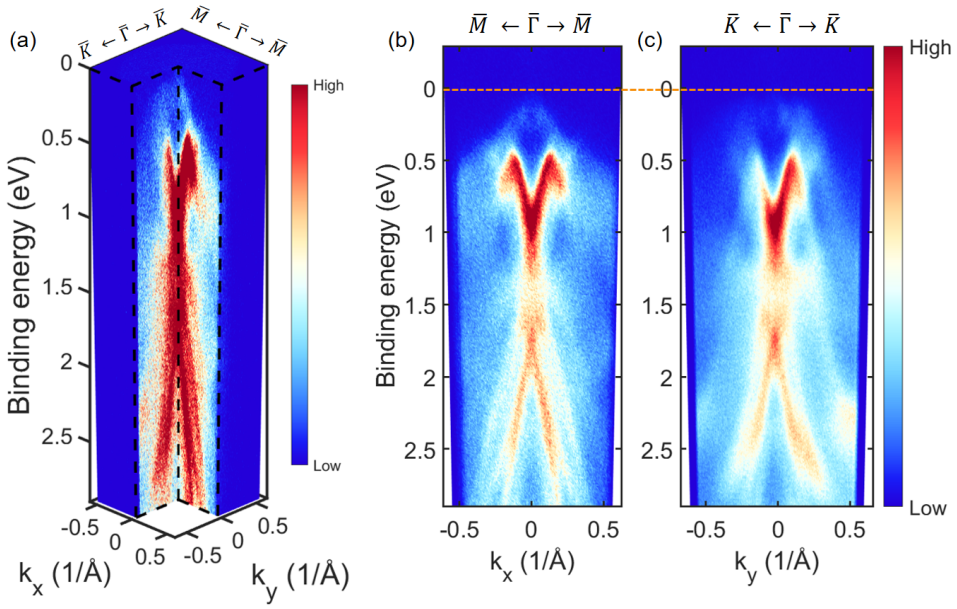

Figure 7.13: Surface electronic structure of the vacuum-transferred BST thin film (from PGI-9) measured with helium lamp in PGI-6. (a) 3D data stack ($I(E_B,k_x,k_y)$) obtained from the Fermi surface mapping of BST thin film, from which the binding energy maps along the $\overline{M}-\overline{\Gamma}-\overline{M}$ direction at $k_y = 0$ in (b) and the $\overline{K}-\overline{\Gamma}-\overline{K}$ direction at $k_x = 0$ in (c) are produced. The sample was provided by Dr. Abdur Rehman Jalil in PGI-9.

Fig. 7.13 presents a 3D data stack ($I(E_B,k_x,k_y)$) in (a) and two E(k) maps cuts at $k_y = 0$ in (b) and at $k_x = 0$ in (c). The orange dashed line marked in (b) and (c) indicate the position of the Fermi level, which approx. aligns with the DP of the material. From the Rutherford

backscattering spectrometry (RBS) measurement in PGI-9, Bi content is approx. 18% so that the DP is located to the Fermi level.

7.2.2 Cleaving of Te-passivated V-alloyed BST thin films using post

Another approach to obtain the clean surface is the post-cleavage, as introduced in Fig. 3.16, This method can be performed on Te-capped samples [126, 260]. A V-alloyed BST thin film sample is in-situ cleaved with the post, successfully removing the Te capping at the PHELIX beamline at the Solaris, Krakow, Poland. Normal ARPES and CD-AREPS measurements are performed on this sample.

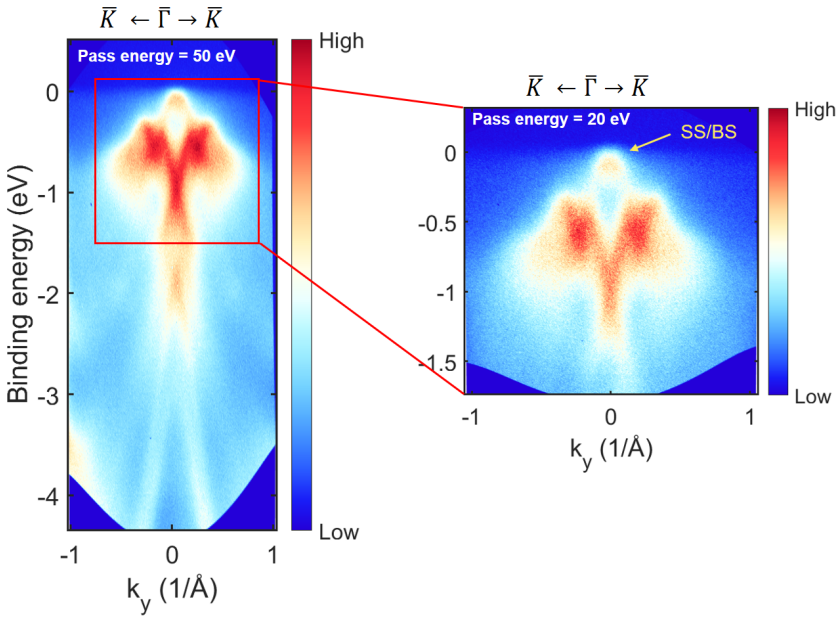

Figure 7.14: Electronic band structure of the VBST thin film measured by p-polarised light $h\nu$ = 68 eV at 30K. From left to right are two E(k) plots along $\overline{K} - \overline{\Gamma} - \overline{K}$ direction at $k_x = 0$, with the pass energy 50 eV and 20 eV, respectively. The ARPES map under pass energy 20 eV has a better energy resolution.

The sample has been provided by Dr. Steffen Schreyeck from Würzburg university, where 7.5 nm thick $V_{0.1}(Bi_{0.2}Sb_{0.8})_{0.9}Te_3$ (VBST) are grown on the Si(111) substrate, with the 200 nm Te capping layer to protect the surface.

The E(k_y) ARPES plots are displayed in Fig. 7.14, where both of the spectra indicate that the DP lies near the Fermi level. In (b), the surface state (SS) is mixed with the bulk state (BS) at the DP position of the thin film.

In addition to the regular ARPES maps, we also acquired CD-ARPES maps from the VBST thin film at different photon energies (60 eV, 85 eV, 90 eV, 105 eV), as shown in Fig. 7.15. In all the spectra, it is noticed that the sign of the CD is reversed between the branch $k_y < 0$ and $k_y > 0$ across the vertical direction at $k_y = 0$ (green dashed line),

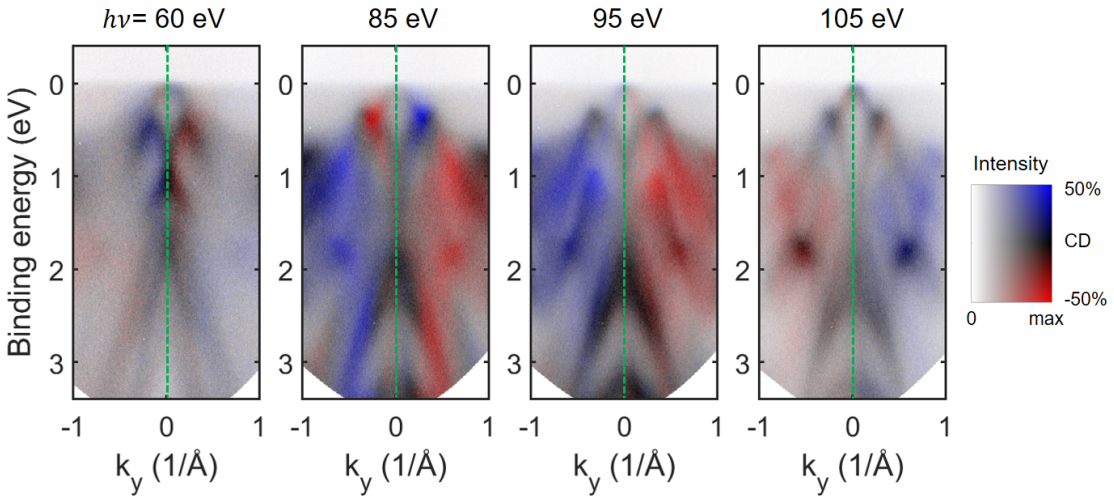

Figure 7.15: CD-ARPES spectra along the $\overline{K}-\overline{\Gamma}-\overline{K}$ direction of post-cleaved VBST thin film taken at different photon energies. The experimental geometry is identical to that in 7.3(a), where the light is incident within the mirror plane ($\overline{M}-\overline{\Gamma}-\overline{M}$ plane). These spectra use the 2D colormap on the right.

which suggests that the vertical green dashed line is the mirror plane. Besides, the CD-ARPES varies under different photon energies, indicating its photon energy dependence. This behavior is also observed in other materials, such as Bi_2Te_3 [250, 251]. Due to the complexity of CD-ARPES process [261], detailed analysis of these maps is beyond of the scope of this thesis.

7.3 Summary

In this chapter, three different terminations, i.e. two different Bi_2Te_3 terraces and a $MnBi_2Te_4$ terrace in $MnBi_6Te_{10}$ crystals are demonstrated to appear after cleavage, through the work function mapping. To identify these terraces generated after cleavage, XPS was performed on each terrace, where the appearance of the peak at approx. 47.5 eV indicates the presence of Mn in one of the terraces, thus distinguishing it from Bi_2Te_3 terraces. However, the two types of Bi_2Te_3 terrace, i.e. 1 QL Bi_2Te_3 and 2QL Bi_2Te_3 termination, can not be identified from the current results.

One of the Bi_2Te_3 terraces in the $MnBi_6Te_{10}$ crystal was investigated with CD-ARPES. As expected, the CD sign is reversed across the mirror plane. This phenomenon has been observed previously. However, the sign reversal is also observed across certain binding energies above the Dirac cone in the spectra. Firstly, DFT calculations were performed on the 9 QL Bi_2Te_3 and 2QL Bi_2Te_3-terminated MBT slabs, which indicate that the experimental results were acquired from the surface terminated with more than 2 QL of Bi_2Te_3. Further detailed calculations from the Bi_2Te_3 slabs suggest that the CD signal observed in the experimental results originates from the OAM of the first Te layer on the Bi_2Te_3 terrace.

In addition, CD-AREPS measurements conducted on different terraces (one of the Bi_2Te_3 terraces and the $MnBi_2Te_4$ terrace) of the same $MnBi_6Te_{10}$ sample at the NanoESCA beamline revealed a low CD magnitude to clearly distinguish the dichroic features from the electronic bands. For future studies, similar experiments with longer acquisition time to accumulate higher intensity will be required.

Moreover, the MBE-grown TI thin films were successfully investigated with the vacuum transfer (without capping) and the post-cleavage of Te capping methods to preserve the clean surface of the thin films, enabling the feasibility of the ARPES measurement. The electronic band structures of the BST thin film and the V-alloyed BST thin film indicate the positions of their Dirac cones, where both of them are located near the Fermi level, making them promising platforms for further device fabrication.

8 Conclusion and Outlook

Commentary: *This chapter presents the conclusions drawn from Chapters 5 to 7 and provides an outlook for the thesis. The content has been compiled by the author.*

Since the discovery of topological insulators (TIs), they have shown significant potentially for application in the field of spintronics and quantum computing, due to their topologically protected conductive edge or surface states with non-degenerated spins. Despite significant progress, scientists still face several challenges from the perspective of material and growth in integrating TIs into devices. For 2D TIs, the limited material choices and stability issues have impeded the development and realization of corresponding quantum devices. Additionally, identifying a suitable material system in 3D TIs, where the Fermi level and Dirac point are positioned within the bulk gap, is critical to access the topological surface states (TSS). Furthermore, scientists have also been struggling in achieving high crystal quality TI materials without defects and ultra-smooth surfaces, as these are essential for maintaining robust topological properties. This work addresses these issues including preparation of defect-free and high crystal quality epilayers in 2D and 3D regime, and the realization of engineering the electronic band structure of 3D TIs.

In this these, systematic growth of the Bi in trigonal (Bi_{TRIG}) and orthorhombic (Bi_{ORTH}) phases on Bi-terminated Si(111) 1×1 surfaces using molecular beam epitaxy (MBE), has been discussed. For the first time, the Bi_{TRIG} and Bi_{ORTH} are grown phase-selectively with high crystal quality, which has been confirmed by the x-ray diffraction patterns (XRD) and atomic characterization via scanning transmission electron microscopy (STEM) investigation. The thickness-controllable high-quality growth of Bi_{TRIG} and 4% - 7% Sb-doped $Bi_{1-x}Sb_x$ (BiSb) epilayers enable the realization of the 2D TI with the thickness up to 4 nm. Besides, the pure Bi_{ORTH} phase with controllable thickness is achieved. This phase is predicted to be in the 2D TI regime when the thickness is below 9 nm, which extends the thickness limit further. The realization of the BiSb and Bi_{ORTH} phases with the thicknesses in the 2D regime enriches the family of 2D TIs.

We have also discussed the epitaxial growth of $Sn_xBi_yTe_z$ series on Bi-terminated Si(111) 1×1 surfaces using MBE. The variation of the stoichiometry in the series (by adjusting the Bi/Sn source temperature and the substrate temperature) enables high quality single crystal growth of $SnBi_4Te_7$, $SnBi_2Te_4$, $Sn_2Bi_2Te_5$ thin films as the 3D topological thin films. The transformation processes from $SnBi_2Te_4$ to $SnBi_4Te_7$ and $Sn_2Bi_2Te_5$ are presented by the corresponding XRDs, respectively. The layer stacking of the stoichiometries evolves from septuple layers to combinations of quintuple and septuple layers, and eventually to 9-atomic layers with the increase of the Sn temperature, as indicated from the atomic-resolution imaging acquired via the STEM measurements. The transport measurement of the $SnBi_4Te_7$ indicates the p-type feature but overall high carrier concentration of

the material. The high carrier concentration might be attributed to the high defect density in the films.

In the last chapter, it has been shown that the $(Bi_xSb_{1-x})_2Te_3$ (BST) thin films (without capping) are successfully characterized by the angle-resolved photoemission spectroscopy (ARPES) via vacuum transfer, enabling the tuning of the Fermi level into the band gap. Meanwhile, the V-alloyed BST thin film with Te capping layer is measured via post cleavage method, which has successfully removed the capping layer in-situ. Moreover, $MnBi_6Te_{10}$ crystal has been investigated using work function mapping and x-ray photoelectron spectroscopy (XPS), revealing the presence of terraces generated after cleavage. Later on, the circular dichroic signals combined with ARPES measurements (CD-ARPES) performed on one of the Bi_2Te_3 terraces indicate the orbital angular momentum (OAM) characteristics of this material, which are further supported by the theoretical calculations.

The results of this work can be incorporated into further experiments to explore the efficient platform for advanced quantum devices, and to understand the crystalline and electronic structure of corresponding materials. The future prospects are as follows:

- The growth of the BiSb and the Bi_{ORTH} thin films with the thickness in the topological regime can be reproduced in combination with an on-chip stencil mask [262] and in-situ surface passivation, to avoid the oxidation of Bi in the atmosphere. This method allows the fabrication of the related quantum devices in the near future, which is promising in the field of topological and quantum computing.

- For $Sn_xBi_yTe_z$ series: with a further increase of the Sn content, the series eventually forms SnTe. SnTe has a cubic structure while the three stoichiometries investigated in this work exhibit a trigonal structure. This suggests that a crystal structure transition occurs at a specific composition as the Sn content increases. Identifying the exact transition point is of significant interest. Additionally, understanding how the electronic band structure evolves with the increasing Sn is crucial for engineering the topological properties. For future, thin films from the $Sn_xBi_yTe_z$ series will be reproduced with increasing Sn composition until the formation of SnTe. These films will be studied with STEM for the crystal structural transformation and ARPES for the electronic structure evolution. Furthermore, the deposition of the superconductor (Sn) on the 3D TI from the $Sn_xBi_yTe_z$ series might offer a promising platform to realized the Majorana zero mode (MZM).

- For $MnBi_6Te_{10}$ crystal investigation, CD-ARPES and spin-polarised ARPES will be performed on the $MnBi_2Te_4$ terrace, which could reveal the OAM and spin features of this terrace. Moreover, since the current setup of the APRES system in PGI-6 allows cooling down to approx. 10 K, this magnetic sample can be measured with our system, where a gap opening from the Dirac point is expected to appear [263].

Appendix

A1 Experimental Setup

Molecular Beam Epitaxy

The epitaxial growth is performed on a 100 mm (4-inch) holder, which transfers the sample inside the chamber. The metal holder is employed throughout this work. The holder has four 10×10 mm^2 pockets that holder the Si substrates, as displayed in Fig. A1.1.

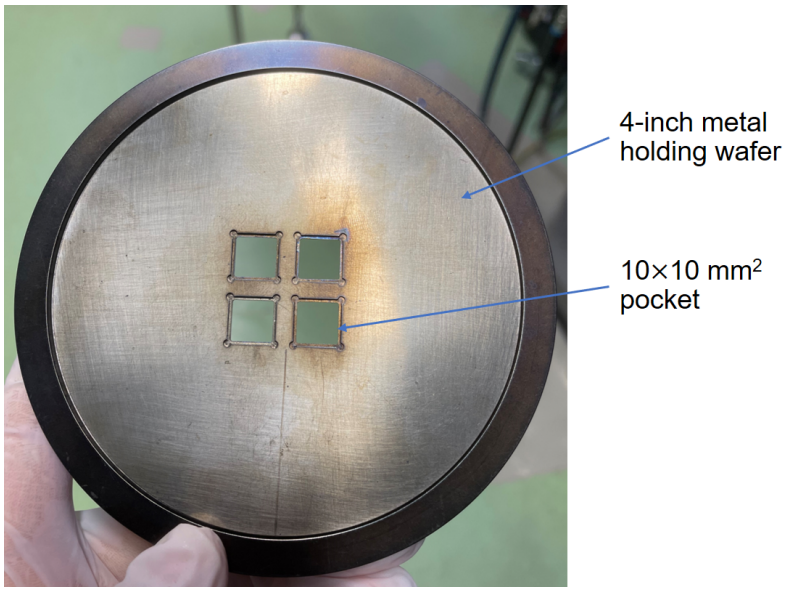

Figure A1.1: Metal holder for the topological insulator (TI) thin film growth with 100 mm diameter that allows to perform the epitaxial growth of 4 different sample at the same time.

Curtain Effect

During the lamella fabrication through focused ion beam, the surface of the specimen should be deposited with Pt or C protection layer with the corresponding ion and electron beam. Since C deposition will destroyed the crystal structure of TI, the Pt deposition is selected. However, this deposition will lead to the curtain effect of the TI thin films, as shown in Fig. A1.2.

Vacuum transfer

To perform the angle-resolved photoemission spectroscopy measurement of TI thin films produced by MBE (without capping layer), the vacuum transfer suitcase is employed to

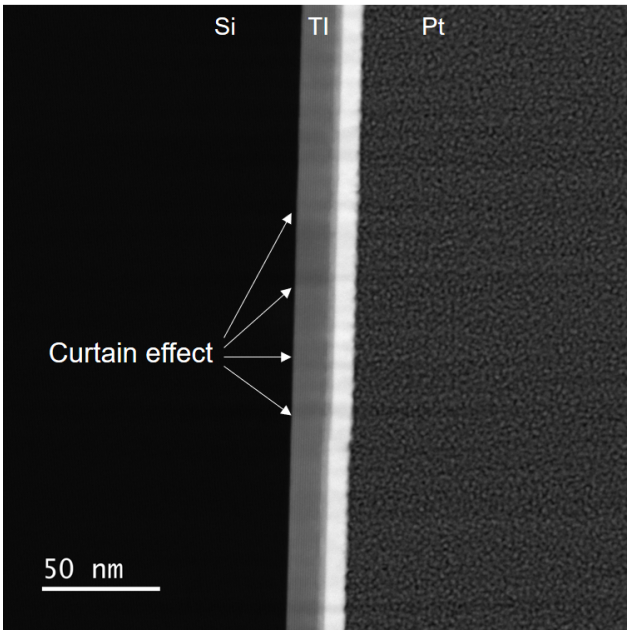

Figure A1.2: STEM-HAADF image indicating the appearance of curtain effect due to the usage of Pt deposition layer during the FIB preparation process.

preserve the surface features of the TI thin films. The structure of the vacuum suitcase is displayed in Fig. A1.3.

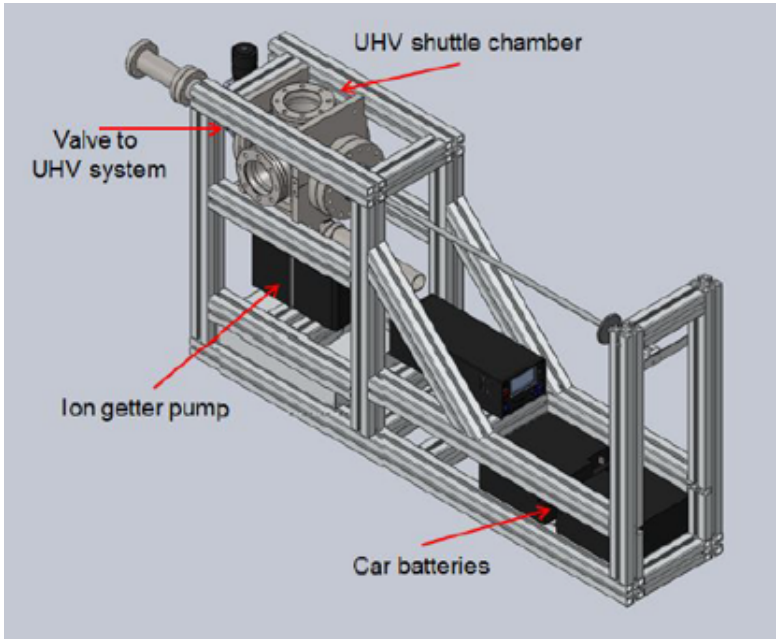

Figure A1.3: Schematic drawing of the UHV vacuum suitcase.

Si Surface Orientations

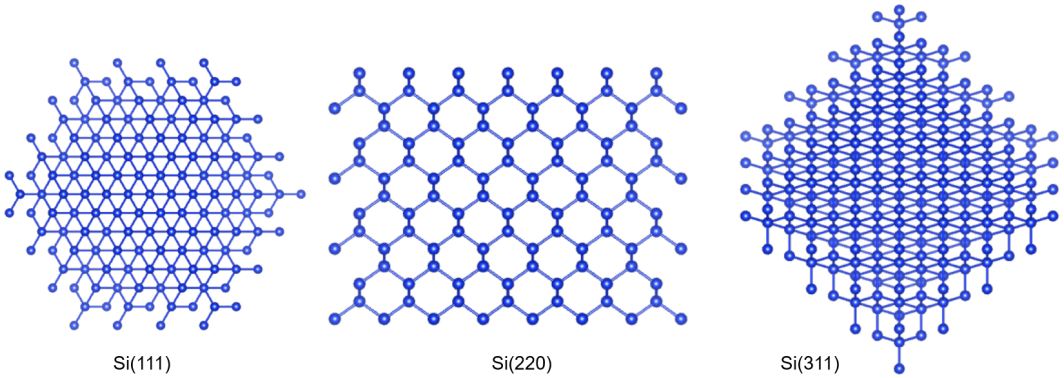

Figure A1.4: Atomic representation of different surface orientations. Here are three atomic surface geometries, i.e. Si(111), Si(220) and Si(311).

A2 Phase-Selective Epitaxy of Trigional and Orthorhombic Bismuth Thin Films

Buckling

Buckling is a strain-induced deformation in a crystal and can be described as the height difference between two atoms of the same monolayer. Taking Bi_{TRIG} (012) as an example shown in Fig. A2.1, from the side view, the height difference between two green atoms of the same Bi monolayer in upper (a) is h, while in lower (a), the 4 green atoms on the black square are at the same height level. Experimental demonstrations with the atomic resolution Scanning Tunneling Microscope (STM) show the actual height difference with A and B lines on the same monolayer Bi_{TRIG}(012) in (b) and (c), confirming the presence of the buckling in Bi_{TRIG} (012).

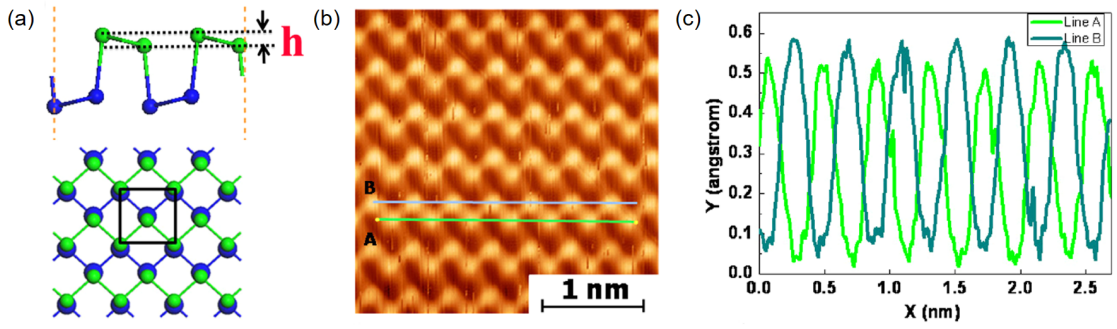

Figure A2.1: Crystal structure of 2D Bi_{TRIG} (012) thin films. (a) Schematic side- and top-views of 2-ML Bi_{TRIG} (012) film with up and down layer represented by green and blue balls, respectively. (c) Atomic-resolution STM image of 4 ML Bi_{TRIG} (012) film on HOPG (Vs = 100 mV, I = 0.08 nA). (d) Line profile along the two lines in panel (c); the height difference for two different atoms in one unit cell is within 0.045 Å. Image taken from [138].

Defects and Amorphization in Bi thin films

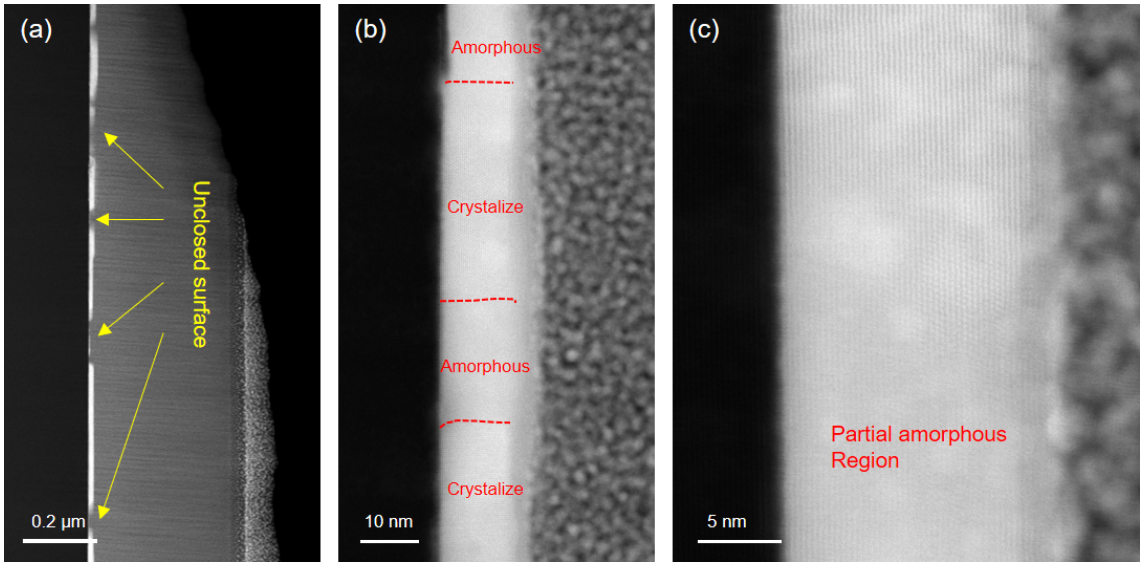

Figure A2.2: HAADF images at low Magnification show (a) discrete whites areas in the center, indicating the discontinuous and unclosed Bi thin films resulted from the imperfect growth; (b) amorphous and crystallized regions within Bi nanofilm; (c) partially amorphous regions in the Bi crystal nanofilm, where the contrast difference within the film is mainly due to FIB preparation process.

Figure A2.2 displays some examples of the problems in the grown Bi epilayers during the STEM investigation. Figure A2.2 clearly shows the unclosed grown thin films with a low magnification image. It is common that the epilayers are mixed with the crystalline and amorphous regions as seen in Fig. A2.2(b). IT can originate in the Ga ion cutting on both side of the lamella in the FIB. Similarly in (c), some regions are also partially amorphized, which can be recognized by the contrast difference within Bi nanofilm. Most of the case, the ambiguity in the film can originate in the FIB preparation or the thicker layer with oxidation on both side of the lamella. An obvious example with the thicker film region is depicted in Fig. A2.3.

Compared to the atom-resolved Si substrate, the Bi nanofilm in Fig. A2.3 appears blurred, indicating the presence of the oxidation layers on the surface of the lamella. Meanwhile, an excessive lamella thickness will also prevent achieving the atomic resolution in the acquired image.

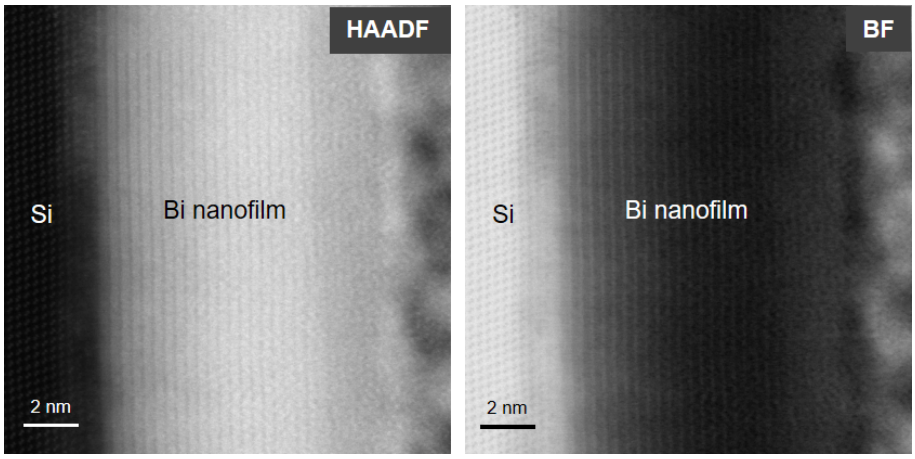

Figure A2.3: HAADF and BF images of a region in Bi nanofilm, where the film is unclear due to the large thickness and surface oxidation of both side of the lamella.

A3 Stoichiometry Growth of SnBiTe Family and Structural Characterization

Atomic Force Microscopy results of SnBT-147 and SnBT-225 thin films

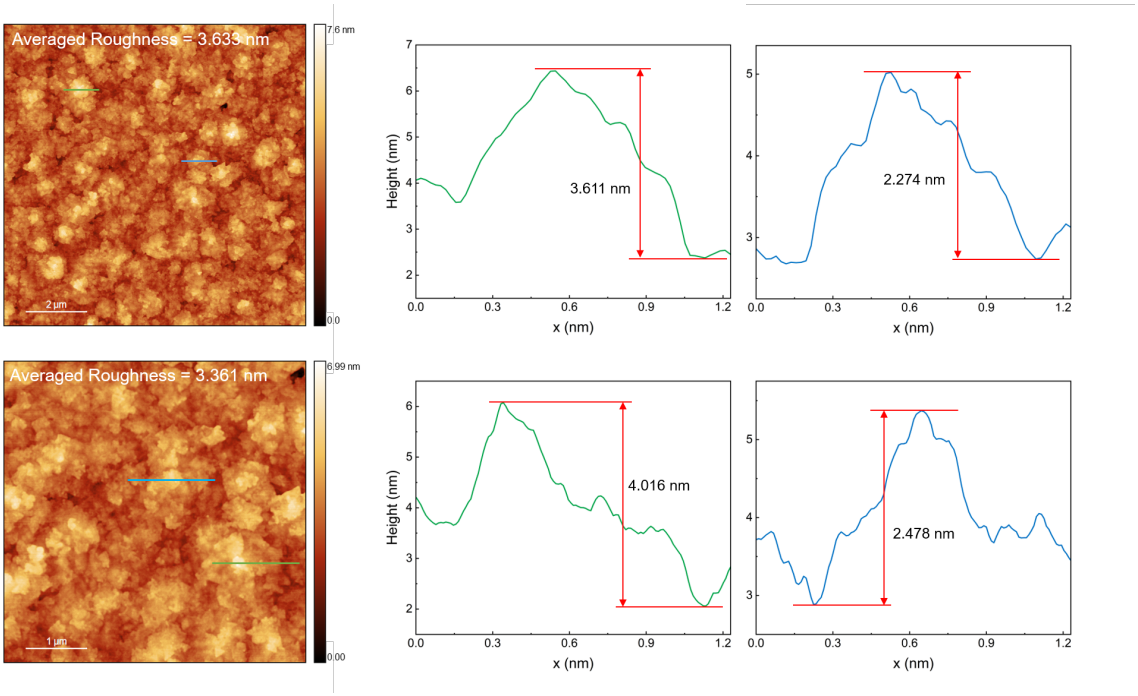

Figure A3.1: AFM images of SnBT-147 sample with low and high magnification. (a) Low magnification image, where the averaged roughness is 3.633 nm. Two line scans of the surface morphology in two positions are demonstrated in (b) and (c) with green and blue respectively. The corresponding height difference is 3.611 nm and 2.274 nm. (d) High magnification image, where the averaged roughness is 3.361 nm. Two line scans of the surface morphology in two positions are demonstrated in (e) and (f) with green and blue respectively. The corresponding height difference is 4.016 nm and 2.478 nm. AFM measurement performed by Dr. Nisha Shahi.

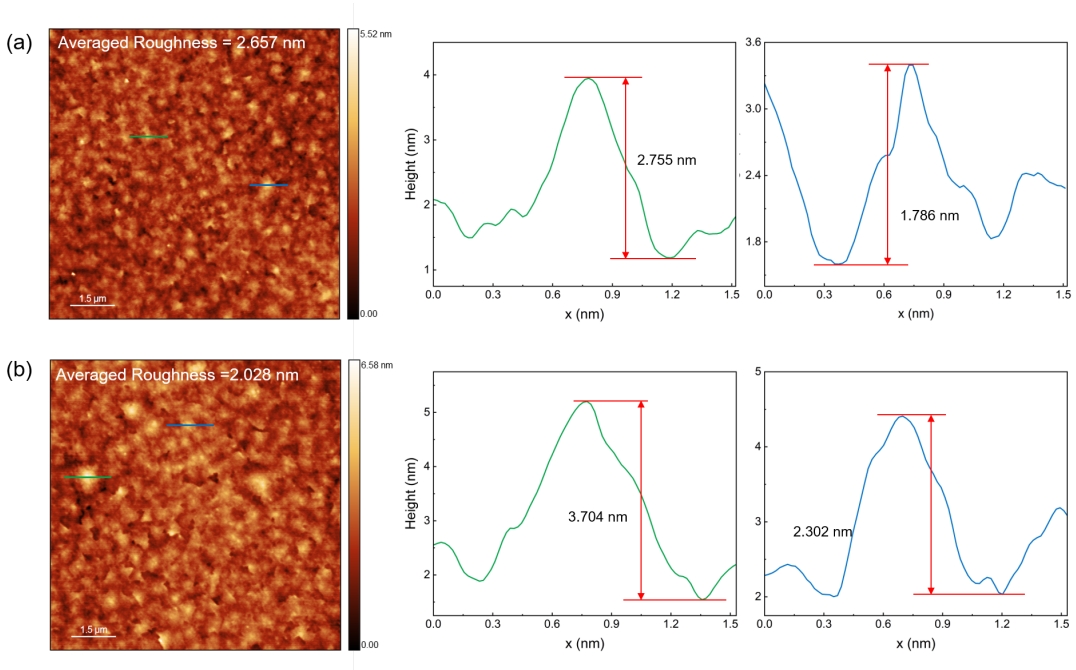

Figure A3.2: AFM images of SnBT-225 sample with low and high magnification. (a) Low magnification image, where the averaged roughness is 2.657 nm. Two line scans of the surface morphology in two positions are demonstrated in (b) and (c) with green and blue respectively. The corresponding height difference is 2.755 nm and 2.786 nm. (d) High magnification image, where the averaged roughness is 2.028 nm. Two line scans of the surface morphology in two positions are demonstrated in (e) and (f) with green and blue respectively. The corresponding height difference is 3.704 nm and 2.302 nm. AFM measurement performed by Dr. Nisha Shahi.

Acknowledgement

PhD is a long and challenging journey that demands extensive dedication and I am deeply grateful to everyone who has supported and guided me along this journey.

Peter Grünberg Institute (PGI-6)

I would like to express my gratitude to my supervisor, Dr. Lukasz Plucinski for his invaluable guidance throughout the research. I respect his passion to science and benefit a lot from the discussion with him. Besides, I would like to extend sincere thanks to the head of the PGI-6 institute, Prof. Claus Michael Schneider, whose presence always bring me a sense of tranquility. During the last few years of this work, I am grateful to my colleagues in PGI-6, especially Mohammed Qahosh and Dr. Honey Boben, for their companionship in the group. I truly cherish the time we spent together, whether conducting experiments or sharing moments in the daily life. Your presence and support is invaluable to me.

Peter Grünberg Institute (PGI-9)

I am extremely thankful to PGI-9, particularly Prof. Detlev Grützmacher for allowing me to use the ultra-high vacuum MBE chamber and other equipment in PGI-9. Furthermore, I am deeply indebted to Dr. Abdur Rehman Jalil, who has supported me throughout my entire PhD, as a supervisor and also as a friend. I have been profoundly influenced by his attitude to science and life. Special thanks to the colleagues in PGI-9, especially Dr. Elmar Neumamn for his dedication to TEM lamella preparation for almost three years, and also Stehpany Bunte and Jinhee Bae. I would also like to thank Abbas Espiari for the introduction to the MBE growth and substrate cleaning, Max Vaßen-Carl for providing the topological insulator thin film sample, and Jonas Buchhorn for performing the transport measurements on SnBiTe-147 thin films. Many thanks as well for the support and insightful discussions over the past three years from Dr. Peter Schüffelgen, Dr. Gregor Mussler, Dr. Kaycee Underwood, Dr. Nisha Shahi.

Ernst Ruska-Centre (ERC)

I would like to express my sincere appreciation to Ernst Ruska-Centre (ERC) for facilitating me to perform TEM measurements during my PhD. Additionally, I deeply grateful to Prof. Joachim Mayer for being my second supervisor, reviewing my thesis and for the valuable discussions in the middle stage of the work. I am also thankful to the colleagues in ERC, Dr. Janghyun Jo for training me on the ChemiSTEM and providing support whenever I encountered difficulties during TEM measurements; Dr. Matina Luysberg and Dr. Xiankui Wei for their discussion of the TEM results in earlier stages of my PhD; Dr. Pengfei Cao for the discussions regarding TEM measurements of topological thin films; and Lea Risters for her assistance in the lamella fabrication.

Additionally, I would like to acknowledge Dr. Steffen Schreyeck (Würzburg University)

for providing the V-doped BST thin film specimens for the AREPS measurement, and all the beamline scientists at the NanoESCA beamline at Elettra and the PHELIX beamline at SOLARIS, for contributing to the ARPES measurements in this thesis.

In the end, I would like to express my deep gratitude to my family and friends. To my friends, thank you for the encouragement and companionship. I really enjoy the memorable time with you. To my parents, thank you for your encouragement and sacrifices, especially during the challenging time of the pandemic and my PhD stage. To my husband, Yi, I can never imagine the life without you, thank you for being together with me and always support me. Your support made this achievement possible.

List of Tables

3.1 An overview of the cleaning steps for Si (111) substrate [22, 88]. 21

6.1 **An overview of SnBT stoichiometric alloys prepared via MBE.** For each state the relative contents of individual elements i.e. Sn, Bi and Te, the number of individual layers of SnTe and Bi_2Te_3 in a unit cell, the out-of-plane predicted ($c_{predicted}$) and measured (c_{actual}) lattice constant together with the in-plane (a_{actual}) lattice constants from XRD are listed. . 86

6.2 Growth parameters of Bi_2Te_3,SnBT-147, SnBT-124 and SnBT-225. 88

6.3 An overview of the measured structural parameters via STEM-HAADF line profiles, including the unit cell length (c_{actual}), vdW gaps sizes, the corresponding projected bond lengths and real bond lengths for the stoichiometric states of SnBT-124, SnBT-147 and SnBT-225. 97

6.4 The summary of the parameters extracted from Hall measurements with varying temperature of SnBT-147 thin films in different thicknesses. MR represents the percentage change in the magnetoresistance in R_{xx} between B = 0 T and B = 10 T. 101

6.5 The summary of the parameters extracted from Hall measurements with varying gate voltage of SnBT-147 thin films in different thicknesses. MR represents the percentage change in the magnetoresistance in R_{xx} between B = 0 T and B = 10 T. 101

List of Figures

2.1 **Insulating phases in two dimensions.** (a) The topologically trivial insulator with electrons bound in localized orbitals (left), where its occupied valence band is separated from the empty conduction band by an energy gap (right). (b) The topological non-trivial quantum Hall state where the external strong magnetic field leads to the closed circular orbits of the electrons, allowing the charge to flow in one-dimensional edge states ("chiral" edge states). (c) The topological non-trivial quantum spin Hall state without external magnetic field, where the SOC leads to "helical" spin-polarized conducting states at the boundary. Image taken from [28]. . 5

2.2 Topological phase transition from normal insulator via Dirac semimetal to the topological insulator with respect to SOC strength, adopted from [34]. 7

2.3 **Evolution of the electronic band structure in Bi_2Se_3.** Degenerated states are lifted up by chemical bonding, crystal-field splitting and SOC, band inversion happens at Γ-point in the end. Images adopted from [27]. . 8

2.4 **Schematic representation of the time-reversal invariant momenta (TRIM) points Γ_{ij}.** (a) Projection of the 4 bulk TRIM points (black circles) in a square 2D Brillouin zone (BZ) onto the egde with 2 edge TRIM points Λ_a. (b) Projection of eight TRIM points on a cubic 3D BZ onto the surface with 4 edge TRIM points. (c)-(d) schematic illustrations of electronic dispersion between two Kramer's degenerate boundary TRIM points Λ_1 and Λ_2 for a trivial insulator $\nu_0 = 0$ in (c) and topological insulator $\nu_0 = 1$ in (d). The number of surface state crossing the Fermi level shown with red dots determine the topological properties, where the odd number of the crossing leads to the topologically protected metallic boundary states. Images adopted from [1, 5]. 10

2.5 **Schematic illustration of the STI with the 3D cubic BZ, which can be identified by the topological invariants** $\nu_0;(\nu_1\nu_2\nu_3)$**.** The parity of the 8 TRIM points in 3D BZ are given in "+" for δ_i = +1 and "-" for δ_i = -1, while the 3D parity projections on the (001) surface with 4 surface TRIM points Λ_a by $\pi_a = \delta_{a1} \cdot \delta_{a2}$ are marked by white (π = +1) and black (π = -1) circles. The thick lines in the bottom panel indicate possible Fermi contours that enclose specific Λ_i. This topological class exhibits the Z_2 variant $\nu_0;(\nu_1\nu_2\nu_3)$ = 1;(111), with one projected surface TRIM exhibiting odd parity, so that all surfaces will have an odd number of black circles. Image adopted from [5]. 11

2.6 **Schematic representation of two types of HOTI with topologically protected hinge excitations of second-order 3D TI.** (a) Time-reversal breaking model with chiral hinge currents flowing along the corners of a cubic crystal which is protected by 4-fold rotational symmetry along along z-axis ($\hat{C}_4^z$). (b) Time-reversal invariant model with anti-propagating Kramers pairs of hinge modes. The highlighted planes in gray represent the mirror planes that protect the hinge states along the xy-plane $\hat{M}_{xy}$ and x$\bar{y}$-plane $\hat{M}_{x\bar{y}}$. Image taken from [46]. 12

2.7 **The quantum anomalous Hall edge states in magnetically doped thin films.** (a) The chiral edge mode that appears in a magnetic topological insulator when the Fermi level, E_F, is located in the mass gap induced by the magnetic exchange interaction. The edge electrons conduct electricity without dissipation in one direction along the edge of the sample. (b) The gapped Dirac-like dispersion of the edge state in a MTI. Images adopted from [53]. 13

2.8 **Schematic diagram representing phase transition in a STI, induced by band crossing when a single control parameter is varied in the system.** The control parameter (white arrow) along the x-axis is modifying the strength of SOC and the size of inverted/non-inverted bandgap. The dotted line represents the topological-trivial transition critical value with 0 eV bandgap (phase boundary). Image adopted from [63]. 14

3.1 **An overview of MBE machine and its working activities.** (a) Schematic diagram of the MBE system showing the main components (growth chamber, buffer chamber, effusion cells, heater, cryo panels and so on). Images modified from [74]. (b) A photograph of BST-MBE chamber setup used in this study. (c) Activities happening in the growth chamber at the substrate, including adsorption, surface migration and dislocation, chemisorption and thermal desorption. 17

3.2 **Vapor pressure of various elements as a function of temperature.** The blue dots represent the melting points of corresponding elements, while their boiling points are generally too high to be included in this graphic. Data taken from the website of Dr. Eberl MBE-Komponenten GmbH [75]. 18

3.3 **Schematic diagram of the Heteroepitaxy and Van der Waals epitaxy (vdWE).** Image modified from [81]. 19

3.4 (a) Schematic illustration of a basic SEM instrument setup; (b) The interaction of electron beam with specimen and various signals emitted from the sample; (c) Mechanisms of emission of secondary electrons (SE) and backscattered electrons (BSE) from the atoms of the sample. Images modified from [92]. 22

3.5 **SEM SE images of Bi_2Te_3 thin film grown on 1×1 cm_2 Si(111) substrate.** (a) from the edge. (b), (c) from the center of the sample, where (c) is the magnified image from the region in red box in (b). 23

3.6 (a) Inter-atomic force vs. distance between AFM tip and sample. (b) Schematic illustration of an atomic force microscope with main components and the main modes used this this study. Image adopted from [96]. . 23

3.7 **Schematic illustration of Bragg diffraction and the working principle of XRD machine.** (a) Geometrical condition of the Bragg diffraction of X-rays from the lattice planes in a crystal [98]. Here, the path difference of the lower path ray and the upper ray is $2dsin\theta$, which must be an integer multiple of the wavelength to satisfy the constructive interference. (b) $\omega/2\theta$ working mode in the XRD instrument (adopted from [99]). The specimen is fixed while the X-ray source tube and the detector rotated simultaneously over certain angle ranges by the goniometer. 25

3.8 **XRD characterization of Bi_2Te_3 epilayer prepared at the optimal growth parameters.** (a) Measured and simulated XRR curves providing information about the thickness and roughness of the epilayer, (b) XRD $\theta/2\theta$ scan confirms the single crystallinity, (c) Rocking Curve acquired at Bi_2Te_3 (000 15) peak, (d) symmetric RSM across Bi_{TRIG} peak to evaluate the out-of-plane lattice parameter and to identify the presence of any tilted grains and (e) asymmetric RSM across Bi_2Te_3 (1 $\bar{1}$ 0 20) peak to evaluate the in-plane lattice parameters. RSM data provided by Dr. Abdur Rehman Jalil. 27

3.9 **STEM system utilized in this study.** (a) FEI Titan G2 80-200 ChemiS-TEM, equipped with a Schottky type high-brightness electron gun (FEI X-FEG), a Cs probe corrector (CEOS DCOR), an in-column Super-X energy dispersive X-ray spectroscopy (EDX). (b) Schematic ray diagrams of convergent probe in STEM, where the HAADF, ADF and BF detectors setup is displayed with respect to the range of electron scattering angles, θ_1, θ_2 and θ_3 represent the angular ranges of the corresponding detectors relative to the vertical direction. Image modified from [100]. 28

3.10 **STEM images acquired along [110] projection of Bi_2Te_3.** (a) HAADF image showing that brighter atoms are Bi while relative lighter ones are Te atoms. (b) BF image depicting that the heavier Bi atoms are darker than Te atoms. HAADF and BF images exhibit inverted contrast. 29

3.11 Schematic illustration of the principle of EDX. Image modified from [97]. 30

3.12 **EDX investigation of a superconductor-TI system.** (a) Top: ADF-STEM image of the $(Bi_xSb_{1-x})_2Te_3$-Vanadium system; Bottom: EDX area-scan spectra across the interface, showing the elemental intensity profile as a function of scanned area. (b) Top: ADF-STEM image of same material system; Bottom: elemental distribution of Pt, V, Bi, Sb, Te, O in the grown system. The sample used in this measurement was provided by Max Vaßen-Carl from PGI-9 at Forschungszentrum Jülich. 31

3.13 **FIB-SEM system.** (a) Appearance of the FEI Helios NanoLab 600i used for the lamella preparation in this work; (b) schematic illustration of the FIB-SEM system during working procedure. GIS: gas injection system. . 32

3.14 **Schematic illustration of FIB operation principles:** (a) imaging; (b) milling; (c) deposition. Images adopted from [116]. 33

3.15 **Primarily TEM lamella preparation procedure.** (a) Electron beam platinum protection layer. (b) Ion beam platinum protection layer. (c) Trenches cut allowing undercut and manipulator approach. (d) Undercut and partially side cut of the lamella. (e) Connection between the needle and the lamella with cutting the side part. (f) Lift off of the lamella with the manipulator. (g) Lamella transfer to the grid. (h) Lamella attachment to the grid and cut from needle. (i) Final lamella after a series of thinning processes. Image taken from Xiao Hou's master thesis [119]. 34

3.16 (a) Sample magazine at PGI-6 ARPES lab. Samples are glued on 10×10 mm^2 Molybdenum plates with silver epoxy. Here, the plates are mounted on the Omicron flag style holders. The samples on the top and middle are prepared for tape cleaving: the main part of the scotch tap is attached to the sample while the other side of the tape grips the wire, which is used to pull off the surface of the sample. The bottom one is prepared for post-cleaving, where two posts are attached on the sample by silver epoxy. (b) and (c) Schematic illustrations of the cleaving process using the scotch tape. (d) and (e) Schematic illustrations of the cleaving process for the TI thin films with capping using the post. The capping layer can be removed by applying forces to the post under UHV, ensuring that the surface of the TI thin film is never exposed to the atmosphere. Images were processed in collaboration with Mohammed Qahosh in PGI-6. 36

3.17 (a) Schematic view of the ARPES system at PGI-6, Forschungszentrum Jülich. The machine consists of load lock chamber, preparation chamber, main chamber, hemispherical electron analyzer, focused Helium lamp, Xe lamp and laser as photon sources, and 5-axis manipulator with a LHe cryostat. (b) Interaction of the photon with the sample. Photon source impinges on the sample surface, electrons are emitted and then pass through the hemispherical electron analyzer, having a certain kinetic energy E_{kin} and emission angle φ and θ. (c) Schematic illustration of the hemispherical electron analyzer. (a) and (c) are taken from Dr. Markus Eschbach's thesis [125]. 37

3.18 **Comparison of the ARPES map of bulk and thin film sample with the helium lamp and laser:** (a) ARPES $E(k_{\parallel,y})$ map of cleaved Sb_2Te_3 bulk sample measured with the helium lamp. (b) and (c) ARPES $E(k_{\parallel,y})$ maps of vacuum-transferred BST thin film measured with the helium lamp and laser, respectively. (Measurements were performed with assistance of Mohammed Qahosh.) 40

3.19 Schematic illustration of the experimental setup in NanoESCA as an example of an energy-filtered photoemission microscope. Image adapted from [130]. 41

4.1 (a) Experimental ARPES measurement on Sb_2Te_3, Bi_2Te_3 and Bi_2Se_3 along $\overline{\Gamma M}$ direction showing the corresponding band structure and Dirac cone. ARPRS measurement in PGI-6 ARPES lab. (b) First-principle calculation of the surface electronic structure showing topological surface states of the three materials at $\overline{\Gamma}$ point, images taken from [27]. 44

4.2 (a) ARPES Fermi surface maps (top row) and band dispersions along $K - \Gamma - M$ (bottom row) directions for bulk single crystals with nominal compositions of Bi_2Te_3, $(Bi_{0.75}Sb_{0.25})_2Te_3$, $(Bi_{0.50}Sb_{0.50})_2Te_3$, $(Bi_{0.25}Sb_{0.75})_2Te_3$ and Sb_2Te_3. Image taken from [145]. (b) Energy diagram of a completely compensated TI with band gap E_g. E_c and E_v are the unperturbed conduction and valance band, μ corresponds to the Fermi level, E_e and E_h in dashed lines are the percolation levels for electrons and holes. Puddles occupied by carriers are shaded. Image taken from [146]. (c) Composition structure diagram of the BSTS system. Image taken from [147]. 46

4.3 **SEM images representing the Bi_2Te_3 epilayer surface imperfections** in (a) due to the cleaning issue during the substrate cleaning process, (b) because of the low Bi source temperature, (c), which has an improved surface but with domains due to the slightly higher substrate temperature. 49

4.4 **STEM-HAADF images acquired along Si[$1\bar{1}0$] projection containing grains/non-twinning domains.** (a) BST epilayer grown exhibits high defect density with grain boundaries (orange line) and also translational shear faults (yellow lines, will be discussed later) as well. (b) $Sn_2Bi_2Te_5$ epilayer exhibits high defect density with similar defects. 50

4.5 **STEM images acquired along Si[$1\bar{1}0$] projection of the BST epilayer representing twin domains.** (a) BF image depicting rotational twin domain through the entire layer, the orientations of the twin domains are indicated by the yellow dotted lines, (b) the corresponding contrast-inverted HAADF image with same information, (c) HAADF image showing the twin domain in a small region of the epilayer, with the magnified twin domain displayed on the upper right. 51

4.6 **STEM-HAADF images acquired along Si[$1\bar{1}0$] projection of $SnBi_2Te_4$ epilayer** in (a), where the QL is marked with blue-colored box and SL is marked with orange-colored box, depicting the stacking fault of the material; and of Bi_2Te_3 epilayers prepared with (b) high and (c) moderate growth rate, indicating the presence of translational shear faults (TSFs). . 51

4.7 **STEM images acquired along Si[$1\bar{1}0$] projection of a 3D TI epilayer grown on Si(111) substrate, indicating the defect-free interface.** (a) HAADF image, (inset) the atomic model. (b) BF image. (c) An area-profile with the atomic intensity obtained from the blue box in (a), showing that the distance between the Si and Te monolayer is 0.31 nm while the distance between Te atoms across the vdW gap is 0.34 nm. 52

4.8 **2D atomic model of Bi_2Te_3 growth on Si(111) substrate, viewed along Si[$1\bar{1}0$] projection.** Here are two possible types of structural defect formed at the Si step edge. (a) Antiphase boundary, when the epilayer is collinear with the Si(311) facet and encounters the Si step edge, it rearranges atoms without any antisite defects or atomic layer swapping, thus forming an antiphase domain. The antiphase boundary is marked with the yellow dashed lines. (b) Screw dislocation, when the epilayer is collinear with Si(220) facet and encounters the Si step edge, it forms antisite defects to swap the atomic layer of Bi and Te, thus generating the screw dislocation. Image taken from Dr. Abdur Rehman Jalil's PhD thesis [22]. 53

4.9 **STEM images acquired along Si[$1\bar{1}0$] projection at the cross section of Bi_2Te_3 epilayer with Si step edge regions.** (a) HAADF images showing the Si step edge (highlighted in the blue box) marked with the green arrow. The bandpass-filtered image is depicted in (b), which provides a clearer view of the Si step edge, enhancing the visibility of the structure. (c) Magnified HAADF image obtained from (a), where the epilayer is collinear with Si(311) and the layer rearranges themselves without antisite defect, thus forming the antiphase boundary. (d) HAADF image indicating the presence of screw dislocation due to the Si step. 53

4.10 **STEM images acquired along Si[$1\bar{1}0$] projection of BST epilayer, indicating the appearance of Si step edge.** (a) HAADF image depicting the Si step edge (green arrow) in the blue box. The magnified bandpass-filtered image from the blue box is shown in (b), which gives better visibility of atoms. There is neither an antiphase domain nor screw dislocation formation, rather than a SL instead of a QL. The growth of a SL compensates the lower Si step, thus enabling the further growth of the QL of BST. (b) BF image of (a) represents the same information with the inverted contrast. 54

4.11 STEM-HAADF images acquired along Si[$1\bar{1}0$] projection of 3D TI epilayers, indicating the appearance of screw dislocation (a) due to the formation of the CrTe alloy in the starting phase of the Cr-doped BST growth, or due to the high grow rate/non-proper growth parameters that leads to the screw dislocations in small scale (b), in large scale in (c), marked with the yellow dashed line, respectively. The samples shown in (a) and (c) were grown by Max Vaßen-Carl and Dr. Abdur Rehman Jalil in PGI-9, respectively. 54

4.12 **Intercalation of the adatoms.** HAADF image acquired in the defect region in $Sn_2Bi_2Te_5$ epilayer depicting intercalated adatoms (red circles) at the TSF (yellow arrow) in the highlighted region (blue box). 55

5.1 **Crystal structure illustrations of bismuth nanofilm allotropes.** (a) Top surface view of $Bi_{TRIG}(001)$ where the blue region highlights the 2D in-plane lattices. Cross-sectional side view of one unit cell thick epilayer of $Bi_{TRIG}(001)$ along (b) Si[$1\bar{1}0$] and (c) Si[211] projections. (d) Top surface view of Bi_{TRIG} (012) orientation with two monolayer thick film, and cross-sectional side view of one unit cell thick epilayer of $Bi_{TRIG}(012)$ along (e) Si[$1\bar{1}0$] and (f) Si[211] projections. (g) Top surface view of Bi_{ORTH} phase, (h) side view at 45°-rotated plane, (i) cross-sectional side view of one unit-cell thick epilayer of $Bi_{ORTH}(010)$ along Si[$1\bar{1}0$] and Si[211] projections. Image taken from [17]. 59

5.2 **Identification of optimum growth parameters of the $Bi_{TRIG}(001)$ phase.** Temperature-dependent changes in surface and crystal quality of $Bi_{TRIG}(001)$ epilayers from -20 °C to 80 °C prepared with (a) R_{TF} = 10 nm/h, (b) R_{TF} = 15 nm/h. SEM images of Bi_{TRIG} (001) epilayer prepared at T_{sub} = 40 °C with R_{TF} increasing from (c) 12 nm/h via (d) 14 nm/h, (e) 16 nm/h, (f) 18 nm/h, (g) 20 nm/h to (h) 22 nm/h. Image taken from [17]. Images were processed in collaboration with Dr. Abdur Rehman Jalil. 61

5.3 **XRD characterization of $Bi_{TRIG}(001)$ epilayer prepared at the optimal growth parameters.** (a) Measured and simulated XRR curves providing information about the thickness and roughness of the epilayer, (b) XRD $\theta/2\theta$ scan confirms the single crystallinity, (c) Rocking curve acquired at $Bi_{TRIG}(0003)$ peak, (d) symmetric RSM across Bi_{TRIG} peak to evaluate the out-of-plane lattice parameter and to identify the presence of any tilted grains and (e) asymmetric RSM across $Bi_{TRIG}(1\bar{1}08)$ peak to evaluate the in-plane lattice parameters. Image taken from [17]. Images were processed in collaboration with Dr. Abdur Rehman Jalil. 62

5.4 **Thickness series of the $Bi_{TRIG}(001)$ phase.** (a) XRR-measured curves of epilayers ranging in thickness from 2.2 nm to 13.5 nm, whereas (b) depicts the corresponding diffraction patterns.The dotted black line in (b) indicates a slight shift in the out-of-plane lattice parameter due to thin-film effect. Image taken from [17]. Images were processed in collaboration with Dr. Abdur Rehman Jalil. 63

5.5 **XRD $\theta/2\theta$ scan of BiSb samples with different thicknesses.** Here, Sb was alloyed into Bi with the content between 4% to 7%. The growth rate of Bi is 22 nm/h, while that of Sb is 1 nm/h. The growth duration for the epilayer at the top (red) and bottom (green) is 75 minutes and 40 minutes, resulting in sample thicknesses of 15.3 nm and 29 nm, respectively. Data provided by Dr. Abdur Rehman Jalil, plotted and analyzed by the author. . 64

5.6 **Structural transformation map from Bi_{TRIG}(001) to Bi_{ORTH}(010) phase in Bi epilayers.** Temperature-dependent changes in surface roughness (indicated by black data points) and crystal quality of Bi epilayers prepared at 40 °C $\leq T_{sub} \leq$ 120 °C, R_{TF} = 22 nm/h, result in continually changing structures from Bi_{TRIG}(001) to Bi_{ORTH}(010) phase via polycrystalline states. Image taken from [17]. Images were processed in collaboration with Dr. Abdur Rehman Jalil. 65

5.7 **Structural transformation in Bi epilayers.** (a) Corresponding diffraction pattern at selected T_{sub} indicates the continually reducing and enhancing contributions of Bi_{TRIG}(001) and Bi_{ORTH}(010) phases, respectively. Bi_{TRIG} (0003) and Bi_{ORTH} (020) peak regions are highlighted with green and blue, respectively. (b)-(g) indicate the corresponding morphological variations via SEM images with epilayers prepared at T_{sub} from 50 °C to 100 °C. Image taken from [17]. Images were processed in collaboration with Dr. Abdur Rehman Jalil. 67

5.8 **Growth optimization and structural characterization of Bi_{ORTH} epilayers.** SEM images represent continually improving surface coverage when the epilayers are prepared with (a) R_{TF} = 26 nm/h, (b) 27 nm/h, (c) 28 nm/h, (d) 29 nm/h, (e) 30 nm/h and (f) 32 nm/h while T_{sub} is kept at 100°C. (g) Diffraction pattern of Bi_{ORTH} epilayer prepared at 32 nm/h, (inset) rocking curve acquired at Bi_{ORTH} peak, (h) symmetric RSM acquired at Bi_{ORTH} peak, providing information about the out-of-plane lattice parameters and confirming high crystal quality of the Bi_{ORTH} epilayer. Image taken from [17]. Images were processed in collaboration with Dr. Abdur Rehman Jalil. 68

5.9 **Thickness series of the Bi_{ORTH}(010) phase.** The presence of a high-intensity Si (111) peak in vicinity of the Bi_{ORTH} (020) peak does not facilitate the analysis of thin films via diffraction pattern; however, it can be adopted as a reference in a symmetric RSM. Various symmetric RSMs of Bi_{ORTH} epilayers are acquired at the (020) peak, while the epilayer thickness is varied from (a) 1.6 nm to (b) 2.1 nm, (c) 2.4 nm, (d) 3.5 nm, (e) 4.9 nm, (f) 6.3 nm, (g) 7.5 nm, (h) 8.7 nm, (i) 11.2 nm and (j) 13.6 nm. Image taken from [17]. Images were processed in collaboration with Dr. Abdur Rehman Jalil. 69

5.10 **Evaluation of in-plane lattice parameters of the Bi_{ORTH}(010) epilayers via asymmetric RSM.** (a) A map acquired at the Bi_{ORTH} $(15\bar{1})$ peak in an 8.4 nm thick epilayer, where Δd represents the difference in length between in-plane lattices while Δh represents buckling, i.e., high difference between Bi atoms of the same monolayer; the 45° in-plane rotation led to the formation of pseudo-cubic sub-lattice, and the acquired maps at the Bi_{CUB} $(\bar{2}40)$ and the Bi_{CUB} $(04\bar{2})$ peaks are represented in (b) and (c), respectively. Similar measurements are performed in a 25 nm thick epilayer at (d) Bi_{ORTH} $(15\bar{1})$, (e) Bi_{CUB} $(\bar{2}40)$ and (f) Bi_{CUB} $(04\bar{2})$ peaks, where a difference in buckling height in (d) is observed to enhance from 0.09 Å to 0.29 Å. Image taken from [17]. Images were processed in collaboration with Dr. Abdur Rehman Jalil. 71

5.11 **Buckling height vs. topology in the Bi_{ORTH} epilayers.** (a) Linear interpolation of thickness-dependent acquired values indicate that the buckling height in Bi_{ORTH} epilayers should reach zero, which would allow the realization of the black-phosphorus-like phase of Bi (Bi_{BP}). Image taken from [17], processed in collaboration with Dr. Abdur Rehman Jalil. (b) Theoretical model which indicates any Bi_{ORTH} epilayer hosting the buckling height $\leq$ 0.1 Å must exhibit topology, and thus, all Bi_{ORTH} epilayers with thickness $\leq$ 9 nm are predicted to exhibit non-trivial attributes. Image taken from [138]. 72

5.12 **Domain analysis of Bi nanofilm allotropes and their alignment with respect to the substrate.** (a) Analysis of the Bi_{TRIG}(001) epilayers performed by probing the $(1\bar{1}02)$ peak. (Top) A pole-figure map representing six distinct peaks originating from two 60° in-plane rotated trigonal domains. (Bottom) The ϕ-scan, a 2D cut at χ= 55.7°, (b) A series of ϕ-scans representing temperature-dependent structural transformation in Bi epilayers. The emergence of three-pointed distinct peaks is found to be related to the Bi_{TRIG}(012), whereas the transformation of those three-pointed peaks into 12 distinct peaks is an indication of the orthorhombic crystal structure. (c) Analysis of the Bi_{ORTH}(010) epilayers conducted via probing $(\bar{1}11)$ peak. (Top) A pole-figure map representing 12 distinct peaks originating from three 30° in-plane rotated orthorhombic domains highlighted with district colored and rotated squares. (Bottom) The ϕ-scan, a 2D cut at χ= 59.9°, provides information about the relative presence of domains in the epilayer. Each peak is marked with a color that corresponds to the associated domain. Image taken from [17]. Images were processed in collaboration with Dr. Abdur Rehman Jalil. 74

5.13 **STEM images acquired along Si[$1\bar{1}0$] projection, indicating the effect of image acquisition time on the Bi_{TRIG}(001) epilayers.** The average acquisition time in (b) is higher than (a). The damaged regions in (b) are the confirmation of Bi instability under prolonged electron beam exposure. 76

5.14 **STEM images acquired along Si[$1\bar{1}0$] projection, representing the continual structural damage of Bi epilayer with increasing electron beam illumination time.** The interface between Bi and Si is observed to be the most affected region. The acquisition time remains constant across all images. 77

5.15 STEM-HAADF images of $Bi_{TRIG}(001)$, $Bi_{TRIG}(012)$ and $Bi_{ORTH}(020)$ epilayers, acquired along Si[$1\bar{1}0$] projection, confirming the large grain sizes and high crystal quality of the epilayers. 77

5.16 **STEM investigation of $Bi_{TRIG}(001)$ phase.** (a) A cross-sectional HAADF image of $Bi_{TRIG}(001)$ epilayer acquired along Si[$1\bar{1}0$] projection. The magnified region at the interface can be visualized via (b) HAADF and (c) BF images, respectively. The central marked region is further magnified and depicted in (d), where the periodic stacking of Bi bilayers can be seen in (e) and (f). Image taken from [17]. 78

5.17 **STEM investigation of $Bi_{TRIG}(012)$ phase.** (a) A HAADF image of $Bi_{TRIG}(012)$ grain in a polycrystalline epilayer acquired along Si[$1\bar{1}0$] projection. The central marked region is magnified, filtered (band-pass) and depicted in (f), where the puckered structures of Bi atoms along with a strong buckling between puckered atoms can be perceived. Image taken from [17]. 79

5.18 **STEM investigation of $Bi_{ORTH}(010)$ phase.** (a) A HAADF image of $Bi_{ORTH}(010)$ epilayer acquired at the cross-section along Si[$1\bar{1}0$] projection. The domain is observed to be 2° in-plane rotated with respect to the substrate, which does not allow acquisition of atomically resolved images at the interface. The central highlighted region is magnified and depicted in (h), where the pseudo-cubic structure of Bi sub-lattice is evident. Image taken from [17]. 79

5.19 STEM-HAADF images of (a) co-existence region of Bi_{TRIG} and Bi_{ORTH} phases, (b) further magnification of the yellow box in (a), (c) 30°-rotated $Bi_{TRIG}(001)$ phase, with the atomic resolution image on the top right. The atomic model from the literature [219] fits the atomic arrangement perfectly. The image in the top right of (c) was provided by JinHee Bae. . . . 80

6.1 **An overview of the unit cells of SnBT = $(SnTe)_m(Bi_2Te_3)_n$, showing the main stoichiometric series together with their stacking sequences.** Different colors of various blocks represent different layer structures. With the increase of the atomic fraction of Sn, yellow, orange, brown, green and indigo represent the quintuple layer (QL), septuple layer (SL), 9-atomic, 11-atomic and 13-atomic layer stacking respectively, while the blue means the non-stacked structure of SnTe. 85

6.2 **Atomic models representing the unit cell of SnBT-124, 147 and 225 from top to bottom, with the layer sequence projected along [110], [1$\bar{1}$0] and [001].** Dark red, yellow and green represent Bi, Sn and Te respectively. SnBT-124 has the unit cell with the building blocks of 3 septuple layers (SL), 147 has the alternative building blocks of a quintuple layer and a septuple layer (QL+SL), where 225 consists of the building block of a 9-atomic layer. Dotted orange lines indicate vdW gaps inside the materials. 87

6.3 XRD $\theta/2\theta$ scan of SnBT-124 epilayer, consisting of (m:n)=(3:3), with the unit cell length c = 41.48 ± 0.01 Å, $\Delta\omega$ scan indicates the FWHM = 389.2 arcseconds, obtained at 2θ = 45.89° at (000 21) peak. 89

6.4 **Lattice parameters analysis of SnBT-124 via XRD.** (a) Evaluation of unit cell length "c" according to Bragg diffraction by XRD $\theta/2\theta$ scan. The plot depicts the relation between diffraction index (n) and incidence angle (θ_n). (b) Asymmetric RSM of SnBT-124 acquired along the (1 $\bar{1}$ 0 28) peak, providing the in-plane and out-of-plane lattice constant. RSM measurement performed by Dr. Abdur Rehman Jalil. 90

6.5 **AFM images of SnBT-124 sample with low and high magnification.** (a) Low magnification image, where the averaged roughness is 2.645 nm. Two line scans of the surface morphology in two positions are demonstrated in (b) and (c) with green and blue respectively. The corresponding height difference is 4.282 nm and 3.563 nm. (d) High magnification image, where the averaged roughness is 2.229 nm. Two line scans of the surface morphology in two positions are demonstrated in (e) and (f) with green and blue respectively. The corresponding height difference is 4.372 nm and 1.814 nm. AFM measurement performed by Dr. Nisha Shahi. . . 90

6.6 **Structural transformation from SnBT-124 to SnBT-147.** (a) XRD $\theta/2\theta$ scans of the growth transformation from SnBT-124 to SnBT-147 epilayer. The characteristic peak (000 6) at 2θ = 12.83° for SnBT-124 is observed to gradually broaden and then split into two peaks with the increase of Bi content and decrease of Sn content. With the further increase the divided peaks can be observed to move in the opposite directions (better visibility with the red arrows). The two splited peaks are the characteristic peak (000 3) and (000 4) for SnBT-147. (b) XRD $\theta/2\theta$ scan of SnBT-147 epilayer, consisting of (m:n)=(1:2), with the unit cell length c = 24.01 ± 0.01 Å, $\Delta\omega$ scan indicates the FWHM = 110.41 arcseconds, obtained at 2θ = 45.33° at (000 12) peak. 91

6.7 **Lattice parameters analysis of SnBT-147 via XRD.** (a) Evaluation of unit cell length "c" according to Bragg diffraction by XRD $\theta/2\theta$ scan. The plot depicts the relation between diffraction index (n) and incidence angle (θ_n). (b) Asymmetric RSM of SnBT-147 acquired along the (1 $\bar{1}$ 0 16) peak, showing that lattice constants "a" and "c" are in good agreement with theoretical value. RSM measurement performed by Dr. Abdur Rehman Jalil. 92

6.8 **Structural transformation from SnBT-124 to SnBT-225.** (a) XRD $2\theta - \theta$ scans of the growth transformation form SnBT-124 to SnBT-225 epilayer. The characteristic peak (000 6) for SnBT-124 is gradually broadened and then split into two peaks with the increase of Bi content and decrease of Sn content. With the further trend of Bi and Sn, the divided peaks can be observed to move in the opposite directions (better visibility with the red arrows). The two splited peaks are the characteristic peak (000 2) and (000 3) for SnBT-225. (b) XRD $\theta/2\theta$ scan of SnBT-225 epilayer, consisting of (m:n)=(2:1), with the unit cell length c = 17.6 ± 0.01 Å, $\Delta\omega$ scan indicates the FWHM = 576.76 arcseconds, obtained at 2θ = 46.42° at (000 9) peak. 93

6.9 **Lattice analysis of SnBT-225 via XRD.** (a) Evaluation of unit cell length "c" according to Bragg diffraction by XRD $\theta/2\theta$ scan. The plot depicts the relation between diffraction index (n) and incidence angle (θ_n). (b) Asymmetric RSM of SnBT-225 acquired on the ($\bar{1}$ 1 0 12) peak, showing that lattice constants "a" and "c" are in good agreement with theoretical value. RSM measurement performed by Dr. Abdur Rehman Jalil. 94

6.10 **STEM-HAADF images acquired along the Si[$1\bar{1}0$] and Si[211] projections in the left and right respectively, representing the unit cells of SnBT-124.** The arrangement of the unit cells in both projections in the HAADF images confirms SL stacking order. The bandpass-filtered HAADF images are shown on the top right of both images, where the atomic model of SnBT-124 could fit perfectly into the experimental atoms. 95

6.11 **STEM-HAADF images acquired along the Si[$1\bar{1}0$] and Si[211] projections in the left and right respectively, representing the unit cells of SnBT-147.** The arrangement of the unit cells in both projections in the HAADF images confirms QL+SL alternate stacking order. The bandpass-filtered HAADF images are shown on the top right of both images, where the atomic model of SnBT-147 could fit perfectly into the experimental atoms. 95

6.12 **STEM-HAADF images acquired along the Si[1$\bar{1}$0] and Si[211] projections in the left and right respectively, representing the unit cells of SnBT-225.** The arrangement of the unit cells in both projections in the HAADF images confirms 9-atomic layer stacking order. The bandpass-filtered HAADF images are shown on the top right of both images, where the atomic model of SnBT-225 could fit perfectly into the experimental atoms. 96

6.13 STEM-HAADF images of 5 alloys in SnBT series with the increase of the Sn content from left to right, where four of them are trigonal phase and SnTe is the cubic phase. 96

6.14 **Atomic model representing (a) the vdW gap between a QL and SL in SnBT-124 as an example.** α is the pristine vdW gap, β represents the projected bond length between neighboring Te atoms on both sides of the vdW gap while θ is the angle of the atomic arrangement based on the horizontal line. 97

6.15 **Schematic illustration of a 16 μm wide Hallbar with metallic contact as an example.** X_1 and X_3 are the input longitudinal terminals with V_{xx} applied between the contacts. Hall voltage (V_{xy}/V_H) is measured between terminals X_2 and Y_2. 98

6.16 **Hall measurements of SnBT-147 at constant voltage with varying the temperature.** (a) Temperature dependent trend in longitudinal resistance (R_{xx}) vs. applied magnetic field (B). (b) Temperature dependent trend of weak anti-localization in R_{xx} at lower magnetic fields. (c) Hall resistance R_{xy} versus applied field. (d) 2D carrier concentration (η_{2D}); (e) mobility (μ); (f) phase coherence length (l_ϕ). Data and images provided by Jonas Buchhorn. 99

6.17 **Hall measurements of SnBT-147 at constant temperature with varying the gate voltage.** (a) Voltage dependent trend in longitudinal resistance (R_{xx}) vs. applied magnetic field (B). (b) Voltage dependent trend of weak anti-localization in R_{xx} at lower magnetic fields. (c) Hall resistance R_{xy} versus applied field. (d) 2D carrier concentration; (e) mobility; (f) phase coherence length. Data and images provided by Jonas Buchhorn. . . 100

6.18 **STEM-HAADF images indicating different types of defects found in the SnBT-147 thin film.** (a) The stacking fault where the sequence follows QQLLQQL rather than the typical alternating Q+L layer structure. (b) Two overlapping grains, as illustrated in the diagram at the bottom left. (c) A layer fault analogous to translational shear fault (TFS) in the thin film. Additionally, screw dislocations are present in both (b) and (c). . 102

7.1 **Terrace study of $MnBi_6Te_{10}$ with work function and XPS measurement.** (a) Illustration of the three possible terminations in $MnBi_6Te_{10}$. (b) Colored work function mapping of the cleaved bulk $MnBi_6Te_{10}$ crystal, with different regions in three contrasts, indicating the presence of the three types of termination presented in (a). (c) Work function plots acquired from the three-colored regions in (b). As indicated from the three-colored circles in (b), the red plot is extracted from the white region, blue and green curves are from the same colored regions in (b) respectively. (d)-(f) XPS spectra acquired at the three-colored regions in (b) respectively. The peak appearing at approx. 47.5 eV in (d) is the characteristic peak of Mn 3p, indicating the presence of Mn in this terrace. Both (e) and (f) depict the XPS spetra of Bi_2Te_3 terraces, though the sequence of the two QLs remains unknown. Data collected at NanoESCA beamline by Dr. Lukasz Plucinski's group, plotted and analyzed by the author. 106

7.2 The Work function map under a series of binding energies from 0.3 eV to 0.8 eV (in steps of o.1 eV) fom (a) to (f). (c)-(e) indicate that there are clear boundaries between the three contrast (black/dark-gray/white). Data collected at NanoESCA beamline by Dr. Lukasz Plucinski's group, exacted and analyzed by the author. 107

7.3 **Experimental CD-ARPES with photon source energy hν = 6 eV on one of Bi_2Te_3 terraces of $MnBi_6Te_{10}$ crystal. ARPES system is cooled down to 5.1 K.** (a) Experimental setup for the measurement. Light impinges on the sample surface within the $\overline{M}-\overline{\Gamma}-\overline{M}$ plane. (b), (c) ARPES maps from Bi_2Te_3 terrace at the Fermi level, taken with RCP and LCP light at 6 eV respectively. (d) CD-ARPES map obtained from (b) and (c), the maps use the color scale shown in (e). In this case, the reaction plane coincides with a mirror plane of the material, which is reflected in the CD-ARPES maps by the sign reversal upon reflection at the mirror plane. Data in (b)-(d) provided by Dr. Lukasz Plucinski, plotted and analyzed by the author. 108

7.4 High-resolution CD-ARPES at different binding energies for the bulk MnBiTe sample, shown in (a)-(e) from the Fermi level to 0.20 eV (in steps of 0.05 eV) and at 0.22 eV in (f), in which the Dirac cone is located. All maps exhibit inverted CD spin with respect to the reaction plane, CD(k_x, k_y) = -CD(k_x, -k_y). Data provided by Dr. Lukasz Plucinski, plotted and analyzed by the author. 109

7.5 CD-ARPES cuts along $\overline{M}-\overline{\Gamma}-\overline{M}$ in (a) and $\overline{K}-\overline{\Gamma}-\overline{K}$ in (b) from the measurement results in Fig. 7.3. Data provided by Dr. Lukasz Plucinski, plotted and analyzed by the author. 109

7.6 **High-resolution CD-ARPES maps of different k_x cuts.** (a) CD-ARPES energy cut at the Fermi level. (b)-(i) represent the corresponding CD-ARPES cuts along $\overline{K}-\overline{\Gamma}-\overline{K}$ at k_x = -0.72 Å^{-1}, -0.48 Å^{-1}, -0.24 Å^{-1}, 0 Å^{-1}, 0.24 Å^{-1}, 0.48 Å^{-1}, 0.72 Å^{-1} and 0.96 Å^{-1}, respectively. It is clearly observed that all E(k_y) spectra have the reversed CD sign over the yellow dashed line marked within the maps. Furthermore, the black dotted lines in (d)-(f) indicate the energy at which the CD sign is reversed. (Data provided by Dr. Lukasz Plucinski, plotted and analyzed by the author.) . . 110

7.7 (a) The atomic model of three unit cells of pure Bi_2Te_3 crystal. (b) The atomic model of a unit cells of $MnBi_6Te_{10}$ crystal. (c)-(d) spin-polarized and Y_l^m calculation of Bi_2Te_3 slabs. (e)-(f) spin-polarized and Y_l^m calculation of the 2QL Bi_2Te_3-terminated $MnBi_6Te_{10}$ crystal (MBT) slabs. Data in (c)-(f) provided by Dr. Lukasz Plucinski, plotted and analyzed by the author. 111

7.8 (a) Y_l^m calculation of the topmost five layers in the Bi_2Te_3 terrace in Fig.7.7(a); (b) Out-of-plane spin calculation of the topmost five layers in Bi_2Te_3 terrace in Fig.7.7(a), using WIEN2k theory. Data provided by Dr. Lukasz Plucinski, plotted and analyzed by the author. 112

7.9 (a) Calculated Y_l^m of the first Te atom layer of the Bi_2Te_3 terrace. (b) Top view of the 3D calculation data. (c) CD-ARPES cut along $\overline{K}-\overline{\Gamma}-\overline{K}$ direction. Data provided by Dr. Lukasz Plucinski, plotted and analyzed by the author. 113

7.10 **CD-ARPES at hν = 40 eV on one of the Bi_2Te_3 terraces and the $MnBi_2Te_4$ terrace.** (a) Experimental setup for the measurement. Light incidents on the sample surface within the $\overline{K}-\overline{\Gamma}-\overline{K}$ plane. (b)-(d) are acquired from Bi_2Te_3 terrace, while (e)-(g) are acquired from $MnBi_2Te_4$ terrace of the $MnBi_6Te_{10}$ crystal. (b) CD-ARPES energy map at E_B = 0.4 eV of the Bi_2Te_3 terrace. The black dashed lines indicate the cut direction where the corresponding 2D cuts along $\overline{M}-\overline{\Gamma}-\overline{M}$ (c) and $\overline{K}-\overline{\Gamma}-\overline{K}$ (d). (e) CD-ARPES energy map of the $MnBi_2Te_4$ terrace at E_B = 0.6 eV. The black dashed lines indicate the cut direction with the corresponding 2D cuts along $\overline{M}-\overline{\Gamma}-\overline{M}$ in (f) and $\overline{K}-\overline{\Gamma}-\overline{K}$ in (g). (b)-(g) Data collected at NanoESCA beamline by Dr. Lukasz Plucinski's group, plotted and analyzed by the author. 114

7.11 CD-ARPES at different binding energies from the Fermi level to 0.7 eV (in steps of 0.1 eV) on one of the Bi_2Te_3 terraces. Data collected at NanoESCA beamline by Dr. Lukasz Plucinski's group, plotted and analyzed by the author. 115

7.12 CD-ARPES at different binding energies from the Fermi level to 0.7 eV (in steps of 0.1 eV) on the $MnBi_2Te_4$ terrace. Data collected at NanoESCA beamline by Dr. Lukasz Plucinski's group, plotted and analyzed by the author. 115

7.13 **Surface electronic structure of the vacuum-transferred BST thin film (from PGI-9) measured with helium lamp in PGI-6.** (a) 3D data stack ($I(E_B, k_x, k_y)$) obtained from the Fermi surface mapping of BST thin film, from which the binding energy maps along the $\overline{M}-\overline{\Gamma}-\overline{M}$ direction at k_y = 0 in (b) and the $\overline{K}-\overline{\Gamma}-\overline{K}$ direction at k_x = 0 in (c) are produced. The sample was provided by Dr. Abdur Rehman Jalil in PGI-9. 116

7.14 Electronic band structure of the VBST thin film measured by p-polarised light $h\nu$ = 68 eV at 30K. From left to right are two E(k) plots along $\overline{K}-\overline{\Gamma}-\overline{K}$ direction at k_x = 0, with the pass energy 50 eV and 20 eV, respectively. The ARPES map under pass energy 20 eV has a better energy resolution. 117

7.15 CD-ARPES spectra along the $\overline{K}-\overline{\Gamma}-\overline{K}$ direction of post-cleaved VBST thin film taken at different photon energies. The experimental geometry is identical to that in 7.3(a), where the light is incident within the mirror plane ($\overline{M}-\overline{\Gamma}-\overline{M}$ plane). These spectra use the 2D colormap on the right. 118

A1.1 Metal holder for the topological insulator (TI) thin film growth with 100 mm diameter that allows to perform the epitaxial growth of 4 different sample at the same time. 122

A1.2 STEM-HAADF image indicating the appearance of curtain effect due to the usage of Pt deposition layer during the FIB preparation process. 123

A1.3 Schematic drawing of the UHV vacuum suitcase. 123

A1.4 Atomic representation of different surface orientations. Here are three atomic surface geometries, i.e. Si(111), Si(220) and Si(311). 124

A2.1 Crystal structure of 2D Bi_{TRIG} (012) thin films. (a) Schematic side- and top-views of 2-ML Bi_{TRIG} (012) film with up and down layer represented by green and blue balls, respectively. (c) Atomic-resolution STM image of 4 ML Bi_{TRIG} (012) film on HOPG (Vs = 100 mV, I = 0.08 nA). (d) Line profile along the two lines in panel (c); the height difference for two different atoms in one unit cell is within 0.045 Å. Image taken from [138]. 124

A2.2 HAADF images at low Magnification show (a) discrete whites areas in the center, indicating the discontinuous and unclosed Bi thin films resulted from the imperfect growth; (b) amorphous and crystallized regions within Bi nanofilm; (c) partially amorphous regions in the Bi crystal nanofilm, where the contrast difference within the film is mainly due to FIB preparation process. 125

A2.3 HAADF and BF images of a region in Bi nanofilm, where the film is unclear due to the large thickness and surface oxidation of both side of the lamella. 126

A3.1 AFM images of SnBT-147 sample with low and high magnification. (a) Low magnification image, where the averaged roughness is 3.633 nm. Two line scans of the surface morphology in two positions are demonstrated in (b) and (c) with green and blue respectively. The corresponding height difference is 3.611 nm and 2.274 nm. (d) High magnification image, where the averaged roughness is 3.361 nm. Two line scans of the surface morphology in two positions are demonstrated in (e) and (f) with green and blue respectively. The corresponding height difference is 4.016 nm and 2.478 nm. AFM measurement performed by Dr. Nisha Shahi. . . 127

A3.2 AFM images of SnBT-225 sample with low and high magnification. (a) Low magnification image, where the averaged roughness is 2.657 nm. Two line scans of the surface morphology in two positions are demonstrated in (b) and (c) with green and blue respectively. The corresponding height difference is 2.755 nm and 2.786 nm. (d) High magnification image, where the averaged roughness is 2.028 nm. Two line scans of the surface morphology in two positions are demonstrated in (e) and (f) with green and blue respectively. The corresponding height difference is 3.704 nm and 2.302 nm. AFM measurement performed by Dr. Nisha Shahi. . . 128

Bibliography

[1] M Zahid Hasan and Charles L Kane. "Colloquium: topological insulators". In: *Reviews of modern physics* 82.4 (2010), p. 3045.

[2] Yoichi Ando. "Topological insulator materials". In: *Journal of the Physical Society of Japan* 82.10 (2013), p. 102001.

[3] Xiao-Liang Qi and Shou-Cheng Zhang. "Topological insulators and superconductors". In: *Reviews of Modern Physics* 83.4 (2011), p. 1057.

[4] Joel E Moore. "The birth of topological insulators". In: *Nature* 464.7286 (2010), pp. 194–198.

[5] Liang Fu and Charles L Kane. "Topological insulators with inversion symmetry". In: *Physical Review B* 76.4 (2007), p. 045302.

[6] Charles L Kane and Eugene J Mele. "Quantum spin Hall effect in graphene". In: *Physical review letters* 95.22 (2005), p. 226801.

[7] B Andrei Bernevig, Taylor L Hughes, and Shou-Cheng Zhang. "Quantum spin Hall effect and topological phase transition in HgTe quantum wells". In: *science* 314.5806 (2006), pp. 1757–1761.

[8] Markus Konig et al. "Quantum spin Hall insulator state in HgTe quantum wells". In: *Science* 318.5851 (2007), pp. 766–770.

[9] Dmytro Pesin and Allan H MacDonald. "Spintronics and pseudospintronics in graphene and topological insulators". In: *Nature materials* 11.5 (2012), pp. 409–416.

[10] Takehito Yokoyama and Shuichi Murakami. "Spintronics and spincaloritronics in topological insulators". In: *Physica E: Low-dimensional Systems and Nanostructures* 55 (2014), pp. 1–8.

[11] Bent Weber et al. "2024 roadmap on 2D topological insulators". In: *Journal of Physics: Materials* 7.2 (2024), p. 022501.

[12] Sankar Das Sarma, Michael Freedman, and Chetan Nayak. "Majorana zero modes and topological quantum computation". In: *npj Quantum Information* 1.1 (2015), pp. 1–13.

[13] Anjana Uday et al. "Induced superconducting correlations in a quantum anomalous Hall insulator". In: *Nature Physics* (2024), pp. 1–7.

[14] R Walter Ogburn and John Preskill. "Topological quantum computation". In: *NASA International Conference on Quantum Computing and Quantum Communications*. Springer. 1998, pp. 341–356.

[15] Chia-Hsiu Hsu et al. “Growth of a predicted two-dimensional topological insulator based on InBi-Si (111)-7× 7”. In: *Physical Review B* 98.12 (2018), p. 121404.

[16] Xiaochun Huang et al. “Epitaxial growth of a two-dimensional topological insulator candidate: monolayer Si_2Te_2”. In: *arXiv preprint arXiv:2206.00919* (2022).

[17] Abdur Rehman Jalil et al. “Phase-Selective Epitaxy of Trigonal and Orthorhombic Bismuth Thin Films on Si (111)”. In: *Nanomaterials* 13.14 (2023), p. 2143.

[18] Xi Chen et al. “Molecular beam epitaxial growth of topological insulators”. In: *Advanced Materials* 23.9 (2011), pp. 1162–1165.

[19] Theresa P Ginley, Yong Wang, and Stephanie Law. “Topological insulator film growth by molecular beam epitaxy: A review”. In: *Crystals* 6.11 (2016), p. 154.

[20] Liang He, Xufeng Kou, and Kang L Wang. *Review of 3D topological insulator thin-film growth by molecular beam epitaxy and potential applications*. 2013.

[21] Rabia Sultana et al. “Crystal growth and characterization of bulk Sb_2Te_3 topological insulator”. In: *Materials research express* 5.4 (2018), p. 046107.

[22] Abdur Rehman Jalil and Detlev Grützmacher. “Engineering topological superlattices and their epitaxial integration in selectively grown hybrid nanostructures via MBE”. PhD thesis. RWTH Aachen University, 2022.

[23] Ying Jiang et al. “Direct atom-by-atom chemical identification of nanostructures and defects of topological insulators”. In: *Nano letters* 13.6 (2013), pp. 2851–2856.

[24] Asteriona-Maria Netsou et al. “Identifying native point defects in the topological insulator Bi_2Te_3”. In: *ACS nano* 14.10 (2020), pp. 13172–13179.

[25] Johan Montagnat, Hervé Delingette, and Nicholas Ayache. “A review of deformable surfaces: topology, geometry and deformation”. In: *Image and vision computing* 19.14 (2001), pp. 1023–1040.

[26] Eduardo Fradkin. *Field theories of condensed matter physics*. Cambridge University Press, 2013.

[27] Haijun Zhang et al. “Topological insulators in Bi_2Se_3, Bi_2Te_3 and Sb_2Te_3 with a single Dirac cone on the surface”. In: *Nature physics* 5.6 (2009), pp. 438–442.

[28] Charles L Kane and Eugene J Mele. “A new spin on the insulating state”. In: *Science* 314.5806 (2006), pp. 1692–1693.

[29] F Duncan M Haldane. “Model for a quantum Hall effect without Landau levels: Condensed-matter realization of the" parity anomaly"”. In: *Physical review letters* 61.18 (1988), p. 2015.

[30] Harald Ibach and Hans Lüth. *Festkörperphysik: Einführung in die Grundlagen*. springer-verlag, 2009.

[31] Yoshinori Tokura, Kenji Yasuda, and Atsushi Tsukazaki. “Magnetic topological insulators”. In: *Nature Reviews Physics* 1.2 (2019), pp. 126–143.

[32] Charles L Kane and Eugene J Mele. "Z_2 topological order and the quantum spin Hall effect". In: *Physical review letters* 95.14 (2005), p. 146802.

[33] Gustav Bihlmayer. "40th IFF Springschool". In: Forschungszentrum Jülich, 2009. Chap. A1.

[34] Shu-Ting Pi et al. "New class of 3D topological insulator in double perovskite". In: *The journal of physical chemistry letters* 8.2 (2017), pp. 332–339.

[35] Yabin Fan and Kang L Wang. "Spintronics based on topological insulators". In: *Spin*. Vol. 6. 02. World Scientific. 2016, p. 1640001.

[36] Stephan Plugge et al. "Majorana box qubits". In: *New Journal of Physics* 19.1 (2017), p. 012001.

[37] Chenxi Yue et al. "Device applications of synthetic topological insulator nanostructures". In: *Electronics* 7.10 (2018), p. 225.

[38] Martin J Klein. "On a degeneracy theorem of kramers". In: *American Journal of Physics* 20.2 (1952), pp. 65–71.

[39] Shun-Qing Shen. *Topological insulators*. Vol. 174. Springer, 2012.

[40] Joel E Moore and Leon Balents. "Topological invariants of time-reversal-invariant band structures". In: *Physical Review B—Condensed Matter and Materials Physics* 75.12 (2007), p. 121306.

[41] S Franca, J van den Brink, and IC Fulga. "An anomalous higher-order topological insulator". In: *Physical Review B* 98.20 (2018), p. 201114.

[42] Eslam Khalaf. "Higher-order topological insulators and superconductors protected by inversion symmetry". In: *Physical Review B* 97.20 (2018), p. 205136.

[43] Leena Aggarwal et al. "Evidence for higher order topology in Bi and $Bi_{0.92}Sb_{0.08}$". In: *Nature communications* 12.1 (2021), p. 4420.

[44] Frank Schindler et al. "Higher-order topology in bismuth". In: *Nature physics* 14.9 (2018), pp. 918–924.

[45] Guido Van Miert and Carmine Ortix. "Higher-order topological insulators protected by inversion and rotoinversion symmetries". In: *Physical Review B* 98.8 (2018), p. 081110.

[46] Frank Schindler et al. "Higher-order topological insulators". In: *Science advances* 4.6 (2018), eaat0346.

[47] Ryo Noguchi et al. "Evidence for a higher-order topological insulator in a three-dimensional material built from van der Waals stacking of bismuth-halide chains". In: *Nature Materials* 20.4 (2021), pp. 473–479.

[48] Pinyuan Wang et al. "Intrinsic magnetic topological insulators". In: *The Innovation* 2.2 (2021).

[49] Jieyi Liu and Thorsten Hesjedal. "Magnetic topological insulator heterostructures: A review". In: *Advanced Materials* 35.27 (2023), p. 2102427.

[50] Rui Yu et al. “Quantized anomalous Hall effect in magnetic topological insulators”. In: *science* 329.5987 (2010), pp. 61–64.

[51] Ke He, Yayu Wang, and Qikun Xue. “Quantum anomalous Hall effect”. In: *Topological Insulators: Fundamentals and Perspectives* (2015), pp. 357–376.

[52] Cui-Zu Chang, Chao-Xing Liu, and Allan H MacDonald. “Colloquium: Quantum anomalous hall effect”. In: *Reviews of Modern Physics* 95.1 (2023), p. 011002.

[53] Chao-Xing Liu, Shou-Cheng Zhang, and Xiao-Liang Qi. “The quantum anomalous Hall effect: theory and experiment”. In: *Annual Review of Condensed Matter Physics* 7.1 (2016), pp. 301–321.

[54] Ke He, Yayu Wang, and Qi-Kun Xue. “Topological materials: quantum anomalous Hall system”. In: *Annual Review of Condensed Matter Physics* 9.1 (2018), pp. 329–344.

[55] Cui-Zu Chang et al. “Experimental observation of the quantum anomalous Hall effect in a magnetic topological insulator”. In: *Science* 340.6129 (2013), pp. 167–170.

[56] Cui-Zu Chang et al. “High-precision realization of robust quantum anomalous Hall state in a hard ferromagnetic topological insulator”. In: *Nature materials* 14.5 (2015), pp. 473–477.

[57] Yujun Deng et al. “Quantum anomalous Hall effect in intrinsic magnetic topological insulator MnBi2Te4”. In: *Science* 367.6480 (2020), pp. 895–900.

[58] B Andrei Bernevig, Claudia Felser, and Haim Beidenkopf. “Progress and prospects in magnetic topological materials”. In: *Nature* 603.7899 (2022), pp. 41–51.

[59] Yao-Yi Li et al. “Intrinsic topological insulator Bi_2Te_3 thin films on Si and their thickness limit”. In: *Adv. Mater* 22.36 (2010), pp. 4002–4007.

[60] Su-Yang Xu et al. “Topological phase transition and texture inversion in a tunable topological insulator”. In: *Science* 332.6029 (2011), pp. 560–564.

[61] Yandong Ma et al. “Quantum spin Hall effect and topological phase transition in two-dimensional square transition-metal dichalcogenides”. In: *Physical Review B* 92.8 (2015), p. 085427.

[62] Zhi Wang et al. “Digging for topological property in disordered alloys: the emergence of Weyl semimetal phase and sequential band inversions in PbSe–SnSe alloys”. In: *Materials Horizons* 6.10 (2019), pp. 2124–2134.

[63] Bohm-Jung Yang and Naoto Nagaosa. “Classification of stable three-dimensional Dirac semimetals with nontrivial topology”. In: *Nature communications* 5.1 (2014), p. 4898.

[64] T Sato et al. “Unexpected mass acquisition of Dirac fermions at the quantum phase transition of a topological insulator”. In: *Nature Physics* 7.11 (2011), pp. 840–844.

[65] K. G Günther. “Aufdampfschidhten aus halbleitenden III-V-Verbindungen”. In: *Zeitschrift für Naturforschung A* 13.12 (1958), pp. 1081–1089.

[66] John E Davey and Titus Pankey. “Epitaxial GaAs films deposited by vacuum evaporation”. In: *Journal of Applied Physics* 39.4 (1968), pp. 1941–1948.

[67] John R Arthur. “Interaction of Ga and As_2 molecular beams with GaAs surfaces”. In: *Journal of Applied Physics* 39.8 (1968), pp. 4032–4034.

[68] Al Y Cho and J R Arthur. “Molecular beam epitaxy”. In: *Progress in solid state chemistry* 10 (1975), pp. 157–191.

[69] Tom Foxon. “History of MBE”. In: *Molecular Beam Epitaxy: Materials and Applications for Electronics and Optoelectronics* (2019), p. 1.

[70] Bruce A Joyce and Tim B Joyce. “Basic studies of molecular beam epitaxy—past, present and some future directions”. In: *Journal of crystal growth* 264.4 (2004), pp. 605–619.

[71] Theodore D Moustakas. “Molecular beam epitaxy: thin film growth and surface studies”. In: *MRS Bulletin* 13.11 (1988), pp. 29–36.

[72] W Patrick McCray. “MBE deserves a place in the history books”. In: *Nature nanotechnology* 2.5 (2007), pp. 259–261.

[73] John R Arthur. “Molecular beam epitaxy”. In: *Surface science* 500.1-3 (2002), pp. 189–217.

[74] Guoqing Wu et al. “An intelligent temperature control algorithm of molecular beam epitaxy system based on the back-propagation neural network”. In: *IEEE Access* 10 (2022), pp. 9848–9855.

[75] *Component Selection Guides*. `https://www.mbe-komponenten.de/selection-guide/`.

[76] Marian A Herman et al. “Molecular beam epitaxy”. In: *Epitaxy: Physical Principles and Technical Implementation* (2004), pp. 131–170.

[77] Jörn Kampmeier. “Molecular beam epitaxy of topological insulator thin films”. PhD thesis. Dissertation, RWTH Aachen University, 2018, 2018.

[78] BA Joyce. “Molecular beam epitaxy”. In: *Reports on Progress in Physics* 48.12 (1985), p. 1637.

[79] Wolfgang Braun. *Applied RHEED: reflection high-energy electron diffraction during crystal growth*. Vol. 154. Springer Science & Business Media, 1999.

[80] Ayahiko Ichimiya and Philip I Cohen. *Reflection high-energy electron diffraction*. Cambridge University Press, 2004.

[81] Atsushi Koma. “Van der Waals epitaxy for highly lattice-mismatched systems”. In: *Journal of crystal growth* 201 (1999), pp. 236–241.

[82] Hyunseok Kim et al. “Remote epitaxy”. In: *Nature Reviews Methods Primers* 2.1 (2022), p. 40.

[83] John E Ayers et al. *Heteroepitaxy of semiconductors: theory, growth, and characterization*. CRC press, 2016.

[84] Yunjo Kim et al. “Remote epitaxy through graphene enables two-dimensional material-based layer transfer”. In: *Nature* 544.7650 (2017), pp. 340–343.

[85] Takato Hotta et al. “Molecular beam epitaxy growth of monolayer niobium diselenide flakes”. In: *Applied Physics Letters* 109.13 (2016).

[86] Atsushi Koma. “Van der Waals epitaxy—a new epitaxial growth method for a highly lattice-mismatched system”. In: *Thin Solid Films* 216.1 (1992), pp. 72–76.

[87] Lee A Walsh and Christopher L Hinkle. “van der Waals epitaxy: 2D materials and topological insulators”. In: *Applied Materials Today* 9 (2017), pp. 504–515.

[88] J Krumrain et al. “MBE growth optimization of topological insulator Bi_2Te_3 films”. In: *Journal of Crystal Growth* 324.1 (2011), pp. 115–118.

[89] Namrata Bansal et al. “Transferring MBE-grown topological insulator films to arbitrary substrates and metal-insulator transition via Dirac gap”. In: *Nano letters* 14.3 (2014), pp. 1343–1348.

[90] Xin Guo et al. “Single domain Bi_2Se_3 films grown on InP (111)-A by molecular-beam epitaxy”. In: *Applied Physics Letters* 102.15 (2013).

[91] Zubair Ahmad et al. “Versatility of hydrogels: from synthetic strategies, classification, and properties to biomedical applications”. In: *Gels* 8.3 (2022), p. 167.

[92] *Scanning electron microscope*. `https://en.wikipedia.org/wiki/Scanning_electron_microscope`.

[93] Karen D Vernon-Parry. “Scanning electron microscopy: an introduction”. In: *III-Vs review* 13.4 (2000), pp. 40–44.

[94] Thomas E Everhart and RFM Thornley. “Wide-band detector for micro-microampere low-energy electron currents”. In: *Journal of scientific instruments* 37.7 (1960), p. 246.

[95] SL Erlandsen, PT Macechko, and C Frethem. “High resolution backscatter electron (BSE) imaging of immunogold with in-lens and below-the-lens field emission scanning electron microscopes”. In: *Scanning Microsc* 13 (1999), pp. 43–54.

[96] Itay Rousso and Akshay Deshpande. “Applications of atomic force microscopy in HIV-1 research”. In: *Viruses* 14.3 (2022), p. 648.

[97] Jonathan McAneney. “Characteristics of Thin and Ultrathin Film Ferroelectric Capacitor Structures”. PhD thesis. Queen’s University of Belfast, 2006.

[98] Lothar Spieß et al. “Moderne Röntgenbeugung: Röntgendiffraktometrie für Materialwissenschaftler, Physiker und Chemiker, 2”. In: *Aufl.(Vieweg+ Teubner, Wiesbaden, Germany, 2009)* (2009), p. 80.

[99] J Epp. “X-ray diffraction (XRD) techniques for materials characterization”. In: *Materials characterization using nondestructive evaluation (NDE) methods*. Elsevier, 2016, pp. 81–124.

[100] David B Williams et al. *The transmission electron microscope*. Springer, 1996.

[101] A Muller and John Grazul. “Optimizing the environment for sub-0.2 nm scanning transmission electron microscopy”. In: *Journal of electron microscopy* 50.3 (2001), pp. 219–226.

[102] Charu Arora, Sanju Soni, and Pathik Maji. “Transmission Electron Microscopy: Theory and Applications”. In: *Essential Techniques for Medical and Life Scientists: A guide to contemporary methods and current applications with the protocols: Part 2* (2020), p. 96.

[103] Earl J Kirkland. *Advanced computing in electron microscopy*. Vol. 12. Springer, 1998.

[104] AV Crewe, J Wall, and LM Welter. “A high-resolution scanning transmission electron microscope”. In: *Journal of Applied Physics* 39.13 (1968), pp. 5861–5868.

[105] Albert V Crewe, J Wall, and J Langmore. “Visibility of single atoms”. In: *science* 168.3937 (1970), pp. 1338–1340.

[106] Christian Kisielowski et al. “Detection of single atoms and buried defects in three dimensions by aberration-corrected electron microscope with 0.5-Å information limit”. In: *Microscopy and Microanalysis* 14.5 (2008), pp. 469–477.

[107] Jingyue Jimmy Liu. “Advances and applications of atomic-resolution scanning transmission electron microscopy”. In: *Microscopy and Microanalysis* 27.5 (2021), pp. 943–995.

[108] Niklas Dellby et al. “Progress in aberration-corrected scanning transmission electron microscopy”. In: *Microscopy* 50.3 (2001), pp. 177–185.

[109] DH Shin, EJ Kirkland, and J Silcox. “Annular dark field electron microscope images with better than 2 Å resolution at 100 kV”. In: *Applied physics letters* 55.23 (1989), pp. 2456–2458.

[110] PE Batson, AG Domenicucci, and E Lemoine. “Atomic resolution electronic structure in device development”. In: *Microscopy and Microanalysis* 3.S2 (1997), pp. 645–646.

[111] Joseph I Goldstein et al. *Scanning electron microscopy and X-ray microanalysis*. springer, 2017.

[112] Daisuke Shindo et al. “Energy dispersive x-ray spectroscopy”. In: *Analytical electron microscopy for materials science* (2002), pp. 81–102.

[113] N Yao and A Epstein. *Surface nanofabrication using focused ion beam*. 2010.

[114] Lucille A Giannuzzi et al. *Introduction to focused ion beams: instrumentation, theory, techniques and practice*. Springer Science & Business Media, 2004.

[115] Lixin Gu et al. “Application of FIB-SEM techniques for the advanced characterization of earth and planetary materials”. In: *Scanning* 2020.1 (2020), p. 8406917.

[116] A Zintler et al. “FIB based fabrication of an operative Pt/HfO_2/TiN device for resistive switching inside a transmission electron microscope”. In: *Ultramicroscopy* 181 (2017), pp. 144–149.

[117] Steve Reyntjens and Robert Puers. “A review of focused ion beam applications in microsystem technology”. In: *Journal of micromechanics and microengineering* 11.4 (2001), p. 287.

[118] ND Bassim et al. “Minimizing damage during FIB sample preparation of soft materials”. In: *Journal of Microscopy* 245.3 (2012), pp. 288–301.

[119] Xiao Hou. *Structural characterization of HfO2 thin films for resistive switching memory applications using transmission electron microscopy techniques*. 2021.

[120] GY Jeong and T Nousiainen. “TEM analysis of the internal structures and mineralogy of Asian dust particles and the implications for optical modeling”. In: *Atmospheric Chemistry and Physics* 14.14 (2014), pp. 7233–7254.

[121] Thomas Henning Loeber et al. “Reducing curtaining effects in FIB/SEM applications by a goniometer stage and an image processing method”. In: *Journal of Vacuum Science & Technology B* 35.6 (2017).

[122] Jian Li. “Advanced techniques in TEM specimen preparation”. In: *The transmission electron microscope* (2012), pp. 69–84.

[123] Anirban Pal. “Photoelectric Effect”. In: ().

[124] M Pl Seah and WA Dench. “Quantitative electron spectroscopy of surfaces: A standard data base for electron inelastic mean free paths in solids”. In: *Surface and interface analysis* 1.1 (1979), pp. 2–11.

[125] Markus Eschbach. “Band Structure Engineering in 3D Topological Insulators Investigated by Angle-Resolved Photoemission Spectroscopy”. PhD thesis. 2016.

[126] Abdul-Vakhab Tcakaev. “Soft X-ray Spectroscopic Study of Electronic and Magnetic Properties of Magnetic Topological Insulators”. PhD thesis. Würzburg University, 2023.

[127] R Mewe. “Relative intensity of helium spectral lines as a function of electron temperature and density”. In: *British Journal of Applied Physics* 18.1 (1967), p. 107.

[128] John Joseph Hopfield. “Spectra of Hydrogen, Nitrogen and Oxygen in the Extreme Ultraviolet”. In: *Physical Review* 20.6 (1922), p. 573.

[129] Albert Einstein. *Über einen die Erzeugung und Verwandlung des Lichtes betreffenden heuristischen Gesichtspunkt*. 1905.

[130] Marten Christopher Patt. “Bulk and surface sensitive energy-filtered photoemission microscopy using synchrotron radiation for the study of resistive switching memories”. PhD thesis. 2016.

[131] L Galletti et al. “Josephson effect in Al/Bi_2Se_3/Al coplanar hybrid devices”. In: *Physica C: Superconductivity and its Applications* 503 (2014), pp. 162–165.

[132] Berthold Jäck et al. “Observation of a Majorana zero mode in a topologically protected edge channel”. In: *Science* 364.6447 (2019), pp. 1255–1259.

[133] Mengyun He, Huimin Sun, and Qing Lin He. “Topological insulator: Spintronics and quantum computations”. In: *Frontiers of Physics* 14 (2019), pp. 1–16.

[134] T Khouri et al. “High-temperature quantum Hall effect in finite gapped HgTe quantum wells”. In: *Physical Review B* 93.12 (2016), p. 125308.

[135] Erwann Bocquillon et al. “Gapless Andreev bound states in the quantum spin Hall insulator HgTe”. In: *Nature Nanotechnology* 12.2 (2017), pp. 137–143.

[136] F Reis et al. “Bismuthene on a SiC substrate: A candidate for a high-temperature quantum spin Hall material”. In: *Science* 357.6348 (2017), pp. 287–290.

[137] Ilya K Drozdov et al. “One-dimensional topological edge states of bismuth bilayers”. In: *Nature Physics* 10.9 (2014), pp. 664–669.

[138] Yunhao Lu et al. “Topological properties determined by atomic buckling in self-assembled ultrathin Bi (110)”. In: *Nano letters* 15.1 (2015), pp. 80–87.

[139] N Borgwardt et al. “Self-organized charge puddles in a three-dimensional topological material”. In: *Physical Review B* 93.24 (2016), p. 245149.

[140] CW Rischau et al. “Charge puddles in a completely compensated topological insulator”. In: *New Journal of Physics* 18.7 (2016), p. 073024.

[141] CB Satterthwaite and RW Ure Jr. “Electrical and thermal properties of Bi_2Te_3”. In: *Physical review* 108.5 (1957), p. 1164.

[142] YL Chen et al. “Experimental realization of a three-dimensional topological insulator, Bi_2Te_3”. In: *science* 325.5937 (2009), pp. 178–181.

[143] T Arakane et al. “Tunable Dirac cone in the topological insulator $Bi_{2-x}Sb_xTe_{3-y}Se_y$”. In: *Nature communications* 3.1 (2012), p. 636.

[144] Faxian Xiu et al. “Manipulating surface states in topological insulator nanoribbons”. In: *Nature nanotechnology* 6.4 (2011), pp. 216–221.

[145] Desheng Kong et al. “Ambipolar field effect in the ternary topological insulator $(Bi_xSb_{1-x})_2Te_3$ by composition tuning”. In: *Nature nanotechnology* 6.11 (2011), pp. 705–709.

[146] Brian Skinner, Tianran Chen, and BI Shklovskii. “Why is the bulk resistivity of topological insulators so small?” In: *Physical review letters* 109.17 (2012), p. 176801.

[147] Zhi Ren et al. “Optimizing $Bi_{2-x}Sb_xTe_{3-y}Se_y$ solid solutions to approach the intrinsic topological insulator regime”. In: *Physical Review B* 84.16 (2011), p. 165311.

[148] BI Shklovskiĭ and AL Efros. “Completely compensated crystalline semiconductor as a model of an amorphous semiconductor”. In: *Soviet Journal of Experimental and Theoretical Physics* 35 (1972), p. 610.

[149] Jens Brede et al. “Characterizing the chemical potential disorder in the topological insulator $(Bi_{1-x}Sb_x)_2Te_3$ thin films”. In: *Physical Review Materials* 8.10 (2024), p. 104202.

[150] Yi Huang, BI Shklovskii, et al. “Disorder effects in topological insulator nanowires”. In: *Physical Review B* 104.5 (2021), p. 054205.

[151] Yuqi Xia et al. “Observation of a large-gap topological-insulator class with a single Dirac cone on the surface”. In: *Nature physics* 5.6 (2009), pp. 398–402.

[152] Che-Yu Li, AL Ruoff, and CW Spencer. “Effect of pressure on the energy gap of Bi_2Te_3”. In: *Journal of Applied Physics* 32.9 (1961), pp. 1733–1735.

[153] Tobias W. Schm Abdur Rehman Jalil. “Engineering Epitaxial Interfaces for Topological Insulator—Superconductor Hybrid Devices with Al Electrodes”. In: *Advanced Quantum Technologies* 3.15 (2024), p. 2400343.

[154] David D Awschalom et al. “Quantum spintronics: engineering and manipulating atom-like spins in semiconductors”. In: *Science* 339.6124 (2013), pp. 1174–1179.

[155] Desheng Kong et al. “Topological insulator nanowires and nanoribbons”. In: *Nano letters* 10.1 (2010), pp. 329–333.

[156] Yulieth C Arango et al. “Quantum transport and nano angle-resolved photoemission spectroscopy on the topological surface states of single Sb_2Te_3 nanowires”. In: *Scientific reports* 6.1 (2016), p. 29493.

[157] Rudooh S Wagner and W Chadwick Ellis. “Vapor-liquid-solid mechanism of single crystal growth”. In: *Applied physics letters* 4.5 (1964), pp. 89–90.

[158] Matt Law, Joshua Goldberger, and Peidong Yang. “Semiconductor nanowires and nanotubes”. In: *Annu. Rev. Mater. Res.* 34.1 (2004), pp. 83–122.

[159] EI Givargizov. “Fundamental aspects of VLS growth”. In: *Vapour Growth and Epitaxy*. Elsevier, 1975, pp. 20–30.

[160] Jin Seok Lee et al. “Vapor–liquid–solid and vapor–solid growth of phase-change Sb_2Te_3 nanowires and Sb_2Te_3/GeTe nanowire heterostructures”. In: *Journal of the American Chemical Society* 130.19 (2008), pp. 6252–6258.

[161] Piet Schönherr et al. “Vapour-liquid-solid growth of ternary Bi_2Se_2Te nanowires”. In: *Nanoscale research letters* 9 (2014), pp. 1–6.

[162] Qixun Guo et al. “Electrically tunable wafer-sized three-dimensional topological insulator thin films grown by magnetron sputtering”. In: *Chinese Physics Letters* 37.5 (2020), p. 057301.

[163] Helin Cao et al. “Topological insulator Bi_2Te_3 films synthesized by metal organic chemical vapor deposition”. In: *Applied Physics Letters* 101.16 (2012).

[164] Hsin-Yen Lee et al. “Epitaxial growth of Bi_2Te_3 topological insulator thin films by temperature-gradient induced physical vapor deposition (PVD)”. In: *Journal of Alloys and Compounds* 686 (2016), pp. 989–997.

[165] Mai Lê Anh et al. “Freestanding Nanolayers of a Wide-Gap Topological Insulator through Liquid-Phase Exfoliation”. In: *Chemistry–A European Journal* 27.2 (2021), pp. 794–801.

[166] Svetlana Borisova et al. “Mode of growth of ultrathin topological insulator Bi_2Te_3 films on Si (111) substrates”. In: *Crystal growth & design* 12.12 (2012), pp. 6098–6103.

[167] M Lanius et al. “Topography and structure of ultrathin topological insulator Sb_2Te_3 films on Si (111) grown by means of molecular beam epitaxy”. In: *Journal of Crystal Growth* 453 (2016), pp. 158–162.

[168] Gert Ehrlich and Fo G Hudda. “Atomic view of surface self-diffusion: tungsten on tungsten”. In: *The Journal of Chemical Physics* 44.3 (1966), pp. 1039–1049.

[169] Martin Lanius. “Topological insulating tellurides: how to tune doping, topology, and dimensionality”. PhD thesis. RWTH Aachen University, 2018.

[170] Robert Joseph Cava et al. “Crystal structure and chemistry of topological insulators”. In: *Journal of Materials Chemistry C* 1.19 (2013), pp. 3176–3189.

[171] Valerie Randle. “Grain boundary engineering: an overview after 25 years”. In: *Materials science and technology* 26.3 (2010), pp. 253–261.

[172] Kwang-Chon Kim et al. “Free-electron creation at the 60 twin boundary in Bi_2Te_3”. In: *Nature communications* 7.1 (2016), p. 12449.

[173] Jörn Kampmeier et al. “Suppressing twin domains in molecular beam epitaxy grown Bi_2Te_3 topological insulator thin films”. In: *Crystal growth & design* 15.1 (2015), pp. 390–394.

[174] Svetlana Borisova. “Fabrication and in-situ STM investigation of growth dynamics of semiconductor nanostructures grown by MBE”. In: (2012).

[175] Wouter Mortelmans et al. “Fundamental limitation of van der Waals homoepitaxy by stacking fault formation in WSe_2”. In: *2D Materials* 7.2 (2020), p. 025027.

[176] Muhammad Iqbal Bakti Utama et al. “Twinning-, Polytypism-, and Polarity-Induced Morphological Modulation in Nonplanar Nanostructures with van der Waals Epitaxy”. In: *Advanced Functional Materials* 23.13 (2013), pp. 1636–1646.

[177] Kuan-Chao Chen et al. “Van der Waals Epitaxy of Large-Area and Single Crystalline Gold Films on MoS_2 for Low-Contact-Resistance 2D–3D Interfaces”. In: *ACS Applied Nano Materials* 3.3 (2020), pp. 2997–3003.

[178] Danielle Reifsnyder Hickey et al. “Structure and basal twinning of topological insulator Bi_2Se_3 grown by MBE onto crystalline $Y_3Fe_5O_{12}$”. In: *Physical Review Materials* 3.6 (2019), p. 061201.

[179] Antonio M Mio et al. “Impact of bonding on the stacking defects in layered chalcogenides”. In: *Advanced Functional Materials* 29.37 (2019), p. 1902332.

[180] Xiaoxu Zhao et al. “Strain modulation by van der Waals coupling in bilayer transition metal dichalcogenide”. In: *ACS nano* 12.2 (2018), pp. 1940–1948.

[181] Seeyearl Seong et al. “Te-Te bonding in copper tellurides”. In: *Journal of the American Chemical Society* 116.16 (1994), pp. 7287–7293.

[182] Charles P Poole Jr. *Encyclopedic dictionary of condensed matter physics*. Academic Press, 2004.

[183] Tatau Nishinaga. *Handbook of crystal growth: fundamentals*. Elsevier, 2014.

[184] Bartlomiej Wiendlocha. "Resonant levels, vacancies, and doping in Bi_2Te_3, Bi_2Te_2Se, and Bi_2Se_3 tetradymites". In: *Journal of Electronic Materials* 45.7 (2016), pp. 3515–3531.

[185] Yuan Wang et al. "Enhanced thermoelectric properties of nanostructured n-type Bi_2Te_3 by suppressing Te vacancy through non-equilibrium fast reaction". In: *Chemical Engineering Journal* 391 (2020), p. 123513.

[186] VR Akshay, MV Suneesh, and M Vasundhara. "Tailoring thermoelectric properties through structure and morphology in chemically synthesized n-type bismuth telluride nanostructures". In: *Inorganic chemistry* 56.11 (2017), pp. 6264–6274.

[187] Chris G Van de Walle. *Wide-band-gap Semiconductors*. Elsevier, 2012.

[188] Michael B Bever. "Encyclopedia of materials science and engineering". In: (1985).

[189] Pekka Pyykkö and Michiko Atsumi. "Molecular single-bond covalent radii for elements 1–118". In: *Chemistry–A European Journal* 15.1 (2009), pp. 186–197.

[190] J Horak, K Čermák, and L Koudelka. "Energy formation of antisite defects in doped Sb_2Te_3 and Bi_2Te_3 crystals". In: *Journal of Physics and Chemistry of Solids* 47.8 (1986), pp. 805–809.

[191] Z Starỳ et al. "Antisite defects in $Sb_{2-x}Bi_xTe_3$ Sb2-xBixTe3 mixed crystals". In: *Journal of Physics and Chemistry of Solids* 49.1 (1988), pp. 29–34.

[192] Jixia Dai et al. "Toward the intrinsic limit of the topological insulator Bi_2Se_3". In: *Physical review letters* 117.10 (2016), p. 106401.

[193] Xian-Lei Sheng et al. "T-carbon: a novel carbon allotrope". In: *Physical review letters* 106.15 (2011), p. 155703.

[194] Beat Meyer. "Solid allotropes of sulfur". In: *Chemical reviews* 64.4 (1964), pp. 429–451.

[195] Xiaohui Ye et al. "Zero to three dimension structure evolution from carbon allotropes to phosphorus allotropes". In: *Advanced Materials Interfaces* 10.5 (2023), p. 2201941.

[196] T Nagao et al. "Nanofilm Allotrope and Phase Transformation of Ultrathin Bi Film on Si (111)-7$\times$ 7". In: *Physical review letters* 93.10 (2004), p. 105501.

[197] A Takayama et al. "One-dimensional edge states with giant spin splitting in a bismuth thin film". In: *Physical review letters* 114.6 (2015), p. 066402.

[198] Hadass S Inbar et al. "Inversion symmetry breaking in epitaxial ultrathin Bi (111) films". In: *arXiv preprint arXiv:2302.00803* (2023).

[199] Jian Gou et al. "Two-dimensional ferroelectricity in a single-element bismuth monolayer". In: *Nature* 617.7959 (2023), pp. 67–72.

[200] Maciej Jankowski et al. "Controlling the growth of Bi (110) and Bi (111) films on an insulating substrate". In: *Nanotechnology* 28.15 (2017), p. 155602.

[201] Nan Wang et al. “Investigation of growth characteristics and semimetal - semiconductor transition of polycrystalline bismuth thin films”. In: *IUCrJ* 7.1 (2020), pp. 49–57.

[202] Zijian Jiang, Victoria Soghomonian, and Jean J Heremans. “Carrier properties of Bi (111) grown on mica and Si (111)”. In: *Physical Review Materials* 6.9 (2022), p. 095003.

[203] Ikuya Kokubo et al. “Ultrathin Bi (110) films on Si (111) $3\times$ 3-B substrates”. In: *Physical Review B* 91.7 (2015), p. 075429.

[204] S Yaginuma et al. “Origin of flat morphology and high crystallinity of ultrathin bismuth films”. In: *Surface science* 601.17 (2007), pp. 3593–3600.

[205] Martin Kammler and Michael Horn-von Hoegen. “Low energy electron diffraction of epitaxial growth of bismuth on Si (111)”. In: *Surface Science* 576.1-3 (2005), pp. 56–60.

[206] T Hirahara et al. “Quantum well states in ultrathin Bi films: Angle-resolved photoemission spectroscopy and first-principles calculations study”. In: *Physical Review B—Condensed Matter and Materials Physics* 75.3 (2007), p. 035422.

[207] Yanfeng Lyu et al. “Flexible atomic buckling and homogeneous edge states in few-layer Bi(110) films”. In: *Nano Research* 15.3 (2022), pp. 2374–2381.

[208] Ph Hofmann. “The surfaces of bismuth: Structural and electronic properties”. In: *Progress in surface science* 81.5 (2006), pp. 191–245.

[209] Abdur Rehman Jalil et al. “Selective area epitaxy of quasi-1-dimensional topological nanostructures and networks”. In: *Nanomaterials* 13.2 (2023), p. 354.

[210] Dima Sadek et al. “Structural and electrical characterizations of BiSb topological insulator layers epitaxially integrated on GaAs”. In: *Crystal Growth & Design* 22.8 (2022), pp. 5081–5091.

[211] Laëtitia Baringthon et al. “Topological surface states in ultrathin $Bi_{1-x}Sb_x$ layers”. In: *Physical Review Materials* 6.7 (2022), p. 074204.

[212] Chan Wook Jang et al. “2D Weyl-Semimetal States Achieved by a Thickness-Dependent Crossover and Topological Phase Transition in Bi0.96Sb0.04 Thin Films”. In: *Advanced Functional Materials* 33.51 (2023), p. 2305179.

[213] Peter Kerres et al. “Scaling and confinement in ultrathin chalcogenide films as exemplified by gete”. In: *Small* 18.21 (2022), p. 2201753.

[214] Sandra Stanionytė et al. “The crystalline structure of thin bismuth layers grown on silicon (111) substrates”. In: *Materials* 15.14 (2022), p. 4847.

[215] SA Scott, MV Kral, and SA Brown. “A crystallographic orientation transition and early stage growth characteristics of thin Bi films on HOPG”. In: *Surface science* 587.3 (2005), pp. 175–184.

[216] Yu M Koroteev et al. “First-principles investigation of structural and electronic properties of ultrathin Bi films”. In: *Physical Review B—Condensed Matter and Materials Physics* 77.4 (2008), p. 045428.

[217] Jian Gou et al. “The effect of moiré superstructures on topological edge states in twisted bismuthene homojunctions”. In: *Science Advances* 6.23 (2020), eaba2773.

[218] Hua Zhou et al. “Interfaces between hexagonal and cubic oxides and their structure alternatives”. In: *Nature communications* 8.1 (2017), p. 1474.

[219] Martina Pilloni et al. “Thermal and structural characterization of ultrasonicated BiSn alloy in the eutectic composition”. In: *Journal of Thermal Analysis and Calorimetry* 120 (2015), pp. 1543–1551.

[220] Sotirios Fragkos et al. “Topological surface states in epitaxial $(SnBi_2Te_4)_n(Bi_2Te_3)_m$ natural van der Waals superlattices”. In: *Physical Review Materials* 5.1 (2021), p. 014203.

[221] Ananya Banik and Kanishka Biswas. “Synthetic nanosheets of natural van der Waals heterostructures”. In: *Angewandte Chemie* 129.46 (2017), pp. 14753–14758.

[222] Bryan A Kuropatwa and Holger Kleinke. “Thermoelectric properties of stoichiometric compounds in the $(SnTe)_x(Bi_2Te_3)_y$ system”. In: *Zeitschrift für anorganische und allgemeine Chemie* 638.15 (2012), pp. 2640–2647.

[223] MB Babanly et al. “Homogeneity ranges and thermodynamic properties of ternary phases in the SnTe-Bi_2Te_3-Te system”. In: *Inorganic Materials* 47.3 (2011), pp. 235–239.

[224] Rui Peng et al. “Stacking-dependent topological phase in bilayer MBi_2Te_4 (M= Ge, Sn, Pb)”. In: *Physical Review B* 101.11 (2020), p. 115427.

[225] Yunlong Li et al. “Topological Dirac surface states in ternary compounds $GeBi_2Te_4$, $SnBi_2Te_4$ and $Sn_{0.571}Bi_{2.286}Te_4$”. In: *Chinese Physics B* 30.12 (2021), p. 127901.

[226] R Vilaplana et al. “Structural and electrical study of the topological insulator $SnBi_2Te_4$ at high pressure”. In: *Journal of Alloys and Compounds* 685 (2016), pp. 962–970.

[227] Ankush Saxena et al. “Detailed structural and topological analysis of $SnBi_2Te_4$ single crystal”. In: *Journal of Physics and Chemistry of Solids* 174 (2023), p. 111169.

[228] Yi-Chao Zou et al. “Atomic disorders in layer structured topological insulator SnBi2Te4 nanoplates”. In: *Nano Research* 11 (2018), pp. 696–706.

[229] Maia G Vergniory et al. “Electronic and spin structure of a family of Sn-based ternary topological insulators”. In: *Physical Review B* 92.4 (2015), p. 045134.

[230] Sergey V Eremeev et al. “Sublattice effect on topological surface states in complex $(SnTe)_{n>1}$ $(Bi_2Te_3)_{m=1}$ compounds”. In: *Physical Review B* 91.24 (2015), p. 245145.

[231] William Henry Bragg and William Lawrence Bragg. “The reflection of X-rays by crystals”. In: *Proceedings of the Royal Society of London. Series A, Containing Papers of a Mathematical and Physical Character* 88.605 (1913), pp. 428–438.

[232] Edwin H Hall et al. “On a new action of the magnet on electric currents”. In: *American Journal of Mathematics* 2.3 (1879), pp. 287–292.

[233] JG Checkelsky et al. “Quantum interference in macroscopic crystals of nonmetallic Bi_2Se_3”. In: *Physical Review Letters* 103.24 (2009), p. 246601.

[234] Hailin Peng et al. “Aharonov-Bohm interference in topological insulator nanoribbons”. In: *Nature materials* 9.3 (2010), pp. 225–229.

[235] Hong-Tao He et al. “Impurity effect on weak antilocalization in the topological insulator Bi_2Te_3”. In: *Physical review letters* 106.16 (2011), p. 166805.

[236] Yong Seung Kim et al. “Thickness-dependent bulk properties and weak antilocalization effect in topological insulator Bi_2Se_3”. In: *Physical Review B—Condensed Matter and Materials Physics* 84.7 (2011), p. 073109.

[237] Hai-Zhou Lu and Shun-Qing Shen. “Weak localization and weak anti-localization in topological insulators”. In: *Spintronics Vii*. Vol. 9167. SPIE. 2014, pp. 263–273.

[238] Wolfgang Kuch and Claus M Schneider. “Magnetic dichroism in valence band photoemission”. In: *Reports on Progress in Physics* 64.2 (2001), p. 147.

[239] Veronika Sunko et al. “Maximal Rashba-like spin splitting via kinetic-energy-coupled inversion-symmetry breaking”. In: *Nature* 549.7673 (2017), pp. 492–496.

[240] J-S Kang et al. “Rare-earth-doped Bi_2X_3 (X=Se,Te) as candidates for magnetic topological insulators”. In: *Philosophical Magazine* 100.10 (2020), pp. 1258–1267.

[241] Franck Vidal et al. “Circular dichroism in photoemission as a fingerprint of surface band structure: The case of ZnSe (001) - c ($2\times$ 2)”. In: *Physical Review B — Condensed Matter and Materials Physics* 76.8 (2007), p. 081302.

[242] M Neupane et al. “Oscillatory surface dichroism of the insulating topological insulator Bi_2Se_2Te”. In: *Physical Review B—Condensed Matter and Materials Physics* 88.16 (2013), p. 165129.

[243] A. Crepaldi et al. “Momentum and photon energy dependence of the circular dichroic photoemission in the bulk Rashba semiconductors BiTeX (X = I, Br, Cl)”. In: *Physical Review B* 89 (2014), p. 125408.

[244] Michael Schüler et al. “How circular dichroism in time-and angle-resolved photoemission can be used to spectroscopically detect transient topological states in graphene”. In: *Physical Review X* 10.4 (2020), p. 041013.

[245] YH Wang et al. “Observation of a Warped Helical Spin Texture in Bi_2Se_3 from Circular Dichroism Angle-Resolved Photoemission Spectroscopy”. In: *Physical Review Letters* 107.20 (2011), p. 207602.

[246] H Mirhosseini and J Henk. “Spin texture and circular dichroism in photoelectron spectroscopy from the topological insulator Bi_2Te_3: first-principles photoemission calculations”. In: *Physical review letters* 109.3 (2012), p. 036803.

[247] Wonsig Jung et al. “Warping effects in the band and angular-momentum structures of the topological insulator Bi_2Te_3”. In: *Physical Review B—Condensed Matter and Materials Physics* 84.24 (2011), p. 245435.

[248] Seung Ryong Park et al. “Chiral orbital-angular momentum in the surface states of Bi_2Se_3”. In: *Physical review letters* 108.4 (2012), p. 046805.

[249] MR Scholz et al. “Reversal of the circular dichroism in angle-resolved photoemission from Bi_2Te_3”. In: *Physical Review Letters* 110.21 (2013), p. 216801.

[250] C-Z Xu et al. “Photoemission circular dichroism and spin polarization of the topological surface states in ultrathin Bi_2Te_3 films”. In: *Physical Review Letters* 115.1 (2015), p. 016801.

[251] Franck Vidal et al. “Photon energy dependence of circular dichroism in angle-resolved photoemission spectroscopy of Bi_2Se_3 Dirac states”. In: *Physical Review B* 88.24 (2013), p. 241410.

[252] RC Vidal et al. “Orbital complexity in intrinsic magnetic topological insulators $MnBi_4Te_7$ and $MnBi_6Te_{10}$”. In: *Physical review letters* 126.17 (2021), p. 176403.

[253] Jin-Hong Park et al. “Orbital Rashba effect and its detection by circular dichroism angle-resolved photoemission spectroscopy”. In: *Physical Review B—Condensed Matter and Materials Physics* 85.19 (2012), p. 195401.

[254] Shu-Hsuan Su et al. “Epitaxial growth and structural characterizations of $MnBi_2Te_4$ thin films in nanoscale”. In: *Nanomaterials* 11.12 (2021), p. 3322.

[255] Claus Michael Schneider. “F03: Photoelectron Emission Spectroscopy”. In: vol. 33. Jülich: Forschungszentrum Jülich GmbH, 2012, F3.1–F3.45.

[256] J-Q Yan et al. “A-type antiferromagnetic order in $MnBi_4Te_7$ and $MnBi_6Te_{10}$ single crystals”. In: *Physical Review Materials* 4.5 (2020), p. 054202.

[257] Karlheinz Schwarz and Peter Blaha. “Solid state calculations using WIEN2k”. In: *Computational Materials Science* 28.2 (2003), pp. 259–273.

[258] Mikhail M Otrokov et al. “Highly-ordered wide bandgap materials for quantized anomalous Hall and magnetoelectric effects”. In: *2D Materials* 4.2 (2017), p. 025082.

[259] Sergey V Eremeev et al. “Atom-specific spin mapping and buried topological states in a homologous series of topological insulators”. In: *Nature communications* 3.1 (2012), p. 635.

[260] Sara E Harrison et al. “Preparation of layered thin film samples for angle-resolved photoemission spectroscopy”. In: *Applied Physics Letters* 105.12 (2014).

[261] Honey Boban et al. “Scattering makes a difference in circular dichroic angle-resolved photoemission”. In: *arXiv preprint arXiv:2410.19652* (2024).

[262] Peter Schüffelgen et al. “Selective area growth and stencil lithography for in situ fabricated quantum devices”. In: *Nature nanotechnology* 14.9 (2019), pp. 825–831.

[263] Su-Yang Xu et al. “Hedgehog spin texture and Berry’s phase tuning in a magnetic topological insulator”. In: *Nature Physics* 8.8 (2012), pp. 616–622.

Curriculum Vitae

Personal Information

Name:	Xiao Hou
Address:	Luitpoldstr.6 82110 Germering
E-Mail:	houxiao518@gmail.com
Birthday:	25.07.1995
Nationality:	China

Education

07/2021 - 02/2025	Ph.D. at PGI-6, Forschungszentrum Jülich
07/2020 - 04/2021	Master Thesis at ERC-1, Forschungszentrum Jülich
04/2018 - 04/2021	Master of Science in Material Science, RWTH Aachen University
09/2013 - 06/2017	Bachelor of Science in Material Science and Engineering, Shandong University

Publications

Articles

A.1 Kevin Janßen, Sergej Liberda, Philipp Rüßmann, Michael Schleenvoigt, **Xiao Hou**, Abdul Rehman Jalil, Florian Lentz, Stefan Trellenkamp, Benjamin Bennemann, Erik Zimmermann, Gregor Mussler, Joachim Mayer, Peter Schüffelgen, Lukasz Plucinski, Claus-Michael Schneider, Stefan Blügel, Detlev Grützmacher, and Thomas Schäpers. Single In-Situ Interface Characterization Composed of Niobium and a Selectively Grown Topological Insulator Nanoribbon. *arXiv preprint arXiv: 2312. 07325* (2023).

A.2 Abdur Rehman Jalil*, **Xiao Hou***, Peter Schüffelgen, Jin Hee Bae, Elmar Neumann, Gregor Mussler, Lukasz Plucinski, and Detlev Grützmacher. Phase-Selective Epitaxy of Trigonal and Orthorhombic Bismuth Thin Films on Si (111). *Nanomaterials* **13(14)**, 2143 (2023).

A.3 Abdur Rehman Jalil, Tobias W. Schmitt, Philipp Rüßmann, Xian-Kui Wei, Benedikt Frohn, Michael Schleenvoigt, Wilhelm Wittl, **Xiao Hou**, Anne Schmidt,Kaycee Underwood, Gustav Bihlmayer, Martina Luysberg, Joachim Mayer, Stefan Blügel, Detlev Grützmacher, and Peter Schüffelgen. Engineering Epitaxial Interfaces for Topological Insulator —Superconductor Hybrid Devices with Al Electrodes. *Advanced Quantum Technologies* 2400343 (2024).

A.4 Honey Boban, Mohammed Qahosh, **Xiao Hou**, Tomasz Sobol, Edyta Beyer, Magdalena Szczepanik, Daniel Baranowski, Simone Mearini, Vitaliy Feyer, Yuriy Mokr ousov, Keda Jin, Tobias Wichmann, Jose Martinez-Castro, Markus Ternes, F. Stefan Tautz, Felix Lüpke, Claus M. Schneider, Jürgen Henk, Claus-Michael Schneider and Lukasz Plucinski. Scattering makes a difference in circular dichroic angle-resolved photoemission. *arXiv preprint arXiv:2410.19652* (2024).

A.5 Mohammed Qahosh, Muthu Thirugnanasambandam Masilamani, Honey Boban, **Xiao Hou**, Gustav Bihlmayer, Yuriy Mokrousov, Wael Karain, Jan Minar, Friedrich Reinert, Jakub Schusser, Claus-Michael Schneider and Lukasz Plucinski. Spin-orbital mixing in the topological ladder of the two-dimensional metal $PtTe_2$. *arXiv preprint arXiv:2502.10865* (2025).

Talks

B.1 Investigation of the V/TI interface by TEM and ARPES: first results. *ML4Q cluster, Cologne, Germany (2022).*

B.2 Epitaxy and Characterization of Bi/BiSb Thin Films *ML4Q cluster, Cologne, Germany (2024).*

B.3 Phase-Selective Epitaxy of Trigonal and Orthorhombic Bismuth Thin Films on Si (111). *DPG spring meeting, Berlin, Germany (2024).*

Poster Contributions

C.1 Investigation of the superconductor and topological insulator interface by TEM and ARPES. *DPG spring meeting, Regensburg, Germany (2022).*

C.2 Growth and structural investigation of the $Sn_xBi_yTe_z$ stoichiometric series via MBE and TEM. *DPG spring meeting, Dresden, Germany (2023).*